

Technische Universität München
TUM School of Engineering and Design

Cavitating Bubbles in Viscoelastic Fluids – Physical Modeling and Numerical Simulations

Christian Lang

Vollständiger Abdruck der von der TUM School of Engineering and Design der Technischen Universität München zur Erlangung eines

Doktors der Ingenieurwissenschaften (Dr.-Ing.)

genehmigten Dissertation.

Vorsitz: Prof. Dr. Dongsheng Wen

Prüfende der Dissertation:

1. Prof. Dr.-Ing. Nikolaus A. Adams
2. Prof. Eric Johnsen, Ph.D.
3. Prof. Mengqi Zhang, Ph.D.

Die Dissertation wurde am 05.12.2023 bei der Technischen Universität München eingereicht und durch die TUM School of Engineering and Design am 24.04.2024 angenommen.

© Christian Lang, 2023
c.lang@tum.de

All rights reserved. No part of this publication may be reproduced, modified, re-written or distributed in any form or by any means without prior written permission of the author.

Typesetting \LaTeX

Abstract

This work aims to numerically investigate the influence of viscoelastic fluids on cavitating flows, precisely cavitation bubble dynamics. Cavitating bubbles occur in various engineering applications involving complex fluids with fundamentally different behavior than Newtonian liquids. Due to the underlying complex microstructure, especially in biomechanical and biomedical applications as well as in polymer processing, viscoelastic effects are encountered. The work presents a three-dimensional (3D) Eulerian approach to numerically simulate cavitating flows in viscoelastic fluids. It utilizes a density-based compressible flow solver with finite volumes for spatial, and an explicit Runge-Kutta approach for time discretization. Viscoelasticity is considered by implementing four different Maxwell-/Oldroyd-like viscoelastic models in conservative form with an appropriate time-derivative in the viscoelastic transport equation regarding compressible flow.

The simulations show a significant influence of viscoelasticity on the spherical and aspherical vapor bubble collapse dynamics. For the spherical collapse, it is demonstrated that viscoelasticity and the related stresses yield a rebounding bubble which is not observed for Newtonian fluids. Collapse behavior is investigated for various elasticity, viscosity and constitutive models. It is shown that viscoelasticity fundamentally alters the collapse behavior and evolution of stresses. It is observed that the viscoelastic stresses develop with a time delay proportional to relaxation and show distinct spatial distributions as opposed to solvent (Newtonian) stresses. Furthermore, it is shown that viscoelasticity introduces isentropic stresses, although the spherical bubble collapse exhibits purely deviatoric (elongational) deformation rates. Additionally, it is demonstrated that the different viscoelastic models distinctly impact the collapse. Moreover, grid-dependent shock-wave emission is observed for the spherical collapse in upper convected Maxwell fluid.

The aspherical collapse is examined for the shear-thinning simplified linear Phan-Thien Tanner fluid. The comparison of the collapse in Newtonian and viscoelastic fluid for different initial standoff distances shows significantly different collapse dynamics. For initially detached bubbles, the shock-wave formation mechanism during first collapse and the amount of vapor produced during rebound is altered by viscoelasticity. The intensity of shock-wave emission is comparable for both fluids or increased for Newtonian fluid for the first collapse of the investigated wall-detached bubbles. The pressure for detached bubbles resulting from the second collapse is higher in viscoelastic fluid. Only the viscoelastic fluid leads to a second jet formation for the initially detached bubbles. The attached bubbles show re-evaporation and a second collapse only for the viscoelastic collapse. The responsible viscous and viscoelastic stress distributions are reviewed, clearly showing the influence of stresses on the amount of vapor produced during rebound. The viscoelastic stresses exhibit a different spatial distribution than solvent stresses caused by relaxation. Additionally, the influence of varying elasticity shows the correlation between relaxation time and re-evaporation.

Kurzfassung

Ziel dieser Arbeit ist es, den Einfluss viskoelastischer Fluide auf kavitierende Strömungen, genauer die Dynamik von Kavitationsblasen, numerisch zu untersuchen. Kavitierende Blasen treten in einer Vielzahl von Ingenieur Anwendungen mit komplexen Fluiden, welche im Vergleich zu Newtonschen Flüssigkeiten grundlegend unterschiedliches Verhalten aufweisen, auf. Wegen der zugrunde liegenden komplexen Mikrostruktur treten insbesondere in biomechanischen und biomedizinischen Anwendungen sowie bei der Verarbeitung von Polymeren viskoelastische Effekte auf. Die Arbeit stellt einen dreidimensionalen Eulerschen Ansatz zur numerischen Simulation von kavitierenden Strömungen in viskoelastischen Fluiden vor. Dabei wird ein dichtebasierter, kompressibler Strömungslöser mit Finiten Volumen für die räumliche Diskretisierung und eine explizite Zeitintegration für die zeitliche Diskretisierung verwendet. Die Viskoelastizität wird durch vier verschiedenen Maxwell-/Oldroyd-ähnliche zeitabhängige viskoelastischen Modellen in konservativer Form berücksichtigt, wobei eine geeignete Zeitableitung in der viskoelastischen Transportgleichung im Hinblick auf kompressible Strömungen angewandt wird.

Die Simulationen zeigen einen deutlichen Einfluss von Viskoelastizität auf die Dynamik des sphärischen und asphärischen Dampfblasenkollapses. Für den sphärischen Kollaps wird gezeigt, dass Viskoelastizität und die damit verbundenen Spannungen zu einer wieder anwachsenden Blase führen, was für Newtonsche Flüssigkeiten nicht beobachtet werden kann. Das Kollapsverhalten wird für verschiedene Elastizitäten, Viskositäten und Konstitutivmodelle untersucht. Es wird gezeigt, dass Viskoelastizität das Kollapsverhalten und die Entwicklung von Spannungen grundlegend beeinflusst. Weiterhin wird beobachtet, dass die viskoelastischen Spannungen mit einer zeitlichen Verzögerung, proportional zur Relaxationszeit, auftreten und eine deutlich veränderte räumliche Verteilung im Vergleich zu Newtonschen Spannungen aufweisen. Darüber hinaus wird gezeigt, dass Viskoelastizität isentrope Spannungen erzeugt, obwohl der sphärische Blasen-kollaps rein deviatorische Verformungsraten (reine Elongation) aufweist. Es wird deutlich, dass die verschiedenen viskoelastischen Modelle den Kollaps unterschiedlich beeinflussen. Für den sphärischen Kollaps mit dem Upper Convected Maxwell-Fluid wird ein gitterabhängiges Auftreten von Schockwellen beobachtet.

Der asphärische Kollaps wird für das scherverdünnende vereinfachte lineare Phan-Thien Tanner-Fluid untersucht. Der Vergleich des Kollapses in Newtonschen und viskoelastischen Fluiden für verschiedene Anfangsabstände zeigt eine deutlich veränderte Kollapsdynamik. Bei anfänglich nicht anliegenden Blasen werden der Mechanismus der Schockwellenbildung während des ersten Kollapses und die Menge des erzeugten Dampfes, während die Blase wieder anwächst, durch Viskoelastizität beeinflusst. Die Intensität der Schockwellenemission ist für den ersten Kollaps der untersuchten nicht anliegenden Blasen vergleichbar für beide oder verstärkt für Newtonsche Flüssigkeiten. Der Druck für nicht anliegende Blasen, der aus dem zweiten Kollaps resultiert, ist in viskoelastischem Fluid höher. Für die anfänglich nicht anliegenden Blasen führt nur das viskoelastische Fluid zur Bildung eines zweiten Jets. Bei anfänglich anliegenden Blasen treten Dampf nach dem ersten Kollaps und ein zweiter Kollaps nur im viskoelastischen Fall auf. Die zugrunde liegenden viskosen und viskoelastischen Spannungsverteilungen werden für die verschiedenen Fälle dargestellt, wobei der Einfluss der auftretenden Spannungen auf die Menge des während des Wiederaanwachsens erzeugten

Dampfes deutlich gezeigt wird. Die viskoelastischen Spannungen zeigen unterschiedliche räumliche Verteilungen im Vergleich zu Newtonschen Spannungen, zurückzuführen auf Relaxation. Darüber hinaus zeigt der Einfluss variabler Elastizität die Korrelation zwischen Relaxationszeit und beim Wiederaanwachsen erzeugtem Dampf auf.

Danksagung

An dieser Stelle möchte ich all jenen meinen herzlichen Dank aussprechen, die auf verschiedenste Art und Weise zum Erfolg der Arbeit einen Beitrag leisteten.

Zuerst danke ich meinem Doktorvater Prof. Nikolaus A. Adams. Vielen Dank für Ihr Vertrauen, wodurch ich mich extrem weiterentwickeln konnte. Die entgegengebrachten Freiheiten und Ihre gleichzeitige Rückendeckung haben dazu beigetragen, dass ich mich immer wohl gefühlt habe. Vielen Dank für Ihre Unterstützung und dass Sie mir den Forschungsaufenthalt in Singapur ermöglichten. Und danke für Ihre Loyalität und Verbindlichkeit, auf Ihr Wort ist Verlass, das erleichtert einem den Alltag als Doktorand und erlaubt es, sich auf die wichtigen Dinge zu konzentrieren.

I want to thank my co-examiners Prof. Mengqi Zhang and Prof. Eric Johnsen. Your interest in my research and the generous invest of your time are immensely appreciated. I must express a special thank you to Mengqi for the warm welcome extended to me in Singapore and for the significant contribution to my second journal publication. Moreover, your visit in Munich was an absolute pleasure, and I am very grateful for the wonderful time we shared.

Ein besonderer Dank gilt Marcus und Stefan, die zu sehr guten Freunden geworden sind. Jeder hat mir auf seine Art in vielen Dingen geholfen und in Herausforderungen zur Seite gestanden. Von Euch habe ich viel gelernt. Vielen Dank. Ich möchte mich außerdem bei Steffen bedanken. Du hast mir geholfen am AER Doktorand werden zu können und mir fachliche Fragen im italienischen Lieblingsrestaurant beantwortet. Weiterhin möchte ich allen Kollegen, die zu mehr als Kollegen geworden sind und meine Zeit geprägt haben, danken. Auch wenn ich Gefahr laufe jemanden zu vergessen: Danke Aaron, Alex, Benedikt, Christopher, David, Deniz, Fabian, Jakob, Josef, Julian, Leopold, Nico, Nils, Rim, Sebastian und Thomas. Ihr habt den Lehrstuhl zu einem Ort gemacht, an dem ich immer gerne war. Die Zeit mit Euch war nicht nur fachlich eine Bereicherung. Außerdem danke ich meinen ehemaligen Studenten Maximilian, Oliver und Ulrich, die im Rahmen von studentischen Arbeiten maßgeblich zum Erfolg beigetragen haben. Und vielen Dank Martin, meinem ersten Mentor im akademischen Umfeld, ohne den ich wahrscheinlich nicht auf die Idee gekommen wäre zu promovieren.

Der größte Dank gebührt meiner Familie, meinen Freunden und Annika. Meinen Eltern und meiner Schwester danke ich für alle schönen Momente, euer Ermutigen und unseren Familienzusammenhalt. Von Herzen vielen Dank für eure bedingungslose Unterstützung. Auch meinen Großeltern danke ich, Ihr habt an mich geglaubt und mich unterstützt. Ich bin sehr froh, dass Ihr diesen Moment mit mir teilen dürft. Dankbar bin ich meinen engen Freunden (Andreas, Benjamin, Dr., Emil, Felix, Fridolin, Julian, Lorin, Martin, Matthias, Peter, Simon, Stefan), die mit ihren unterschiedlichen Herkünften und Interessen Ausgleich und Rückhalt bieten. Außerdem bedanke ich mich bei einer ganz besonderen Person in meinem Leben, die mich in den letzten Jahren begleitet. Die mir Zuversicht gibt, wenn ich zweifle, mich dazu ermutigt, Dinge einfach zu machen, die ich sonst nicht wagen würde und mit der ich immer wieder unvergessliche Momente erlebe. Vielen Dank Annika, ich freue mich auf unsere gemeinsame Zukunft.

Contents

1	Introduction and Motivation	1
2	Model and Numerical Approach	3
2.1	Mathematical and physical model	3
2.1.1	Conservation equations in differential form	3
2.1.2	Compressible viscoelastic constitutive model of the Maxwell-/ Oldroyd-type	3
2.1.3	Conservative form of the governing equations	8
2.1.4	Single fluid homogeneous mixture cavitation model	9
2.1.5	Non-dimensional numbers	11
2.2	Numerical approach	13
2.2.1	Spatial discretization and numerical flux calculation	13
2.2.2	Explicit time discretization	14
2.2.3	Classification and eigenvalue calculation of the quasi-linear system . . .	15
2.2.4	Boundary conditions	17
2.2.5	Sequences of the numerical algorithm	21
3	Summary and Accomplishments	23
3.1	<i>A compressible 3D finite volume approach for the simulation of unsteady vis- coelastic cavitating flows</i>	23
3.2	<i>On spherical vapor bubble collapse in viscoelastic fluids</i>	26
3.3	<i>Viscoelastic vapor bubble collapse near solid walls and corresponding shock wave formation</i>	29
4	List of Publications	33
5	Concluding Discussion with Respect to the State of the Art	34
A	Peer-Reviewed Journal Publications	38
A.1	<i>A compressible 3D finite volume approach for the simulation of unsteady vis- coelastic cavitating flows</i>	38
A.2	<i>On spherical vapor bubble collapse in viscoelastic fluids</i>	57
A.3	<i>Viscoelastic vapor bubble collapse near solid walls and corresponding shock wave formation</i>	82

Chapter 1

Introduction and Motivation

Cavitation can be defined as the phenomenon that arises when the fluid pressure falls below the vapor pressure, causing the liquid to undergo phase change and the formation of vapor-filled cavities. Subsequently, if the pressure rises above the vapor pressure, the vapor condensates, leading to the collapse of these cavities. The collapse of cavitating vapor bubbles can generate intense pressure wave emission and may give rise to the formation of liquid jets. Consequently, the emitted pressure waves and liquid jets can exert a significant pressure impact on the surrounding medium, which can lead to surface erosion. Engineering problems include applications where surface erosion is harmful and unwanted such as liquid fuel injectors [38], pumps and ship propellers [26]. However, there also exist applications like surface cleaning [101] and biomedical applications [19, 30, 64, 67, 85, 100, 116, 141], where cavitation is beneficial. In several of these applications, cavitation occurs in complex fluids. When dealing with such fluids involving complex microstructure with long-chained molecules, the physical behavior of the fluid cannot be accurately described using Newtonian models. However, a non-Newtonian behavior can be observed. Many of these fluids can be characterized as viscoelastic, as they simultaneously exhibit viscous and elastic properties. Cavitation bubbles appear in various application scenarios of such materials. In biomaterials, cavitation bubbles are exploited in applications such as drug delivery [30, 85, 100, 116], shock-wave lithotripsy [64], histotripsy [141], and microbubble contrast agents for ultrasound diagnostics and treatment [19, 67]. Other applications involving cavitation in complex fluids are the usage of ultrasonics in food processing [17], rheological measurements for the determination of material properties [123, 145], and polymeric foam production [39].

Several experimental [7, 10, 25, 145] and numerical studies [4, 5, 24, 45, 46, 70, 79, 132, 143, 150] proved that viscoelastic material behavior can crucially influence cavitation and bubble dynamics. A comprehensive summary on cavitating flow applications in viscoelastic media is provided by Brujan [23] and Dollet et al. [33]. This work aims to obtain detailed insight in the influence of viscoelasticity on the spherical and aspherical vapor bubble collapse considering cavitation, compressible shock wave formation, and different viscoelastic constitutive models. For cavitating vapor bubbles considering condensation and evaporation, it is necessary to apply an appropriate cavitation model. Furthermore, resolving compressible shock-wave dynamics requires a fully-compressible approach to capturing the related time scales. Additionally, for a detailed understanding of the influence of viscous and viscoelastic stresses, it is necessary to employ a 3D approach considering stresses in the entire flow field.

The three peer-reviewed journal publications on which this work is based can be summarized as follows. In Lang et al. [75], an approach meeting the above-mentioned requirements is presented. A fully compressible 3D solver using finite volume spatial discretization and explicit time integration resolving the relevant timescales is combined with viscoelastic constitutive models of the Oldroyd-type in conservative formulation. Furthermore, the appropriate time derivative for viscoelastic stresses in compressible flows is derived, and the explicit time integration is adapted. The approach is validated against (semi-)analytical reference solutions with excellent agreement. A significant influence of viscoelasticity on the spherical vapor bubble collapse and the corresponding shock wave emission is shown. In the second study Lang et al. [78], the approach is used to investigate the spherical vapor bubble collapse in viscoelastic fluids. 3D simulations of the collapse with varying elasticity, viscosity, and for distinct viscoelastic models are carried out. Moreover, collapse dynamics, occurring deformations, stress distributions, and the emission of shock waves are presented. The third study Lang et al. [74] examines the aspherical viscoelastic collapse in the vicinity of solid walls. The collapse dynamics and the shock wave formation mechanism for Newtonian and viscoelastic fluids are compared for different initial standoff distances. Furthermore, the influence of varying elasticity is studied. It is shown that viscoelasticity can significantly alter the collapse dynamics, shock wave formation, and the amount of re-evaporated vapor during rebound.

The work is structured as follows. Firstly, the theoretical foundation, including the underlying models and corresponding equations, is presented. Subsequently, the numerical approach and the applied boundary conditions are discussed. Furthermore, the journal publications are summarized, and the own contribution is outlined. In the following a list of the journal publications, and a concluding discussion with respect to the state of the art is given.

Chapter 2

Model and Numerical Approach

2.1 Mathematical and physical model

2.1.1 Conservation equations in differential form

Unsteady, three-dimensional, compressible, and cavitating flow is considered together with constitutive equations for viscoelastic fluids in an Eulerian framework. The phase change is assumed to be isentropic, and hence a barotropic equation of state is applied. The internal energy can be changed by viscous dissipation or shock wave formation, which is effectively negligible for the investigated problems. Furthermore, the temperature changes due to the isentropic phase change are negligibly small, and the heat capacity of the liquid phase is relatively large. Consequently, the changes in internal energy are not considered. By neglecting the surface tension and gravitational forces, the governing equations are the conservation equations for mass and momentum. The differential form of the conservation equations read:

$$\frac{\partial \rho}{\partial t} = -\text{div}(\rho \mathbf{u}), \quad (2.1)$$

$$\frac{\partial (\rho \mathbf{u})}{\partial t} = -\text{div}(\rho \mathbf{u} \otimes \mathbf{u} - \boldsymbol{\sigma}). \quad (2.2)$$

Therein, $\rho = \rho(\mathbf{x}, t)$, $\mathbf{u} = \mathbf{u}(\mathbf{x}, t)$ and $\boldsymbol{\sigma} = \boldsymbol{\sigma}(\mathbf{x}, t)$ represent the density field, the velocity field and the Cauchy stress tensor field in the current configuration and for the time instant t , respectively. Surface tension is neglected, wherefore the Cauchy stress tensor is composed of the isentropic contribution of thermodynamic pressure $p = p(\mathbf{x}, t)$ and the additional stress tensor $\boldsymbol{\tau}$.

$$\boldsymbol{\sigma} = -p\mathbf{I} + \boldsymbol{\tau}. \quad (2.3)$$

2.1.2 Compressible viscoelastic constitutive model of the Maxwell-/Oldroyd-type

There are mainly three mechanisms underlying most viscoelastic effects. Firstly, due to its concurrently viscous and elastic behavior, a specific part of deformation is stored elastically, whereas the other part causes dissipation. As a result, viscoelastic materials exhibit a time-

dependent stress or fading memory behavior. Viscoelastic stresses depend not only on the current shear rate but also on past deformations and past viscoelastic stresses. In contrast to Newtonian fluids, that leads, amongst others, to the convective transport of viscoelastic stresses. Furthermore, the time dependency introduces time-delayed stress development, where the stress is not directly linked to the current deformation rate. Secondly, due to the complex microstructure, normal stress effects can occur, introducing normal stresses in pure shear deformations. Third, viscoelasticity can introduce shear rate-dependent viscosities resulting in shear-thinning or -thickening behavior.

The employed viscoelastic models are of the Maxwell-/Oldroyd-type. Thus, the additional stress tensor comprises Newtonian (solvent) stresses τ_s and viscoelastic stresses τ_M . The viscoelastic stresses are also denoted as Maxwell stresses in the following. The constitutive equations for the applied Maxwell-/Oldroyd-like models read

$$\boldsymbol{\tau} = \boldsymbol{\tau}_s + \boldsymbol{\tau}_M, \quad (2.4)$$

$$\boldsymbol{\tau}_s = 2\mu_s \mathbf{d}^d \quad (2.5)$$

$$\boldsymbol{\tau}_M + \lambda \overset{\nabla}{\boldsymbol{\tau}}_M + f(\boldsymbol{\tau}_M) \boldsymbol{\tau}_M = 2\mu_M \mathbf{d}^d, \quad (2.6)$$

where $\mathbf{d}^d = \mathbf{d} - \frac{1}{3} \text{tr}(\mathbf{d}) \mathbf{I}$ is the deviatoric part of the strain rate tensor $\mathbf{d} = \frac{1}{2}(\mathbf{l} + \mathbf{l}^T)$, which itself represents the symmetrical part of the spatial velocity gradient $\mathbf{l} = \nabla \mathbf{u}$. The solvent viscosity is described by μ_s . μ_M represents the polymeric viscosity, denoted as Maxwell viscosity. $\lambda = \frac{\mu_M}{G}$ represents the relaxation time and relates the Maxwell viscosity to the modulus of elasticity. $\overset{\nabla}{\boldsymbol{\tau}}_M$ is the objective time derivative of the Maxwell stress tensor and is discussed in detail in the following subsection 2.1.2. By the additional parameter f , different viscoelastic models can be realized, as described hereunder. The one-dimensional (1D) rheological representation for such models is a dashpot, representing the Newtonian solvent contribution, in parallel arrangement to a Maxwell element as shown in fig. 2.1. The Maxwell element, responsible for the viscoelastic behavior, including relaxation, contains a series arrangement of dashpot and spring. The capability of predicting the aforementioned effects is summarized in section 2.1.2 for the applied models.

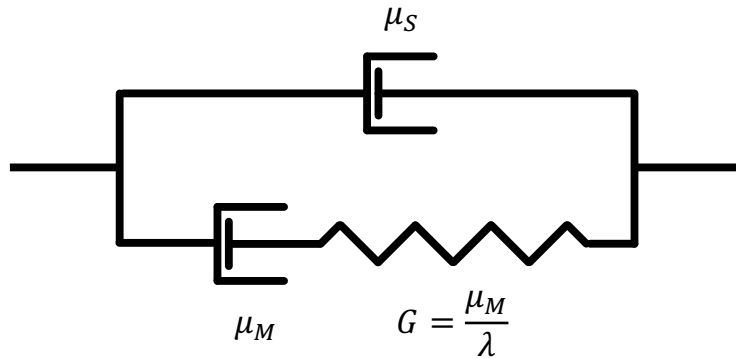


Figure 2.1: Schematic 1D rheological representation of materials of the Oldroyd-type (parallel arrangement of dashpot and Maxwell element; Maxwell element is represented by series arrangement of dashpot and spring).

By assuming that only deviatoric deformations contribute to viscous dissipation, compressibility is considered for the Newtonian as well as for the viscoelastic contributions (cf. [14, 68, 69, 104]). The isentropic part, responsible for purely volumetric deformation, does not contribute to viscous dissipation. Accordingly, bulk viscosity, which considers viscous stresses introduced by volume change, is neglected. However, the applied objective rate (eq. (2.15)) can introduce a nonzero trace $\text{tr}(\tau_M) \neq 0$ in the Maxwell stress leading to isotropic (spherical) Maxwell stresses $\tau_M^{sph} \neq \mathbf{0}$ as shown in Lang et al. [78]. The approach is similar to the formulation of Keshtiban et al. [68, 69] and Belblidia et al. [14] but differs in not explicitly excluding the isotropic part of the stress tensor τ . Otherwise put, isotropic stresses initiated by the objective rate, which is associated with the deformation itself, would not contribute to the momentum equation (2.2) if the isotropic part would be excluded. The physical motivation for such formulation is that spherical stresses, which occur due to deformation and involved transformations ensuring frame invariance (see section 2.1.2), shall be considered in the momentum balance. Bollada et al. [21] support this approach by applying non-equilibrium thermodynamics to show that the thermodynamic pressure p and the trace of the Cauchy stress tensor $\text{tr}(\sigma)$ should not necessarily coincide. Our formulation of the constitutive equations agrees with that of Housiadas et al. [56, 57]. Moreover, a different objective time derivative is used with the Truesdell rate, which appears more appropriate for compressible flows.

Furthermore, the viscoelastic transport equation can be extended by an additional term $f(\tau_M)$. The modification addresses the issue of an unbounded extensional viscosity and can account for the description of shear-thinning behavior [20, 80, 107]. Different constitutive models can be recovered by using a differential constitutive equation of the type of eq. (2.6) like the Johnson and Segalman [66], the Giesekus [49, 50] and the Phan-Thien Tanner (PTT) model [109, 110]. The PTT model originates from the network theory of polymeric fluids, predicts bounded extensional viscosity and shear thinning behavior, and is well suited to simulate flows of polymer melts and solutions. For this work, the upper-convected Maxwell (UCM) model, the Oldroyd-B (OLD-B) model [102, 103], the linear PTT (LPPT) [109] and the exponential PTT (EPPT) [110] model are implemented. The simplified versions of the PTT models are utilized where the Truesdell rate replaces the originally used Gordon-Schowalter rate. By selecting the upper-convected derivative as objective rate and $f(\tau_M) = 0$, the original Oldroyd-B model (OLD-B) is regained. By additionally neglecting the solvent part and exclusively considering the Maxwell part for the stress tensor, the upper-convected Maxwell model (UCM) is recovered. Nevertheless, throughout this work, the UCM and the OLD-B model are exclusively employed together with the Truesdell rate. The PTT models comprise the extensibility parameter $\epsilon = [0, 1]$. A commonly used value of $\epsilon = 0.25$ is chosen for the LPPT or the EPPT model.

Objective time derivative for the stress tensor in the context of compressible flows

Particular attention is paid to using a consistent time derivative for the stress tensor $\overset{\nabla}{\tau}_M$ in the context of compressible flows. The correct formulation of the time derivative has to fulfill the following requirements. To obtain a frame invariant description of the material behavior, it is necessary to observe the principle of material objectivity or material frame invariance [54,

Table 2.1: Applied viscoelastic models and their features.

Model	Solvent viscosity	$f(\boldsymbol{\tau}_M)$	Features			
			relaxation	normal stress effects	solvent contribution	shear-thinning
Newtonian	$\neq 0$	0			•	
UCM	0	0	•	•		
OLD-B	$\neq 0$	0	•	•	•	
LPTT	$\neq 0$	$\epsilon \frac{\lambda}{\mu_M} \text{tr}(\boldsymbol{\tau}_M)$	•	•	•	•
EPTT	$\neq 0$	$\exp\left(\epsilon \frac{\lambda}{\mu_M} \text{tr}(\boldsymbol{\tau}_M)\right) - 1$	•	•	•	•

137], i.e. to apply an objective time derivative. However, an infinite number of time derivatives meet this criterion [92]. A time rate shall be used, which is also physically consistent with compressible flows. Therefore, the stricter restriction of work conjugacy shall be fulfilled additionally [15, 62]. The concept of deriving the physically correct time derivative by applying the Lie derivative $\mathcal{L}_{\mathbf{u}}$ with respect to the spatial velocity field \mathbf{u} [35, 112] adapted to compressible flow is applied. To calculate the Lie derivative, a mapping between the current (spatial) and the material (reference) configuration is introduced. The mapping is given by the deformation gradient \mathbf{F} . \mathbf{F} maps an infinitesimal material element in reference configuration $d\mathbf{X}_0$ onto its spatial counterpart in the current configuration $d\mathbf{x}$, given a motion defined by the current position of a point $\mathbf{x} = \mathbf{x}(\mathbf{X}_0, t)$ with its position in the reference configuration $\mathbf{X}_0 = \mathbf{x}(\mathbf{X}_0, t = t_0)$:

$$\mathbf{F} := \frac{\partial \mathbf{x}}{\partial \mathbf{X}_0}. \quad (2.7)$$

For a second order tensor \mathbf{a} in the current configuration, the pull-back operation¹ is

$$\phi^*(\mathbf{a}) := \mathbf{F}^{-1} \mathbf{a} \mathbf{F}^{-T}. \quad (2.8)$$

The corresponding operation transforming a tensor \mathbf{A} in the reference configuration to its spatial description is called push-forward:

$$\phi_*(\mathbf{A}) := \mathbf{F} \mathbf{A} \mathbf{F}^T. \quad (2.9)$$

The concept of finding the objective rate of a tensor field described in the Eulerian configuration is initially performing a pull-back operation to obtain the corresponding tensor field in the reference configuration. Subsequently, the material time derivative $\frac{D(\dots)}{Dt}$ of the field in the reference configuration is calculated. Since that configuration remains unchanged, performing the material time derivative of an objective tensor in the reference configuration again results in an objective tensor. Finally, the push-forward operation is applied, and the

¹Note that contravariant coordinates in conjunction with a covariant basis are assumed to obtain these forms of the pull-back and push-forward. For other isomers used to describe the tensor fields, the pull-back and push-forward operations have a different form. Yet, it can be shown that the representation mentioned above should be used for a physically consistent formulation [130].

objective time derivative in spatial description is obtained. Thus, the objective rate is given by

$$\mathcal{L}_{\mathbf{u}}[\mathbf{a}] := \phi_* \left[\frac{D}{Dt} (\phi^*(\mathbf{a})) \right] =: \overset{\nabla}{\mathbf{a}}. \quad (2.10)$$

Since the stress tensor in the spatial configuration represents a volume-specific quantity, compressibility must be considered for the pull-back and push-forward operations. To consider volume changes, the Jacobian J is introduced:

$$J := \det \mathbf{F} = \frac{dv}{dV_0}. \quad (2.11)$$

The Jacobian relates the differential volume element in the spatial configuration dv to the one in reference configuration dV_0 .

The concept of the Lie derivative is applied to a volume-specific quantity as performed similarly in Pinsky et al. [112]. The objective rate of the Cauchy stress tensor $\boldsymbol{\sigma}$ in spatial configuration is calculated by using the material counterpart represented by the second Piola-Kirchhoff stress tensor $\mathbf{S}(\mathbf{X}_0)$. The corresponding transformation acting as pull-back of $\boldsymbol{\sigma}$ and push-forward of \mathbf{S} is the Piola transformation:

$$\mathbf{S} = \phi^*(\boldsymbol{\sigma}) := J \mathbf{F}^{-1} \boldsymbol{\sigma} \mathbf{F}^{-T}, \quad (2.12)$$

$$\boldsymbol{\sigma} = \phi_*(\mathbf{S}) := J^{-1} \mathbf{F} \mathbf{S} \mathbf{F}^T. \quad (2.13)$$

Thus, the objective rate of the Cauchy stress calculates to

$$\begin{aligned} \overset{\nabla}{\boldsymbol{\sigma}} &= \phi_* \left[\frac{D}{Dt} (\phi^*(\boldsymbol{\sigma})) \right] = \\ &= \frac{D\boldsymbol{\sigma}}{Dt} - \mathbf{l} \cdot \boldsymbol{\sigma} - \boldsymbol{\sigma} \cdot \mathbf{l}^T + \text{tr}(\mathbf{l}) \boldsymbol{\sigma}, \end{aligned} \quad (2.14)$$

which is called Truesdell rate [135, 136]. Since the Truesdell rate is linear in its argument and the Cauchy stress tensor is an additive combination of pressure, solvent stress, and Maxwell contribution $\boldsymbol{\sigma} = -p\mathbf{I} + 2\mu_s \mathbf{d}^d + \boldsymbol{\tau}_M$, it can be directly applied to the Maxwell stress tensor:

$$\overset{\nabla}{\boldsymbol{\tau}}_M = \frac{D\boldsymbol{\tau}_M}{Dt} - \mathbf{l} \cdot \boldsymbol{\tau}_M - \boldsymbol{\tau}_M \cdot \mathbf{l}^T + \text{tr}(\mathbf{l}) \boldsymbol{\tau}_M. \quad (2.15)$$

For incompressible flows with $\text{tr}(\mathbf{l}) = \text{div}(\mathbf{u}) = 0$ the upper-convected Oldroyd rate [102] is retrieved.

As already mentioned, the derived Truesdell rate not only represents an objective time derivative but also fulfills the requirement of work conjugacy which has been proven by Bazant [11], Bažant et al. [12], Bergander [15], and Ji et al. [62]. Bollada et al. [21] deploying the integral form of constitutive models and convected time derivatives also concluded that the Truesdell rate is appropriate in a compressible context. Rouhaud et al. [120] utilize the four-dimensional formalism “to show [that] the Truesdell transport is thus the only objective transport that represents a frame-indifferent time derivative of the Cauchy stress.” Mackay et al. [93] used the generalized bracket framework to ascertain that the Truesdell

rate constitutes the thermodynamically consistent objective rate in compressible viscoelastic fluid models.

2.1.3 Conservative form of the governing equations

By substituting the mass conservation eq. (2.1) in the transport equation for the Maxwell stress eq. (2.6), the governing equations are reformulated in conservative form for an arbitrary spatial control volume $\mathcal{V} \in \mathbb{R}^3$ as follows:

$$\int_{\mathcal{V}} \frac{\partial \rho}{\partial t} dV = - \int_{\mathcal{V}} \nabla \cdot (\rho \mathbf{u}) dV, \quad (2.16)$$

$$\int_{\mathcal{V}} \frac{\partial (\rho \mathbf{u})}{\partial t} dV = - \int_{\mathcal{V}} \nabla \cdot (\rho \mathbf{u} \otimes \mathbf{u} + p \mathbf{I} - 2\mu_S \mathbf{d}^d - \boldsymbol{\tau}_M) dV, \quad (2.17)$$

$$\int_{\mathcal{V}} \frac{\partial (\rho \boldsymbol{\tau}_M)}{\partial t} dV = - \int_{\mathcal{V}} \nabla \cdot (\rho \boldsymbol{\tau}_M \otimes \mathbf{u}) dV + \int_{\mathcal{V}} \mathbf{s}_{\rho \boldsymbol{\tau}_M} dV, \quad (2.18)$$

with the source term

$$\mathbf{s}_{\rho \boldsymbol{\tau}_M} = \rho \left[\mathbf{l} \cdot \boldsymbol{\tau}_M + \boldsymbol{\tau}_M \cdot \mathbf{l}^T - (\nabla \cdot \mathbf{u}) \boldsymbol{\tau}_M + \frac{1}{\lambda} [2\mu_M \mathbf{d}^d - f(\boldsymbol{\tau}_M) \boldsymbol{\tau}_M - \boldsymbol{\tau}_M] \right]. \quad (2.19)$$

By introducing the state vector $\mathbf{U} = [\rho, \rho \mathbf{u}, \rho \boldsymbol{\tau}_M]^T$, applying Gauss' theorem and group convective fluxes, diffusive fluxes and source terms together, the governing equations can be written in compact notation:

$$\int_{\mathcal{V}} \frac{\partial \mathbf{U}}{\partial t} dV = - \oint_{\partial \mathcal{V}} (\mathbf{F}^c + \mathbf{F}^d) dS + \int_{\mathcal{V}} \mathbf{s} dV, \quad (2.20)$$

with the convective flux, the diffusive flux and the source term

$$\mathbf{F}^c = \begin{bmatrix} F_{\rho}^c \\ \mathbf{F}_{\rho \mathbf{u}}^c \\ \mathbf{F}_{\rho \boldsymbol{\tau}_M}^c \end{bmatrix} = \begin{bmatrix} (\rho \mathbf{u}) \cdot \mathbf{n} \\ (\rho \mathbf{u} \otimes \mathbf{u} + p \mathbf{I}) \cdot \mathbf{n} \\ (\rho \boldsymbol{\tau}_M \otimes \mathbf{u}) \cdot \mathbf{n} \end{bmatrix}, \quad (2.21)$$

$$\mathbf{F}^d = \begin{bmatrix} F_{\rho}^d \\ \mathbf{F}_{\rho \mathbf{u}}^d \\ \mathbf{F}_{\rho \boldsymbol{\tau}_M}^d \end{bmatrix} = \begin{bmatrix} 0 \\ (-2\mu_S \mathbf{d}^d - \boldsymbol{\tau}_M) \cdot \mathbf{n} \\ \mathbf{0} \end{bmatrix}, \quad (2.22)$$

$$\mathbf{s} = \begin{bmatrix} 0 \\ \mathbf{0} \\ \mathbf{s}_{\rho \boldsymbol{\tau}_M} \end{bmatrix} = \begin{bmatrix} 0 \\ \mathbf{0} \\ \rho \left[\mathbf{l} \cdot \boldsymbol{\tau}_M + \boldsymbol{\tau}_M \cdot \mathbf{l}^T - (\nabla \cdot \mathbf{u}) \boldsymbol{\tau}_M + \frac{1}{\lambda} (2\mu_M \mathbf{d}^d - f(\boldsymbol{\tau}_M) \boldsymbol{\tau}_M - \boldsymbol{\tau}_M) \right] \end{bmatrix}, \quad (2.23)$$

where \mathbf{n} describes the outward pointing unit normal vector perpendicular to the surface $\partial \mathcal{V}$ of the control volume. The aforementioned governing equations are equally applicable for single-phase and multiphase flows without limitation if the field variables are thought of

as volume-averaged homogeneous mixture quantities. In the context of the applied finite volume spatial discretization, all quantities are assumed to be cell-centered and volume-averaged over discrete control volumes Ω . The volume-averaging operator $\bar{\square}$ is introduced as follows:

$$\bar{\square} := \frac{1}{V_\Omega} \int_{\Omega} \square \, dV, \quad (2.24)$$

where V_Ω represents the volume of a computational cell. Thus, the phases are not treated separately, but a homogeneous mixture is considered. The applied cavitation model is likewise based on volume-averaging homogeneous mixture quantities and will be explained together with the considered equations of state in section 2.1.4. The governing equations for a finite volume can be written in discretized form:

$$\frac{\partial \bar{\mathbf{U}}}{\partial t} = -\frac{1}{V_\Omega} \oint_{\partial\Omega} (\tilde{\mathbf{F}}^c(\bar{\mathbf{U}}) + \tilde{\mathbf{F}}^d(\bar{\mathbf{U}})) \, dS + \frac{1}{V_\Omega} \int_{\Omega} \tilde{\mathbf{S}}(\bar{\mathbf{U}}) \, dV. \quad (2.25)$$

$\tilde{\square}$ depicts numerical approximations including flux calculations and face reconstructions as described in more detail in section 2.2.1.

2.1.4 Single fluid homogeneous mixture cavitation model

The two-phase cavitating flow, including evaporation and condensation, is modeled assuming volume-averaged single-fluid homogeneous mixtures in thermodynamic and mechanical equilibrium for each computational finite volume [127]. Phase change processes occur infinitely fast without time delay. Cell-centered volume-averaged quantities describe the homogeneous mixture for each discrete volume. Our approach ensures that only homogeneous fluids, either pure liquid or mixtures of vapor and liquid, are considered within each computational cell. Condensation and evaporation is therefore implicitly modeled by the equation of state for the mixture as it represents a direct correlation of the vapor volume fraction and the thermodynamic variables, as explained hereafter. Because of the equilibrium assumption, the corresponding vapor volume fraction instantaneously adapts to the flow properties, and an additional model for the condensation rate or relaxation is not needed. Figure 2.2 illustrates the concept of the single fluid model. On the left, an exemplary real situation of a two-phase mixture with discrete regions of vapor and liquid is illustrated. Assuming that the cell size is larger than the discrete regions, the corresponding numerical description resolved by our model would be a homogeneous mixture with the corresponding vapor volume fraction for a computational cell Ω . To appropriately simulate vapor bubbles during their collapse, enough cells must be used to resolve the bubble size with sufficient accuracy. The approach was extensively applied to investigate cloud cavitation [127], to simulate cavitating flows including non-condensable gas [105, 106], turbulent cavitating flows [37, 38], to predict cavitation erosion [95] and to examine condensation shocks [26, 139]. A further detailed description of the model can be found in Budich et al. [26], Schnerr et al. [127], and Sezal [128].

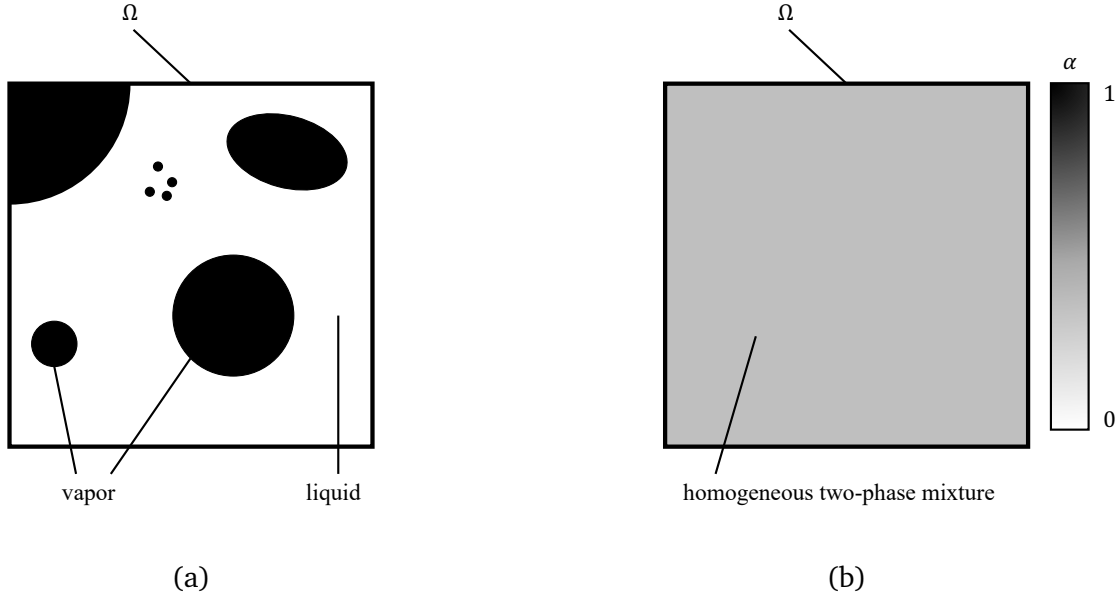


Figure 2.2: Schematic of the single-fluid homogeneous mixture model for a computational cell Ω . (a) Real physical situation. (b) Numerical model approximation with the corresponding vapor volume fraction α .

The homogenous mixture density is described by

$$\bar{\rho} = \alpha \rho_{v,sat} + (1 - \alpha) \rho_{l,sat}, \quad (2.26)$$

where $\bar{\rho}$, α , $\rho_{v,sat}$, $\rho_{l,sat}$ are the mixture density, the vapor volume fraction, the saturated vapor density and the saturated liquid density, respectively. In the framework of the applied explicit density-based method, the cell-averaged density is not computed by eq. (2.26). Instead, the density is obtained by the time integration of the continuity equation (2.25) and subsequently utilized to ascertain whether a cell contains a two-phase mixture of liquid and vapor or comprises pure liquid as shown hereunder:

$$\alpha = \frac{V_{v,\Omega}}{V_{\Omega}} = \begin{cases} 0, & \text{if } \bar{\rho} \geq \rho_{l,sat} \text{ (pure liquid)} \\ \frac{\rho_{l,sat} - \bar{\rho}}{\rho_{l,sat} - \rho_{v,sat}}, & \text{else (liquid-vapor mixture),} \end{cases} \quad (2.27)$$

where $V_{v,\Omega}$ represents the volume occupied by vapor within the computational cell. Since the flow is considered barotropic, constant fluid properties apply as summarized in table 2.2. To close the equation of state, a relation for the pressure is required. It is distinguished between pure liquid and liquid-vapor mixtures. For pure liquid regions, a modified Tait equation of state as introduced by Saurel et al. [125] is used:

$$p = B \left[\left(\frac{\bar{\rho}}{\rho_{l,sat}} \right)^N - 1 \right] + p_{sat}, \quad (2.28)$$

where $N = 7.15$ and $B = 3.3 \times 10^8$ Pa at reference temperature. The speed of sound for pure

liquid thus is calculated to

$$c = \left(\frac{N(p+B)}{\bar{\rho}} \right)^{1/2}. \quad (2.29)$$

For the pressure calculation in two-phase mixtures the integration of the isentropic speed of sound definition is used:

$$c^2 = \left. \frac{\partial p}{\partial \rho} \right|_{s=const.} \Rightarrow p(\bar{\rho}) - p_{sat} = \int_{\rho_{l,sat}}^{\bar{\rho}} c^2 d\rho. \quad (2.30)$$

The speed of sound is substituted by the formulation of Franc et al. [47], which considers the latent heat of vaporization:

$$\frac{1}{\bar{\rho}c^2} = \frac{\alpha}{\rho_{v,sat}c_{v,sat}^2} + \frac{1-\alpha}{\rho_{l,sat}c_{l,sat}^2} + \frac{((1-\alpha)\rho_{l,sat}c_{p,l,sat} - \alpha\rho_{v,sat}c_{p,v,sat})T_{ref}}{(\rho_{v,sat}l_v)^2}. \quad (2.31)$$

The last term on the right-hand side accounts for mass transfer through vaporization. The speed of sound of pure liquid and vapor is represented by $c_{l,sat}$ and $c_{v,sat}$. $c_{p,sat,l}$ and l_v are the specific heat capacity of saturated liquid and the latent heat of vaporization, respectively. All variables correspond to values at reference temperature as listed in table 2.2. Further explanations leading to this formulation can be found in Sezal [128] and Budich et al. [26]. By introducing eq. (2.31) in eq. (2.30) and subsequent integration, the pressure in the two-phase region is obtained as

$$p = \frac{1}{A} \ln \left(\frac{\rho}{A+B\rho} \right) - \frac{1}{A} \ln \left(\frac{\rho_{l,sat}}{A+B\rho_{l,sat}} \right) + p_{sat},$$

$$\text{with } A = - \frac{\rho_{l,sat}}{\rho_{v,sat} - \rho_{l,sat}} \left(\frac{1}{\rho_{v,sat}c_{v,sat}^2} - \frac{1}{\rho_{l,sat}c_{l,sat}^2} + C \right)$$

$$+ \frac{1}{\rho_{l,sat}c_{l,sat}^2} + \frac{\rho_{l,sat}c_{p,l,sat}T_{ref}}{(\rho_{v,sat}l_v)^2}, \quad (2.32)$$

$$B = \frac{1}{\rho_{v,sat} - \rho_{l,sat}} \left(\frac{1}{\rho_{v,sat}c_{v,sat}^2} - \frac{1}{\rho_{l,sat}c_{l,sat}^2} + C \right),$$

$$C = \frac{T_{ref}(\rho_{v,sat}c_{p,v,sat} - \rho_{l,sat}c_{p,l,sat})}{(\rho_{v,sat}l_v)^2}.$$

2.1.5 Non-dimensional numbers

The cavitating viscoelastic flows can be characterized by the Reynolds number Re and the Deborah number De . The Reynolds number relates the timescale of the diffusive momentum

Table 2.2: Fluid properties of the barotropic model at $T_{ref} = 293.15K$

Property	Symbol	Value
Reference temperature	T_{ref}	293.15 K
Density of saturated liquid	$\rho_{l,sat}$	998.16 kg/m ³
Density of saturated vapor	$\rho_{v,sat}$	0.01721 kg/m ³
Saturation pressure	p_{sat}	2339.3 Pa
Dynamic viscosity of saturated liquid	$\mu_{l,sat}$	1.0014×10^{-3} Pa s
Dynamic viscosity of saturated vapor	$\mu_{v,sat}$	9.7275×10^{-6} Pa s
Speed of sound of saturated liquid	$c_{l,sat}$	1482.2 m/s
Speed of sound of saturated vapor	$c_{v,sat}$	423.18 m/s
Specific heat capacity of saturated liquid	$c_{p,l,sat}$	4184.4 J/(kg K)
Specific heat capacity of saturated vapor	$c_{p,v,sat}$	1905.9 J/(kg K)
Latent heat of vaporization	l_v	2453.5×10^3 J/kg

transport to the characteristic inertia-related timescale:

$$Re = \frac{\rho UL}{\mu_0}, \quad (2.33)$$

where U and L represent characteristic velocity and length scale, respectively. High Reynolds number flows correspond to inertia-dominated problems, whereas a low Reynolds number is associated with flows dominated by viscous forces. The Deborah number relates the timescale of viscoelastic relaxation, i.e. the relaxation time, to the characteristic inertia-related time of the flow problem:

$$De = \frac{\lambda U}{L}. \quad (2.34)$$

Large Deborah numbers correlate with high elasticities and long relaxation times. Increasing the Deborah number leads to delayed development of stresses. Thinking of the 1D representation of the Maxwell fluid, the series arrangement of damper and spring, increasing the Deborah number corresponds to a softer spring that allows for larger deformations before the viscous damper can react. The smaller the elasticity, the harder the spring and the smaller the relaxation time, which leads to a less delayed response of the dashpot.

2.2 Numerical approach

2.2.1 Spatial discretization and numerical flux calculation

The finite volume discretization is performed by subdividing the physical domain into body-fitted, hexahedral cells with non-staggered cell-centered variables. The governing equations are formulated in Cartesian coordinates. The numerical calculation of cell face fluxes is performed separately for convective fluxes $\tilde{\mathbf{F}}^c(\bar{\mathbf{U}})$, diffusive fluxes $\tilde{\mathbf{F}}^d(\bar{\mathbf{U}})$ and source terms $\tilde{\mathbf{S}}(\bar{\mathbf{U}})$, respectively. The content of an individual cell is thereby treated as a homogeneous mixture irrespective of whether the cell contains pure liquid or a water-vapor mixture.

For the convective fluxes $\tilde{\mathbf{F}}_\rho^c, \tilde{\mathbf{F}}_{\rho\mathbf{u}}^c, \tilde{\mathbf{F}}_{\rho\tau_M}^c$ an upwind-biased low-Mach number consistent approximate Riemann solver is used. The method combines an AUSM-type (Advection Upstream Splitting Method) based Riemann solver with a MUSCL (Monotone Upstream-Centered Schemes for Conservation Laws) reconstruction on a four-point stencil with TVD (Total Variation Diminishing) limiters for the numerical calculation of convective fluxes. The numerical flux calculation separately addresses the density, velocities, pressure, and viscoelastic stresses. For the different variables, distinct limiter functions can be applied. In Lang et al. [75, 78] the density is reconstructed applying the MinMod limiter [119] for improved numerical robustness, which is required due to steep density and pressure gradients in two-phase flows. In smooth regions, this limiter is of second-order accuracy [128]. The velocities are calculated with the Koren limiter function [73], which is third-order accurate in smooth regions. The viscoelastic stresses are reconstructed applying the weighted essentially non-oscillatory reconstruction procedure (WENO-3) [63]. Due to increased stability requirements, the MinMod limiter is used to reconstruct all variables (density, pressure, velocities, and viscoelastic stresses) in Lang et al. [74].

The diffusive flux $\tilde{\mathbf{F}}_{\rho\mathbf{u}}^d$ and the source term $\tilde{\mathbf{F}}_{\rho\tau_M}$ are calculated by a second order central reconstruction. By additionally introducing the numerical approximation of the surface and volume integrals of the already approximated fluxes and the approximated source

$$\mathcal{F}_\square^{\square \text{ num}} \equiv \oint_{\partial\Omega} \tilde{\mathbf{F}}_\square^{\square} dS, \quad \mathcal{S}_{\rho\tau_M}^{\text{num}} \equiv \int_{\Omega} \tilde{\mathbf{S}}_{\rho\tau_M} dV, \quad (2.35)$$

the equations can be written in abbreviated form by its fully discretized fluxes for a computational volume Ω :

$$\frac{\partial \bar{\rho}}{\partial t} = -\frac{1}{V_\Omega} \mathcal{F}_\rho^c, \quad (2.36)$$

$$\frac{\partial (\bar{\rho\mathbf{u}})}{\partial t} = -\frac{1}{V_\Omega} \{\mathcal{F}_{\rho\mathbf{u}}^c + \mathcal{F}_{\rho\mathbf{u}}^d\}, \quad (2.37)$$

$$\frac{\partial (\bar{\rho\tau_M})}{\partial t} = -\frac{1}{V_\Omega} \mathcal{F}_{\rho\tau_M}^c + \frac{1}{V_\Omega} \mathcal{S}_{\rho\tau_M}. \quad (2.38)$$

2.2.2 Explicit time discretization

To capture compressible wave dynamics, time integration is performed by an explicit second-order accurate low-storage four-step Runge-Kutta method with enhanced stability region. A detailed description can be found in Schmidt [126] and Sezal [128]. Equations (2.39) to (2.41) show one sub-step of the four-step time integration, where the operator $\mathcal{L}_\square[\square]$ summarizes the Runge-Kutta substep of the respective transport equation. The coefficients of the Runge-Kutta scheme are given in table 2.3.

$$\begin{aligned} \bar{\rho}|^{n+j/4} &= \bar{\rho}|^n - \xi_j \frac{\Delta t}{V_\Omega} \mathcal{F}_\rho^c \Big|^{n+(j-1)/4} \left(\bar{\rho}|^{n+(j-1)/4}, \bar{\mathbf{u}}|^{n+(j-1)/4}, \bar{p}|^{n+(j-1)/4} \right) \\ &=: \mathcal{L}_\rho \left[\mathcal{F}_\rho^c \Big|^{n+(j-1)/4} \right], \end{aligned} \quad (2.39)$$

$$\begin{aligned} (\overline{\rho\mathbf{u}})|^{n+j/4} &= (\overline{\rho\mathbf{u}})|^n \\ &\quad - \xi_j \frac{\Delta t}{V_\Omega} \left\{ \mathcal{F}_{\rho\mathbf{u}}^c \Big|^{n+(j-1)/4} \left(\bar{\rho}|^{n+(j-1)/4}, \bar{\mathbf{u}}|^{n+(j-1)/4}, \bar{p}|^{n+(j-1)/4} \right) \right. \\ &\quad \left. + \mathcal{F}_{\rho\mathbf{u}}^d \Big|^{n+(j-1)/4} \left(\bar{\mathbf{u}}|^{n+(j-1)/4}, \bar{\tau}_M|^{n+(j-1)/4} \right) \right\} \\ &=: \mathcal{L}_{\rho\mathbf{u}} \left[\mathcal{F}_{\rho\mathbf{u}}^c \Big|^{n+(j-1)/4}, \mathcal{F}_{\rho\mathbf{u}}^d \Big|^{n+(j-1)/4} \right], \end{aligned} \quad (2.40)$$

$$\begin{aligned} (\overline{\rho\tau_M})|^{n+j/4} &= (\overline{\rho\tau_M})|^n \\ &\quad - \xi_j \frac{\Delta t}{V_\Omega} \left\{ \mathcal{F}_{\rho\tau_M}^c \Big|^{n+(j-1)/4} \left(\bar{\rho}|^{n+(j-1)/4}, \bar{\mathbf{u}}|^{n+(j-1)/4}, \bar{\tau}_M|^{n+(j-1)/4}, \bar{p}|^{n+(j-1)/4} \right) \right. \\ &\quad \left. + \xi_j \frac{\Delta t}{V_\Omega} \mathcal{S}_{\rho\tau_M} \Big|^{n+(j-1)/4} \left(\bar{\rho}|^{n+(j-1)/4}, \bar{\mathbf{u}}|^{n+(j-1)/4}, \bar{\tau}_M|^{n+(j-1)/4} \right) \right\} \\ &=: \mathcal{L}_{\rho\tau_M} \left[\mathcal{F}_{\rho\tau_M}^c \Big|^{n+(j-1)/4}, \mathcal{S}_{\rho\tau_M} \Big|^{n+(j-1)/4} \right]. \end{aligned} \quad (2.41)$$

Table 2.3: Runge-Kutta sub-step coefficients

j	1	2	3	4
ξ_j	0.11	0.2766	0.5	1.0

The time step criterion is defined following the concept of convection-dominated flow analysis and introducing the Courant-Friedrich-Lewy (CFL) number [43, 55, 134]

$$\Delta t = \frac{\text{CFL}}{i_c + i_d}, \quad (2.42)$$

where $i_c = \frac{1}{\Delta t_c}$ and $i_d = \frac{1}{\Delta t_d}$ represent the inverse convective and diffusive timestep respectively. The convective and diffusive timesteps are limited by the fastest transport mechanism occurring for each computational cell. For defining the inverse diffusive time step, Hirsch

[55] applies a linear von Neumann stability analysis for a standard diffusion problem. For the analysis, an explicit time and central difference space discretization is assumed. Schmidt [126] and Sezal [128] adapted the criterion to incorporate diffusion processes in n dimensions. The diffusive time step Δt_d is limited by

$$\Delta t_d < \frac{1}{i_d} := \min \left(\frac{\rho (\Delta x_i / n)^2}{2\mu_s} \right), \quad i = 1, 2, 3, \quad n = 3, \quad (2.43)$$

with the cell length Δx_i in space direction i and $n = 3$ for 3D flows. It proved suitable to only consider the solvent viscosity for the diffusive timestep limitations. Multiple simulations for different scenarios, where the Maxwell viscosity was neglected for the viscous timestep calculation, showed stable behavior and led to physically correct results, concluding that the overall timestep criterion is dominated by convection. The assertion can be emphasized by the fact that the transport equation (2.6) for Maxwell-/Oldroyd-like fluids represents a system of first-order hyperbolic equations [107]. Besides, in the subsequent section, it will be shown that a simplified system of equations results in a hyperbolic system of equations. Thus, a diffusive transport mechanism for the timestep criterion of the Maxwell stress transport is not considered. To determine the appropriate convective time step criterion, the quasi-linear system is analyzed hereunder.

2.2.3 Classification and eigenvalue calculation of the quasi-linear system

For the convective timestep criterion, the linearized wave speeds corresponding to the relevant parts of the transport equations (2.1), (2.2) and (2.18) are calculated. To do so, the Eigenvalues of a simplified system in 1D are examined. The analysis is similar to Edwards et al. [36], Guy et al. [51], and Rodriguez et al. [117]. Thus, the viscous solvent contribution ($\mu_s = 0$) and lower order terms in the source term of eq. (2.18) are neglected. Due to the omission of all lower order terms, the analysis correlates with the one of the UCM model and is sufficient to characterize constitutive equations of Oldroyd-like models described by eq. (2.6). Only the x_1 -direction is considered, taking into account the momentum in the remaining two directions to quantify shear wave speeds and longitudinal wave speeds. The simplified 1D equations for the eigenvalue analysis are presented in Cartesian coordinates hereafter:

$$\begin{aligned}
\frac{\partial}{\partial t} \rho + \frac{\partial}{\partial x_1} (\rho u_1) &= 0 \\
\frac{\partial}{\partial t} (\rho u_1) + \frac{\partial}{\partial x_1} (\rho u_1^2 + p - \tau_{M,11}) &= 0 \\
\frac{\partial}{\partial t} (\rho u_2) + \frac{\partial}{\partial x_1} (\rho u_2 u_1 - \tau_{M,12}) &= 0 \\
\frac{\partial}{\partial t} (\rho u_3) + \frac{\partial}{\partial x_1} (\rho u_3 u_1 - \tau_{M,13}) &= 0 \\
\frac{\partial}{\partial t} (\rho \tau_{M,11}) + \frac{\partial}{\partial x_1} (\rho \tau_{M,11} u_1) - \rho \left(\frac{4}{3} G + \tau_{M,11} \right) \frac{\partial u_1}{\partial x_1} &= 0 \\
\frac{\partial}{\partial t} (\rho \tau_{M,22}) + \frac{\partial}{\partial x_1} (\rho \tau_{M,22} u_1) + \rho \left(\frac{2}{3} G + \tau_{M,22} \right) \frac{\partial u_1}{\partial x_1} - 2\rho \tau_{M,12} \frac{\partial u_2}{\partial x_1} &= 0 \\
\frac{\partial}{\partial t} (\rho \tau_{M,33}) + \frac{\partial}{\partial x_1} (\rho \tau_{M,33} u_1) + \rho \left(\frac{2}{3} G + \tau_{M,33} \right) \frac{\partial u_1}{\partial x_1} - 2\rho \tau_{M,13} \frac{\partial u_3}{\partial x_1} &= 0 \\
\frac{\partial}{\partial t} (\rho \tau_{M,12}) + \frac{\partial}{\partial x_1} (\rho \tau_{M,12} u_1) - \rho (G + \tau_{M,11}) \frac{\partial u_2}{\partial x_1} &= 0 \\
\frac{\partial}{\partial t} (\rho \tau_{M,13}) + \frac{\partial}{\partial x_1} (\rho \tau_{M,13} u_1) - \rho (G + \tau_{M,11}) \frac{\partial u_3}{\partial x_1} &= 0 \\
\frac{\partial}{\partial t} (\rho \tau_{M,23}) + \frac{\partial}{\partial x_1} (\rho \tau_{M,23} u_1) + \rho \tau_{M,23} \frac{\partial u_1}{\partial x_1} - \rho \tau_{M,13} \frac{\partial u_2}{\partial x_1} - \rho \tau_{M,12} \frac{\partial u_3}{\partial x_1} &= 0.
\end{aligned} \tag{2.44}$$

With the definition of the speed of sound for barotropic flows $c^2 := \left. \frac{\partial p}{\partial \rho} \right|_{s=\text{const.}}$ the system of partial differential equations (2.44) is rewritten in quasi-linear form

$$\frac{\partial \mathbf{q}}{\partial t} + \mathbf{A}(\mathbf{q}) \frac{\partial \mathbf{q}}{\partial x_1} = \mathbf{0}, \tag{2.45}$$

with the vector of primitive variables \mathbf{q} and the Jacobian matrix \mathbf{A} ,

$$\mathbf{q} = \begin{bmatrix} \rho \\ u_1 \\ u_2 \\ u_3 \\ \tau_{M,11} \\ \tau_{M,22} \\ \tau_{M,33} \\ \tau_{M,12} \\ \tau_{M,13} \\ \tau_{M,23} \end{bmatrix}, \quad \mathbf{A}(\mathbf{q}) = \begin{bmatrix} u_1 & \rho & 0 & 0 & 0 & 0 & 0 & 0 & 0 & 0 \\ \frac{c^2}{\rho} & u_1 & 0 & 0 & -\frac{1}{\rho} & 0 & 0 & 0 & 0 & 0 \\ 0 & 0 & u_1 & 0 & 0 & 0 & 0 & -\frac{1}{\rho} & 0 & 0 \\ 0 & 0 & 0 & u_1 & 0 & 0 & 0 & 0 & -\frac{1}{\rho} & 0 \\ 0 & -\frac{4G}{3} - \tau_{M,11} & 0 & 0 & u_1 & 0 & 0 & 0 & 0 & 0 \\ 0 & \frac{2G}{3} + \tau_{M,22} & -2\tau_{M,12} & 0 & 0 & u_1 & 0 & 0 & 0 & 0 \\ 0 & \frac{2G}{3} + \tau_{M,33} & 0 & -2\tau_{M,13} & 0 & 0 & u_1 & 0 & 0 & 0 \\ 0 & 0 & -G - \tau_{M,11} & 0 & 0 & 0 & 0 & u_1 & 0 & 0 \\ 0 & 0 & 0 & -G - \tau_{M,11} & 0 & 0 & 0 & 0 & u_1 & 0 \\ 0 & \tau_{M,23} & -\tau_{M,13} & -\tau_{M,12} & 0 & 0 & 0 & 0 & 0 & u_1 \end{bmatrix}. \tag{2.46}$$

The quasi-linear system depicted in eq. (2.45) is linearized by assuming the coefficients in $\mathbf{A}(\mathbf{q})$ to be constant [86]. The Eigenvalues λ_i of the matrix $\mathbf{A}(\mathbf{q})$, which correspond to the

wave speeds, are calculated to

$$\lambda_{1,2,3,4} = u_1, \quad (2.47)$$

$$\lambda_{5,6} = u_1 + \sqrt{\frac{1}{\rho} (G + |\tau_{M,11}|)}, \quad (2.48)$$

$$\lambda_{7,8} = u_1 - \sqrt{\frac{1}{\rho} (G + |\tau_{M,11}|)}, \quad (2.49)$$

$$\lambda_9 = u_1 + \sqrt{a^2 + \frac{1}{\rho} \left(\frac{4}{3}G + |\tau_{M,11}| \right)}, \quad (2.50)$$

$$\lambda_{10} = u_1 - \sqrt{a^2 + \frac{1}{\rho} \left(\frac{4}{3}G + |\tau_{M,11}| \right)}, \quad (2.51)$$

where $\lambda_{5,6,7,8}$ are the shear wave speeds and $\lambda_{9,10}$ quantify the longitudinal (pressure) wave speeds. Owens et al. [107] showed that the Maxwell stress transport equation itself (2.6) exhibits hyperbolic behavior independently of the chosen $f(\boldsymbol{\tau}_M, \mathbf{d}^d)$ since this term comprises only lower order terms.

Regarding absolute values of the wave speeds, the longitudinal waves propagate the fastest and are considered for calculating the convective time step criterion. The corresponding expression for the convective time step Δt_c in n dimensions reads as follows

$$\begin{aligned} \Delta t_c &< \frac{1}{i_c} := \min \left(\frac{\Delta x_i / n}{\lambda_i^{\max}} \right) \\ &= \min \left(\left(|u_i| + \sqrt{c^2 + \frac{1}{\rho} \left(\frac{4}{3}G + |\tau_{M,ii}| \right)} \right)^{-1} \frac{\Delta x_i}{n} \right), \quad i = 1, 2, 3, \quad n = 3 \end{aligned} \quad (2.52)$$

where the remaining two directions in space are incorporated again. The obtained convective and diffusive time step, or more specifically the inverse convective and diffusive time step i_c and i_d are applied together with eq. (2.42) for all cells to acquire the appropriate global timestep. Extensive investigations for several flow scenarios were conducted by Schmidt [126] and led to the result that the employed Runge-Kutta method remains stable up to CFL = 1.5. A CFL number of CFL = 1.4 is eventually chosen for all presented computations.

2.2.4 Boundary conditions

To solve the described problem numerically, proper conditions for the variables have to be imposed at the boundary of the computational domain. Boundary conditions are implemented by attaching two layers of virtual cells, denoted ghost cells ($|_g$), to the cells of the computational domain ($|_d$) as illustrated in fig. 2.3. $\mathbf{n}|_\Gamma$ is the unit normal vector pointing outward at the boundary face. These ghost cells contain values for the primitive variables to meet the physically correct constraints at the boundary face. In doing so, the variables within the ghost cells are not restricted to physically reasonable values but are defined to result in correct reconstructions at the face between the computational domain and the ghost cells. A central

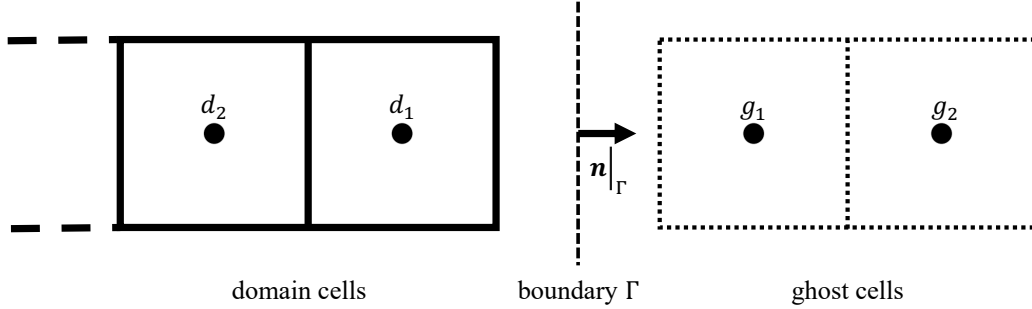


Figure 2.3: Computational cells d_1 , d_2 and adjacent ghost cells g_1 , g_2 separated by the boundary face Ω . $\mathbf{n}|_\Gamma$ represents the outward pointing unit normal vector at the boundary.

reconstruction scheme for the calculation of variables at the cell face

$$\begin{aligned}
 p|_\Gamma &= \frac{1}{2} (p|_d + p|_g), \\
 \mathbf{u}|_\Gamma &= \frac{1}{2} (\mathbf{u}|_d + \mathbf{u}|_g), \\
 \boldsymbol{\tau}_{s/M}|_\Gamma &= \frac{1}{2} \left(\boldsymbol{\tau}_{s/M}|_d + \boldsymbol{\tau}_{s/M}|_g \right),
 \end{aligned} \tag{2.53}$$

is applied. The density is calculated according the vapor volume fraction with the above-mentioned equation of state. The following boundary conditions are implemented for the studies presented in this work.

Inlet boundary conditions

For channel or duct flow simulations, inlet boundary conditions yielding a specific mass flow inside the geometry are required. For the channel flow simulations carried out within this work, a fixed pressure at the inlet and a Neumann condition, namely a zero-gradient condition for the velocity and the solvent stress, is specified. As a result of the hyperbolic nature of the Maxwell stress transport equation, only an upstream Dirichlet boundary condition for the Maxwell stress is required at the inlet [144]. By imposing conditions for the Maxwell stresses at the inlet, the history of deformation of the viscoelastic fluid in the upstream region of the domain is determined. The inlet face's desired value is specified in the ghost cell layer [104]. If there is no deformation history present in the upstream direction of the inlet, the physical condition for the Maxwell stresses at the inlet is $\boldsymbol{\tau}_{M,in} = \mathbf{0}$. Gradients of solvent and Maxwell stresses in the upstream direction shall be zero to obtain a developed flow. Hence,

the corresponding inlet conditions read

$$\begin{aligned}
p|_{\Gamma_{in}} = p_{in} &\longrightarrow p|_g = p_{in}, \\
\nabla \mathbf{u}|_{\Gamma_{in}} \cdot \mathbf{n}|_{\Gamma_{in}} = \mathbf{0} &\longrightarrow \mathbf{u}|_g = \mathbf{u}|_d, \\
\nabla \boldsymbol{\tau}_s|_{\Gamma_{in}} \cdot \mathbf{n}|_{\Gamma_{in}} = \mathbf{0} &\longrightarrow \boldsymbol{\tau}_s|_g = \boldsymbol{\tau}_s|_d, \\
\boldsymbol{\tau}_M|_{\Gamma_{in}} = \boldsymbol{\tau}_{M,in} &\longrightarrow \boldsymbol{\tau}_M|_g = \boldsymbol{\tau}_M|_{\Gamma_{in}},
\end{aligned} \tag{2.54}$$

where the left side of \longrightarrow depicts the physical constraint at the boundary face Γ , and the right side shows the numerical implementation. p_{in} represents a user-defined value for the pressure. The zero gradient conditions are ensured by copying the variables from the domain into the ghost cells.

Outlet boundary conditions

At the outlet face, the pressure is imposed and a zero-gradient condition for velocity and solvent stresses is assumed. Due to the hyperbolic behavior of the transport equation for the Maxwell stresses, there is no need to define specific values for the stress tensor components, except for the upstream inlet boundary. As the reconstruction in eq. (2.53) requires a specified value in the ghost cell, a zero gradient assumption $\nabla(\boldsymbol{\tau}|_{\Gamma_{out}}) \cdot \mathbf{n}|_{\Gamma_{out}} = \mathbf{0}$ is applied (cf. [41]). The boundary conditions summarize as follows:

$$\begin{aligned}
p|_{\Gamma_{out}} = p_{out} &\longrightarrow p|_g = p|_d, \\
\nabla \mathbf{u}|_{\Gamma_{out}} \cdot \mathbf{n}|_{\Gamma_{out}} = \mathbf{0} &\longrightarrow \mathbf{u}|_g = \mathbf{u}|_d, \\
\nabla \boldsymbol{\tau}_{s/M}|_{\Gamma_{out}} \cdot \mathbf{n}|_{\Gamma_{out}} = \mathbf{0} &\longrightarrow \boldsymbol{\tau}_{s/M}|_g = \boldsymbol{\tau}_{s/M}|_d.
\end{aligned} \tag{2.55}$$

Viscous wall boundary conditions

The viscous wall stipulates no-slip conditions for all velocity components at the face. Consequently, all velocity components have to be zero at the face. To ascertain the no-slip condition, the velocities are mirrored. For the stress tensors, solvent and polymeric, a zero gradient condition applies with the same explanation as for outlet boundary conditions. Moreover, a zero gradient condition also applies to the pressure. The corresponding boundary conditions read as follows:

$$\begin{aligned}
\nabla p|_{\Gamma_{visc}} \cdot \mathbf{n}|_{\Gamma_{visc}} = \mathbf{0} &\longrightarrow p|_g = p|_d, \\
\mathbf{u}|_{\Gamma_{visc}} = \mathbf{0} &\longrightarrow \mathbf{u}|_g = -\mathbf{u}|_d, \\
\nabla \boldsymbol{\tau}_{s/M}|_{\Gamma_{visc}} \cdot \mathbf{n}|_{\Gamma_{visc}} = \mathbf{0} &\longrightarrow \boldsymbol{\tau}_{s/M}|_g = \boldsymbol{\tau}_{s/M}|_d.
\end{aligned} \tag{2.56}$$

Symmetry boundary conditions

The symmetry boundary is treated similarly to an inviscid wall. The pressure follows a zero gradient Neumann condition. The slip condition holds for velocities. Therefore, normal velocities must not occur at the boundary

$$\left(\mathbf{u}|_{\Gamma_{sym}} \cdot \mathbf{n}|_{\Gamma_{sym}} \right) \mathbf{n}|_{\Gamma_{sym}} = \mathbf{0}, \quad (2.57)$$

and tangential velocities remain unchanged

$$\mathbf{u}|_{\Gamma_{sym}} = \mathbf{u}|_{\Gamma_{sym}} - \left(\mathbf{u}|_{\Gamma_{sym}} \cdot \mathbf{n}|_{\Gamma_{sym}} \right) \mathbf{n}|_{\Gamma_{sym}} = \mathbf{u}|_d - \left(\mathbf{u}|_d \cdot \mathbf{n}|_{\Gamma_{sym}} \right) \mathbf{n}|_{\Gamma_{sym}}. \quad (2.58)$$

Only normal velocities are mirrored. Considering the reconstruction eq. (2.53) for the velocities, the following calculation of velocities in the ghost cells fulfills the conditions above:

$$\mathbf{u}|_g = \mathbf{u}|_d - 2 \left(\mathbf{u}|_d \cdot \mathbf{n}|_{\Gamma_{sym}} \right) \mathbf{n}|_{\Gamma_{sym}}. \quad (2.59)$$

Although symmetry boundary conditions are commonly applied in numerical simulations, there are few publications where the physical conditions for the stress tensor at a symmetry plane are explicitly formulated. An appropriate symmetry boundary condition for the stress tensor is derived in the following, beginning with a physical condition followed by a corresponding ghost cell formulation. Subsequently, all conditions at a symmetry boundary face are summarized. Baaijens et al. [8] and Huilgol et al. [60] formulate the vanishing tangential traction condition. At first, the traction vector

$$\mathbf{t} := \boldsymbol{\tau} \cdot \mathbf{n} \quad (2.60)$$

describing the resultant force occurring at a face with the outward pointing normal vector \mathbf{n} , is defined. Vanishing tangential traction at the symmetry face is formulated as follows

$$t_t|_{\Gamma_{sym}} := \left(\mathbf{n}_t|_{\Gamma_{sym}} \cdot \boldsymbol{\tau}|_{\Gamma_{sym}} \cdot \mathbf{n}|_{\Gamma_{sym}} \right) = 0, \quad \forall \mathbf{n}_t : \mathbf{n}_t \cdot \mathbf{n} = 0, \quad (2.61)$$

where \mathbf{n}_t represents any tangential vector perpendicular to the outward pointing normal vector \mathbf{n} . Consequently, the stress tensor $\boldsymbol{\tau}|_{\Gamma_{sym}}$ and the corresponding traction vector at the boundary face $\mathbf{t}|_{\Gamma_{sym}}$ have to fulfill the following condition to ensure that all traction other than the normal traction $t_n|_{\Gamma_{sym}}$ vanishes

$$\begin{aligned} \mathbf{t}|_{\Gamma_{sym}} - t_n|_{\Gamma_{sym}} \mathbf{n}|_{\Gamma_{sym}} &= \mathbf{0} \\ \mathbf{t}|_{\Gamma_{sym}} - \left(\mathbf{t}|_{\Gamma_{sym}} \cdot \mathbf{n}|_{\Gamma_{sym}} \right) \mathbf{n}|_{\Gamma_{sym}} &= \mathbf{0}, \\ \Leftrightarrow \mathbf{t}|_{\Gamma_{sym}} &= \left(\mathbf{n}|_{\Gamma_{sym}} \cdot \boldsymbol{\tau}|_{\Gamma_{sym}} \cdot \mathbf{n}|_{\Gamma_{sym}} \right) \mathbf{n}|_{\Gamma_{sym}}. \end{aligned} \quad (2.62)$$

A related condition was described by Oliveira et al. [104]. Furthermore, the boundary condition should only suppress tangential traction, and the normal traction should remain unal-

tered, coinciding with the traction that corresponds to the stress inside the physical domain.

$$t_n|_{\Gamma_{sym}} = t_n|_d, \quad (2.63)$$

$$\left(\mathbf{n}|_{\Gamma_{sym}} \cdot \boldsymbol{\tau}|_{\Gamma_{sym}} \cdot \mathbf{n}|_{\Gamma_{sym}} \right) = \left(\mathbf{n}|_{\Gamma_{sym}} \cdot \boldsymbol{\tau}|_d \cdot \mathbf{n}|_{\Gamma_{sym}} \right).$$

To the author's best knowledge, there was no work prior to the attached studies explicitly describing the formulation of symmetry boundary conditions for the stress tensor in a ghost cell approach. The stress tensor formulation in the ghost cells can be derived by proceeding with the aforementioned conditions. By taking into account the reconstruction eq. (2.53), the equation for the traction vector is rewritten to

$$\mathbf{t}|_{\Gamma_{sym}} = \left(\mathbf{n}|_{\Gamma_{sym}} \cdot \boldsymbol{\tau}|_d \cdot \mathbf{n}|_{\Gamma_{sym}} \right) \mathbf{n}|_{\Gamma_{sym}} = \frac{1}{2} (\boldsymbol{\tau}|_d + \boldsymbol{\tau}|_g) \cdot \mathbf{n}|_{\Gamma_{sym}}. \quad (2.64)$$

Instead of the last equation, a corresponding equation can be formulated to

$$\frac{1}{2} (\boldsymbol{\tau}|_d + \boldsymbol{\tau}|_g) - \left(\mathbf{n}|_{\Gamma_{sym}} \cdot \boldsymbol{\tau}|_d \cdot \mathbf{n}|_{\Gamma_{sym}} \right) \mathbf{I} = \mathbf{0}, \quad (2.65)$$

which allows calculating an equation for the stress tensor in the ghost cell

$$\boldsymbol{\tau}|_g = 2 \left(\mathbf{n}|_{\Gamma_{sym}} \cdot \boldsymbol{\tau}|_d \cdot \mathbf{n}|_{\Gamma_{sym}} \right) \mathbf{I} - \boldsymbol{\tau}|_d. \quad (2.66)$$

The reconstructed Maxwell stresses from eq. (2.66) at the symmetry plane fulfill the conditions eqs. (2.61) to (2.63). The conditions at the symmetry boundary face and the conditions imposed for the ghost cells can be summarized as follows:

$$\begin{aligned} \nabla p|_{\Gamma_{sym}} \cdot \mathbf{n}|_{\Gamma_{sym}} &= \mathbf{0} \longrightarrow p|_g = p|_d, \\ \mathbf{u}|_{\Gamma_{sym}} \cdot \mathbf{n}|_{\Gamma_{sym}} &= 0 \longrightarrow \mathbf{u}|_g = \mathbf{u}|_d - 2 \left(\mathbf{u}|_d \cdot \mathbf{n}|_{\Gamma_{sym}} \right) \mathbf{n}|_{\Gamma_{sym}}, \\ t_t|_{\Gamma_{sym}} &= 0 \longrightarrow \boldsymbol{\tau}_{s/M}|_g = 2 \left(\mathbf{n}|_d \cdot \boldsymbol{\tau}_{s/M}|_d \cdot \mathbf{n}|_d \right) \mathbf{I} - \boldsymbol{\tau}_{s/M}|_d. \end{aligned} \quad (2.67)$$

2.2.5 Sequences of the numerical algorithm

Algorithm 1 describes the procedures and relevant variables in one Runge-Kutta sub-step. Before executing the four sub-steps, the variables of the previous timestep are cached. The storage is necessary since a low-storage Runge-Kutta algorithm is applied, which retrieves the variables of each sub-step by adding the numerical flux and source terms to the variables of the previous time step as explained in eqs. (2.39) to (2.41). There are various ways to incorporate the transport equation for the Maxwell stress (2.38). As indicated by eq. (2.41), the Maxwell stresses of the subsequent sub-step $\boldsymbol{\tau}_M|^{n+j/4}$ are calculated exclusively by taking variables of the current sub-step $n + (j - 1)/4$. Thereby, a consistent state of all conserved variables during each solution sub-step is achieved for the segregated explicit solution scheme. The source term is computed based on the primary variables $\bar{\rho}|^{n+(j-1)/4}$, $\bar{\mathbf{u}}|^{n+(j-1)/4}$, $\bar{\boldsymbol{\tau}}_M|^{n+(j-1)/4}$ before being overwritten by the corresponding ones

of the subsequent timestep $\bar{\rho}|^{n+j/4}$, $\bar{\mathbf{u}}|^{n+j/4}$, $\bar{\tau}_M|^{n+j/4}$. To improve efficiency, the Maxwell stress source term $S_{\rho\tau_M}$ is calculated at the end to avoid the necessity of buffering the primary variables. Subsequently, the convective fluxes $\mathcal{F}_{\rho}^c, \mathcal{F}_{\rho\mathbf{u}}^c, \mathcal{F}_{\rho\tau_M}^c$ and the diffusive flux $\mathcal{F}_{\rho\mathbf{u}}^d$ are computed. Thereafter, the primary variables of the next sub-step $n + j/4$ are computed by conducting the time integration. Dividing the primary variables by the density of the new sub-step $\bar{\rho}|^{n+j/4}$ leads to the updated primitive variables $\bar{\mathbf{u}}|^{n+j/4}$, $\bar{\tau}_M|^{n+j/4}$. With the help of the updated density, the updated vapor content $\alpha_i^{n+j/4}$ is initially computed and eventually the pressure $p_i^{n+j/4}$ of the new sub-step, as described in section 2.1.4, is obtained. Finally, all variables within the ghost cells are updated at the end of one Runge-Kutta loop, meeting physically correct boundary conditions.

Algorithm 1: Operations during a substep of the explicit Runge-Kutta method
eqs. (2.39) to (2.41)

```

subroutine RungeKutta4
  SaveOldVars()
  // Save primitive variables of previous time step

  for j ← 1 to 4 do
    // Calculation of convective fluxes
    ComputeConvectiveFluxes()
     $\mathcal{F}_{\rho}^c|^{n+(j-1)/4} \left( \bar{\rho}|^{n+(j-1)/4}, \bar{\mathbf{u}}|^{n+(j-1)/4} \right)$ 
     $\mathcal{F}_{\rho\mathbf{u}}^c|^{n+(j-1)/4} \left( \bar{\rho}|^{n+(j-1)/4}, \bar{\mathbf{u}}|^{n+(j-1)/4}, \bar{p}|^{n+(j-1)/4} \right)$ 
     $\mathcal{F}_{\rho\tau_M}^c|^{n+(j-1)/4} \left( \bar{\rho}|^{n+(j-1)/4}, \bar{\mathbf{u}}|^{n+(j-1)/4}, \bar{\tau}_M|^{n+(j-1)/4} \right)$ 

    // Calculation of diffusive/viscous fluxes
    ComputeDiffusiveFluxes()
     $\mathcal{F}_{\rho\mathbf{u}}^d|^{n+(j-1)/4} \left( \bar{\mathbf{u}}|^{n+(j-1)/4}, \bar{\tau}_M|^{n+(j-1)/4} \right)$ 

    // Time marching for primary variables  $n + (j-1)/4 \rightarrow n + j/4$ 
     $\bar{\rho}|^{n+j/4} \leftarrow \mathcal{L}_{\rho} \left[ \mathcal{F}_{\rho}^c|^{n+(j-1)/4} \right]$ 
     $(\bar{\rho}\bar{\mathbf{u}})|^{n+j/4} \leftarrow \mathcal{L}_{\rho\mathbf{u}} \left[ \mathcal{F}_{\rho\mathbf{u}}^c|^{n+(j-1)/4}, \mathcal{F}_{\rho\mathbf{u}}^d|^{n+(j-1)/4} \right]$ 
     $(\bar{\rho}\bar{\tau}_M)|^{n+j/4} \leftarrow \mathcal{L}_{\rho\tau_M} \left[ \mathcal{F}_{\rho\tau_M}^c|^{n+(j-1)/4}, S_{\rho\tau_M}|^{n+(j-1)/4} \right]$ 

    // Update primitive variables
     $\bar{\mathbf{u}}|^{n+j/4} \leftarrow \frac{(\bar{\rho}\bar{\mathbf{u}})|^{n+j/4}}{\bar{\rho}|^{n+j/4}}$ 

     $\bar{\tau}_M|^{n+j/4} \leftarrow \frac{(\bar{\rho}\bar{\tau}_M)|^{n+j/4}}{\bar{\rho}|^{n+j/4}}$ 

    // Evaluate barotropic equation of state
     $p_i^{n+j/4} \leftarrow \text{EOS}(\rho_i^{n+j/4})$ 

    // Calculation source term for the Maxwell stress
    Viscoelastic()
     $S_{\rho\tau_M}|^{n+j/4} \left( \bar{\rho}|^{n+j/4}, \bar{\mathbf{u}}|^{n+j/4}, \bar{\tau}_M|^{n+j/4} \right)$ 

    // Update boundary conditions
    BoundaryConditions()
  end for
end subroutine

```

Chapter 3

Summary and Accomplishments

3.1 *A compressible 3D finite volume approach for the simulation of unsteady viscoelastic cavitating flows*

Christian Lang, Oliver Boolakee, Steffen J. Schmidt, Nikolaus A. Adams: *A compressible 3D finite volume approach for the simulation of unsteady viscoelastic cavitating flows.* International Journal of Multiphase Flow, Volume 150, 2022, 103981, ISSN 0301-9322, <https://doi.org/10.1016/j.ijmultiphaseflow.2022.103981>. [75]

Summary and accomplishments

The publication introduces a novel Eulerian approach for the numerical simulation of cavitating flows in viscoelastic fluids. It presents a fully compressible, three-dimensional, density-based finite volume solver that combines a single-fluid homogeneous-mixture model for cavitation with compressible viscoelastic models of the Maxwell-/Oldroyd-type. As viscoelastic models, the upper convected Maxwell (UCM) model, the Oldroyd-B (OLD-B) model, the simplified linearized Phan-Thien Tanner (LPTT) model and the exponential Phan-Thien Tanner (EPTT) model are implemented in conservative form. The Truesdell rate is derived as appropriate objective time derivative applied in the viscoelastic transport equation considering compressible flows. The single-fluid cavitation model considers condensation and evaporation and assumes both phases, liquid and vapor, to be in thermodynamic and mechanical equilibrium. To capture wave dynamics, the approach employs explicit time integration. The respective timestep criterion is adapted for viscoelastic fluids by calculating the eigenvalues of the corresponding quasi-linear 1D system of the governing equations to estimate the modified wave speeds. The study introduces a novel symmetry boundary condition for the viscoelastic stress tensor for ghost cell approaches. Moreover, the sequences of the numerical approach are explained in detail.

The implemented viscoelastic models are successfully validated against (semi-)analytical reference solutions as illustrated in figs. 3.1 and 3.2. Furthermore, the influence of viscoelasticity on cavitation dynamics is demonstrated by simulating spherical cavitation bubble collapses in viscoelastic fluids.

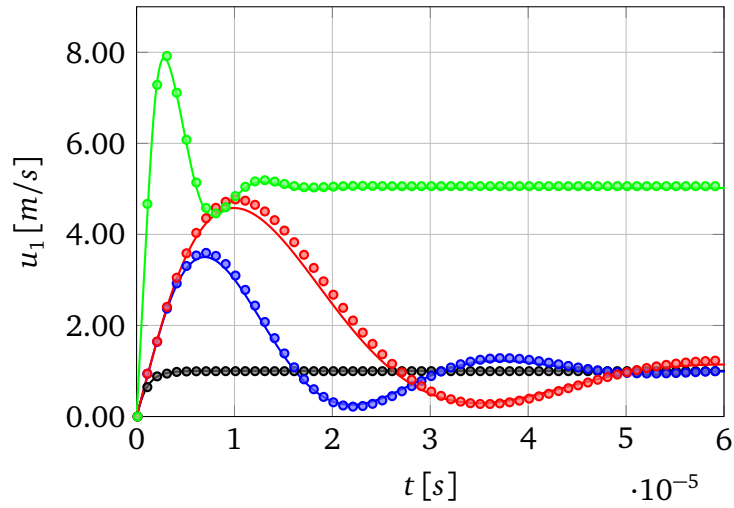


Figure 3.1: Validation of the velocity evolution during the start-up of a channel flow for different elasticities against reference solution in OLD-B fluid from Lang et al. [75]. Solid lines represent the reference solution, symbols simulation results. —/• $Re = 1, De = 0$ (Newtonian), —/• $Re = 1, De = 2$, —/• $Re = 1, De = 5$, —/• $Re = 5, De = 1$

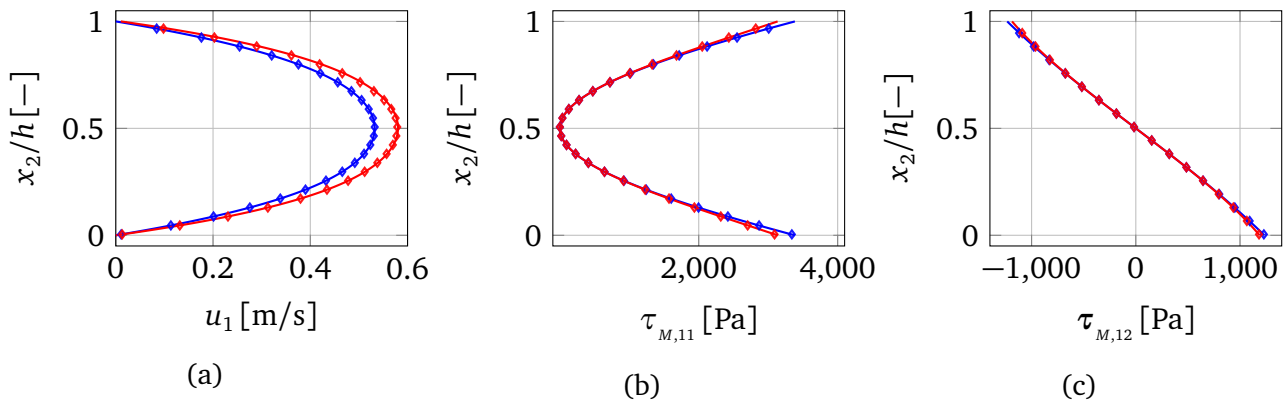


Figure 3.2: Validation of the steady state simulation results against references from Lang et al. [75]. Solid lines represent the reference solution and symbols simulation results. Left: velocity in x_1 -direction. Middle and right: —/• LPTT, —/• EPTT at $Re = 0.375, De = 0.375$.

A significant effect on collapse dynamics is observed as illustrated for the collapse behavior in Newtonian compared to UCM fluid in fig. 3.3. Moreover, the capability of resolving the emission of shock waves in cavitating viscoelastic fluids is demonstrated for a violent bubble collapse in UCM fluid.

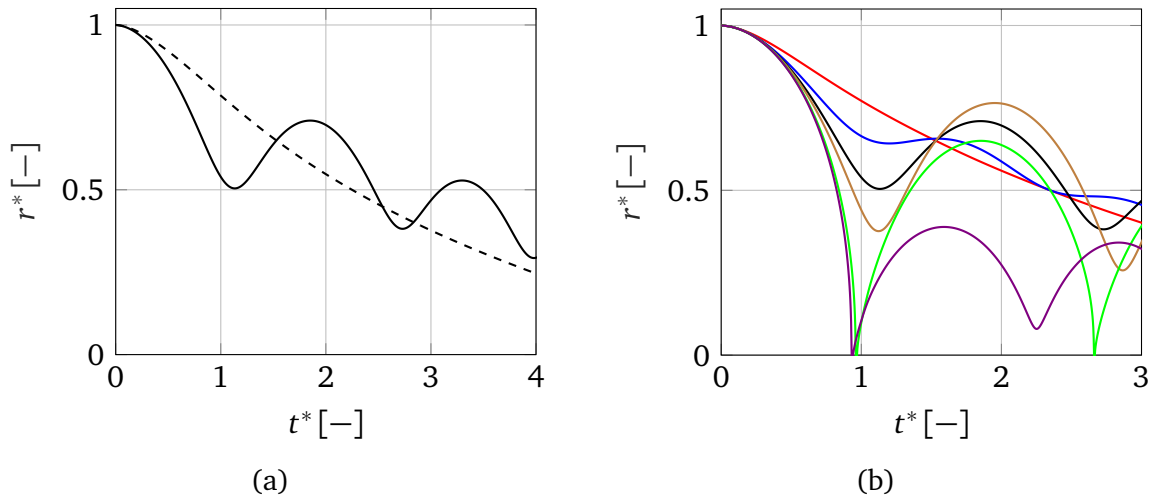


Figure 3.3: Spherical vapor bubble collapse: Non-dimensional bubble radius over time. (a) --- Newtonian against — UCM fluid at $Re = 1, De = 1$; (b) UCM fluid for different relaxation times at $Re = 1$: — $De = 0.1$, — $De = 0.5$, — $De = 1$, — $De = 1.5$, — $De = 5$, — $De = 10$. Results as presented in Lang et al. [75].

Individual contributions of the candidate

This article was published in the peer-reviewed *International Journal of Multiphase Flow*. My contributions to this publication include the conceptualization, deriving the mathematical foundation, and the implementation of the numerical methodology and software to perform numerical simulations of cavitating flows in viscoelastic fluids. I conducted the numerical investigations, the validation against references, performed the post-processing of the data, and visualized the results. The original manuscript of the publication was written by me.

3.2 On spherical vapor bubble collapse in viscoelastic fluids

Christian Lang, Mengqi Zhang, Steffen J. Schmidt, Nikolaus A. Adams: *On spherical vapor bubble collapse in viscoelastic fluids*. Applied Mathematical Modelling, Volume 123, 2023, Pages 484-506, ISSN 0307-904X, <https://doi.org/10.1016/j.apm.2023.07.004>. [78]

Summary and accomplishments

With the approach introduced in the aforementioned publication, numerical simulations are performed to investigate the spherical bubble collapses in viscoelastic fluids. Specifically, 3D simulations of the spherical vapor bubble collapse for different elasticities, viscosities, and different viscoelastic models are conducted. The collapse behavior, the viscous and viscoelastic stress development in correlation with the occurring strain rate distributions, and the pressure distribution during shock wave emission are examined.

It is shown that although the motion during spherical collapse is associated with pure deviatoric strain rates, the viscoelastic collapse also exhibits spherical (isotropic) stresses, even though the dissipation term only considers deviatoric strains as illustrated in fig. 3.4.

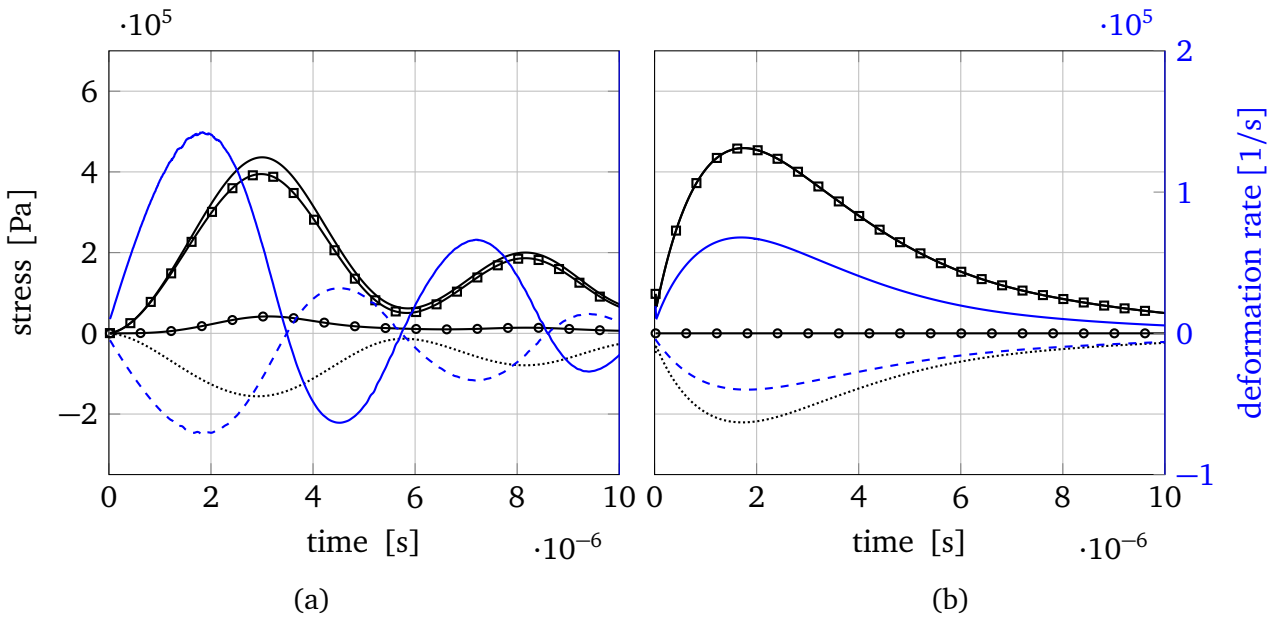
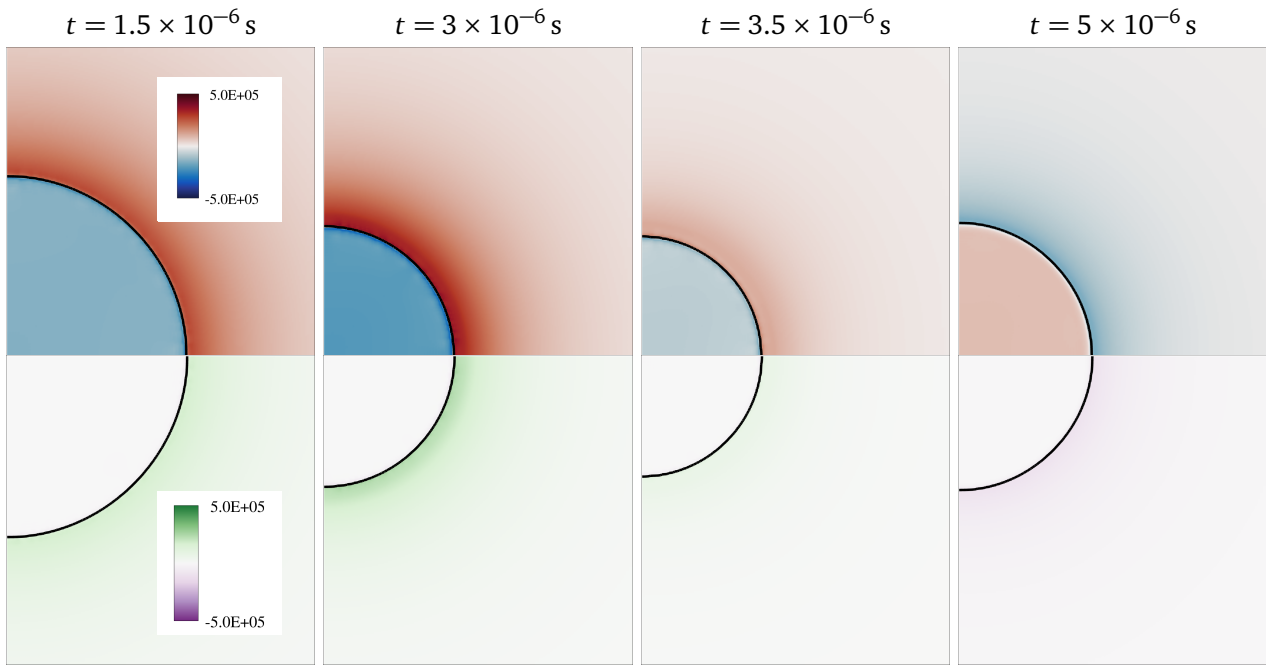


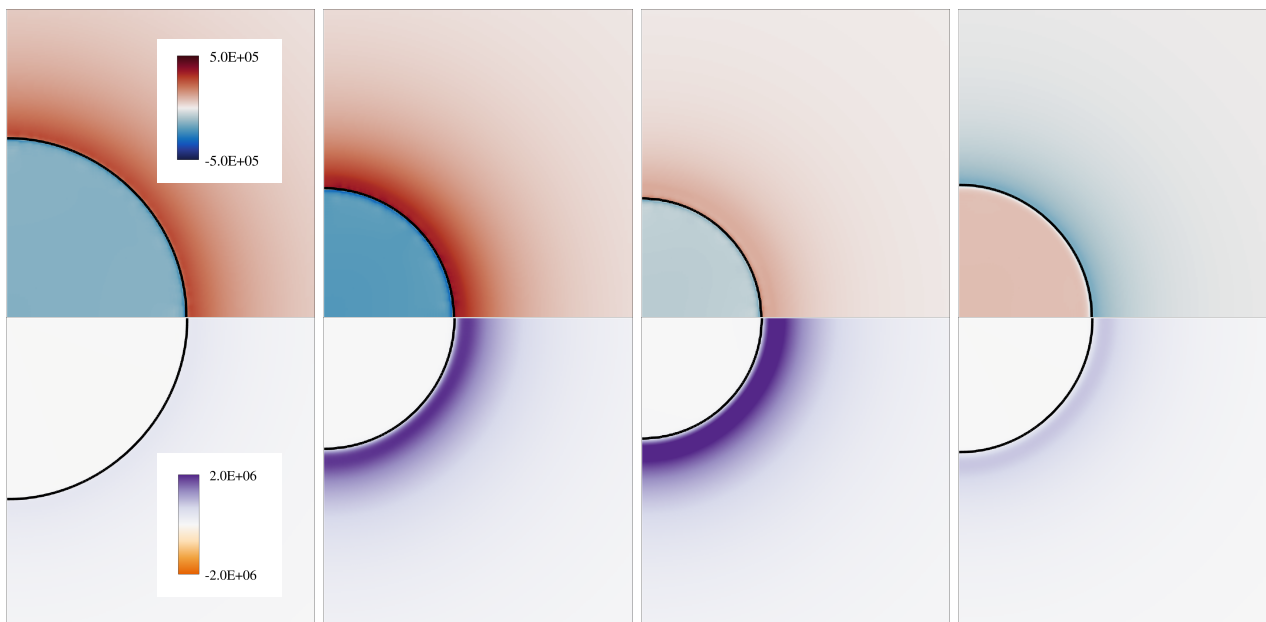
Figure 3.4: Stress evolution for the spherical bubble collapse at the position $r/R_0 = 1.2$. (a) For the UCM fluid the viscoelastic stress components $\tau_{M,rr}$, $\tau_{M,\psi\psi}$, $\tau_{M,rr}^d$, $\tau_{M,rr}^{sph}$ and the related deformation rates d_{rr} , $d_{\psi\psi}$ at $Re = 1$, $De = 1$ are illustrated. (b) For the Newtonian model the viscous stress components $\tau_{S,rr}$, $\tau_{S,\psi\psi}$, $\tau_{S,rr}^d$, $\tau_{S,rr}^{sph}$ and the corresponding deformation rates d_{rr} , $d_{\psi\psi}$ at $Re = 1$ are depicted. Results from Lang et al. [78].

Furthermore, the time-delayed viscoelastic stress development is examined and visualized, clearly illustrating a substantial difference compared to the solvent stress build-up (cf. fig. 3.5). It is also shown that viscoelasticity significantly alters the collapse dynamics, and increasing relaxation yields an acceleration of the collapse and higher collapse velocities for the investigated parameters. Furthermore, an increased relaxation time increases shear-rates and more out-of-phase stress development since the time for stress development is increased.

It is observed, that the rebound radius is increased and the viscoelastic stresses decrease with increasing the relaxation time. On the other hand, the influence of the variation of the Reynolds number, and thus the influence of viscous forces, is examined. It is ascertained that reducing the Reynolds number or increasing viscous to inertial forces, respectively, reduces strain rates but increases the occurring stresses. Reducing the viscosity leads to less dampened collapse resulting in higher strain rates, but lower stresses.



(a) Top: d_{rr} [1/s], bottom: $\tau_{s,rr}$ [Pa]



(b) Top: d_{rr} [1/s], bottom: $\tau_{M,rr}$ [Pa]

Figure 3.5: Development of (a) solvent stresses $\tau_{s,rr}$ and (b) Maxwell stresses $\tau_{M,rr}$ and the occurring deformation rates d_{rr} for different time instances during the collapse for the OLD-B model at $Re = 1$, $De = 1$ as presented in Lang et al. [78].

Distinct collapse dynamics are observed for the different viscoelastic models. As expected, the models with solvent contribution exhibit a more dampened collapse compared to the collapse in UCM fluid, where only the viscoelastic stresses affect the dynamics. It is found, that the LPTT model shows slightly increased viscoelastic stresses, despite including shear-thinning behavior, as compared to the OLD-B fluid. Moreover, shock wave emission is presented for increased elasticity. A mesh study with three different resolutions was carried out for the case with increased elasticity, and it is found that shock wave formation depends on the resolution for the applied parameters as shown in fig. 3.6. For the finest mesh used, the shock wave formation is suppressed.

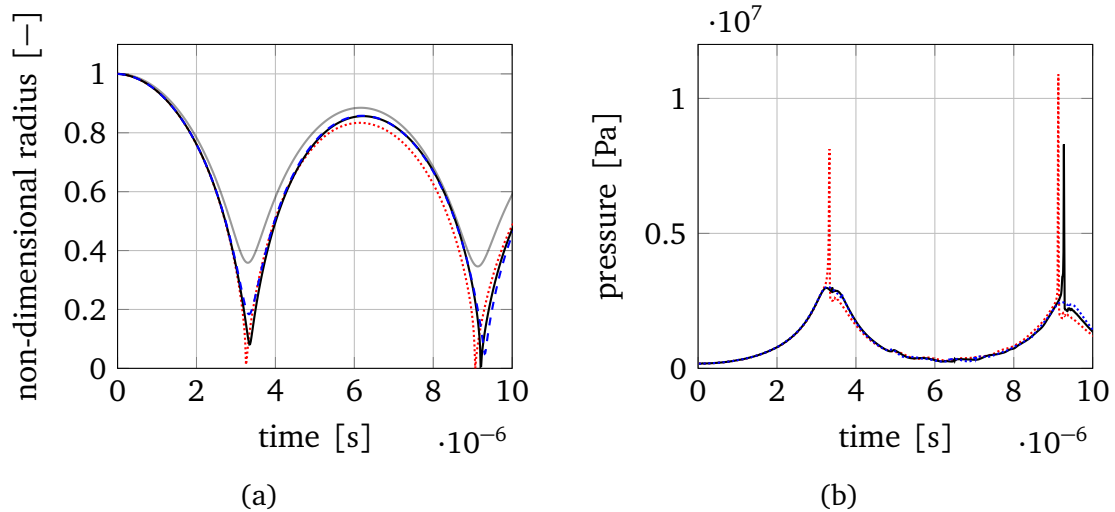


Figure 3.6: Spherical bubble collapse for increased elasticity $Re = 1$, $De = 3$ and different mesh resolutions as shown in Lang et al. [78]. (a) Radius (— shows the solution of the Keller-Miksis equation) and (b) corresponding pressures at $r/R_0 = 1.2$ over time during the collapse for the UCM model at $Re = 1$, $De = 3$ and three different grid refinements. Resolution in number of cells per initial radius: \cdots 100/ R_0 , — 140/ R_0 , - - - 200/ R_0 .

Individual contributions of the candidate

This article was published in the peer-reviewed journal *Applied Mathematical Modelling*. My contributions to this publication lie in the conceptualization, selecting the simulation parameters, and performing the numerical simulations yielding the presented results. Furthermore, I implemented the necessary post-processing routines and visualized the results. The original manuscript of the publication for the publication was written by me.

3.3 Viscoelastic vapor bubble collapse near solid walls and corresponding shock wave formation

Christian Lang, Stefan Adami, Nikolaus A. Adams: *Viscoelastic vapor bubble collapse near solid walls and corresponding shock wave formation*. *Physics of Fluids* 1 January 2024; 36 (1): 013110. <https://doi.org/10.1063/5.0175807>, licensed under a Creative Commons Attribution (CC BY) license. [74]

Summary and accomplishments

This study investigates the influence of viscoelasticity on cavitating vapor bubble collapses close to a solid wall. Due to the solid boundary, an aspherical collapse forms, and liquid jetting can be observed for particular conditions. The approach mentioned above is applied to conduct 3D simulations in Newtonian and the simplified linear Phan-Thien Tanner (LPTT) fluid. The general collapse dynamics in Newtonian and viscoelastic fluids are compared, and shock wave formation and liquid jetting are examined. Furthermore, the viscous and viscoelastic stress distributions are presented. Newtonian versus LPTT fluid simulations are performed for three different initial standoff distances. Moreover, the influence of elasticity is examined using three distinct relaxation times for LPTT fluid simulations.

It was found that viscoelasticity significantly alters the collapse dynamics (cf. figs. 3.7 and 3.8) and shock wave formation mechanism (cf. fig. 3.9).

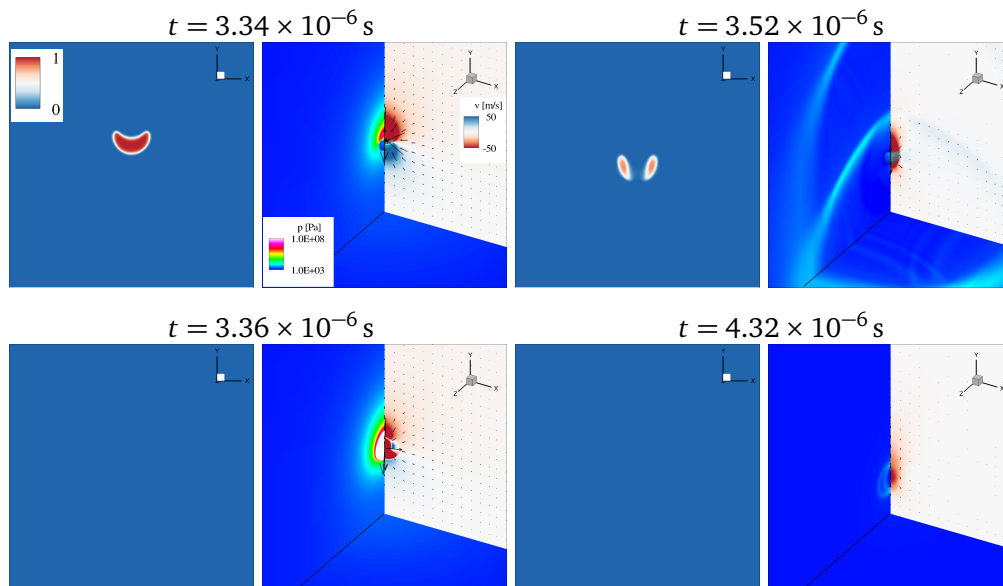


Figure 3.7: Aspherical bubble collapse in Newtonian fluid, $Re = 40$, $h^* = 1.5$ as presented in Lang et al. [74]. First and third column: vapor volume fraction α [-]. Second and fourth column: Wall normal velocity in x_2 -direction u_2 [m/s] through the x_1/x_2 -midplane and velocity vectors scaled by the velocity magnitude; pressure distribution p [Pa] through the x_2/x_3 -midplane and at the wall. Isosurface shows $\alpha = 0.01$.

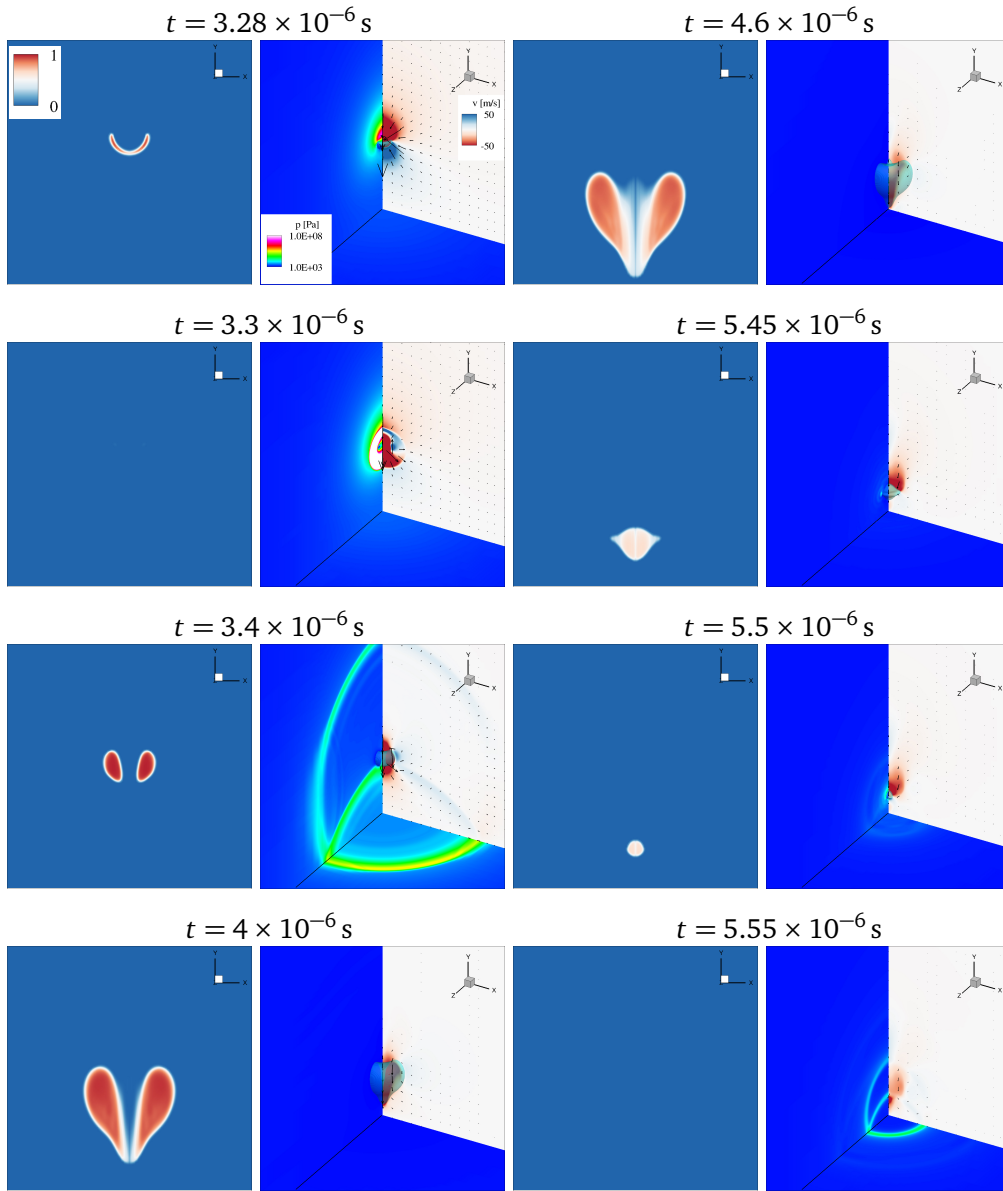


Figure 3.8: Aspherical bubble collapse in LPTT fluid, $Re = 40$, $De = 2$, $h^* = 1.5$ as presented in Lang et al. [74]. First and third column: vapor volume fraction α [–]. Second and fourth column: Velocity in x_2 -direction u_2 [m/s] through the x_1/x_2 -midplane and velocity vectors scaled by the velocity magnitude; pressure distribution p [Pa] through the x_2/x_3 -midplane and at the wall. Isosurface shows $\alpha = 0.01$.

For the initially wall-detached bubbles examined, viscoelasticity yields jet piercing, which is not observed for the Newtonian collapse, where a complete condensation of the vapor cavity without prior jet impingement occurs. The amount of re-evaporated fluid during the second collapse is increased for the viscoelastic collapse. As illustrated in fig. 3.11, it is ascertained that the pressure wave emission is of comparable intensity or stronger for the first collapse in the Newtonian fluid. However, the pressure resulting from the second collapse is much larger in the viscoelastic case (cf. fig. 3.11). For initially wall-attached bubbles, a second collapse is only observed for the viscoelastic collapse which can be seen from jet velocities as illustrated in figs. 3.10 and 3.11.

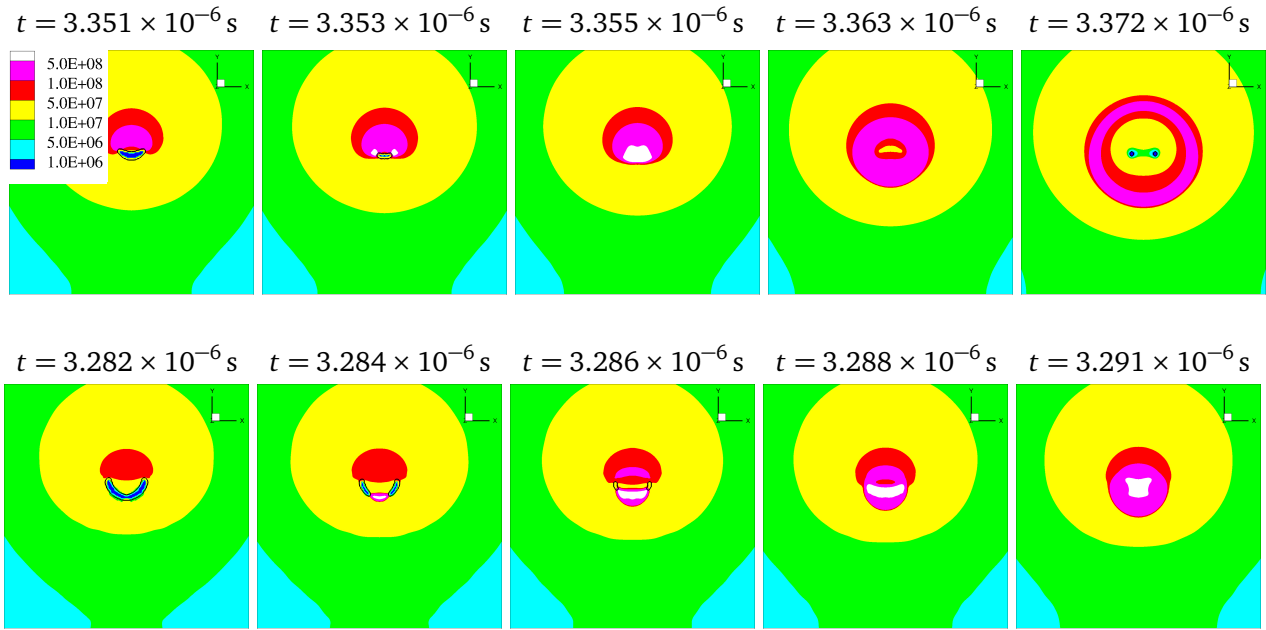


Figure 3.9: Shock wave formation during the aspherical bubble collapse from Lang et al. [74]. Pressure distribution p [Pa] in the x_1/x_2 -midplane for $Re = 40$, $De = 2$, $h^* = 1.5$. Top: Newtonian fluid, bottom: LPTT fluid. Black isoline shows vapor content of $\alpha = 0.01$.

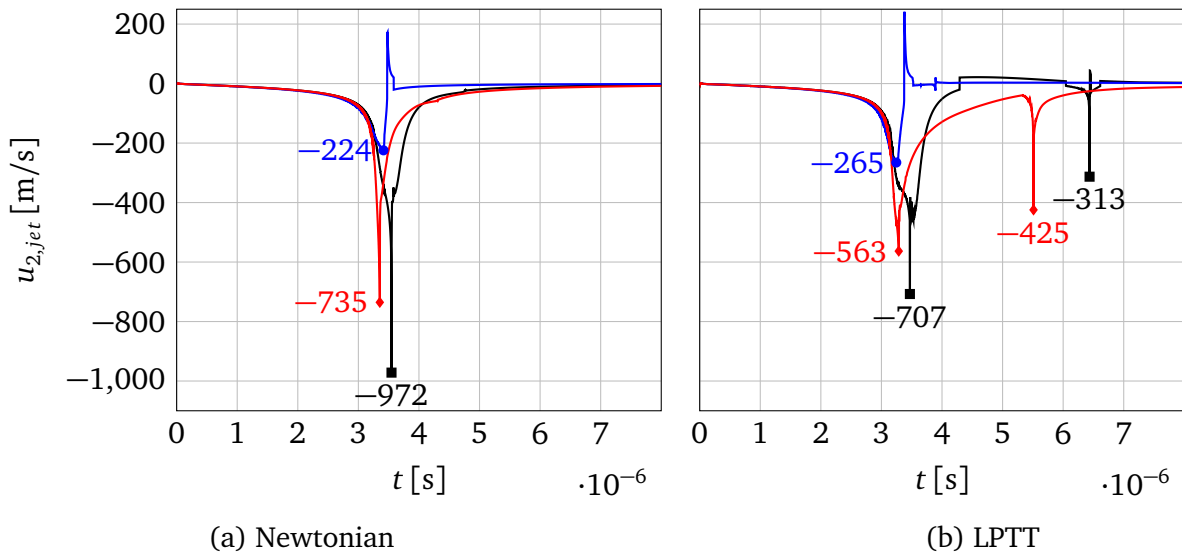


Figure 3.10: Jet velocity $u_{2,jet}$ [m/s] in x_2 -direction over time measured at centerline for $Re = 40$, $De = 2$ and different initial standoff distances as presented in Lang et al. [74]. (a) Newtonian fluid: — $h^* = 0.35$, — $h^* = 1.1$, — $h^* = 1.5$. (b) LPTT fluid: — $h^* = 0.35$, — $h^* = 1.1$, — $h^* = 1.5$.

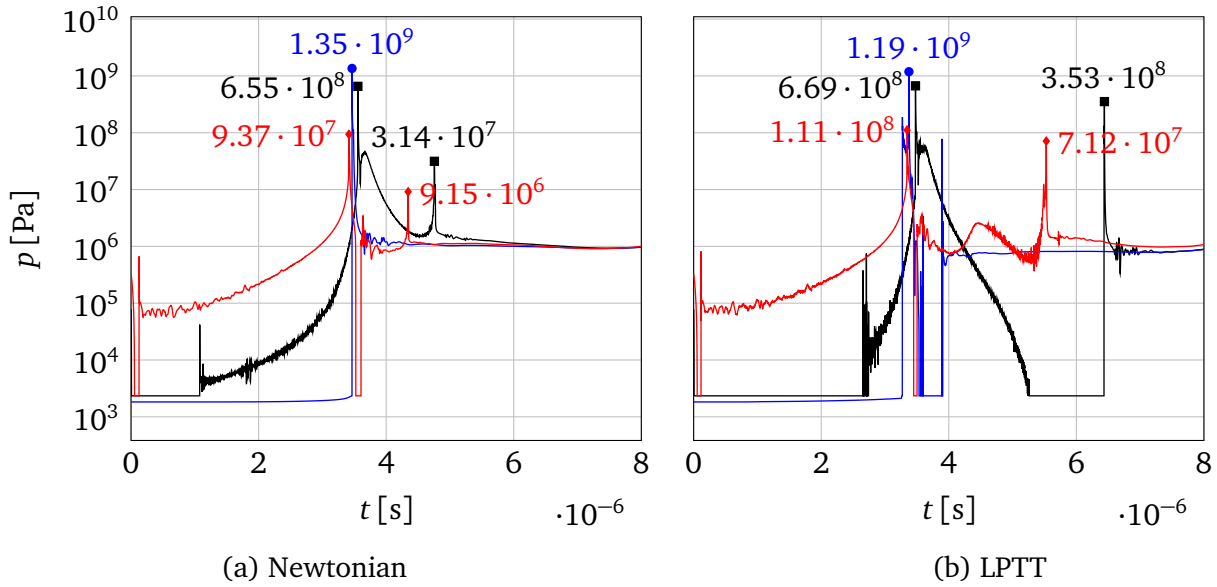


Figure 3.11: Pressure evolution p [Pa] at the wall ($x_2^* = 0$) at the position of maximum occurring pressure for different initial standoff distances at $Re = 40$, $De = 2$ (logarithmic scale). (a) Newtonian fluid \bullet $h^* = 0.35$ at $r^* = 0.25$, \blacksquare reference case ($h^* = 1.1$) at $r^* = 0.02$, \blacktriangleright $h^* = 1.5$ at $r^* = 0.02$. (b) LPTT: \bullet at $r^* = 0$, \blacksquare reference case ($h^* = 1.1$) at $r^* = 0$, \blacktriangleright $h^* = 1.5$ at $r^* = 0$. Results from Lang et al. [74].

The elasticity variation reveals that the amount of re-evaporation during rebound correlates to the investigated cases' relaxation time. Studying the viscous and viscoelastic stress distributions showed a direct influence of the occurring stresses on the flow field and the re-evaporation during rebound. The viscoelastic stresses exhibit a smoother distribution, whereas the viscous (solvent) stress fields exhibit more fluctuations. The different distributions can be explained by the direct relation of viscous stresses and strain rate, which can exhibit large oscillations, especially when shock waves are reflected and interfere, as in the present problem. The viscoelastic stress field develops with a time delay, depending on the relaxation time, which again yields much smoother stress distributions.

Individual contributions of the candidate

This article was published in the peer-reviewed journal *Physics of Fluids*. I contributed to this publication in doing the literature review, developing the conceptualization, selecting the relevant cases and simulation parameters, and conducting the numerical simulations. I implemented the necessary post-processing routines and generated the visualizations. The original manuscript of the publication for the publication was written by me.

Chapter 4

List of Publications

Peer-Reviewed Journal Publications

- **Christian Lang, Oliver Boolakee, Steffen J. Schmidt, Nikolaus A. Adams:** *A compressible 3D finite volume approach for the simulation of unsteady viscoelastic cavitating flows.* International Journal of Multiphase Flow, Volume 150, 2022, 103981, ISSN 0301-9322, <https://doi.org/10.1016/j.ijmultiphaseflow.2022.103981>. [75]
- **Christian Lang, Mengqi Zhang, Steffen J. Schmidt, Nikolaus A. Adams:** *On spherical vapor bubble collapse in viscoelastic fluids.* Applied Mathematical Modelling, Volume 123, 2023, Pages 484-506, ISSN 0307-904X, <https://doi.org/10.1016/j.apm.2023.07.004>. [78]
- **Christian Lang, Stefan Adami, Nikolaus A. Adams:** *Viscoelastic vapor bubble collapse near solid walls and corresponding shock wave formation.* Physics of Fluids 1 January 2024; 36 (1): 013110. <https://doi.org/10.1063/5.0175807>, licensed under a Creative Commons Attribution (CC BY) license. [74]

Conference Proceedings

- **Christian Lang, Steffen J. Schmidt, Nikolaus A. Adams:** *Compressible 3D-simulations of spherical bubble collapses in viscoelastic fluids.* Proceedings of the 11th International Symposium on Cavitation, Daejeon, South Korea, 2021. [76]
- **Christian Lang, Steffen J. Schmidt, Nikolaus A. Adams:** *Einfluss rein viskoser Nicht-Newtonscher Fluide auf den Einzelblasenkollaps.* Drittes Kolloquium Kavitation und Kavitationserosion, Bochum, 2018. [77]

Chapter 5

Concluding Discussion with Respect to the State of the Art

The method introduced in Lang et al. [75] represents a density-based approach with finite-volume discretization, explicit time integration, and a single fluid homogeneous mixture cavitation model for the simulation of fully compressible cavitating flows in viscoelastic fluids. Different viscoelastic models (Upper convected Maxwell model, Oldroyd-B model, linear and exponential Phan-Thien Tanner model) are implemented in conservative formulation. Existing numerical studies on viscoelastic flows commonly assume incompressibility and single-phase media [1, 6, 9, 31, 40, 42, 52, 104, 108, 124] often in connection with a (semi-)implicit time discretization [1, 6, 40, 104, 108] and are frequently employed for steady-state flows. In the 1990s, methods emerged, using finite volume spatial discretization to simulate 2D/3D unsteady, but still mainly incompressible, flows. Yul Yoo et al. [148] simulated the unsteady incompressible flow through a 2D planar contraction of an OLD-B fluid employing finite volumes and the SIMPLER algorithm. Sato et al. [124] conducted unsteady simulations of the UCM and OLD-B fluid using an explicit time integration and a mixed finite volume/finite element discretization. Mompean et al. [96] used an explicit time integration together with a finite volume discretization and the OLD-B model to investigate the time dependent incompressible flow through 2D and 3D planar contractions.

In several studies, multiphase flows are considered incorporating viscoelasticity assuming incompressible flows [32, 34, 44, 53, 61, 88, 123, 129, 146, 147, 151, 152]. A few studies considered compressibility combined with viscoelasticity and multiphase flows by using 1D formulations to study the bubble dynamics in viscoelastic fluids [22, 24, 59, 87, 143, 150]. Furthermore, methods for the simulation of compressible viscoelastic flows in more dimensions [14, 29, 68, 69, 89, 93, 94, 97, 98, 111, 117, 118, 121] have been developed, but only few consider unsteady, multiphase flows [97, 117, 118]. In Rodriguez et al. [117, 118] solid-like viscoelastic models are employed, not considering cavitation, i.e., evaporation and condensation. Naseri et al. [97] numerically investigates cavitating flows combined with viscoelastic fluids, considering compressibility only in the mixture, whereas pure phases are treated as incompressible, hence emitted shock waves cannot be fully resolved. To the author's knowledge, there is no other than the presented method to simulate unsteady, fully compressible, three-dimensional flows considering cavitation and viscoelasticity. The density-based approach allows for the simulation of two-phase cavitating flows with viscoelastic con-

stitutive equations and to resolve shock-wave dynamics. In Lang et al. [75], the approach is validated against (semi-)analytical references with excellent agreement by performing unsteady start-up simulations of channel flows. Furthermore, viscoelasticity leads to oscillating spherical bubble collapse in contrast to the Newtonian collapse. The different constitutive models result in distinct collapse behaviors, where fluids with solvent contribution exhibit smaller rebound radii during the oscillations. Moreover, it is shown that viscoelasticity can lead to shock wave emission during collapse.

In Lang et al. [78] the approach mentioned above is applied to conduct 3D simulations of the spherical vapor bubble collapse in three different viscoelastic fluids (UCM, OLD-B, LPTT). Subsequently, the viscoelastic collapse dynamics, viscous and viscoelastic stress development, and the relation between stress development and the occurring deformation rates are investigated. Furthermore, the isolated influence of the variation of elasticity and viscosity is examined, and the effect of the distinct viscoelastic models is determined. Existing numerical studies on spherical bubble dynamics in viscoelastic fluids are typically based on 1D formulations [2–5, 22, 24, 45, 48, 59, 91, 123, 132, 143, 146, 150]. There are only a few studies known by the author using 3D methods to investigate spherical bubble dynamics. Foteinopoulou et al. [46] apply a finite element-based discretization to study the asphericity and oscillatory behavior of bubbles in Phan-Thien Tanner fluid, assuming the flow to be incompressible. Laridon et al. [79] used a finite element method together with a multimode Maxwell model to simulate the growth of bubbles in an incompressible medium. For the numerical simulation of the spherical bubble collapse in viscoelastic media, compressibility was only taken into account by some 1D approaches [22, 24, 48, 59, 143, 150]. For the simulation of aspherical bubble dynamics in the vicinity of a rigid wall, Lind et al. [89] employ a 2D approach. From the aforementioned 1D methods, only Zilonova et al. [150] takes into account cavitation. To the author's best knowledge, 3D simulations of cavitating bubbles in viscoelastic fluid have not been conducted thus far. Additionally, there have been no existing numerical 3D simulations of cavitating bubbles in viscoelastic fluids considering compressibility. Hence, Lang et al. [78] presents the first numerical study investigating the different viscous and viscoelastic stress components, the relation to the occurring deformation rates, and deviatoric and spherical stresses during viscoelastic bubble collapse. Furthermore, 3D simulations of the bubble collapse with parameter variation of elasticity and viscosity have not been conducted before. Moreover, there was no existing study to show 3D shock wave emission for the viscoelastic bubble collapse yet.

The study shows the fundamental impact of viscoelasticity leading to oscillations during collapse, which results from different viscoelastic stresses. The development of the viscoelastic stresses is substantially different from Newtonian ones. It is illustrated that solvent stresses appear without time delay directly proportional to the deformation rate. The viscoelastic stresses develop with time-delay attributed to relaxation, which is described by the constitutive equation. Viscoelastic stresses feature convective transport related to the flow field. Moreover, viscoelasticity introduces isotropic stresses, although the deformation rate and the corresponding dissipation term are entirely deviatoric. Furthermore, the significant influence of relaxation time is exhibited. For the investigated parameters, increasing the elasticity accelerates the collapse in the early stages due to delayed stress development. The rebound radii increase with increased elasticity since less viscous dissipation is present during the collapse.

The comparison between the different viscoelastic models reveals more substantial viscous damping and smaller rebound radii for models with solvent contribution. For the UCM model, increasing the elasticity results in the emission of shock waves. It is demonstrated that, for the investigated parameters, shock wave emission depends on the mesh resolution, and an entire collapse is required to generate a shock wave.

Using a 3D method also allows simulating aspherical bubble collapses. In Lang et al. [74], the approach is exploited to examine the viscoelastic vapor bubble collapse in the vicinity of a solid wall. The study examines the generic dynamics of Newtonian versus viscoelastic bubble collapse close to a rigid wall. Viscoelasticity is introduced by the simplified linear Phan-Thien Tanner (LPTT) model, considering shear-thinning behavior. Besides the collapse dynamics, the viscous and viscoelastic stress development, responsible for the distinct dynamics of Newtonian and viscoelastic behavior, is investigated. Furthermore, the influence of initial standoff distance and distinct elasticities is presented. Additionally, the study examines shock wave formation and emission during collapse. Most of the existing numerical studies on wall-influenced bubble collapse consider inviscid [16, 18, 58, 65, 81, 82, 84, 113, 114, 131, 133, 138, 146] or Newtonian fluids [13, 27, 28, 71, 72, 83, 90, 99, 115, 122, 140, 149]. Some of the existing numerical studies on wall-influenced bubble collapse in viscoelastic media assume irrotational and incompressible flow applying the Boundary Element Method (BEM) [88, 142]. In Lind et al. [88], the Maxwell model combined with the material derivative as time rate is applied as constitutive model. Walters et al. [142] use the Oldroyd-B model to model viscoelasticity, incorporating solvent contributions and the upper convected derivative for the viscoelastic stress tensor. The BEM is computationally very efficient but comprises some disadvantages. First, stresses are only incorporated at the interface, neglecting stresses in the remaining field. Second, if two points at the bubble surface coincide, a singularity forms, yielding the simulation to fail. Liquid jet piercing and subsequent toroidal bubble shapes can thus not be resolved. To overcome this disadvantage, Walters et al. [142] introduces a non-singular formulation of the BEM to simulate toroidal-shaped bubbles and jet formation. Lind et al. [89] employs a spectral element marker particle approach considering rotational and compressible flows to simulate aspherical bubble collapses in viscoelastic fluid. The Oldroyd-B model with upper convected time rate is used as viscoelastic model. The approaches mentioned above [88, 89, 142] all consider gas-filled bubbles neglecting evaporation and condensation. Furthermore, none of these studies examines shock-wave emission generated during the collapse. Additionally, the present study Lang et al. [74] incorporates shear-thinning effects by using the LPTT viscoelastic model. In sum, the major novelties in Lang et al. [74] are the fully compressible 3D approach combined with a viscoelastic model accounting for shear-thinning behavior and a cavitation model considering evaporation and condensation. To the author's best knowledge, this is the first study examining shock wave emission during the aspherical vapor bubble collapse in the vicinity of a solid wall in viscoelastic fluid.

The study illustrates that viscoelasticity significantly influences the collapse dynamics close to solid walls. It is shown that viscoelasticity increases re-evaporation during the first rebound, resulting in larger pressures during the second collapse. The pressure wave emitted during the first collapse is of comparable intensity for both fluids or more intense in Newtonian liquid. For initially wall-detached bubbles, viscoelasticity changes the shock emission

mechanism by introducing jet-piercing. Moreover, wall-detached bubbles exhibit jet formation during the second collapse only in the viscoelastic cases. It is shown that the viscoelastic stresses are responsible for the increased amount of vapor produced during rebound. The variation of elasticity reveals the correlation between relaxation time and re-evaporation. Increased relaxation time results in more vapor following the first collapse. The jet velocity is highest for the lowest elasticity.

Chapter A

Peer-Reviewed Journal Publications

A.1 *A compressible 3D finite volume approach for the simulation of unsteady viscoelastic cavitating flows*

(Reproduced from [75])



RightsLink

Home

Help ▾

Live Chat

Sign in

Create Account



A compressible 3D finite volume approach for the simulation of unsteady viscoelastic cavitating flows

Author: Christian Lang, Oliver Boolakee, Steffen J. Schmidt, Nikolaus A. Adams

Publication: International Journal of Multiphase Flow

Publisher: Elsevier

Date: May 2022

© 2022 Elsevier Ltd. All rights reserved.

Journal Author Rights

Please note that, as the author of this Elsevier article, you retain the right to include it in a thesis or dissertation, provided it is not published commercially. Permission is not required, but please ensure that you reference the journal as the original source. For more information on this and on your other retained rights, please visit: <https://www.elsevier.com/about/our-business/policies/copyright#Author-rights>

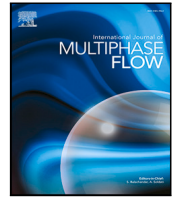
BACK

CLOSE WINDOW



Contents lists available at ScienceDirect

International Journal of Multiphase Flow

journal homepage: www.elsevier.com/locate/ijmulflow

A compressible 3D finite volume approach for the simulation of unsteady viscoelastic cavitating flows

Christian Lang^{a,*}, Oliver Boolakee^b, Steffen J. Schmidt^a, Nikolaus A. Adams^a

^a Chair of Aerodynamics and Fluid Mechanics, Technical University of Munich, Boltzmannstr. 15, 85748 Garching bei München, Germany

^b Department of Mechanical and Process Engineering, ETH Zürich, Tannenstrasse 3, 8092 Zürich, Switzerland

ARTICLE INFO

Keywords:

Viscoelasticity
Cavitation
Compressible flow
Objective time derivative
Stress tensor symmetry boundary condition
Bubble dynamics

ABSTRACT

We present a fully compressible, density-based finite volume solver for the simulation of 3D cavitating flows in viscoelastic Maxwell-/Oldroyd-like fluids. The upper-convected Maxwell model, the Oldroyd-B model and the linear and exponential simplified Phan-Thien Tanner models are implemented as viscoelastic constitutive equations in conservative formulation, and we identified the Truesdell rate as appropriate objective time derivative for compressible flows. Cavitation is modeled by a single-fluid homogeneous mixture equilibrium approach considering condensation and evaporation assuming volume averaged mixture quantities. The corresponding simplified quasilinear system is analyzed, and the wave speeds are calculated in order to adapt the employed four step Runge–Kutta explicit time stepping concerning the viscoelastic transport equations. We introduce a novel ghost cell boundary condition for the viscoelastic stress tensor. The approach is tested against (semi-)analytical unsteady and steady-state references and shows very good agreement. 3D simulations of the spherical vapor bubble collapse are performed for all implemented viscoelastic models and show a distinct influence compared to the Newtonian case. For the upper-convected Maxwell fluid a variation of the relaxation time exhibits its perspicuous influence on the dynamics of the collapse.

1. Introduction

Cavitating flows play an important role in different fields of science and engineering such as acoustics, biomedical applications and process engineering. The applications range from liquid fuel injectors (Egerer et al., 2014), pumps and ship propellers (Budich, 2018) to sonochemical reactors (Gogate et al., 2003), cleaning (Ohl et al., 2006a) and medical applications such as shock-wave lithotripsy (Johnsen and Colonius, 2008), histotripsy (Vlaisavljevich et al., 2015) and medical drug delivery by means of sonoporation (Price and Kaul, 2002; Ohl et al., 2006b; Lentacker et al., 2014) just to name a few examples. Most of the research on cavitating flow has been conducted for purely viscous Newtonian fluids. However, dependent on the relaxation time and the time-scale of observation many materials can exhibit viscous and simultaneously elastic behavior and therefore be described as viscoelastic materials (Barnes, 1989; Owens and Phillips, 2002). Several fields of application in which cavitation occurs are also influenced by viscoelasticity. For instance, biomaterials most of the materials used in biomedical applications where cavitation takes place in form of bubble dynamics exhibit viscoelasticity (Brujan, 2011; Vlaisavljevich et al., 2015; Walters, 2015). If cavitation occurs in polymeric materials

viscoelastic influence has to be considered (Brujan, 2019), too. Also in industrial applications such as lubricants in bearings, viscoelasticity affects cavitation (Berker et al., 1995). A comprehensive overview of cavitation in non-Newtonian fluids is given in the textbook of Brujan (2011). Viscoelasticity can heavily alter cavitation and therefore it is of crucial interest to understand its influence.

The majority of the developed solvers for viscoelastic flow problems assume incompressible flow (Crochet and Bezy, 1979; Perera and Strauss, 1979; Oliveira et al., 1998; Sato and Richardson, 1994; Aboubacar and Webster, 2001; Alves et al., 2003; Favero et al., 2010; Al-Baldawi, 2012; Habla et al., 2012; Ferrás et al., 2020) often in combination with a (semi-)implicit time discretization scheme (Perera and Strauss, 1979; Oliveira et al., 1998; Aboubacar and Webster, 2001; Alves et al., 2003; Favero et al., 2010). In the 1990s, several studies emerged using a finite volume discretization for the calculation of 2D and 3D unsteady viscoelastic flows. Yul Yoo and Na (1991) simulated the unsteady incompressible flow through a 2D planar contraction of a OLD-B fluid employing finite volumes and the SIMPLER algorithm. Sato and Richardson (1994) conducted unsteady simulations of the UCM and OLD-B fluid using an explicit time integration and a mixed finite

* Corresponding author.

E-mail address: c.lang@tum.de (C. Lang).

URL: <http://www.aer.mw.tum.de> (C. Lang).

<https://doi.org/10.1016/j.ijmultiphaseflow.2022.103981>

Received 22 May 2021; Received in revised form 1 September 2021; Accepted 13 January 2022

Available online 31 January 2022

0301-9322/© 2022 Elsevier Ltd. All rights reserved.

volume/finite element discretization. Mompean and Deville (1997) used an explicit time discretization together with a spatial finite volume discretization and the OLD-B model to investigate the time dependent incompressible flow through 2D and 3D planar contractions.

Additionally, in some approaches compressibility was taken into account. Some of these consider the 1D formulation of the conservation and constitutive equations to investigate bubble dynamics in viscoelastic fluids (Brujan, 1999, 2001; Lind, 2010; Hua and Johnsen, 2013; Warnez and Johnsen, 2015; Zilonova et al., 2018). Only a few numerical methods for the simulation of compressible viscoelastic flows in more dimensions (Phelan et al., 1989; Nithiarasu, 2004; Keshtiban et al., 2005; Belblidia et al., 2006; Lind and Phillips, 2013; Chakraborty and Sader, 2015; Rowlatt and Lind, 2017; Naseri et al., 2018; Rodriguez and Johnsen, 2019; Rodriguez et al., 2019) were developed so far. Again, only few of these works on compressible viscoelastic flows investigate unsteady effects by use of an explicit time discretization (Phelan et al., 1989; Nithiarasu, 2004; Rodriguez and Johnsen, 2019; Rodriguez et al., 2019).

Most of the existing numerical studies connecting cavitation and viscoelasticity focus on bubble dynamics and their collapse. In 1970, Fogler and Goddard (1970) found out that viscoelasticity can alter the spherical bubble collapse based on the 1D formulation of the governing equations for a Maxwell fluid and incompressible flow. He examined that the collapse can be retarded, and oscillatory motion is possibly initiated. Kim (1994) likewise investigated the bubble collapse considering the 1D conservation and constitutive equations for a Maxwell fluid and comparing two different finite element methods. Jiménez-Fernández and Crespo (2006) showed the influence of viscoelasticity on the collapse of gas bubbles and empty voids. Hua and Johnsen (2013) and Warnez and Johnsen (2015) revealed that compressibility can be relevant for bubble dynamics in viscoelastic materials. Hua and Johnsen (2013) showed that damping can be influenced essentially by compressible as well as viscoelastic effects considering the Zener model for a viscoelastic solid in 1D together with the Keller–Miksis equation. Warnez and Johnsen (2015) employ a generalized constitutive relation to realize several viscoelastic models and likewise solve the compressible 1D Keller–Miksis equation to investigate the influence of relaxation time on bubble dynamics. They found out that relaxation can lead to faster bubble growth and that the differences between the viscoelastic constitutive models become more conspicuous with increasing relaxation time. Numerical studies that combine multiphase flows in more dimensions (2D & 3D) with viscoelastic fluids are quite rare. Lind and Phillips (2013) and Rowlatt and Lind (2017) used a spectral element method to study the influence of viscoelasticity on bubble dynamics. They applied a marker particle method and the compressible OLD-B constitutive model. In Lind and Phillips (2013), they perceived that viscoelasticity is able to reduce cavitation damage by inhibiting jet formation. A boundary element method and the vortex ring method were employed by Walters (2015) to examine the aspherical bubble collapse in viscoelastic fluids near a solid wall, too. They also detected that jet formation may be suppressed by viscoelasticity. Figueiredo et al. (2016) developed a two-phase 3D approach to study the Weissenberg effect for several viscoelastic materials. To the best of our knowledge, only the works of Naseri et al. (2018), Rodriguez and Johnsen (2019) and Rodriguez et al. (2019) present compressible solvers to calculate viscoelastic cavitating flows in more dimensions. In Naseri et al. (2018), only the liquid–vapor mixture is considered compressible whereas the liquid phase is assumed to be incompressible. They employed the cavitation model of Schnerr and Sauer (2001) and implemented the linear PTT (LPTT) model in a 3D finite volume framework. The cavitation model does not account for condensation and time integration is realized by an implicit time discretization. 3D simulations were conducted to investigate the influence of viscoelasticity on cavitating flows. In particular, the flow in two different nozzles together with cloud and string cavitation was examined. They ascertained that the viscoelastic contribution significantly reduces the occurrence of cavitation and

the resulting vapor volume fraction. Rodriguez and Johnsen (2019) introduced a compressible 3D flow solver based on finite difference discretization together with explicit time marching. They combine the five-equations multiphase model with constitutive equations of viscoelastic solids and implemented the Maxwell, Kelvin–Voigt and generalized Zener model. In Rodriguez et al. (2019) a quite similar methodology is employed. Like in Rodriguez and Johnsen (2019), their multiphase approach does not take condensation into consideration. They performed various test cases to validate their implementation and demonstrated that the method correctly predicts wave propagation in viscoelastic heterogeneous/multiphase materials. To date, there is no 3D flow simulation and numerical analysis of fully compressible, viscoelastic, cavitating flows, especially no consideration of condensation and resulting shock wave dynamics. In order to capture shock and wave dynamics during sudden re-condensation and collapse of cavitation structures it is crucial to employ an unsteady compressible formulation of the governing conservation and transport equations (Sezal, 2009). Moreover, Hua and Johnsen (2013) and Warnez and Johnsen (2015) stated that compressible effects have to be taken into account when studying the influence of viscoelasticity on cavitation. For the spherical collapse of a single vapor bubble the Keller–Miksis equation can be employed, although it has the disadvantage of considering compressibility only in the far-field. Additionally, for aspherical bubble collapses a 3D formulation is required.

Our research group has developed a density-based compressible 3D flow solver with spatial finite volume discretization and explicit time integration to calculate unsteady cavitating flows. A single-fluid homogeneous mixture equilibrium approach which is described in more detail in Section 2.3 is deployed to model cavitation with evaporation and condensation. By means of this method several studies on cavitating flows were conducted. Within the scope of this work, we present a compressible viscoelastic flow solver for Maxwell/Oldroyd-like constitutive models with a proper compressible objective time derivative which allows us to simulate unsteady cavitating flows and resolve shock and wave dynamics in time. The UCM, OLD-B, the simplified linear PTT (LPTT) and exponential PTT (EPTT) are implemented. We present a novel formulation for the symmetry boundary condition of the viscoelastic stress tensor that becomes necessary when employing a ghost cell boundary condition approach. The solver is validated against (semi-)analytical reference solutions and viscoelastic simulations of the spherical vapor bubble collapse are performed exhibiting distinct influence of viscoelasticity on the bubble dynamics.

2. Mathematical and physical model

2.1. Conservation equations for compressible flow

We employ the 3D conservation equations for compressible flow in an Eulerian frame. We assume the phase change to be isentropic and apply a barotropic equation of state (see Section 2.3). The temperature changes due to isentropic phase change are very small. Furthermore, the internal energy can only be altered by either shock wave emission or viscous dissipation. For the investigated cases, the intensity of the shock waves are of limited intensity and the heat capacity of the fluid is rather large. Accordingly, the temperature changes due to modified internal energy or phase change are small and can therefore be neglected. Hence, the conservation equations of mass and momentum are sufficient to describe the flow. By neglecting body forces the following equations describe the mixture:

$$\frac{\partial \rho}{\partial t} + \operatorname{div}(\rho \mathbf{u}) = 0, \quad (1)$$

$$\frac{\partial(\rho \mathbf{u})}{\partial t} + \operatorname{div}(\rho \mathbf{u} \otimes \mathbf{u}) = \operatorname{div}(\boldsymbol{\sigma}), \quad (2)$$

where $\rho = \rho(\mathbf{x}, t)$, $\mathbf{u} = \mathbf{u}(\mathbf{x}, t)$ and $\boldsymbol{\sigma} = \boldsymbol{\sigma}(\mathbf{x}, t)$ are the mixture density, the fluid velocity and the Cauchy stress tensor with respect to the position \mathbf{x} in current configuration and time t . The Cauchy stress tensor

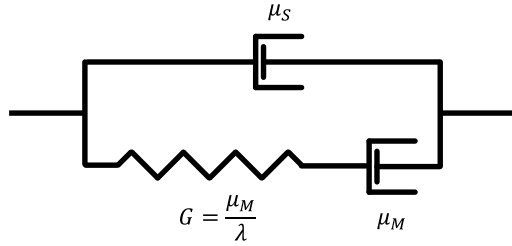


Fig. 1. 1D mechanical/rheological representation of an Oldroyd-like constitutive model. Upper dashpot represents a Newtonian solvent; below: Maxwell element consisting of dashpot and Hookean spring in series arrangement.

is composed of the thermodynamic pressure p and the viscous stress tensor τ neglecting surface tension:

$$\sigma = -p\mathbf{I} + \tau. \quad (3)$$

Note that for the two phases of water and vapor these equations are solved assuming a homogeneous mixture of both. The calculation of mixture quantities is explained in Section 2.3. The formulation of the viscous stress tensor which comprises the viscoelastic contribution is described hereafter.

2.2. Viscoelastic constitutive model

2.2.1. Compressible Maxwell-/Oldroyd-type model

We consider a compressible Maxwell-/Oldroyd-type constitutive model which consists of a Newtonian solvent stress τ_S and a viscoelastic part. The viscoelastic part can be regarded as polymeric stress contribution in a Newtonian solvent and is denoted as Maxwell stress τ_M . The 1D rheological representation of Oldroyd-like models is illustrated in Fig. 1. The Oldroyd element consists of a Newtonian dashpot element and a Maxwell element in parallel. The upper dashpot element represents the Newtonian solvent. The Maxwell element itself is a series arrangement of a dashpot and a Hookean spring and is responsible for the viscoelastic behavior introducing a time dependent stress response.

By introducing the velocity gradient $l = \text{grad}(\mathbf{u})$, the symmetric part of the velocity gradient $\mathbf{d} = \frac{1}{2}(\mathbf{l} + \mathbf{l}^T)$ and the deviatoric (traceless) strain rate tensor $\mathbf{d}^d = \mathbf{d} - \frac{1}{3}\text{tr}(\mathbf{d})\mathbf{I}$ the constitutive model reads

$$\tau = \tau_S + \tau_M, \quad (4)$$

$$\tau_S = 2\mu_S \mathbf{d}^d, \quad (5)$$

$$\tau_M + \lambda \overset{\nabla}{\tau}_M + f(\tau_M, \mathbf{d}^d) \tau_M = 2\mu_M \mathbf{d}^d. \quad (6)$$

The solvent viscosity is described by μ_S and μ_M represents the polymeric viscosity which we call Maxwell viscosity. $\overset{\nabla}{\tau}_M$ is an objective time derivative of the Maxwell stress and is discussed in further detail in Section 2.2.2. $\lambda = \frac{\mu_M}{G}$ represents the relaxation time and relates the Maxwell viscosity to the modulus of polymeric elasticity. Special attention was paid to the formulation for compressible flow. We include compressibility in the solvent as well as in the Maxwell part of the fluid (cf. Oliveira et al., 1998; Keshtiban et al., 2004, 2005; Belblidia et al., 2006) and consequently assume that only the deviatoric part of the deformation contributes to dissipation in both the solvent and the Maxwell part. The isotropic part, i.e. the part responsible for purely volumetric deformation, however, does not. Thus, bulk viscosity which models the viscous stress response to volume change is also neglected. Nevertheless, the objective time derivative (cf. Section 2.2.2) used in this work can introduce a nonzero trace $\text{tr}(\tau_M) \neq 0$ in the Maxwell stress tensor which leads to an isotropic part in the viscous stress tensor τ .

The approach resembles the formulation of Keshtiban et al. (2004, 2005) and Belblidia et al. (2006) but differs from that by not explicitly excluding the trace of the stress tensor τ . Otherwise, isotropic stresses initiated by the objective rate which is connected with the deformation itself would not contribute to the momentum Eq. (2). The physical motivation for such formulation is that spherical stresses which occur due to deformation and involved transformations ensuring frame invariance (see Section 2.2.2) are considered in the momentum balance. Bollada and Phillips (2012) support this approach by applying non-equilibrium thermodynamics to show that the thermodynamic pressure p and the trace of the Cauchy stress tensor $\text{tr}(\sigma)$ should not necessarily coincide. Our formulation of the constitutive equations agrees with that of Housiadas and Georgiou (2011), Housiadas et al. (2012). Moreover, we use a different objective rate, which appears to be more appropriate for compressible flows.

Furthermore, the Maxwell model in differential form is extended by an additional term $f(\tau_M, \mathbf{d}^d)$. The modification addresses the issue of an unbounded extensional viscosity and accounts for the description of shear-thinning (Larson, 1992; Böhme, 2000; Owens and Phillips, 2002). Different constitutive models can be recovered by using a differential constitutive equation of the type of Eq. (6) like the Johnson and Segalman (Johnson and Segalman, 1977), the Giesekus (Giesekus, 1966, 1982) and the Phan-Thien Tanner (PTT) model (Phan-Thien and Tanner, 1977; Phan-Thien, 1978). The PTT model originates from the network theory of polymer fluids and predicts bounded extensional viscosity as well as shear thinning behavior for the viscosity and is well suited to simulate flows of polymer melts and solutions. For this work, the upper-convected Maxwell (UCM) model, the Oldroyd-B (OLD-B) model (Oldroyd, 1950, 1984), the linear (LPPT) (Phan-Thien and Tanner, 1977) and the exponential PTT (EPPT) (Phan-Thien, 1978) model are implemented. We utilize the simplified versions of the PTT models where the originally used Gordon-Schowalter rate is replaced by the Truesdell rate. For these models the additional term reads as follows:

$$\text{LPPT: } f(\tau_M, \mathbf{d}^d) = \epsilon \frac{\lambda}{\mu_M} \text{tr}(\tau_M), \quad (7)$$

$$\text{EPPT: } f(\tau_M, \mathbf{d}^d) = \exp\left(\epsilon \frac{\lambda}{\mu_M} \text{tr}(\tau_M)\right) - 1. \quad (8)$$

The PTT model comprises the extensibility parameter $\epsilon = [0, 1]$. Throughout this work a commonly used value of $\epsilon = 0.25$ is chosen for the LPPT or EPPT model. By selecting the upper-convected derivative as objective rate and $f(\tau_M, \mathbf{d}^d) = 0$ the original Oldroyd-B model (OLD-B) is regained. By additionally neglecting the solvent part and exclusively considering the Maxwell part for the viscous stress tensor we recover the upper-convected Maxwell model (UCM). Nevertheless, we exclusively employ the UCM and the OLD-B model together with the Truesdell rate in this study (cf. Section 2.2.2).

2.2.2. Objective rate for the stress tensor in compressible flows

We paid particular attention to use a consistent time derivative for the stress tensor τ_M in the context of compressible flows. The correct formulation of the time derivative has to fulfill the following requirements. In order to obtain a frame invariant description of the material behavior, it is necessary to respect the principle of material objectivity or material frame invariance (Truesdell and Noll, 2004; Haupt, 2000). i.e. to apply an objective time derivative. However, there exists an infinite number of time derivatives meeting this criterion (Lippmann, 1996). We decided to use a time rate, which is also physically consistent with the simulation of compressible flows. Therefore, the stricter restriction of work conjugacy shall be fulfilled additionally (Bergander, 1987; Ji et al., 2013). We follow the concept of deriving the physically correct time derivative by applying the Lie derivative with respect to the spatial velocity field \mathbf{u} (Pinsky et al., 1983; Dvorkin and Goldschmit, 2005) adapted to compressible flow denoted by $\mathcal{L}_\mathbf{u}$. To be able to calculate the Lie derivative a mapping

between the current (spatial) and the material (reference) configuration is introduced. The mapping is given by the deformation gradient \mathbf{F} . \mathbf{F} maps an infinitesimal material element in reference configuration $d\mathbf{X}_0$ onto its spatial counterpart in the current configuration $d\mathbf{x}$, given a motion defined by the current position of a point $\mathbf{x} = \mathbf{x}(\mathbf{X}_0, t)$ with its position in the reference configuration $\mathbf{X}_0 = \mathbf{x}(\mathbf{X}_0, t = t_0)$:

$$\mathbf{F} := \frac{\partial \mathbf{x}}{\partial \mathbf{X}_0}. \quad (9)$$

For a second order tensor \mathbf{a} in current configuration the pull-back operation is¹

$$\phi^*(\mathbf{a}) := \mathbf{F}^{-1} \mathbf{a} \mathbf{F}^{-T}. \quad (10)$$

The corresponding operation transforming a tensor \mathbf{A} in the reference configuration to its spatial description is called push-forward

$$\phi_*(\mathbf{A}) := \mathbf{F} \mathbf{A} \mathbf{F}^T. \quad (11)$$

The concept of finding the objective rate of a tensor field described in Eulerian configuration is to initially perform a pull-back operation to obtain the corresponding tensor field in the reference configuration. Subsequently, the material time derivative $\frac{D(\cdot)}{Dt}$ of the field in the reference configuration is calculated. Performing the material time derivative of an objective tensor in the reference configuration again results in an objective tensor, since that configuration remains unchanged. Finally, the push-forward operation is applied, and we receive the objective time derivative in spatial description. Thus, the objective rate is given by

$$\mathcal{L}_{\mathbf{u}}[\mathbf{a}] := \phi_* \left[\frac{D}{Dt} (\phi^*(\mathbf{a})) \right] =: \overset{\nabla}{\mathbf{a}}. \quad (12)$$

Since the stress tensor in the spatial configuration represents a volume specific quantity, compressibility has to be taken into account for the pull-back and push-forward operations. To consider volume changes the Jacobian J is introduced

$$J := \det \mathbf{F} = \frac{dv}{dV_0}. \quad (13)$$

The Jacobian relates the differential volume element in the spatial configuration dv to the one in reference configuration dV_0 .

We apply the concept of the Lie derivative to a volume specific quantity as performed in similar fashion in Pinsky et al. (1983). The objective rate of the Cauchy stress tensor $\boldsymbol{\sigma}$ in spatial configuration is calculated by using the material counterpart represented by the second Piola–Kirchhoff stress tensor $\mathbf{S}(\mathbf{X}_0)$. The corresponding transformation acting as pull-back of $\boldsymbol{\sigma}$ and push-forward of \mathbf{S} is the Piola transformation:

$$\mathbf{S} = \phi^*(\boldsymbol{\sigma}) := J \mathbf{F}^{-1} \boldsymbol{\sigma} \mathbf{F}^{-T}, \quad (14)$$

$$\boldsymbol{\sigma} = \phi_*(\mathbf{S}) := J^{-1} \mathbf{F} \mathbf{S} \mathbf{F}^T. \quad (15)$$

Thus, we calculate the objective rate of the Cauchy stress by

$$\begin{aligned} \overset{\nabla}{\boldsymbol{\sigma}} &= \phi_* \left[\frac{D}{Dt} (\phi^*(\boldsymbol{\sigma})) \right] = \\ &= \frac{D\boldsymbol{\sigma}}{Dt} - \mathbf{l} \cdot \boldsymbol{\sigma} - \boldsymbol{\sigma} \cdot \mathbf{l}^T + \text{tr}(\mathbf{l}) \boldsymbol{\sigma} \end{aligned} \quad (16)$$

which is called Truesdell rate (Truesdell, 1953, 1955). Since the Truesdell rate is linear in its argument and the Cauchy stress tensor is an additive combination of pressure, solvent stress and Maxwell contribution $\boldsymbol{\sigma} = -p\mathbf{1} + 2\mu_S \mathbf{d}^d + \boldsymbol{\tau}_M$ it can be directly applied to the Maxwell stress tensor

$$\overset{\nabla}{\boldsymbol{\tau}}_M = \frac{D\boldsymbol{\tau}_M}{Dt} - \mathbf{l} \cdot \boldsymbol{\tau}_M - \boldsymbol{\tau}_M \cdot \mathbf{l}^T + \text{tr}(\mathbf{l}) \boldsymbol{\tau}_M. \quad (17)$$

¹ Note that contravariant coordinates in conjunction with a covariant basis are assumed to obtain these forms of the pull-back and push-forward. For other isomers used to describe the tensor fields the pull-back and push-forward operations turn out to have a different form. Yet, it can be shown that the representation mentioned above should be used for a physically consistent formulation (Surana et al., 2010).

For incompressible flows with $\text{tr}(\mathbf{l}) = \text{div}(\mathbf{u}) = 0$ the upper-convected Oldroyd rate (Oldroyd, 1950) is retrieved.

As already mentioned, the derived Truesdell rate does not only represent an objective time derivative but also fulfills the requirement of work conjugacy which has been proven by Bergander (1987), Ji et al. (2013) and Bazant (2010, 1971). Bollada and Phillips (2012) deploying the integral form of constitutive models and convected time derivatives also came to the conclusion that the Truesdell rate is appropriate in a compressible context. Rouhaud et al. (2013) utilize the four-dimensional formalism “to show [that] the Truesdell transport is thus the only objective transport that represents a frame-indifferent time derivative of the Cauchy stress.” Recently, Mackay and Phillips (2019) made use of the generalized bracket framework to ascertain that the Truesdell rate constitutes the thermodynamically consistent objective rate in compressible viscoelastic fluid models.

2.2.3. Conservative formulation of the constitutive model

By substituting the mass conservation (1) into the Maxwell transport Eq. (6), the corresponding transport equation for the Maxwell stresses in conservative formulation is extracted:

$$\frac{\partial (\rho \boldsymbol{\tau}_M)}{\partial t} + \text{div} (\rho \boldsymbol{\tau}_M \otimes \mathbf{u}) = \mathbf{S}_{\rho \boldsymbol{\tau}_M}, \quad (18)$$

with the source term

$$\begin{aligned} \mathbf{S}_{\rho \boldsymbol{\tau}_M} &= \rho \left[\mathbf{l} \cdot \boldsymbol{\tau}_M + \boldsymbol{\tau}_M \cdot \mathbf{l}^T - \text{div}(\mathbf{u}) \boldsymbol{\tau}_M \right. \\ &\quad \left. + \frac{1}{\lambda} \left[2\mu_M \mathbf{d}^d - f(\boldsymbol{\tau}_M, \mathbf{d}^d) \boldsymbol{\tau}_M - \boldsymbol{\tau}_M \right] \right], \end{aligned} \quad (19)$$

Regarding the implementation in a finite volume scheme, we introduce the convective flux terms

$$F_\rho^c = \rho(\mathbf{u} \cdot \mathbf{n}), \quad (20)$$

$$\mathbf{F}_{\rho \mathbf{u}}^c = \rho \mathbf{u}(\mathbf{u} \cdot \mathbf{n}) + p \mathbf{n}, \quad (21)$$

$$\mathbf{F}_{\rho \boldsymbol{\tau}_M}^c = \rho \boldsymbol{\tau}_M(\mathbf{u} \cdot \mathbf{n}), \quad (22)$$

and the diffusive flux term

$$\mathbf{F}_{\rho \mathbf{u}}^d = (-\boldsymbol{\tau}_S - \boldsymbol{\tau}_M) \cdot \mathbf{n}. \quad (23)$$

Finally, we formulate the governing equations in integral form for a control volume V and apply Gauss' theorem yielding the compact form:

$$\int_V \frac{\partial \rho}{\partial t} dV + \oint_{\partial V} F_\rho^c dS = 0, \quad (24)$$

$$\int_V \frac{\partial (\rho \mathbf{u})}{\partial t} dV + \oint_{\partial V} \mathbf{F}_{\rho \mathbf{u}}^c dS + \oint_{\partial V} \mathbf{F}_{\rho \mathbf{u}}^d dS = \mathbf{0}, \quad (25)$$

$$\int_V \frac{\partial (\rho \boldsymbol{\tau}_M)}{\partial t} dV + \oint_{\partial V} \mathbf{F}_{\rho \boldsymbol{\tau}_M}^c dS - \int_V \mathbf{S}_{\rho \boldsymbol{\tau}_M} dV = \mathbf{0}. \quad (26)$$

2.3. Single-fluid homogeneous mixture equilibrium cavitation model

To model the two-phase behavior of cavitating flows a single-fluid approach which assumes volume averaged homogeneous mixture quantities in each finite volume is employed. We consider fluids composed of liquid and vapor with evaporation and condensation and take into account compressibility of all phases. Our approach assumes that a computational cell either contains pure liquid or a homogeneous mixture of water and vapor. Fig. 2 illustrates the concept of our model for a cell Ω . If a cell (Fig. 2a) contains vapor bubbles of discrete size our model does not resolve the liquid–vapor interfaces. As depicted in Fig. 2b, our approach models the volume averaged quantities of the contained homogeneous mixture. The two-phase mixture is assumed to be in mechanical and thermodynamic equilibrium and the phase change is supposed to be isentropic, infinitely fast and without time delay. Condensation and evaporation is therefore implicitly modeled by the equation of state for the two-phase mixture as it represents a

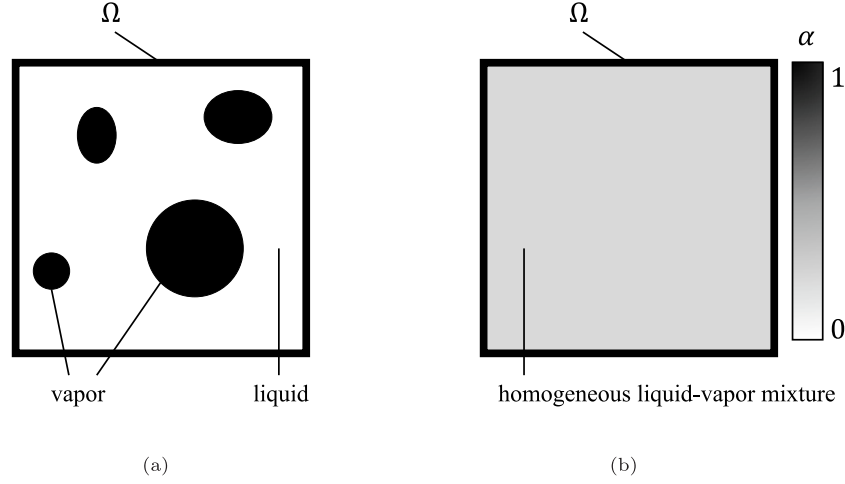


Fig. 2. Single-fluid homogeneous mixture model for a computational cell Ω . (a) Exemplary real physical situation, (b) Numerical model approximation with the corresponding vapor volume fraction α .

direct correlation of the vapor volume fraction and the thermodynamic variables as explained hereafter. Because of the equilibrium assumption, the appropriate vapor volume fraction instantaneously adapts to the flow properties and an additional model for the condensation rate or for relaxation is not needed. The approach was extensively used to investigate cloud cavitation (Schnerr et al., 2008), to simulate cavitating flows including non-condensable gas (Örley et al., 2015b,a), turbulent cavitating flows (Egerer et al., 2014, 2016), to predict cavitation erosion (Mihatsch et al., 2015) and to examine condensation shocks (Budich et al., 2018; Trummier et al., 2020). Schenke et al. (2019) showed for similar timescales of the flow and phase change, the condensation rates are rather high so that for typical engineering applications the equilibrium assumption is justified. A further detailed description of the model can be found in Sezal (2009) and Budich et al. (2018). The variables used for the transport equations Eqs. (37) to (39) further express volume averaged variables representing the mixture within a finite volume V_Ω , see Eq. (35). For the application to viscoelastic fluids, we suppose that the thermodynamic properties of pure liquid water and liquid–vapor mixtures of water remain unchanged. The mixture density results in a combination dependent on the vapor volume fraction α :

$$\rho = \alpha \rho_{v,sat} + (1 - \alpha) \rho_{l,sat}. \quad (27)$$

In the framework of an explicit density-based solver Eq. (27) is never used to compute the cell-averaged density which is obtained by the time integration of the continuity Eq. (1) and subsequently utilized to ascertain whether a cell contains a two-phase mixture of liquid and vapor or comprises pure liquid. The vapor volume fraction α describing the ratio of vapor volume $V_{v,\Omega}$ to the entire cell volume V_Ω is calculated depending on the mixture density within the cell according to

$$\alpha = \frac{V_{v,\Omega}}{V_\Omega} = \begin{cases} 0, & \text{if } \rho \geq \rho_{l,sat} \text{ (pure liquid)} \\ \frac{\rho_{l,sat} - \rho}{\rho_{l,sat} - \rho_{v,sat}}, & \text{else (liquid–vapor mixture).} \end{cases} \quad (28)$$

Throughout this work we suppose the flow to be barotropic and apply constant values at a reference temperature of $T = 293.15$ K summarized in Table 1.

To close the system of equations thermodynamic relations for the liquid phase ($\alpha = 0$) and the liquid–vapor mixture ($0 < \alpha < 1$) are employed. Our method employs separate equations of state for pure liquid and two-phase mixtures. If a cell is composed of pure liquid, the modified Tait equation of state by Saurel et al. (1999) with the parameters $N = 7.15$ and $B = 3.3 \cdot 10^8$ Pa at a reference temperature of

Table 1
Parameters of the barotropic model at $T_{ref} = 293.15$ K.

Property	Symbol	Value
Reference temperature	T_{ref}	[K] 293.15
Density of saturated liquid	$\rho_{l,sat}$	[kg m ⁻³] 998.16
Density of saturated vapor	$\rho_{v,sat}$	[kg m ⁻³] 0.017214
Saturation pressure	p_{sat}	[Pa] 2339.3
Dynamic viscosity of saturated liquid	$\mu_{l,sat}$	[Pa s] $1.0014 \cdot 10^{-3}$
Dynamic viscosity of saturated vapor	$\mu_{v,sat}$	[Pa s] $9.7275 \cdot 10^{-6}$
Speed of sound of saturated liquid	$c_{l,sat}$	[m s ⁻¹] 1482.2
Speed of sound of saturated vapor	$c_{v,sat}$	[m s ⁻¹] 423.18
Specific heat capacity of saturated liquid	$c_{p,l,sat}$	[J kg ⁻¹ K ⁻¹] 4184.4
Latent heat of vaporization	l_v	[J K ⁻¹] $2453.5 \cdot 10^3$

$$T_{ref} = 293.15 \text{ K}$$

$$p = B \left[\left(\frac{\rho}{\rho_{l,sat}} \right)^N - 1 \right] + p_{sat}. \quad (29)$$

is adopted. Accordingly, the speed of sound for pure liquid is given by

$$c = \left(\frac{N(p+B)}{\rho} \right)^{1/2}. \quad (30)$$

In the two-phase region of saturated liquid and vapor mixtures we exploit the definition for the isentropic speed of sound c to calculate the pressure by integration:

$$c^2 = \frac{\partial p}{\partial \rho} \Big|_{s=const.} \Rightarrow p(\rho) - p_{sat} = \int_{\rho_{l,sat}}^{\rho} c^2 d\tilde{\rho}. \quad (31)$$

For the definition of the speed of sound in two-phase regions we refer to Brennen (1995) and Franc and Michel (2005). Since we want to regard both phases to be in thermodynamic equilibrium and incorporate phase transitions the latent heat of vaporization has to be considered and the speed of sound c of the two-phase mixture can be extracted from:

$$\frac{1}{\rho c^2} = \frac{\alpha}{\rho_{v,sat} c_{v,sat}^2} + \frac{1-\alpha}{\rho_{l,sat} c_{l,sat}^2} + \frac{(1-\alpha) \rho_{l,sat} c_{p,l,sat} T_{ref}}{(\rho_{v,sat} l_v)^2}. \quad (32)$$

The last term on the right-hand side accounts for mass transfer through vaporization. The speed of sound of pure liquid and vapor are represented by $c_{l,sat}$ and $c_{v,sat}$. $c_{p,sat,l}$ and l_v are the specific heat capacity of saturated liquid and the latent heat of vaporization respectively. All variables correspond to values at reference temperature listed in Table 1. Further explanations leading to this formulation can be found in Sezal (2009) and Budich et al. (2018). By introducing Eq. (32) in

Eq. (31) and subsequent integration we obtain the pressure in the two-phase region as

$$p = \frac{1}{A} \ln \left(\frac{\rho}{A + B\rho} \right) - \frac{1}{A} \ln \left(\frac{\rho_{l,sat}}{A + B\rho_{l,sat}} \right) + p_{sat},$$

$$\text{with } A = -\frac{\rho_{l,sat}}{\rho_{v,sat} - \rho_{l,sat}} \left(\frac{1}{\rho_{v,sat} c_{v,sat}^2} - \frac{1}{\rho_{l,sat} c_{l,sat}^2} + C \right) + \frac{1}{\rho_{l,sat} c_{l,sat}^2} + \frac{\rho_{l,sat} c_{p,l,sat} T_{ref}}{(\rho_{v,sat} l_v)^2},$$

$$B = \frac{1}{\rho_{v,sat} - \rho_{l,sat}} \left(\frac{1}{\rho_{v,sat} c_{v,sat}^2} - \frac{1}{\rho_{l,sat} c_{l,sat}^2} + C \right),$$

$$C = \frac{T_{ref} (\rho_{v,sat} c_{p,v,sat} - \rho_{l,sat} c_{p,l,sat})}{(\rho_{v,sat} l_v)^2}.$$

The dynamic viscosity for pure liquid as well as for liquid–vapor mixture regions is computed following (Beattie and Whalley, 1982)

$$\mu_S = (1 - \alpha) \left(1 + \frac{5}{2} \alpha \right) \mu_{l,sat} + \alpha \mu_{v,sat}, \quad (34)$$

where μ_S corresponds to the solvent viscosity used in Section 2.2.1. $\mu_{l,sat}$ and $\mu_{v,sat}$ represent the dynamic viscosity of pure liquid and liquid–vapor mixture at reference temperature respectively.

3. Numerical method

3.1. Discretization and numerical flux calculation

The governing equations are spatially discretized by subdividing the physical domain in body-fitted, structured hexahedral finite volumes (Sezal, 2009; Mihatsch et al., 2015; Budich et al., 2018). A non-staggered cell-centered variable layout within each finite volume is utilized. We introduce a discrete volume averaging operator as

$$\bar{\square} := \frac{1}{V_\Omega} \int_\Omega \square \, dV, \quad \text{with } V_\Omega := \int_\Omega dV, \quad (35)$$

where V_Ω represents the volume of a discrete computational cell. We introduce the numerically approximated fluxes F_\square^\square and source term $S_{\rho\tau_M}$ comprising the corresponding numerical reconstruction and the calculation of surface and volume integrals:

$$F_\square^\square \stackrel{\text{num}}{=} \oint_{\partial\Omega} F_\square^\square \, dS, \quad S_{\rho\tau_M} \stackrel{\text{num}}{=} \int_\Omega S_{\rho\tau_M} \, dV, \quad (36)$$

Using the cell-averaged variables the governing equations read

$$\frac{\partial \bar{\rho}}{\partial t} + F_\rho^c = 0, \quad (37)$$

$$\frac{\partial (\bar{\rho}\mathbf{u})}{\partial t} + F_{\rho\mathbf{u}}^c + F_{\rho\mathbf{u}}^d = \mathbf{0}, \quad (38)$$

$$\frac{\partial (\bar{\rho}\boldsymbol{\tau}_M)}{\partial t} + F_{\rho\boldsymbol{\tau}_M}^c - S_{\rho\boldsymbol{\tau}_M} = \mathbf{0}. \quad (39)$$

An upwind-biased low-Mach number consistent approximate Riemann solver is applied to calculate the convective numerical fluxes F_ρ^c , $F_{\rho\mathbf{u}}^c$, $F_{\rho\boldsymbol{\tau}_M}^c$. The cell face variables are obtained by a higher-order spatial reconstruction on a four-point stencil. The calculation of the numerical fluxes is explained in more detail in Egerer (2016) where it is referred to as *baseline finite-volume scheme*. Velocities at cell faces are reconstructed using the total variation diminishing (TVD) limiter of Koren (1993) which is third order accurate in smooth regions. For the reconstruction of density the MinMod limiter of Roe (1986) is applied since an improved numerical robustness is required due to steep density and pressure gradients in two-phase flows. In smooth regions, this limiter is of second order accuracy Sezal (2009). This combination of limiters proved to provide numerically stable and accurate results (Mihatsch et al., 2015; Budich et al., 2018). The reconstruction procedures are explained in further detail in Egerer (2016). The Maxwell stresses

Table 2
Runge–Kutta sub-step coefficients.

j	1	2	3	4
ξ_j	0.11	0.2766	0.5	1.0

are reconstructed employing the weighted essentially non-oscillatory reconstruction procedure (WENO-3) (Jiang and Shu, 1996). Since the other reconstruction schemes are of second and third order accuracy, respectively, we conducted our simulations solely with this limiter, although a fifth-order accurate WENO (WENO-5) reconstruction would result in less numerical dissipation.

It is crucial to treat the convective flux terms of the Maxwell stress transport different to the diffusive flux due to the hyperbolic nature which will be revealed in Section 3.3. The diffusive flux $F_{\rho\mathbf{u}}^d$ as well as the gradients in the source term $S_{\rho\tau_M}$ are calculated by a second-order accurate central-difference scheme.

3.2. Explicit time discretization

To capture compressible wave dynamics, time integration is performed by an explicit second-order accurate low-storage four step Runge–Kutta method with an enhanced stability region. A detailed description can be found in Sezal (2009) and Schmidt (2015). Eqs. (40) to (42) show one sub-step of the four step time integration. The coefficients of the Runge–Kutta scheme are given in Table 2.

$$\begin{aligned} \bar{\rho}^{n+j/4} &= \bar{\rho}^n - \xi_j \Delta t \frac{1}{V_\Omega} F_\rho^c \Big|^{n+(j-1)/4} \left(\bar{\rho}^{n+(j-1)/4}, \bar{\mathbf{u}}^{n+(j-1)/4}, \bar{p}^{n+(j-1)/4} \right) \\ &=: \mathcal{L}_\rho \left[F_\rho^c \Big|^{n+(j-1)/4} \right], \end{aligned} \quad (40)$$

$$\begin{aligned} (\bar{\rho}\mathbf{u})^{n+j/4} &= (\bar{\rho}\mathbf{u})^n \\ &\quad - \xi_j \Delta t \frac{1}{V_\Omega} \left\{ F_{\rho\mathbf{u}}^c \Big|^{n+(j-1)/4} \left(\bar{\rho}^{n+(j-1)/4}, \bar{\mathbf{u}}^{n+(j-1)/4}, \bar{p}^{n+(j-1)/4} \right) \right. \\ &\quad \left. + F_{\rho\mathbf{u}}^d \Big|^{n+(j-1)/4} \left(\bar{\mathbf{u}}^{n+(j-1)/4}, \bar{\boldsymbol{\tau}}_M \Big|^{n+(j-1)/4} \right) \right\} \\ &=: \mathcal{L}_{\rho\mathbf{u}} \left[F_{\rho\mathbf{u}}^c \Big|^{n+(j-1)/4}, F_{\rho\mathbf{u}}^d \Big|^{n+(j-1)/4} \right], \end{aligned} \quad (41)$$

$$\begin{aligned} (\bar{\rho}\boldsymbol{\tau}_M)^{n+j/4} &= (\bar{\rho}\boldsymbol{\tau}_M)^n \\ &\quad - \xi_j \Delta t \frac{1}{V_\Omega} \left\{ F_{\rho\boldsymbol{\tau}_M}^c \Big|^{n+(j-1)/4} \left(\bar{\rho}^{n+(j-1)/4}, \bar{\mathbf{u}}^{n+(j-1)/4}, \right. \right. \\ &\quad \left. \left. \bar{\boldsymbol{\tau}}_M \Big|^{n+(j-1)/4}, \bar{p}^{n+(j-1)/4} \right) \right. \\ &\quad \left. + S_{\rho\boldsymbol{\tau}_M} \Big|^{n+(j-1)/4} \left(\bar{\rho}^{n+(j-1)/4}, \bar{\mathbf{u}}^{n+(j-1)/4}, \bar{\boldsymbol{\tau}}_M \Big|^{n+(j-1)/4} \right) \right\} \\ &=: \mathcal{L}_{\rho\boldsymbol{\tau}_M} \left[F_{\rho\boldsymbol{\tau}_M}^c \Big|^{n+(j-1)/4}, S_{\rho\boldsymbol{\tau}_M} \Big|^{n+(j-1)/4} \right]. \end{aligned} \quad (42)$$

The operators $\mathcal{L}_\square[\square]$ represent the Runge–Kutta substep of the differential transport equations.

The time step criterion is defined following the concept of convection dominated flow analysis and introducing the Courant–Friedrich–Lewy (CFL) number (Toro, 2009; Ferziger and Perić, 2002; Hirsch, 2007)

$$\Delta t = \frac{\text{CFL}}{i_c + i_d}, \quad (43)$$

where i_c and i_d constitute the inverse convective and diffusive time step respectively. For the definition of the inverse diffusive time step [Hirsch \(2007\)](#) applies a linear von Neumann stability analysis for a standard diffusion problem. For the analysis an explicit time and central difference space discretization is assumed. [Sezal \(2009\)](#) and [Schmidt \(2015\)](#) adapted the criterion to incorporate diffusion processes in n dimensions. We obtain the diffusive time step Δt_d being limited by

$$\Delta t_d < \frac{1}{i_d} := \min \left(\frac{\rho (\Delta x_i / n)^2}{2\mu_S} \right), \quad (44)$$

with the cell length Δx_i in space direction i . Since the transport Eq. (6) for Maxwell-/Oldroyd-like fluids represents a system of first order hyperbolic equations ([Owens and Phillips, 2002](#)) only the solvent viscosity is considered for the time step. Multiple simulations for different scenarios where the Maxwell viscosity was neglected for the viscous time step calculation showed stable behavior and lead to physically correct results. Besides, in the subsequent section we will show that a simplified system of equations will result in a hyperbolic system of equations. Thus, we do not consider a diffusive transport mechanism for the timestep criterion of the Maxwell stress transport.

3.3. Classification and eigenvalue calculation of the quasi-linear system

In order to determine the appropriate convective time step criterion necessary to account for shock-wave phenomena, the linearized wave speeds corresponding to the relevant parts of the transport Eqs. (1),(2) and (18) are calculated. In order to do so, the Eigenvalues of a simplified system in 1D are examined. The analysis is conducted similar to [Edwards and Beris \(1990\)](#), [Guy and Fogelson \(2008\)](#) and [Rodriguez and Johnsen \(2019\)](#). Thus, we neglect the viscous solvent contribution ($\mu_S = 0$) and lower order terms on the right-hand side of Eq. (18). Due to the omission of all lower order terms the analysis correlates with the one of the UCM model and is sufficient to characterize constitutive equations of Oldroyd-like models described by Eq. (6). We consider only the x_1 -direction taking into account the momentum in the remaining two directions to quantify shear as well as longitudinal wave speeds. The simplified 1D equations for the eigenvalue analysis are presented in Cartesian coordinates hereafter:

$$\begin{aligned} \frac{\partial}{\partial t} \rho + \frac{\partial}{\partial x_1} (\rho u_1) &= 0 \\ \frac{\partial}{\partial t} (\rho u_1) + \frac{\partial}{\partial x_1} (\rho u_1^2 + p - \tau_{M,11}) &= 0 \\ \frac{\partial}{\partial t} (\rho u_2) + \frac{\partial}{\partial x_1} (\rho u_2 u_1 - \tau_{M,12}) &= 0 \\ \frac{\partial}{\partial t} (\rho u_3) + \frac{\partial}{\partial x_1} (\rho u_3 u_1 - \tau_{M,13}) &= 0 \\ \frac{\partial}{\partial t} (\rho \tau_{M,11}) + \frac{\partial}{\partial x_1} (\rho \tau_{M,11} u_1) - \rho \left(\frac{4}{3} G + \tau_{M,11} \right) \frac{\partial u_1}{\partial x_1} &= 0 \\ \frac{\partial}{\partial t} (\rho \tau_{M,22}) + \frac{\partial}{\partial x_1} (\rho \tau_{M,22} u_1) + \rho \left(\frac{2}{3} G + \tau_{M,22} \right) \frac{\partial u_1}{\partial x_1} - 2\rho \tau_{M,12} \frac{\partial u_2}{\partial x_1} &= 0 \\ \frac{\partial}{\partial t} (\rho \tau_{M,33}) + \frac{\partial}{\partial x_1} (\rho \tau_{M,33} u_1) + \rho \left(\frac{2}{3} G + \tau_{M,33} \right) \frac{\partial u_1}{\partial x_1} - 2\rho \tau_{M,13} \frac{\partial u_3}{\partial x_1} &= 0 \\ \frac{\partial}{\partial t} (\rho \tau_{M,12}) + \frac{\partial}{\partial x_1} (\rho \tau_{M,12} u_2) - \rho (G + \tau_{M,11}) \frac{\partial u_2}{\partial x_1} &= 0 \\ \frac{\partial}{\partial t} (\rho \tau_{M,13}) + \frac{\partial}{\partial x_1} (\rho \tau_{M,13} u_3) - \rho (G + \tau_{M,11}) \frac{\partial u_3}{\partial x_1} &= 0 \\ \frac{\partial}{\partial t} (\rho \tau_{M,23}) + \frac{\partial}{\partial x_1} (\rho \tau_{M,23} u_1) + \rho \tau_{M,23} \frac{\partial u_1}{\partial x_1} - \rho \tau_{M,13} \frac{\partial u_2}{\partial x_1} - \rho \tau_{M,12} \frac{\partial u_3}{\partial x_1} &= 0. \end{aligned} \quad (45)$$

With the definition of the speed of sound in barotropic flows $c^2 := \frac{\partial p}{\partial \rho} \Big|_{s=const.}$ we rewrite the system of partial differential Eqs. (45) in quasi-linear form

$$\frac{\partial \mathbf{q}}{\partial t} + \mathbf{A}(\mathbf{q}) \frac{\partial \mathbf{q}}{\partial x_1} = 0, \quad (46)$$

with the vector of primitive variables \mathbf{q} and the Jacobian matrix \mathbf{A} Eq. (47) as given in [Box I](#).

The quasi-linear system depicted in Eq. (46) is linearized by assuming the coefficients in $\mathbf{A}(\mathbf{q})$ to be constant ([LeVeque, 1992](#)). The Eigenvalues λ_i of the matrix $\mathbf{A}(\mathbf{q})$, which correspond with the wave speeds are calculated to

$$\lambda_{1,2,3,4} = u_1, \quad (48)$$

$$\lambda_{5,6} = u_1 + \sqrt{\frac{1}{\rho} (G + \tau_{M,11})}, \quad (49)$$

$$\lambda_{7,8} = u_1 - \sqrt{\frac{1}{\rho} (G + \tau_{M,11})}, \quad (50)$$

$$\lambda_9 = u_1 + \sqrt{a^2 + \frac{1}{\rho} \left(\frac{4}{3} G + \tau_{M,11} \right)}, \quad (51)$$

$$\lambda_{10} = u_1 - \sqrt{a^2 + \frac{1}{\rho} \left(\frac{4}{3} G + \tau_{M,11} \right)}, \quad (52)$$

where $\lambda_{5,6,7,8}$ are the shear wave speeds and $\lambda_{9,10}$ quantify the longitudinal (pressure) wave speeds. Real valued wave speeds and thereby a hyperbolic quasi-linear system (46) is obtained if the condition $G + \tau_{M,11} > 0$ holds. Furthermore, if we require the problem to be well posed, the conformation tensor $\tau_C := \tau_M + G\mathbf{I}$ has to be positive definite ([Owens and Phillips, 2002](#)). It is straightforward to show that this requirement implicitly leads to only real valued characteristic velocities and assures that the system (46) is hyperbolic ([Owens and Phillips, 2002](#)). Otherwise put, if the problem is stable and well posed, the quasi-linear system will also be hyperbolic. Beyond that [Owens and Phillips \(2002\)](#) showed that the Maxwell stress transport equation itself (6) exhibits hyperbolic behavior independently of the chosen $f(\tau_M, \mathbf{d}^d)$ since this term comprises only lower order terms.

By regarding absolute values of the wave speeds the longitudinal waves propagate the fastest and are considered for the calculation of the convective time step criterion. The corresponding expression for the convective time step Δt_c in n dimensions reads as follows

$$\begin{aligned} \Delta t_c < \frac{1}{i_c} := \min \left(\frac{\Delta x_i / n}{\lambda_i^{max}} \right) \\ = \left[|u_i| + \sqrt{a^2 + \frac{1}{\rho} \left(\frac{4}{3} G + \tau_{M,ii} \right)} \right]^{-1} \frac{\Delta x_i}{n}, \quad i = 1, 2, 3, \end{aligned} \quad (53)$$

where we incorporate the remaining two directions in space again. The obtained convective and diffusive time step or more specifically the inverse convective and diffusive time step i_c and i_d are applied together with Eq. (43) for all cells to acquire the appropriate global timestep. Extensive investigations for several flow scenarios were conducted by [Schmidt \(2015\)](#) and led to the result that the employed Runge–Kutta method remains stable up to CFL = 1.5. A CFL number of CFL = 1.4 is chosen for all presented computations eventually.

3.4. Boundary conditions

The implementation of boundary conditions is realized by employing two layers of ghost cells ($|_g$) adjacent to the last cells of the computational domain ($|_d$) as illustrated in [Fig. 3](#). The ghost cell variables are defined in order to compute physically consistent fluxes on the face of the domain boundary ($|_r$) between the last domain cell and the first ghost cell. Hereafter, we firstly describe the physical condition occurring at a particular boundary and subsequently discuss the variables to impose within the ghost cells. Note that it is not relevant whether the variables in the ghost cells constitute physically meaningful values, but that reconstructed fluxes at the cell face meet the flow conditions at the boundary with respect to the underlying reconstruction. Since the boundary conditions for all variables except those added through the implementation of the viscoelastic model are already well described in [Sezal \(2009\)](#) and [Schmidt \(2015\)](#), exclusively the boundary conditions and ghost cell definitions for the Maxwell

$$\mathbf{q} = \begin{bmatrix} \rho \\ u_1 \\ u_2 \\ u_3 \\ \tau_{M,11} \\ \tau_{M,22} \\ \tau_{M,33} \\ \tau_{M,12} \\ \tau_{M,13} \\ \tau_{M,23} \end{bmatrix}, \quad \mathbf{A}(\mathbf{q}) = \begin{bmatrix} u_1 & \rho & 0 & 0 & 0 & 0 & 0 & 0 & 0 & 0 \\ \frac{u_1^2}{\rho} & u_1 & 0 & 0 & -\frac{1}{\rho} & 0 & 0 & 0 & 0 & 0 \\ 0 & 0 & u_1 & 0 & 0 & 0 & 0 & -\frac{1}{\rho} & 0 & 0 \\ 0 & 0 & 0 & u_1 & 0 & 0 & 0 & 0 & -\frac{1}{\rho} & 0 \\ 0 & -\frac{4G}{3} - \tau_{M,11} & 0 & 0 & u_1 & 0 & 0 & 0 & 0 & 0 \\ 0 & \frac{2G}{3} + \tau_{M,22} & -2\tau_{M,12} & 0 & 0 & u_1 & 0 & 0 & 0 & 0 \\ 0 & \frac{2G}{3} + \tau_{M,33} & 0 & -2\tau_{M,13} & 0 & 0 & u_1 & 0 & 0 & 0 \\ 0 & 0 & -G - \tau_{M,11} & 0 & 0 & 0 & 0 & u_1 & 0 & 0 \\ 0 & 0 & 0 & -G - \tau_{M,11} & 0 & 0 & 0 & 0 & u_1 & 0 \\ 0 & \tau_{M,23} & -\tau_{M,13} & -\tau_{M,12} & 0 & 0 & 0 & 0 & 0 & u_1 \end{bmatrix}. \quad (47)$$

Box I.

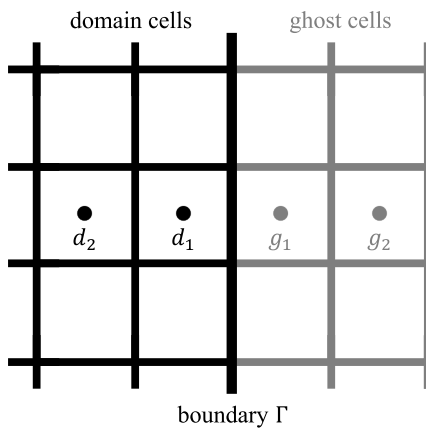


Fig. 3. Cells in the computational domain d_1, d_2 and adjacent ghost cell layers g_1, g_2 separated by the domain boundary face Γ .

stress tensor τ_M are explained below. The diffusive fluxes at the boundary face are reconstructed following a central reconstruction scheme as follows:

$$\tau_M|_{\Gamma} = \frac{1}{2} (\tau_M|_d + \tau_M|_g). \quad (54)$$

3.4.1. Inlet boundary conditions

As a result of the hyperbolic nature of the Maxwell stress transport equation only an upstream Dirichlet boundary condition for the Maxwell stress is required at the inlet (Xue et al., 1998). By imposing conditions for the Maxwell stresses at the inlet we determine the history of deformation of the viscoelastic fluid in the upstream region of the domain. We neglect gradients of Maxwell stresses in upstream direction and therefore specify the same value in the ghost cell layer as it is desired at the inlet face (Oliveira et al., 1998):

$$\tau_M|_g = \tau_M|_{\Gamma_{in}}. \quad (55)$$

If there is no deformation history present in upstream direction at the inlet, the physical condition for the Maxwell stresses at the face is $\tau_M|_{\Gamma_{in}} = \mathbf{0}$. This condition is applied as inlet boundary condition throughout the present study.

3.4.2. Outlet and viscous wall boundary conditions

Due to the hyperbolic behavior of the governing transport equation, there is no need to define specific values for the components of the Maxwell stress tensor except for the upstream inlet boundary. As the reconstruction Eq. (54) demands for a specified value in the ghost

cell, a Neumann boundary condition is applied namely a zero gradient assumption for outflow and viscous wall boundaries $\text{grad}(\tau|_{\Gamma_{out/wall}}) \cdot \mathbf{n} = 0$, with \mathbf{n} describing the outward pointing unit normal vector perpendicular to the boundary face (cf. Fernandes et al., 2019). We implement the boundary condition by copying the components of Maxwell stresses from the last domain cell layers into the ghost cell layers:

$$\tau_M|_g = \tau_M|_d. \quad (56)$$

3.4.3. Symmetry boundary condition

Although in many simulations conducted for viscoelastic fluids symmetry boundary conditions are employed, there are just a few publications where the physical conditions for the stress tensor at a symmetry plane are formulated. During this work it turned out that for channel flow simulations the symmetry boundary condition does not cause severe issues due to small valued stresses at the midplane of the channel but for the spherical bubble collapse presented in Section 4.2 an appropriate symmetry boundary condition is crucial. Baaijens et al. (1995) and Huilgol and Phan-Thien (1997) formulate the vanishing tangential traction condition. At first, we define the traction vector $\mathbf{t} := \tau \cdot \mathbf{n}$ describing the resultant force occurring at a face with the outward pointing normal vector \mathbf{n} . We can formulate the vanishing tangential traction at the boundary as

$$\mathbf{t}|_{\Gamma_{sym}} := (\mathbf{n}_t \cdot \tau|_{\Gamma_{sym}} \cdot \mathbf{n}) = 0, \quad \forall \mathbf{n}_t : \mathbf{n}_t \cdot \mathbf{n} = 0, \quad (57)$$

where \mathbf{n}_t represents any tangential vector perpendicular to the outward pointing normal vector \mathbf{n} . Consequently, the stress tensor $\tau|_{\Gamma_{sym}}$ and the corresponding traction vector at the boundary face $\mathbf{t}|_{\Gamma_{sym}}$ has to fulfill the following condition to ensure that all traction other than the normal traction has to vanish

$$\begin{aligned} \mathbf{t}|_{\Gamma_{sym}} - (\mathbf{t}|_{\Gamma_{sym}} \cdot \mathbf{n}) \mathbf{n} &= \mathbf{0}, \\ \Leftrightarrow \mathbf{t}|_{\Gamma_{sym}} &= (\mathbf{n} \cdot \tau|_{\Gamma_{sym}} \cdot \mathbf{n}) \mathbf{n}, \end{aligned} \quad (58)$$

to ensure that exclusively normal traction acts on the symmetry plane. This condition was described in a similar way by Oliveira et al. (1998). To the author's best knowledge there is no work by now explicitly describing the formulation for stress tensor values for a ghost cell approach to satisfy the symmetry boundary conditions. By taking into account our reconstruction Eq. (54) and the condition for the traction in normal direction Eq. (58) we can rewrite the equation for the traction vector

$$\mathbf{t}|_{\Gamma_{sym}} = (\mathbf{n} \cdot \tau|_{\Gamma_{sym}} \cdot \mathbf{n}) \mathbf{n} = \frac{1}{2} (\tau|_d + \tau|_g) \cdot \mathbf{n}. \quad (59)$$

If we additionally assume that the values of the stress tensor components at the boundary face coincide with those of the next cell in the computational domain, we get

$$(\mathbf{n} \cdot \tau|_d \cdot \mathbf{n}) \mathbf{n} = \frac{1}{2} (\tau|_d + \tau|_g) \cdot \mathbf{n}. \quad (60)$$

Instead of the last equation we can formulate a corresponding equation

$$\frac{1}{2} (\boldsymbol{\tau}|_d + \boldsymbol{\tau}|_g) - (\mathbf{n} \cdot \boldsymbol{\tau}|_d \cdot \mathbf{n}) \mathbf{I} = \mathbf{0}, \quad (61)$$

that allows us to calculate an equation for the Maxwell stress tensor in the ghost cell

$$\boldsymbol{\tau}_M|_g = 2 (\mathbf{n} \cdot \boldsymbol{\tau}_M|_d \cdot \mathbf{n}) \mathbf{I} - \boldsymbol{\tau}_M|_d. \quad (62)$$

It can be easily shown that the reconstructed Maxwell stresses from Eq. (62) at the symmetry plane fulfills both conditions Eqs. (57) and (58). We conducted extensive investigations on different formulations for the symmetry boundary condition by simulating the symmetrical vapor bubble collapse within viscoelastic liquid using three symmetry planes, i.e. simulating one eighth of the vapor bubble (cf. Section 4.2). It turned out that the formulation of the symmetry boundary condition for the Maxwell stress tensor has a strong influence on the simulation results and the aforementioned formulation provided a physically meaningful outcome and a spherically shaped bubble during the collapse event. The results obtained by using the symmetry condition for the simulation of the collapse of one eighth of the vapor bubble were compared and are in perfect agreement with the simulation of a full 8-quadrant simulation.

3.5. Program structure

The subsequential procedures together with the relevant variables within one Runge–Kutta time integration sub-step are described in algorithm 1. Before executing the four sub-steps, the variables of the previous timestep are cached. The storage is necessary since we utilize a low-storage Runge–Kutta algorithm, which retrieves the variables of each sub-step by adding the numerical flux and source terms to the variables of the previous time step as explained in Eqs. (40) to (42). There are several ways to incorporate the transport equation for the Maxwell stress (39). As already indicated by Eq. (42) we decided to calculate the Maxwell stress of the subsequent sub step $\boldsymbol{\tau}_M|^{n+j/4}$ exclusively by taking variables of the current sub step $n + (j - 1)/4$. Thereby, a consistent state of all conserved variables during each solution sub-step is achieved for the segregated explicit solution scheme. The primary variables $\bar{\rho}|^{n+(j-1)/4}$, $\bar{\mathbf{u}}|^{n+(j-1)/4}$, $\bar{\boldsymbol{\tau}}_M|^{n+(j-1)/4}$ are overwritten by the corresponding ones $\bar{\rho}|^{n+j/4}$, $\bar{\mathbf{u}}|^{n+j/4}$, $\bar{\boldsymbol{\tau}}_M|^{n+j/4}$ before the source term is involved which requires these likewise. To improve efficiency the Maxwell stress source term $S_{\rho\boldsymbol{\tau}_M}$ is calculated at the end to avoid the necessity of buffering the primary variables. Subsequently, we compute the convective fluxes F_{ρ}^c , $F_{\rho\mathbf{u}}^c$, $F_{\rho\boldsymbol{\tau}_M}^c$ and the diffusive flux $F_{\rho\mathbf{u}}^d$. Thereafter, by conducting the time integration, the primary variables of the next sub step $n + j/4$ are computed. Dividing the primary variables by the density of the new sub step $\bar{\rho}|^{n+j/4}$ leads to the updated primitive variables $\bar{\mathbf{u}}|^{n+j/4}$, $\bar{\boldsymbol{\tau}}_M|^{n+j/4}$. With the help of the updated density, we primarily calculate the updated vapor content $\alpha_i|^{n+j/4}$ and eventually the pressure $p_i|^{n+j/4}$ of the new sub step as described in Section 2.3. Finally, all variables within the ghost cells are updated at the end of one Runge–Kutta loop meeting physically correct boundary conditions at the cell faces of the boundaries.

4. Numerical results and validation

In this section we examine the correct implementation of our solver, validate it against analytical and semi-analytical results and present 3D vapor bubble collapse simulations with viscoelastic influence. Initially, we compare the unsteady results for the start-up of a planar 2D channel flow to an analytical solution. Hereafter, we validate steady state results for the 2D channel flow. Finally, we present results for simulations of

Algorithm 1: Operations during a substep of the explicit Runge–Kutta method Eq. (56)

```

subroutine RungeKutta4
  SaveOldVars()
  // Save primitive variables of previous time step

  for j ← 1 to 4 do
    // Calculation of convective fluxes
    ComputeConvectiveFluxes()
     $F_{\rho}^c|^{n+(j-1)/4} = (\bar{\rho}|^{n+(j-1)/4}, \bar{\mathbf{u}}|^{n+(j-1)/4})$ 
     $F_{\rho\mathbf{u}}^c|^{n+(j-1)/4} = (\bar{\rho}|^{n+(j-1)/4}, \bar{\mathbf{u}}|^{n+(j-1)/4}, \bar{\rho}|^{n+(j-1)/4})$ 
     $F_{\rho\boldsymbol{\tau}_M}^c|^{n+(j-1)/4} = (\bar{\rho}|^{n+(j-1)/4}, \bar{\mathbf{u}}|^{n+(j-1)/4}, \bar{\boldsymbol{\tau}}_M|^{n+(j-1)/4})$ 

    // Calculation of diffusive/viscous fluxes
    ComputeDiffusiveFluxes()
     $F_{\rho\mathbf{u}}^d|^{n+(j-1)/4} = (\bar{\mathbf{u}}|^{n+(j-1)/4}, \bar{\boldsymbol{\tau}}_M|^{n+(j-1)/4})$ 

    // Time marching for primary variables  $n + (j - 1)/4 \rightarrow n + j/4$ 
     $\bar{\rho}|^{n+j/4} \leftarrow \mathcal{L}_{\rho} [F_{\rho}^c|^{n+(j-1)/4}]$ 
     $(\bar{\rho\mathbf{u}})|^{n+j/4} \leftarrow \mathcal{L}_{\rho\mathbf{u}} [F_{\rho\mathbf{u}}^c|^{n+(j-1)/4}, F_{\rho\mathbf{u}}^d|^{n+(j-1)/4}]$ 
     $(\bar{\rho\boldsymbol{\tau}_M})|^{n+j/4} \leftarrow \mathcal{L}_{\rho\boldsymbol{\tau}_M} [F_{\rho\boldsymbol{\tau}_M}^c|^{n+(j-1)/4}, S_{\rho\boldsymbol{\tau}_M}|^{n+(j-1)/4}]$ 

    // Update primitive variables
     $\bar{\mathbf{u}}|^{n+j/4} \leftarrow \frac{(\bar{\rho\mathbf{u}})|^{n+j/4}}{\bar{\rho}|^{n+j/4}}$ 

     $\bar{\boldsymbol{\tau}}_M|^{n+j/4} \leftarrow \frac{(\bar{\rho\boldsymbol{\tau}_M})|^{n+j/4}}{\bar{\rho}|^{n+j/4}}$ 

    // Evaluate barotropic equation of state
     $p_i|^{n+j/4} \leftarrow \text{EOS}(\rho_i|^{n+j/4})$ 

    // Calculation source term for the Maxwell stress
    Viscoelastic()
     $S_{\rho\boldsymbol{\tau}_M}|^{n+j/4} = (\bar{\rho}|^{n+j/4}, \bar{\mathbf{u}}|^{n+j/4}, \bar{\boldsymbol{\tau}}_M|^{n+j/4})$ 

    // Update boundary conditions
    BoundaryConditions()
  end for

```

the compressible spherical vapor bubble collapse in the different implemented viscoelastic fluids. The flow properties concerning viscoelastic fluids are characterized by the Reynolds number Re and the Deborah number De . The Reynolds number for viscoelastic flows is defined as

$$Re = \frac{\rho U L}{\mu_0}, \quad (63)$$

where U and L represent a characteristic velocity and length respectively. The viscosity used to calculate the Reynolds number in viscoelastic flows is the sum of solvent and Maxwell viscosity $\mu_0 = \mu_S + \mu_M$. The Deborah number is given as

$$De = \frac{\lambda U}{L}, \quad (64)$$

and describes the ratio of the relaxation time λ to a characteristic time of the flow process and quantifies the influence of elasticity. The higher the Deborah number, the more time is needed until the fluid responds and the larger is the elastic contribution. The influence of elasticity can also be described by the Weissenberg number We . The use of Deborah and Weissenberg numbers is not consistent in literature, and we will refer exclusively to the Deborah number as defined in Eq. (64). For a constitutive model with solvent viscosity (OLD-B, LPTT, EPTT), the ratio of polymer viscosity to total viscosity is described by

$$\beta = \frac{\mu_S}{\mu_0} = \frac{\mu_S}{\mu_M + \mu_S}. \quad (65)$$

4.1. Planar channel flow

First we consider 2D simulations for a planar 2D Poiseuille flow between two parallel no-slip walls parallel to the x_1 -axis driven by a pressure gradient Δp in x_1 -direction. The dimensionless numbers are

Table 3
Mesh parameters for the 2D channel flow simulations.

Mesh name	N_{x_1} [-]	N_{x_2} [-]	$\sum N$ [-]	Δx_1 [m]	Δx_2 [m]
M80	50	80	4000	$2 \cdot 10^{-5}$	$1.25 \cdot 10^{-7}$
M120	50	120	6000	$2 \cdot 10^{-5}$	$8.33 \cdot 10^{-8}$
M240	50	240	12000	$2 \cdot 10^{-5}$	$4.17 \cdot 10^{-8}$

Table 4
Flow parameters for the 2D channel flow simulations carried out with the OLD-B model.

Re [-]	De [-]	β [-]	λ [s]	Δp [Pa]
1	0	-	-	$-8 \cdot 10^5$
0.01	0.01	0.1	$9.96 \cdot 10^{-6}$	$-0.08 \cdot 10^5$
0.1	0.1	0.1	$9.96 \cdot 10^{-6}$	$-0.8 \cdot 10^5$
1	1	0.1	$9.96 \cdot 10^{-6}$	$-8 \cdot 10^5$
1	5	0.1	$4.98 \cdot 10^{-5}$	$-8 \cdot 10^5$
5	1	0.1	$1.99 \cdot 10^{-6}$	$-40 \cdot 10^5$

evaluated using the height h of the channel and the maximum velocity in the x_1 -direction u_0 at the centerline:

$$Re = \frac{\rho u_0 h}{\mu_0}, \quad De = \frac{\lambda u_0}{h}, \quad u_0 = -\frac{\Delta p h^2}{8 \mu_0 l}. \quad (66)$$

The channel dimensions $h = 1 \cdot 10^{-5}$ m, $l = 1 \cdot 10^{-3}$ m, are chosen in order to achieve fast convergence but also ensure the continuum hypothesis to be valid. The channel is of sufficient length in order to ascertain developed flow conditions. The remaining quantities are in accordance with the ones mentioned at reference temperature in Table 1. We impose the derived boundary conditions, in particular the inlet boundary conditions at the channel inlet, outlet boundary conditions at the outlet and no-slip conditions at the lower and upper wall. The complete domain is initialized with zero velocity and polymeric stress. All the parameters of the homogeneous, structured meshes used for our simulations are listed in Table 3. The velocities in streamwise direction u_1 are measured at $x/l = 0.5$ to ascertain developed flow conditions and suppress influences of the inlet and outlet boundaries.

Firstly, we compare unsteady results for an OLD-B fluid during the unsteady start-up of a 2D Poiseuille flow as there exists an analytical solution for this constitutive model. As reference, we employ the solution of Waters and King (1970). It assumes incompressible, creeping flow such that the convective term $\mathbf{u} \cdot \nabla \mathbf{u}$ in the momentum equation is omitted. In order to obtain comparable results, the simulations are carried out at low Reynolds numbers. The flow parameters for which all channel flow simulations were conducted are listed in Table 4. The case with $De = 0$ corresponds to a Newtonian fluid without relaxation. Different Deborah numbers were realized by the variation of the relaxation time, the Reynolds number was modified by the pressure gradient.

Initially, a mesh refinement study is conducted $Re = 0.1$ and $De = 0.1$ to ascertain the appropriate resolution. Fig. 4 shows the unsteady velocity evolution for and three different mesh refinements in x_2 -direction. We compare the results at two distinct x_2 -positions. The velocity evolution at the centerline ($x_2/h = 1/2$) is independent of the different resolutions, and the results agree very well with the exact solution. Only slight deviations can be observed during the first minimum from the start-up. Such deviations between the incompressible and fully developed analytical solution is attributed to compressibility and the contribution of inertia terms that are present in the numerical method. For the position near the viscous wall ($x_2/h = 1/4$), the differences between the results obtained with the different meshes are more pronounced, which can be explained by the higher velocity gradients and therefore finer mesh resolutions required near the wall. We therefore proceed with the finest mesh M240 for the ensuing unsteady results.

Applying the finest mesh, additional simulations are conducted to prove that our solver provides accurate results for lower and higher values as well as other ratios of Reynolds and Deborah numbers, too. In

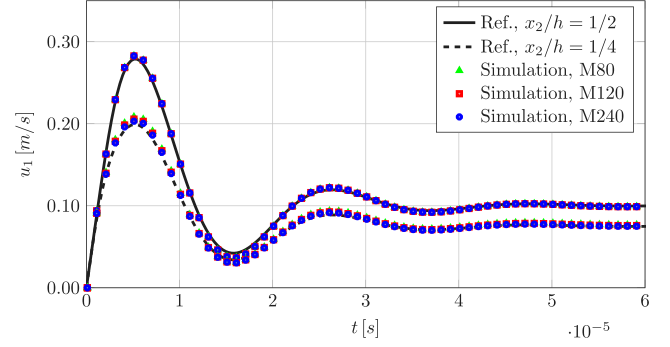


Fig. 4. Comparison of the velocities u_1 of the reference solution (Waters and King, 1970) and the results of our simulation for the start-up of planar channel flow measured at two different x_2 -positions with $Re = 0.1$, $De = 0.1$ for the OLD-B constitutive model. The results obtained with three different meshes (M80, M120, M240) and corresponding distinct resolutions in x_2 -direction are presented.

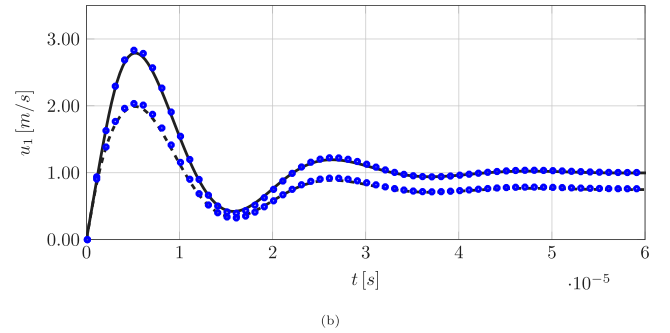
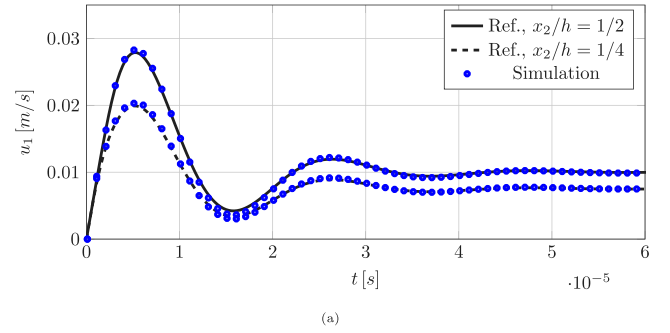


Fig. 5. Comparison of the velocities u_1 of the reference solution and the results of simulations with two different combinations at two different x_2 -positions with (a) $Re = 0.01$, $De = 0.01$ and (b) $Re = 1$, $De = 1$ for the OLD-B constitutive model. The simulations are carried out on the M240-mesh.

Fig. 5, the unsteady velocity evolutions for the two aforementioned x_2 -positions are displayed for the previous ratio of Reynolds and Deborah for $Re = 0.01$, $De = 0.01$ and $Re = 1$, $De = 1$. We can observe a very good agreement with the analytical reference for both simulations.

Furthermore, simulations with a distinct ratio of Reynolds and Deborah numbers ($Re = 1$, $De = 2$; $Re = 1$, $De = 5$; $Re = 5$, $De = 1$), and a case without relaxation ($Re = 1$, $De = 0$), i.e. the Newtonian equivalent, are conducted to prove the capability of simulating flows with higher elasticity and highlight its effect on the velocity evolution (see Fig. 6). For the highest relaxation time ($Re = 1$, $De = 5$), a slightly higher deviation from the analytical solution during the first overshoot is observable. However, the results of the simulation agree very well with the reference. Furthermore, it is apparent that the steady-state velocity of the viscoelastic cases at $Re = 1$ coincides with the steady-state velocity obtained for the Newtonian fluid.

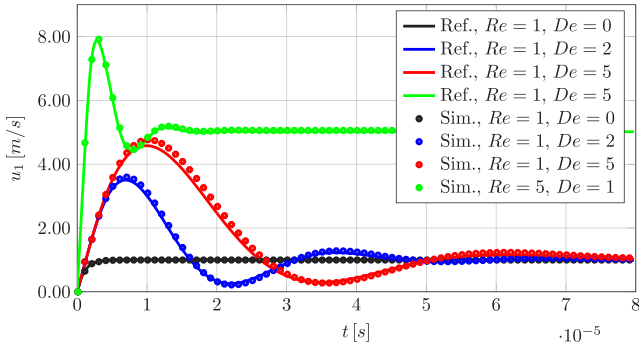


Fig. 6. Comparison of the velocity evolution during the start-up of a channel flow for different elasticities and for a case without relaxation ($De = 0$, Newtonian fluid).

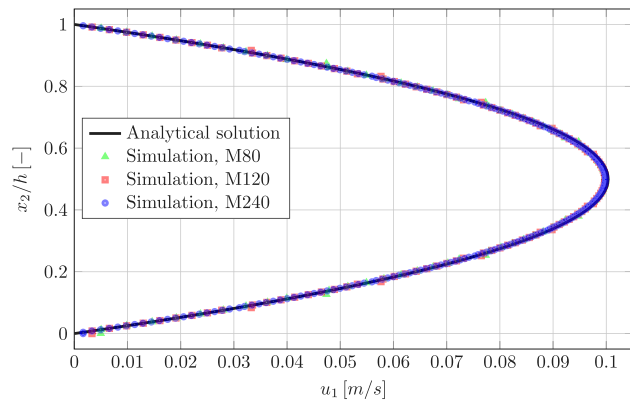


Fig. 7. Validation of the steady state velocity profiles for three different mesh resolutions against the analytical solution with $Re = 0.1$, $De = 0.1$ for the OLD-B constitutive model.

Table 5

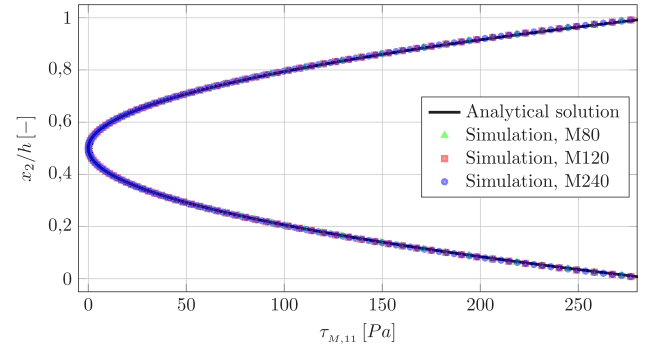
Flow parameters for the 2D channel flow simulations carried out with the PTT fluids.

Re [-]	De [-]	β [-]	ϵ [-]	λ [s]	Δp [Pa]
0.375	0.375	0.1	0.25	$9.98 \cdot 10^{-6}$	$-0.3 \cdot 10^5$

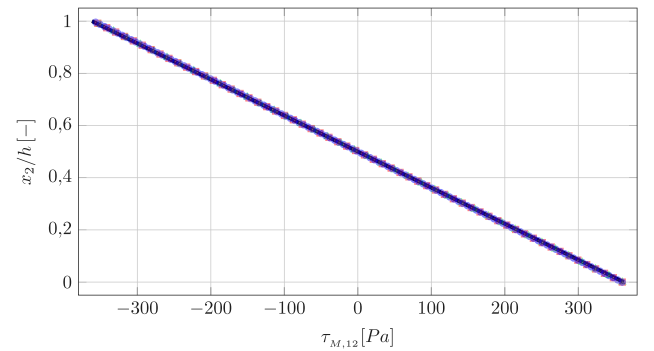
Finally, for the validation of the OLD-B model we compare steady-state results of the velocity and stress profiles along the cross-section of the channel for $Re = 0.1$, $De = 0.1$ for the three resolutions. The analytical steady-state velocity profile for viscoelastic channel flow with an OLD-B fluid corresponds to the profile obtained by a Newtonian fluid with the same total viscosity μ_0 (cf. Waters and King, 1970). In Fig. 7 the velocity profiles for the different meshes are compared against the exact solution. The numerical results agree very well with the analytical ones. Minor deviations can only be observed for the coarser resolutions $M80$, $M120$.

Furthermore, the steady-state profiles of Maxwell stresses $\tau_{M,11}$ and $\tau_{M,12}$ are validated against the analytical reference in Fig. 8. The profiles coincide perfectly with the analytical solution independent of the mesh refinements. The well captured nonzero normal stress and the corresponding first normal stress difference in shear flows is unique for viscoelastic fluids and would not emerge for a Newtonian fluid.

Subsequently, the implementation of both of the simplified PTT models are validated. The steady-state velocity and Maxwell stress profiles obtained by simulations performed on the $M240$ mesh are examined. Due to the shear-thinning behavior of PTT fluids, the velocity profiles differ from the OLD-B case. To highlight these deviations more clearly the simulations are carried out with higher Reynolds and Deborah numbers, different from those mentioned in Table 4. The modified flow parameters are listed in Table 5. For comparison,



(a)



(b)

Fig. 8. Validation of the steady state Maxwell stress profiles for three different mesh resolutions against the analytical solution with $Re = 0.1$, $De = 0.1$ for the OLD-B constitutive model. (a) $\tau_{M,11}$; (b) $\tau_{M,12}$.

we show the results of the corresponding simulation with the OLD-B model. Furthermore, for the simplified LPTT an analytical steady-state solution is available (Cruz et al., 2005). For the EPTT with solvent contribution no analytical solution has been found hitherto. Thus, we follow the approach presented in Cruz and Pinho (2007) to obtain a semi-analytical solution by numerical integration. Our results show excellent agreement with the analytical and semi-analytical solution, respectively. As shown in Fig. 9 the velocities are much higher in both PTT cases compared to the OLD-B case caused by the shear-thinning behavior and the corresponding decreased effective viscosity at higher shear-rates. The shear-thinning is more emphasized for the EPTT, since an exponential relation for the velocity gradient is taken into account for the Maxwell stress.

Fig. 10 shows the Maxwell stress profiles. The differences compared to the OLD-B fluid are clearly perceptible. Likewise, the shear-thinning property is illustrated. The viscosity is decreased in the vicinity of the wall due to smaller velocity gradients, resulting in the largest stress deviations between the OLD-B model and the PTT models in this region.

4.2. Two-phase cavitating flow — Spherical bubble collapse

In order to demonstrate the capability of simulating cavitating flows with viscoelastic constitutive models, we present simulation results of a collapsing spherical vapor bubble in a viscoelastic liquid. We exploit spherical symmetry and simulate one eighth of the bubble and apply symmetry boundary conditions at the three adjacent walls. While doing so, we can also check the validity of the symmetry boundary condition for the stress tensor described in Section 3.4.3. Furthermore, the influence of viscoelasticity is illustrated by comparing the viscoelastic with the Newtonian case. The viscoelastic bubble collapse is characterized

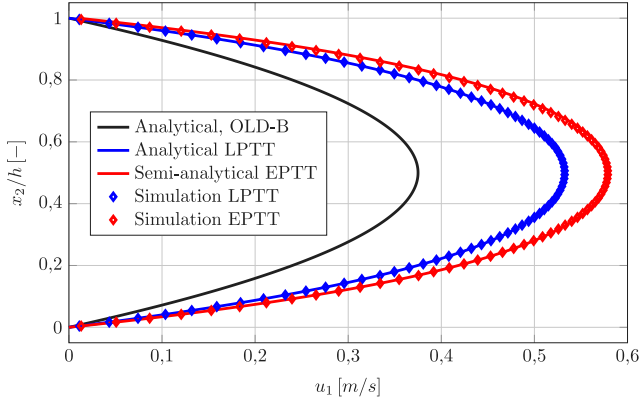


Fig. 9. Validation of the steady state velocity profiles for three different mesh resolutions against the analytical solution at $Re = 0.375$, $De = 0.375$ for the LPTT and EPTT constitutive model against analytical and semi-analytical solutions. The analytical result for the OLD-B model for the same driving pressure is presented to illustrate the shear-thinning behavior.

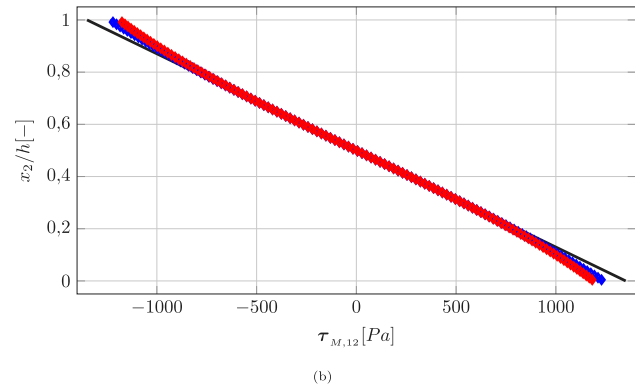
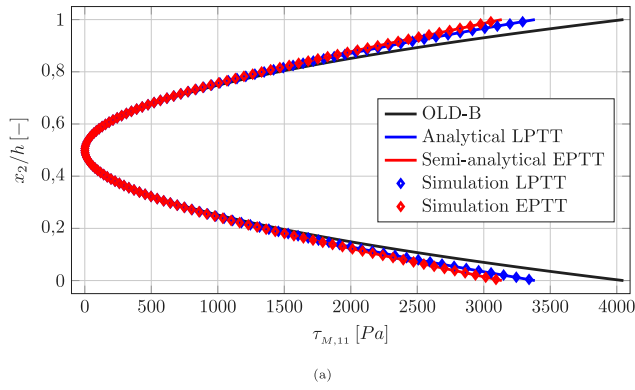


Fig. 10. Validation of the steady state Maxwell stress profiles at $Re = 0.375$, $De = 0.375$ for the LPTT and EPTT constitutive model compared to analytical and semi-analytical solutions. (a) $\tau_{M,11}$, (b) $\tau_{M,12}$.

by the Reynolds and the Deborah number:

$$Re = \frac{R_0 \sqrt{\rho \Delta p}}{\mu_0}, \quad De = \frac{\lambda}{R_0} \sqrt{\frac{\Delta p}{\rho}}, \quad (67)$$

where R_0 and $\Delta p = p_\infty - p_{sat}$ are the initial radius and the pressure difference of the surrounding and the saturation pressure inside the bubble. The parameters used for the simulations are summarized in Table 6. In order to compare the Newtonian with the UCM fluid, the viscosity of water is modified for the Newtonian case and differs from the viscosity described in Table 1. All simulations were carried out with

Table 6

Flow parameters for the simulations for the 3D spherical bubble collapse with different viscoelastic models.

Constitutive model	Re [-]	De [-]	R_0 [m]	λ [s]	μ_0 [Pa s]
Newtonian	1	-	$1 \cdot 10^{-4}$	-	3.1554
UCM	1	0.5	$1 \cdot 10^{-4}$	$1.5814 \cdot 10^{-6}$	3.1554
	1	1	$1 \cdot 10^{-4}$	$3.1628 \cdot 10^{-6}$	3.1554
	1	1.5	$1 \cdot 10^{-4}$	$4.7442 \cdot 10^{-6}$	3.1554
	1	5	$1 \cdot 10^{-4}$	$1.5814 \cdot 10^{-5}$	3.1554
	1	10	$1 \cdot 10^{-4}$	$3.1628 \cdot 10^{-5}$	3.1554
OLD-B	1	1	$1 \cdot 10^{-4}$	$3.1628 \cdot 10^{-6}$	3.1554
LPTT	1	1	$1 \cdot 10^{-4}$	$3.1628 \cdot 10^{-6}$	3.1554
EPTT	1	1	$1 \cdot 10^{-4}$	$3.1628 \cdot 10^{-6}$	3.1554

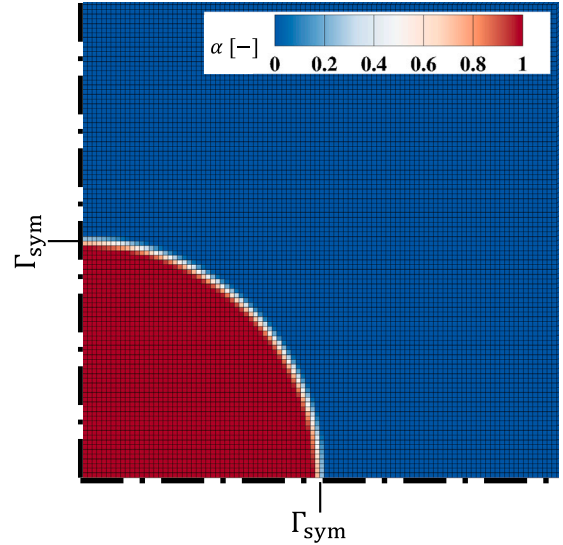


Fig. 11. Contour plot of the initial vapor content α for a slice through the x_1 - x_2 -plane at $x_3 = 0$ showing the computational mesh and the applied boundary conditions.

at a driving pressure of $p_\infty = 10 \cdot 10^5$ Pa. For the constitutive models with solvent contribution a ratio of viscosities of $\beta = 0.1$ is chosen and an extensibility factor of $e = 0.25$ is applied for the PTT models.

For all simulations a resolution of 50 cells/radius is employed. Fig. 11 shows a slice of the x_1 - x_2 -plane at $x_3 = 0$ of our setup and the initial shape of the bubble in terms of vapor content and sketches the applied symmetry boundary conditions. Adjacent to the refined region displayed in Fig. 11 a coarsened mesh is attached in order to dissipate perturbations and to avoid reflections.

Firstly, we compare the bubble collapse in the Newtonian and the UCM fluid. In Fig. 12 the results in terms of the non-dimensionalized radius $r^* = r/R_0$ over the non-dimensionalized time $t^* = t/t_0$ where $t_0 = R_0 \sqrt{\rho/\Delta p}$ are illustrated. Fig. 12a shows the comparison of the collapse with Newtonian and UCM fluid for $Re = 1$, $De = 1$. A significant difference in the collapse behavior can be observed. The bubble collapse in the UCM fluid shows oscillations and the bubble size initially decreases faster compared to the Newtonian case. The faster shrinkage in the initial stages can be traced back to the stress relaxation of the constitutive model and the corresponding delayed build up of the viscous stresses. To get a better understanding of this mechanism we compare the UCM-collapse for different levels of elasticity, i.e. for different relaxation times. The different bubble size evolutions are compared in Fig. 12b for the listed Deborah numbers. The collapse is determined by the interaction of driving inertia forces of the collapsing liquid towards the center of the vapor bubble and viscous stresses generated during the collapse and compressible damping. An increased elasticity and a corresponding higher relaxation time leads to a slower build up of viscous stresses and coincidentally to less

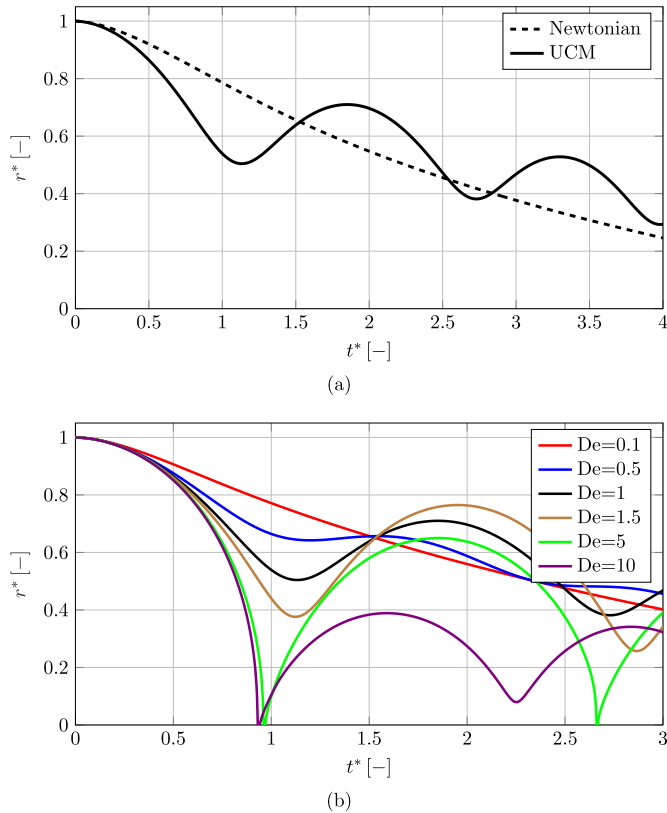


Fig. 12. Spherical vapor bubble collapse: Comparison of the non-dimensional bubble size for (a) the Newtonian against the UCM fluid at $Re = 1$, $De = 1$; (b) the UCM fluid with different relaxation times (different De) at $Re = 1$.

viscous dissipation. In the simplified mechanical representation of the Maxwell model sketched in the lower half of Fig. 1, the increase of elasticity corresponds to a softer spring that leads to delayed transfer of stress to the damper. That leads to larger rebound radii, which can be detected in the range of $De = 0.5$ to $De = 1.5$. By further increasing the elasticity the build-up of viscous stresses takes so long, that the bubble collapses before rebound ($De = 5$, $De = 10$). If we would increase the elasticity even more, the collapse would be equivalent to an inviscid Rayleigh collapse (Lind and Phillips, 2010). A direct comparison of the obtained results with Warnetz and Johnsen (2015) is not feasible, since they consider a bubble filled with gas as opposed to vapor-filled bubbles used in the present work. The gas-filled bubble does not fully collapse and reaches an equilibrium radius during the Rayleigh collapse, whereas the vapor bubbles investigated in our study fully disappear due to condensation. Furthermore, Warnetz and Johnsen (2015) include surface tension, which is neglected here. However, the overall evolutions of the bubbles in viscoelastic surroundings from our study qualitatively agree with those of Warnetz and Johnsen (2015) and the following effects are observable in both works. For the collapse with the UCM model, an increased relaxation time initially leads to larger rebound radii, since the fluid has a longer time to accelerate resulting in larger velocity gradients. Again, this causes less viscous dissipation in the early stages of the collapse but higher viscoelastic stresses at later stages. If the relaxation time is increased further, again smaller rebound radii are observable, since the inertia forces become more dominant.

For a more detailed analysis of the Maxwell stress build up we examine the temporal evolution of these stress components during the first collapse in the UCM fluid at $Re = 1$, $De = 1$. Fig. 13 shows the corresponding shape of the bubble, visualized by the vapor volume fraction and three different components of the Maxwell stress

at different stages of the collapse. We can clearly notice very low stress levels at the beginning of the collapse and increasing amounts at later stages. The maximum stress values which are acting against the inertia forces of the accelerated liquid occur just before the bubble reached its minimum size and decrease right afterwards.

Furthermore, the influence of elasticity or relaxation time, respectively, on the intensity of the collapse is examined for the UCM model. Therefore, the emitted pressure waves are compared qualitatively for different Deborah numbers. The intensity of the pressure waves is visualized in Fig. 14 for the UCM model at $Re = 1$ and different Deborah numbers. The observations agree with the conclusions drawn from the collapse dynamics for different relaxation times shown in Fig. 12b. A small Deborah number ($De = 0.5$) corresponds to a small relaxation time and viscous forces rapidly develop. The resultant pressure waves emitted during collapse are rather weak. An initial increase of relaxation time leads to a delayed viscous response and less initial viscous dissipation. The intensity of the pressure waves consequently increases ($De = 1.5$). A complete collapse before the first rebound can be observed for $De = 5$, which leads to the emission of a shock wave corresponding with very high pressures. A further increased relaxation time would lead to a collapse behavior increasingly resembling the inviscid case during the initial collapse and would result in more intense shock waves.

Finally, we compare the bubble collapse for the different viscoelastic models at $Re = 1$, $De = 1$ illustrated in Fig. 15. All models different from the UCM incorporate solvent viscosity which is responsible for an immediate damping from the start of the collapse without relaxation. The 1D representation of a solvent viscosity is the dashpot connected in parallel, as outlined in the upper part of Fig. 1. Thus, the collapse in the initial stages is slower than compared to the UCM case where instant viscous damping is not present. Due to the increased viscous dissipation, the rebound radii are smaller in those fluids with solvent contribution. The PTT models furthermore show a distinct behavior due to their shear-thinning properties. The viscosity is decreased dependent on the shear rate in the fluid. Therefore, the bubble collapses faster in the final stages of the first collapse compared to the OLD-B model. Again, the results qualitatively agree with those of Warnetz and Johnsen (2015), viz. the largest rebound radius is obtained for the UCM model followed by the collapse radii with the OLD-B and PTT models.

5. Summary and outlook

We presented an Eulerian method for the numerical simulation of viscoelastic, compressible cavitating flows. The density-based 3D approach uses finite volumes for space discretization and an explicit Runge-Kutta scheme for time integration. Cavitation is modeled by a single-fluid homogeneous mixture model assuming mechanical and thermodynamical equilibrium and including condensation. We have implemented different viscoelastic constitutive models namely the upper-convected Maxwell, the Oldroyd-B and the simplified linear and exponential Phan-Thien Tanner model. The Truesdell rate is identified as proper objective time derivative in connection with compressible flows. The time integration is adapted with respect to the viscoelastic transport equations. For that purpose the eigensystem of a simplified 1D system was examined, and the relevant eigenvalues were identified. A new formulation for the symmetry boundary conditions of the stress tensor has been proposed that depends only on the stress coordinates itself and does not require a calculation of boundary conditions based on other primitive variables. The implemented viscoelastic models were successfully validated against analytical or semi-analytical solutions, respectively. The results of our numerical simulations show very good to excellent agreement with the reference solutions. Finally, the capability for the simulation of two-phase viscoelastic flow problems is demonstrated for the spherical vapor bubble collapse using the different implemented viscoelastic models. It is apparent that viscoelasticity significantly influences the collapse behavior and that the different

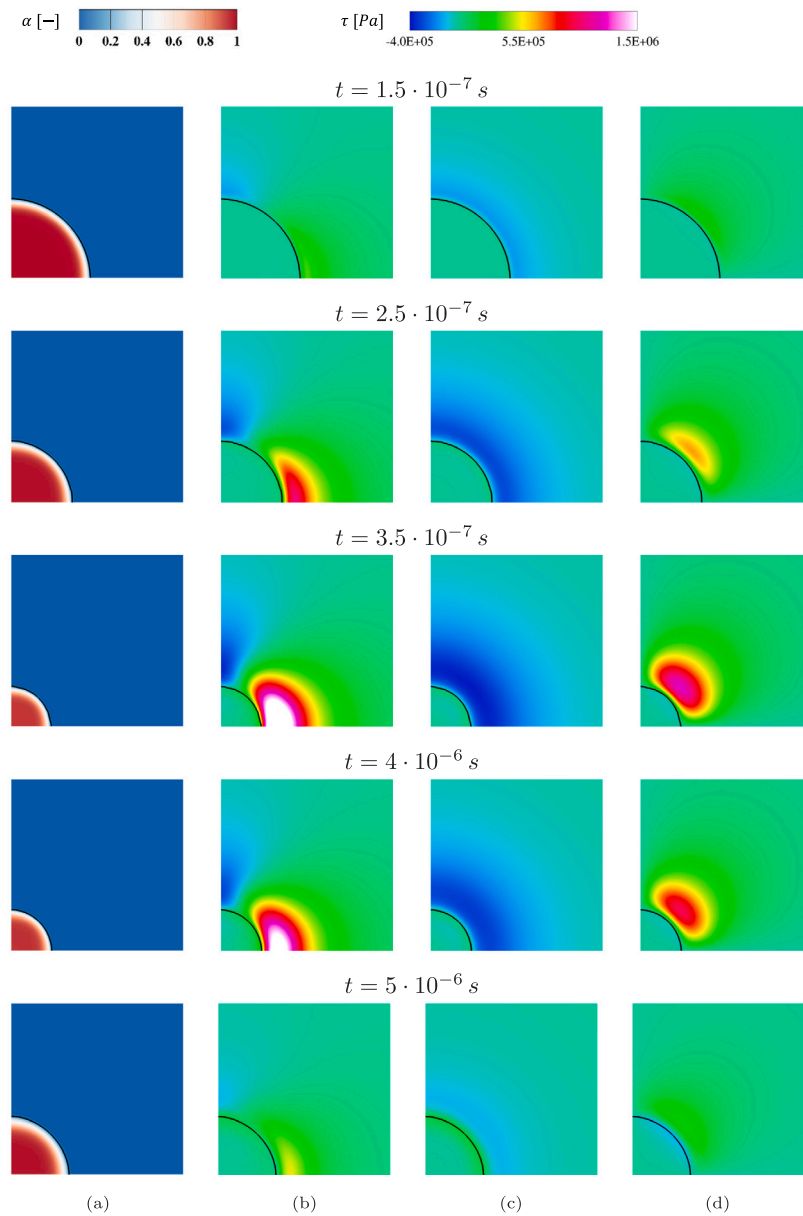


Fig. 13. Contour plots of (a) the volume vapor fraction α and the Maxwell stress components (b) $\tau_{M,11}$, (c) $\tau_{M,33}$, (d) $\tau_{M,12}$ in the x_1 -/ x_2 -plane through the midplane of the vapor bubble for different stages of the collapse. Black isocline: $\alpha = 1\%$.

models show a distinct impact on the temporal evolution of the bubble size. Furthermore, it was shown for the UCM model that the influence of viscoelasticity strongly depends on the relaxation time and an oscillatory motion of the bubble can only be observed for certain combinations of Reynolds and Deborah numbers which corresponds to the requirement of relaxation and collapse time have to of the same order. We could also ascertain that for different relaxation times either a violent or damped collapse event takes place. Depending on the bubble evolution before the first rebound a shock wave can be emitted. The intensity of such a shock wave in terms of the maximum pressure is a good indicator to the potential damage caused by the bubble collapse. Since our framework allows to resolve these shocks, the influence of viscoelastic parameters on shocks will be in the scope of future studies. Besides, the method can be used to investigate the aspherical bubble

collapse in the vicinity of solid walls and examine the influence of viscoelasticity on jet formation during the collapse.

CRediT authorship contribution statement

Christian Lang: Conceptualization, Methodology, Software, Validation, Formal analysis, Investigation, Data curation, Writing – original draft, Writing – Review & Editing, Visualization. **Oliver Boola-kee:** Methodology, Software, Validation, Formal analysis, Investigation, Writing – review & editing. **Steffen J. Schmidt:** Methodology, Writing – review & editing, Supervision, Project administration. **Nikolaus A. Adams:** Methodology, Resources, Writing – review & editing, Supervision, Project administration, Funding acquisition.

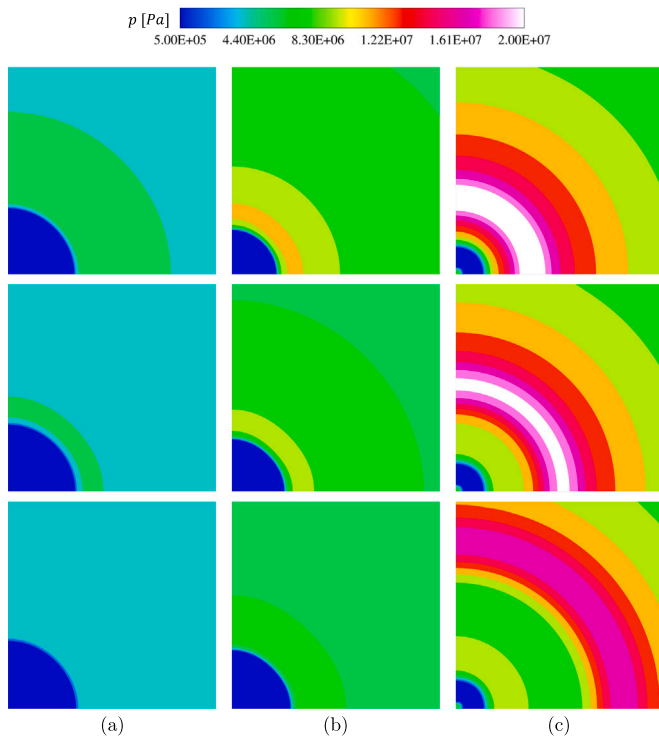


Fig. 14. Temporal evolution (from top to bottom) of the pressure distribution (exponential scale) in the x_1/x_2 -plane through the midplane of the vapor bubble during the first rebound for the UCM model at $Re = 1$ and (a) $De = 0.5$, (b) $De = 1.5$, (c) $De = 5$.

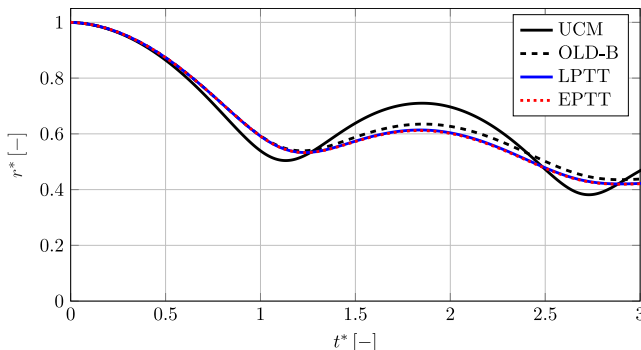


Fig. 15. Spherical vapor bubble collapse: Evolution of the dimensionless bubble radius for the different viscoelastic models at $Re = 1$, $De = 1$.

Declaration of competing interest

The authors declare that they have no known competing financial interests or personal relationships that could have appeared to influence the work reported in this paper.

Acknowledgments

The authors gratefully acknowledge the Leibniz Supercomputing Centre for funding this project by providing computing time and support on its Linux-Cluster.

References

- Aboubacar, M., Webster, M.F., 2001. A cell-vertex finite volume/element method on triangles for abrupt contraction viscoelastic flows. *J. Non-Newton. Fluid Mech.* 98 (2–3), 83–106. [http://dx.doi.org/10.1016/S0377-0257\(00\)00196-8](http://dx.doi.org/10.1016/S0377-0257(00)00196-8).
- Al-Baldawi, A., 2012. Modellierung und Simulation viskoelastischer Polymerschmelzen (Ph.D. thesis). Universität Kassel, URL: <https://kobra.bibliothek.uni-kassel.de/bitstream/urn:nbn:de:hebis:34-2013012842468/1/DissertationAmmarAlBaldawi.pdf>.
- Alves, M.A., Oliveira, P.J., Pinho, F.T., 2003. Benchmark solutions for the flow of Oldroyd-B and PTT fluids in planar contractions. *J. Non-Newton. Fluid Mech.* 110 (1), 45–75. [http://dx.doi.org/10.1016/S0377-0257\(02\)00191-X](http://dx.doi.org/10.1016/S0377-0257(02)00191-X), URL: <https://linkinghub.elsevier.com/retrieve/pii/S037702570200191X>.
- Baaijens, H.P.W., Peters, G.W.M., Baaijens, F.P.T., Meijer, H.E.H., 1995. Viscoelastic flow past a confined cylinder of a polyisobutylene solution. *J. Rheol.* 39 (6), 1243–1277. <http://dx.doi.org/10.1122/1.550635>.
- Barnes, H.A., 1989. *An Introduction to Rheology*.
- Bazant, Z.P., 1971. A correlation study of formulations of incremental deformation and stability of continuous bodies. *J. Appl. Mech.* 38 (4), 919–928. <http://dx.doi.org/10.1115/1.3408976>, URL: <https://asmdigitalcollection.asme.org/appliedmechanics/article/38/4/919/423627/A-Correlation-Study-of-Formulations-of-Incremental-Formulations-of-Incremental>.
- Bazant, Z.P., 2010. *Stability of Structures*.
- Beattie, D., Whalley, P., 1982. A simple two-phase frictional pressure drop calculation method. *Int. J. Multiph. Flow.* 8 (1), 83–87. [http://dx.doi.org/10.1016/0301-9322\(82\)90009-X](http://dx.doi.org/10.1016/0301-9322(82)90009-X), URL: <https://linkinghub.elsevier.com/retrieve/pii/030193228290009X>.
- Belblidia, F., Keshitban, L.J., Webster, M.F., 2006. Stabilised computations for viscoelastic flows under compressible implementations. *J. Non-Newton. Fluid Mech.* 134 (1–3 SPEC. ISS.), 56–76. <http://dx.doi.org/10.1016/j.jnnfm.2005.12.003>.
- Bergander, H., 1987. *Deformationsgesetze der standardform in konvektiver metrik*. *Tech. Mech.* 8, 31–40.
- Berker, A., Bouldin, M.G., Kleis, S.J., VanArsdale, W.E., 1995. Effect of polymer on flow in journal bearings. *J. Non-Newton. Fluid Mech.* 56 (3), 333–347. [http://dx.doi.org/10.1016/0377-0257\(94\)01299-W](http://dx.doi.org/10.1016/0377-0257(94)01299-W).
- Böhme, G., 2000. *Strömungsmechanik Nichtnewtonscher Fluide*. Teubner.
- Bollada, P.C., Phillips, T.N., 2012. On the mathematical modelling of a compressible viscoelastic fluid. *Arch. Ration. Mech. Anal.* 205 (1), 1–26. <http://dx.doi.org/10.1007/s00205-012-0496-5>, URL: <http://link.springer.com/10.1007/s00205-012-0496-5>.
- Brennen, C.E., 1995. *Cavitation and Bubble Dynamics*, Vol. 9. pp. 145–185. <http://dx.doi.org/10.1017/CBO9781107338760>, URL: <http://arjournals.annualreviews.org/doi/abs/10.1146/annurev.fl.09.010177.001045>. arXiv:arXiv:1011.1669v3.
- Brujan, E.A., 1999. A first-order model for bubble dynamics in a compressible viscoelastic liquid. *J. Non-Newton. Fluid Mech.* 84 (1), 83–103. [http://dx.doi.org/10.1016/S0377-0257\(98\)00144-X](http://dx.doi.org/10.1016/S0377-0257(98)00144-X).
- Brujan, E.A., 2001. The equation of bubble dynamics in a compressible linear viscoelastic liquid. *Fluid Dyn. Res.* 29 (5), 287–294. [http://dx.doi.org/10.1016/S0169-5983\(01\)00030-2](http://dx.doi.org/10.1016/S0169-5983(01)00030-2).
- Brujan, E., 2011. *Cavitation in Non-Newtonian Fluids*. Springer Berlin Heidelberg, Berlin, Heidelberg, <http://dx.doi.org/10.1007/978-3-642-15343-3>, URL: <http://link.springer.com/10.1007/978-3-642-15343-3>.
- Brujan, E.A., 2019. Shock wave emission and cavitation bubble dynamics by femtosecond optical breakdown in polymer solutions. *Ultrason. Sonochem.* 58 (March), 104694. <http://dx.doi.org/10.1016/j.ultsonch.2019.104694>.
- Budich, B., 2018. *Numerical Simulation and Analysis of Shock Phenomena in Cavitating Flow and its Application to Ship Propellers* (Ph.D. thesis). Technical University of Munich.
- Budich, B., Schmidt, S.J., Adams, N.A., 2018. Numerical simulation and analysis of condensation shocks in cavitating flow. *J. Fluid Mech.* 838, 759–813. <http://dx.doi.org/10.1017/jfm.2017.882>.
- Chakraborty, D., Sader, J.E., 2015. Constitutive models for linear compressible viscoelastic flows of simple liquids at nanometer length scales. *Phys. Fluids* 27 (5), <http://dx.doi.org/10.1063/1.4919620>.
- Crochet, M., Bezy, M., 1979. Numerical solution for the flow of viscoelastic fluids. *J. Non-Newton. Fluid Mech.* 5, 201–218. [http://dx.doi.org/10.1016/0377-0257\(79\)85014-4](http://dx.doi.org/10.1016/0377-0257(79)85014-4), URL: <https://linkinghub.elsevier.com/retrieve/pii/0377025779850144>.
- Cruz, D.O.A., Pinho, F.T., 2007. Fully-developed pipe and planar flows of multimode viscoelastic fluids. *J. Non-Newton. Fluid Mech.* 141 (2–3), 85–98. <http://dx.doi.org/10.1016/j.jnnfm.2006.09.001>.
- Cruz, D.O.A., Pinho, F.T., Oliveira, P.J., 2005. Analytical solutions for fully developed laminar flow of some viscoelastic liquids with a Newtonian solvent contribution. *J. Non-Newton. Fluid Mech.* 132 (1–3), 28–35. <http://dx.doi.org/10.1016/j.jnnfm.2005.08.013>.
- Dvorkin, E.N., Goldschmit, M.B., 2005. *Nonlinear Continua*. In: *Computational Fluid and Solid Mechanics*, Springer Berlin Heidelberg, Berlin, Heidelberg, p. 586. <http://dx.doi.org/10.1007/3-540-29264-0>, URL: <http://link.springer.com/10.1007/3-540-29264-0>.

- Edwards, B.J., Beris, A.N., 1990. Remarks concerning compressible viscoelastic fluid models. *J. Non-Newton. Fluid Mech.* 36, 411–417. [http://dx.doi.org/10.1016/0377-0257\(90\)85021-P](http://dx.doi.org/10.1016/0377-0257(90)85021-P), URL: <https://linkinghub.elsevier.com/retrieve/pii/037702579085021P>.
- Egerer, C.P., 2016. Large-Eddy Simulation of Turbulent Cavitating Flows (Ph.D. thesis). Technical University of Munich, p. 145.
- Egerer, C.P., Hickel, S., Schmidt, S.J., Adams, N.A., 2014. Large-eddy simulation of turbulent cavitating flow in a micro channel. *Phys. Fluids* 26 (8), <http://dx.doi.org/10.1063/1.4891325>.
- Egerer, C.P., Schmidt, S.J., Hickel, S., Adams, N.A., 2016. Efficient implicit LES method for the simulation of turbulent cavitating flows. *J. Comput. Phys.* 316, 453–469. <http://dx.doi.org/10.1016/j.jcp.2016.04.021>.
- Favero, J.L., Secchi, A.R., Cardozo, N.S.M., Jasak, H., 2010. Viscoelastic flow analysis using the software OpenFOAM and differential constitutive equations. *J. Non-Newton. Fluid Mech.* 165 (23–24), 1625–1636. <http://dx.doi.org/10.1016/j.jnnfm.2010.08.010>.
- Fernandes, C., Vukčević, V., Uroić, T., Simoes, R., Carneiro, O.S., Jasak, H., Nóbrega, J.M., 2019. A coupled finite volume flow solver for the solution of incompressible viscoelastic flows. *J. Non-Newton. Fluid Mech.* 265 (January), 99–115. <http://dx.doi.org/10.1016/j.jnnfm.2019.01.006>.
- Ferrás, L.L., Afonso, A.M., Alves, M.A., Nóbrega, J.M., Pinho, F.T., 2020. Newtonian and viscoelastic fluid flows through an abrupt 1:4 expansion with slip boundary conditions. *Phys. Fluids* 32 (4), 043103. <http://dx.doi.org/10.1063/1.5145092>.
- Ferziger, J.H., Perić, M., 2002. Computational Methods for Fluid Dynamics. Springer Berlin Heidelberg, Berlin, Heidelberg, <http://dx.doi.org/10.1007/978-3-642-56026-2>, URL: <http://link.springer.com/10.1007/978-3-642-56026-2>.
- Figueiredo, R.A., Oishi, C.M., Afonso, A.M., Tasso, I.V., Cuminato, J.A., 2016. A two-phase solver for complex fluids: Studies of the weissenberg effect. *Int. J. Multiph. Flow.* 84, 98–115. <http://dx.doi.org/10.1016/j.ijmultiphaseflow.2016.04.014>.
- Fogler, H.S., Goddard, J.D., 1970. Collapse of spherical cavities in viscoelastic fluids. *Phys. Fluids* 13 (5), 1135–1141. <http://dx.doi.org/10.1063/1.1693042>.
- Franc, J.-P., Michel, J.-M., 2005. Fundamentals of Cavitation. In: Fluid Mechanics and Its Applications, vol. 76, Kluwer Academic Publishers, Dordrecht, <http://dx.doi.org/10.1007/1-4020-2233-6>, URL: <http://link.springer.com/10.1007/1-4020-2233-6>.
- Giesekus, H., 1966. Die elastizität von flüssigkeiten. *Rheol. Acta* 5 (1), 29–35. <http://dx.doi.org/10.1007/BF01973575>, URL: <http://link.springer.com/10.1007/BF01973575>.
- Giesekus, H., 1982. A simple constitutive equation for polymer fluids based on the concept of deformation-dependent tensorial mobility. *J. Non-Newton. Fluid Mech.* 11 (1–2), 69–109. [http://dx.doi.org/10.1016/0377-0257\(82\)85016-7](http://dx.doi.org/10.1016/0377-0257(82)85016-7).
- Gogate, P.R., Wilhelm, A.M., Pandit, A.B., 2003. Some aspects of the design of sonochemical reactors. *Ultrasound. Sonochem.* 10 (6), 325–330. [http://dx.doi.org/10.1016/S1350-4177\(03\)00103-2](http://dx.doi.org/10.1016/S1350-4177(03)00103-2).
- Guy, R.D., Fogelson, A.L., 2008. A wave propagation algorithm for viscoelastic fluids with spatially and temporally varying properties. *Comput. Methods Appl. Mech. Engrg.* 197 (25–28), 2250–2264. <http://dx.doi.org/10.1016/j.cma.2007.11.022>.
- Habla, F., Woitalka, A., Neuner, S., Hinrichsen, O., 2012. Development of a methodology for numerical simulation of non-isothermal viscoelastic fluid flows with application to axisymmetric 4 : 1 contraction flows. *Chem. Eng. J.* 207–208, 772–784. <http://dx.doi.org/10.1016/j.cej.2012.07.060>.
- Haupt, P., 2000. Continuum Mechanics and Theory of Materials. <http://dx.doi.org/10.1007/978-3-662-04109-3>.
- Hirsch, C., 2007. Numerical Computation of Internal and External Flows. Elsevier, <http://dx.doi.org/10.1016/B978-0-7506-6594-0.X5037-1>, URL: <https://linkinghub.elsevier.com/retrieve/pii/B9780750665940X50371>.
- Housiadas, K.D., Georgiou, G.C., 2011. Perturbation solution of Poiseuille flow of a weakly compressible Oldroyd-B fluid. *J. Non-Newton. Fluid Mech.* 166 (1–2), 73–92. <http://dx.doi.org/10.1016/j.jnnfm.2010.10.007>.
- Housiadas, K.D., Georgiou, G.C., Mamoutos, I.G., 2012. Laminar axisymmetric flow of a weakly compressible viscoelastic fluid. *Rheol. Acta* 51 (6), 511–526. <http://dx.doi.org/10.1007/s00397-011-0610-x>.
- Hua, C., Johnsen, E., 2013. Nonlinear oscillations following the Rayleigh collapse of a gas bubble in a linear viscoelastic (tissue-like) medium. *Phys. Fluids* 25 (8), <http://dx.doi.org/10.1063/1.4817673>.
- Huilgol, R.R., Phan-Thien, N., 1997. Fluid Mechanics of Viscoelasticity.
- Ji, W., Waas, A.M., Bazant, Z.P., 2013. On the importance of work-conjugacy and objective stress rates in finite deformation incremental finite element analysis. *J. Appl. Mech. Trans. ASME* 80 (4), 1–9. <http://dx.doi.org/10.1115/1.4007828>.
- Jiang, G.S., Shu, C.W., 1996. Efficient implementation of weighted ENO schemes. *J. Comput. Phys.* 126 (1), 202–228. <http://dx.doi.org/10.1006/jcph.1996.0130>.
- Jiménez-Fernández, J., Crespo, A., 2006. The collapse of gas bubbles and cavities in a viscoelastic fluid. *Int. J. Multiph. Flow.* 32 (10–11), 1294–1299. <http://dx.doi.org/10.1016/j.ijmultiphaseflow.2006.06.001>.
- Johnsen, E., Colonius, T., 2008. Shock-induced collapse of a gas bubble in shockwave lithotripsy. *J. Acoust. Soc. Am.* 124 (4), 2011–2020. <http://dx.doi.org/10.1121/1.2973229>.
- Johnson, M.W., Segalman, D., 1977. A model for viscoelastic fluid behavior which allows non-affine deformation. *J. Non-Newton. Fluid Mech.* 2 (3), 255–270. [http://dx.doi.org/10.1016/0377-0257\(77\)80003-7](http://dx.doi.org/10.1016/0377-0257(77)80003-7).
- Keshtiban, I.J., Belblidia, F., Webster, M.F., 2004. Numerical simulation of compressible viscoelastic liquids. *J. Non-Newton. Fluid Mech.* 122 (1–3), 131–146. <http://dx.doi.org/10.1016/j.jnnfm.2003.12.008>.
- Keshtiban, I.J., Belblidia, F., Webster, M.F., 2005. Computation of incompressible and weakly-compressible viscoelastic liquids flow: Finite element/volume schemes. *J. Non-Newton. Fluid Mech.* 126 (2-3 SPEC. ISS.), 123–143. <http://dx.doi.org/10.1016/j.jnnfm.2004.07.020>.
- Kim, C., 1994. Collapse of spherical bubbles in Maxwell fluids. *J. Non-Newton. Fluid Mech.* 55 (1), 37–58. [http://dx.doi.org/10.1016/0377-0257\(94\)80059-6](http://dx.doi.org/10.1016/0377-0257(94)80059-6), URL: <https://linkinghub.elsevier.com/retrieve/pii/0377025794800596>.
- Koren, B., 1993. A robust upwind discretization method for advection, diffusion and source terms. *Numer. Methods Advection-Diffus. Probl.* 45 (c), 117–138.
- Larson, R.G., 1992. Instabilities in viscoelastic flows. *Rheol. Acta* 31, 213–263. <http://dx.doi.org/10.1007/BF01974447>.
- Lentacker, I., De Cock, I., Deckers, R., De Smedt, S.C., Moonen, C.T., 2014. Understanding ultrasound induced sonoporation: Definitions and underlying mechanisms. *Adv. Drug Deliv. Rev.* 72, 49–64. <http://dx.doi.org/10.1016/j.addr.2013.11.008>.
- LeVeque, R., 1992. Numerical Methods for Conservation Laws. Birkhäuser Basel, Basel, <http://dx.doi.org/10.1007/978-3-0348-8629-1>, URL: <http://link.springer.com/10.1007/978-3-0348-8629-1>.
- Lind, S.J., 2010. A Numerical Study of the Effect of Viscoelasticity on Cavitation and Bubble Dynamics (Ph.D. thesis). Cardiff University, p. 305.
- Lind, S.J., Phillips, T.N., 2010. Spherical bubble collapse in viscoelastic fluids. *J. Non-Newton. Fluid Mech.* 165 (1–2), 56–64. <http://dx.doi.org/10.1016/j.jnnfm.2009.09.002>.
- Lind, S.J., Phillips, T.N., 2013. Bubble collapse in compressible fluids using a spectral element marker particle method. Part 2. Viscoelastic fluids. *Internat. J. Numer. Methods Fluids* 71 (9), 1103–1130. <http://dx.doi.org/10.1002/flid.3701>, URL: <http://doi.wiley.com/10.1002/flid.3701>.
- Lippmann, H., 1996. Angewandte Tensorrechnung. Springer Berlin Heidelberg, Berlin, Heidelberg, <http://dx.doi.org/10.1007/978-3-642-80292-8>, URL: <http://link.springer.com/10.1007/978-3-642-80292-8>.
- Mackay, A.T., Phillips, T.N., 2019. On the derivation of macroscopic models for compressible viscoelastic fluids using the generalized bracket framework. *J. Non-Newton. Fluid Mech.* 266 (February), 59–71. <http://dx.doi.org/10.1016/j.jnnfm.2019.02.006>.
- Mihatsch, M.S., Schmidt, S.J., Adams, N.A., 2015. Cavitation erosion prediction based on analysis of flow dynamics and impact load spectra. *Phys. Fluids* 27 (10), <http://dx.doi.org/10.1063/1.4932175>.
- Mompean, G., Deville, M., 1997. Unsteady finite volume simulation of Oldroyd-B fluid through a three-dimensional planar contraction. *J. Non-Newton. Fluid Mech.* 72 (2–3), 253–279. [http://dx.doi.org/10.1016/S0377-0257\(97\)00033-5](http://dx.doi.org/10.1016/S0377-0257(97)00033-5).
- Naseri, H., Koukouvini, P., Malgarinos, I., Gavaises, M., 2018. On viscoelastic cavitating flows: A numerical study. *Phys. Fluids* 30 (3), <http://dx.doi.org/10.1063/1.5011978>.
- Nithiarasu, P., 2004. A fully explicit characteristics based split (CBS) scheme for viscoelastic flow calculations. *Internat. J. Numer. Methods Engrg.* 60 (5), 949–978. <http://dx.doi.org/10.1002/nme.993>.
- Ohl, C.D., Arora, M., Dijkink, R., Janve, V., Lohse, D., 2006a. Surface cleaning from laser-induced cavitation bubbles. *Appl. Phys. Lett.* 89 (7), <http://dx.doi.org/10.1063/1.2337506>.
- Ohl, C.D., Arora, M., Ikin, R., De Jong, N., Versluis, M., Delius, M., Lohse, D., 2006b. Sonoporation from jetting cavitation bubbles. *Biophys. J.* 91 (11), 4285–4295. <http://dx.doi.org/10.1529/biophysj.105.075366>.
- Oldroyd, J.G., 1950. On the formulation of rheological equations of state. *Proc. R. Soc. A* 200 (1063), 523–541. <http://dx.doi.org/10.1098/rspa.1950.0035>, URL: <http://rspa.royalsocietypublishing.org/cgi/doi/10.1098/rspa.1950.0035>.
- Oldroyd, J.G., 1984. An approach to non-newtonian fluid mechanics. *J. Non-Newton. Fluid Mech.* 14, 9–46. [http://dx.doi.org/10.1016/0377-0257\(84\)80035-x](http://dx.doi.org/10.1016/0377-0257(84)80035-x).
- Oliveira, P.J., Pinho, F.T., Pinto, G.A., 1998. Numerical simulation of non-linear elastic flows with a general collocated finite-volume method. *J. Non-Newton. Fluid Mech.* 79 (1), 1–43. [http://dx.doi.org/10.1016/S0377-0257\(98\)00082-2](http://dx.doi.org/10.1016/S0377-0257(98)00082-2).
- Örley, F., Pasquariello, V., Hickel, S., Adams, N.A., 2015a. Cut-element based immersed boundary method for moving geometries in compressible liquid flows with cavitation. *J. Comput. Phys.* 283, 1–22. <http://dx.doi.org/10.1016/j.jcp.2014.11.028>.
- Örley, F., Trummer, T., Hickel, S., Mihatsch, M.S., Schmidt, S.J., Adams, N.A., 2015b. Large-eddy simulation of cavitating nozzle flow and primary jet break-up. *Phys. Fluids* 27 (8), <http://dx.doi.org/10.1063/1.4928701>.
- Owens, R.G., Phillips, T.N., 2002. Computational Rheology. <http://dx.doi.org/10.1142/9781860949425>, URL: <http://ebooks.worldscinet.com/ISBN/9781860949425/9781860949425.html>.
- Perera, M.G., Strauss, K., 1979. Direct numerical solutions of the equations for viscoelastic fluid flow. *J. Non-Newton. Fluid Mech.* 5 (C), 269–283. [http://dx.doi.org/10.1016/0377-0257\(79\)85018-1](http://dx.doi.org/10.1016/0377-0257(79)85018-1).
- Phan-Thien, N., 1978. A nonlinear network viscoelastic model. *J. Rheol.* 22 (3), 259–283. <http://dx.doi.org/10.1122/1.549481>, URL: <http://sor.scitation.org/doi/10.1122/1.549481>.

- Phan-Thien, N., Tanner, R.I., 1977. A new constitutive equation derived from network theory. *J. Non-Newton. Fluid Mech.* 2 (4), 353–365. [http://dx.doi.org/10.1016/0377-0257\(77\)80021-9](http://dx.doi.org/10.1016/0377-0257(77)80021-9), URL: <https://linkinghub.elsevier.com/retrieve/pii/S0377025777800219>.
- Phelan, F.R., Malone, M.F., Winter, H.H., 1989. A purely hyperbolic model for unsteady viscoelastic flow. *J. Non-Newton. Fluid Mech.* 32 (2), 197–224. [http://dx.doi.org/10.1016/0377-0257\(89\)85036-0](http://dx.doi.org/10.1016/0377-0257(89)85036-0).
- Pinsky, P.M., Ortiz, M., Pister, K.S., 1983. Numerical integration of rate constitutive equations in finite deformation analysis. *Comput. Methods Appl. Mech. Engrg.* 40 (2), 137–158. [http://dx.doi.org/10.1016/0045-7825\(83\)90087-7](http://dx.doi.org/10.1016/0045-7825(83)90087-7).
- Price, R.J., Kaul, S., 2002. Contrast ultrasound targeted drug and gene delivery: An update on a new therapeutic modality. *J. Cardiovasc. Pharmacol. Ther.* 7 (3), 171–180. <http://dx.doi.org/10.1177/107424840200700307>.
- Rodriguez, M., Johnsen, E., 2019. A high-order accurate five-equations compressible multiphase approach for viscoelastic fluids and solids with relaxation and elasticity. *J. Comput. Phys.* 379, 70–90. <http://dx.doi.org/10.1016/j.jcp.2018.10.035>.
- Rodriguez, M., Johnsen, E., Powell, K.G., 2019. A high-order accurate AUSM + -up approach for simulations of compressible multiphase flows with linear viscoelasticity. *Shock Waves* 29 (5), 717–734. <http://dx.doi.org/10.1007/s00193-018-0884-3>.
- Roe, P., 1986. Characteristic-based schemes for the Euler equations. *Annu. Rev. Fluid Mech.* 18 (1), 337–365. <http://dx.doi.org/10.1146/annurev.fluid.18.1.337>.
- Rouhaud, E., Panicaud, B., Kerner, R., 2013. Canonical frame-indifferent transport operators with the four-dimensional formalism of differential geometry. *Comput. Mater. Sci.* 77, 120–130. <http://dx.doi.org/10.1016/j.commatsci.2013.04.032>.
- Rowlatt, C.F., Lind, S.J., 2017. Bubble collapse near a fluid-fluid interface using the spectral element marker particle method with applications in bioengineering. *Int. J. Multiph. Flow.* 90, 118–143. <http://dx.doi.org/10.1016/j.ijmultiphaseflow.2016.11.010>.
- Sato, T., Richardson, S.M., 1994. Explicit numerical simulation of time-dependent viscoelastic flow problems by a finite element/finite volume method. *J. Non-Newton. Fluid Mech.* 51 (3), 249–275. [http://dx.doi.org/10.1016/0377-0257\(94\)85019-4](http://dx.doi.org/10.1016/0377-0257(94)85019-4).
- Saurel, R., Cocchi, J.P., Butler, P.B., 1999. Numerical study of cavitation in the wake of a hypervelocity underwater projectile. *J. Propul. Power* 15 (4), 513–522. <http://dx.doi.org/10.2514/2.5473>.
- Schenke, S., Melissaris, T., Terwisga, T.J.C.V., 2019. On the relevance of kinematics for cavitation implosion loads on the relevance of kinematics for cavitation implosion loads. *Phys. Fluids* 31 (5), <http://dx.doi.org/10.1063/1.5092711>.
- Schmidt, S.J., 2015. *A Low Mach number Consistent Compressible Approach for Simulation of Cavitating Flow* (Ph.D. thesis). Technical University of Munich.
- Schnerr, G., Sauer, J., 2001. Physical and numerical modeling of unsteady cavitation dynamics. In: 4th International Conference on Multiphase Flow (ICMF).
- Schnerr, G.H., Sezal, I.H., Schmidt, S.J., 2008. Numerical investigation of three-dimensional cloud cavitation with special emphasis on collapse induced shock dynamics. *Phys. Fluids* 20 (4), 1–9. <http://dx.doi.org/10.1063/1.2911039>.
- Sezal, I.H., 2009. *Compressible Dynamics of Cavitating 3-D Multi-Phase Flows* (Ph.D. thesis). Technical University of Munich.
- Surana, K.S., Ma, Y., Romkes, A., Reddy, J.N., 2010. The rate constitutive equations and their validity for progressively increasing deformation. *Mech. Adv. Mater. Struct.* 17 (7), 509–533. <http://dx.doi.org/10.1080/15376494.2010.509195>.
- Toro, E.F., 2009. *Riemann Solvers and Numerical Methods for Fluid Dynamics*, Vol. 40. Springer Berlin Heidelberg, Berlin, Heidelberg, p. 9823. <http://dx.doi.org/10.1007/b79761>, URL: <http://link.springer.com/10.1007/b79761>.
- Truesdell, C., 1953. Corrections and additions to "The mechanical foundations of elasticity and fluid dynamics".
- Truesdell, C., 1955. The simplest rate theory of pure elasticity. *Comm. Pure Appl. Math.* 8 (1), 123–132. <http://dx.doi.org/10.1002/cpa.3160080109>.
- Truesdell, C., Noll, W., 2004. *The Non-Linear Field Theories of Mechanics*.
- Trummler, T., Schmidt, S.J., Adams, N.A., 2020. Investigation of condensation shocks and re-entrant jet dynamics in a cavitating nozzle flow by large-eddy simulation. *Int. J. Multiph. Flow.* 125, <http://dx.doi.org/10.1016/j.ijmultiphaseflow.2020.103215>.
- Vlaisavljevich, E., Lin, K.W., Warnez, M.T., Singh, R., Mancina, L., Putnam, A.J., Johnsen, E., Cain, C., Xu, Z., 2015. Effects of tissue stiffness, ultrasound frequency, and pressure on histotripsy-induced cavitation bubble behavior. *Phys. Med. Biol.* 60 (6), 2271–2292. <http://dx.doi.org/10.1088/0031-9155/60/6/2271>.
- Walters, M.J., 2015. *An Investigation into the Effects of Viscoelasticity on Cavitation Bubble Dynamics with Applications to Biomedicine* (Ph.D. thesis). Cardiff University, URL: <http://orca.cf.ac.uk/73461/1/Thesisdraft.pdf>.
- Warnez, M.T., Johnsen, E., 2015. Numerical modeling of bubble dynamics in viscoelastic media with relaxation. *Phys. Fluids* 27 (6), 1–28. <http://dx.doi.org/10.1063/1.4922598>.
- Waters, N.D., King, M.J., 1970. Unsteady flow of an elastico-viscous liquid. *Rheol. Acta* 9 (3), 345–355. <http://dx.doi.org/10.1007/BF01975401>, URL: <http://link.springer.com/10.1007/BF01975401>.
- Xue, S.-C., Phan-Thien, N., Tanner, R., 1998. Three dimensional numerical simulations of viscoelastic flows through planar contractions. *J. Non-Newton. Fluid Mech.* 74 (1–3), 195–245. [http://dx.doi.org/10.1016/S0377-0257\(97\)00072-4](http://dx.doi.org/10.1016/S0377-0257(97)00072-4), URL: <https://linkinghub.elsevier.com/retrieve/pii/S0377025797000724>.
- Yul Yoo, J., Na, Y., 1991. A numerical study of the planar contraction flow of a viscoelastic fluid using the SIMPLER algorithm. *J. Non-Newton. Fluid Mech.* 39 (1), 89–106. [http://dx.doi.org/10.1016/0377-0257\(91\)80005-5](http://dx.doi.org/10.1016/0377-0257(91)80005-5).
- Zilonova, E., Solovchuk, M., Sheu, T.W.H., 2018. Bubble dynamics in viscoelastic soft tissue in high-intensity focal ultrasound thermal therapy. *Ultrason. Sonochem.* 40 (35), 900–911. <http://dx.doi.org/10.1016/j.ulsonch.2017.08.017>.

A.2 *On spherical vapor bubble collapse in viscoelastic fluids*

(Reproduced from [78])



RightsLink

Home

Help

Live Chat

Sign in

Create Account



On spherical vapor bubble collapse in viscoelastic fluids

Author: Christian Lang, Mengqi Zhang, Steffen J. Schmidt, Nikolaus A. Adams

Publication: Applied Mathematical Modelling

Publisher: Elsevier

Date: November 2023

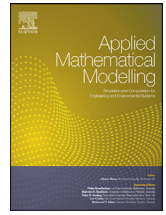
© 2023 Published by Elsevier Inc.

Journal Author Rights

Please note that, as the author of this Elsevier article, you retain the right to include it in a thesis or dissertation, provided it is not published commercially. Permission is not required, but please ensure that you reference the journal as the original source. For more information on this and on your other retained rights, please visit: <https://www.elsevier.com/about/our-business/policies/copyright#Author-rights>

BACK

CLOSE WINDOW



On spherical vapor bubble collapse in viscoelastic fluids

Christian Lang^{a,b,*}, Mengqi Zhang^b, Steffen J. Schmidt^a, Nikolaus A. Adams^a



^a Technical University of Munich, TUM School of Engineering and Design, Chair of Aerodynamics and Fluid Mechanics, Boltzmannstr. 15, Garching bei München 85748, Germany

^b Department of Mechanical Engineering, National University of Singapore, 9 Engineering Drive 1, 117575 Singapore

ARTICLE INFO

Article history:

Received 16 January 2023

Revised 9 May 2023

Accepted 3 July 2023

Available online 8 July 2023

Keywords:

Viscoelasticity

Bubble collapse

Multiphase flows

Computational fluid dynamics

Numerical simulation

Complex fluids

ABSTRACT

Cavitating vapor bubbles, occur in variety of engineering applications, employing complex fluids as operating medium. Especially in biomechanics, biomedical applications as well as in polymer processing, fluids exhibit viscoelastic properties and fundamentally different behavior than Newtonian fluids. To explain the influence of viscoelasticity on cavitation a detailed understanding of the viscoelastic influence on bubble dynamics and of the underlying mechanisms is essential. With this study we provide in-depth numerical investigations of the spherical vapor bubble collapse in viscoelastic fluids. A compressible, density-based, 3D finite-volume solver with explicit time integration is used together with a conservative, compressible formulation for the constitutive equations of three different viscoelastic models, namely the upper convected Maxwell model, the Oldroyd-B model and the simplified linear Phan-Thien Tanner model. 3D simulations of the collapse dynamics are carried out to show the viscous and viscoelastic stress development during the collapse, and its relation to the occurring deformations. Collapse behavior is investigated for various elasticity, viscosity and constitutive models. It is demonstrated that viscoelasticity fundamentally alters the collapse behavior and evolution of stresses. It is observed that viscoelastic stresses develop with a time delay proportional to elasticity and show different spatial distributions as opposed to Newtonian stresses. Viscoelasticity introduces isotropic stress components even though the spherical collapse leads to purely deviatoric (elongational) deformation. Furthermore, the distinct influence of constitutive models is illustrated and the influence of viscoelastic models with solvent contribution is explained. For the upper convected Maxwell model, we show that for increased elasticity shock wave emission can be observed depending on the applied grid resolution.

© 2023 Published by Elsevier Inc.

1. Introduction

Many applications involving cavitation and cavitating bubbles incorporate materials that concurrently show viscous and elastic behavior. Viscoelastic behavior can be attributed to the underlying complex microstructure comprising long-chained molecules. Cavitation bubbles can be present in a wide range of application scenarios of such materials. In biological media cavitation bubbles are exploited in applications such as drug delivery [1,2], shock-wave lithotripsy [3], histotripsy [4,5] and microbubble contrast agents for ultrasound diagnostics and treatment [6,7]. Other applications with cavitation in materials of

* Corresponding author.

E-mail address: c.lang@tum.de (C. Lang).

URL: <https://www.epc.ed.tum.de/en/aer/home/> (C. Lang)

complex microstructure are the usage of ultrasonics in food processing [8], rheological measurements for the determination of material properties [9,10] and polymeric foam production [11]. The interested reader is referred to Brujan [12], Dollet et al. [13] for a comprehensive summary on applications of cavitation in viscoelastic media.

The alteration of cavitation bubble dynamics by viscoelastic effects was clearly proven experimentally. Barnett [14] performed experiments of dissolving bubbles in water and viscoelastic fluids and assessed a retardation of the process caused by viscoelasticity. Ashworth and Procter [15] conducted experiments with dilute polymer solutions to investigate cavitation damage through bubble collapse and revealed that small amounts of polymers in water can significantly change the erosion potential. Brujan [16] conducted experiments and simulations to show the viscoelastic impact on cavitation bubble dynamics and detected a reduction the oscillation size and period, and a pressure reduction of the emitted pressure wave in polyacrylamide gel compared to water. Recently, Yang et al. [10] utilize cavitation in viscoelastic materials for the purpose of rheometry extracting material parameters during the collapse of laser-generated bubbles. In doing so, they additionally applied a numerical 1D formulation based on the Kelvin-Voigt viscoelastic model.

Aside from experiments, mathematical models were formulated and simulations were carried out to investigate viscoelastic bubble dynamics. Numerical studies of Fogler and Goddard [17], Tanasawa and Yang [18] ascertained that viscoelasticity has a significant impact on the spherical bubble collapse in a Maxwell- and an Oldroyd-fluid, respectively. In both studies modifications of the 1D Rayleigh-Plesset equation are applied, neglecting compressibility. Brujan [19] performed simulations using a 1D formulation of the equation of motion including compressibility. They applied the Oldroyd viscoelastic model with the material time derivative as stress rate. By using a singular perturbation method they ascertained that only for $Re < 100$ viscoelastic effects become significant for the spherical bubble collapse. Allen and Roy [20,21] studied oscillations of spherical gas bubbles in viscoelastic fluids with the help of the generalized Rayleigh-Plesset equations assuming incompressible flows. For the linear case Allen and Roy [20] used a traceless stress tensor formulation, the partial time derivative as stress rate and the Oldroyd viscoelastic constitutive model. In the second part [21] they extended their model using a nonzero trace formulation for the viscoelastic stress tensor and the upper convected Maxwell (UCM) model including the upper convected time derivative for the stress rate that ensures frame invariance, also for large deformations. They showed that elasticity or the corresponding relaxation strongly influences the amplitude of oscillations. The limitations of the traceless formulation with non-objective stress rates were highlighted by showing distinct differences in the oscillatory motion for large deformations. Furthermore, the viscoelastic stresses during bubble oscillations were examined. Bubble oscillations and non-spherical shape change were studied by Foteinopoulou and Laso [22]. They used the incompressible equations of motion combined with the exponential Phan-Thien Tanner (EPTT) viscoelastic model which includes shear-thinning, and solved the 3D equations using a finite element discretization. They found an increased oscillation amplitude by increasing the relaxation time or decreasing the viscosity. Furthermore, they stated that a traceless formulation of the viscoelastic stress tensor may lead to incorrect results. Lind and Phillips [23] formulated a generalized Bernoulli equation assuming incompressible flow. The (generalized) Maxwell and the Oldroyd viscoelastic model were applied with the material time derivative as stress rate. A boundary element method was utilized to numerically solve the equations and find a rebound condition for the viscoelastic bubble collapse. In a later study [24] the same authors used a model based on the compressible 2D conservation equations and the Oldroyd-B model, which is equipped with the upper convected derivative for the viscoelastic stresses to study the bubble collapse in the vicinity of a rigid wall. The governing equations were discretized by a spectral element method and a particle marker method was employed to model two-phase flow. They found that viscoelasticity can crucially affect the shape during collapse and is able to suppress jet formation which is related to possible cavitation damage. Assuming incompressible flow and a traceless stress tensor, Aliabadi and Taklifi [25] combined the UCM model with the Rayleigh-Plesset equation to investigate the influence of magnetic fields on gas bubble oscillations in viscoelastic media. Different magnitudes of magnetic fields were applied, and it was concluded that magnetic fields can considerably dampen collapse dynamics. Albernaz and Cunha [26] present a model to simulate bubbles in fluids with anisotropic additives and examine the influence of the additive orientation. Hua and Johnsen [27], Warnez and Johnsen [28] used the 1D Keller-Miksis equation, that accounts for far-field compressibility, and applied viscoelastic models to investigate spherical bubble dynamics. In Hua and Johnsen [27] the Maxwell, Kelvin-Voigt and Zener viscoelastic models with the partial time derivative as viscoelastic stress rate and a traceless stress tensor were used. They showed that for the applied models, bubble oscillations are clearly affected by both viscoelasticity and compressibility, and that the influence of compressibility increases with increasing relaxation time. Warnez and Johnsen [28] used a generalized formulation to simulate the dynamics of different viscoelastic models with the upper convected derivative as time rate and a nonzero trace assumption for the viscoelastic stresses. They ascertained that relaxation exclusively is responsible for the bubble rebound. Furthermore, they found that large relaxation times lead to weak damping and more intense collapses. Both studies emphasize the importance of considering compressibility for viscoelastic bubble dynamics. The growth of a bubble in cheese is modelled and examined in Laridon et al. [29]. A generalized multimode Maxwell model with partial time derivative was used to describe viscoelastic behavior of the incompressible medium. The governing equations were solved by using a finite element discretization and the results were validated against experiments. Dastjerdi et al. [30] recently modelled the SARS-CoV-2 virus assuming viscoelastic material behavior, applied the nonlocal elasticity model of Eringen and thereby numerically investigated the application of loads and vibrations as an approach for treatment.

The aforementioned studies showed the importance of viscoelasticity for the bubble collapse dynamics. The majority of the approaches employs 1D equations and in the case of compressible implementations, compressibility is commonly incorporated only in the far-field and the near field is treated incompressible. Moreover, there is no general agreement in the

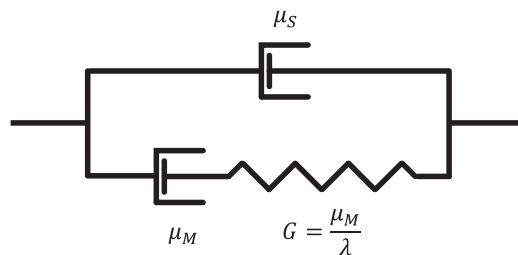


Fig. 1. Schematic 1D rheological representation of materials of the Oldroyd-type (parallel arrangement of dashpot and Maxwell element).

Table 1
Applied viscoelastic models and their features.

Model	Solvent viscosity μ_S	$f(\boldsymbol{\tau}_m)$	Features			
			relaxation	normal stress effects	solvent contribution	shear-thinning
Newtonian	$\neq 0$	0			•	
UCM	0	0	•	•		
OLD-B	$\neq 0$	0	•	•	•	
LPTT	$\neq 0$	$\epsilon \frac{\lambda}{\mu_M} \text{tr}(\boldsymbol{\tau}_m)$	•	•	•	•

literature whether the stress tensor should be assumed traceless or not. Collapse intensity and cavitation damage potential are immediately related to the viscoelastic impact on the bubble collapse dynamics. For a profound understanding of the viscous and viscoelastic stress development and their influence on the collapse, a time-dependent, compressible approach capable of resolving stress contributions is necessary.

There are mainly three mechanisms driving most of the viscoelastic effects. First, due to its concurrently viscous and elastic behavior, viscoelastic materials exhibit a time dependent stress or fading memory behavior where viscoelastic stresses do not only depend on the current shear rate but also on past deformations and past viscoelastic stresses. Contrary to Newtonian fluids, memory effects necessitate convective transport of viscoelastic stresses and correspondingly, to non-local stress effects. Furthermore, time dependency introduces time-delayed stress development. Second, due to complex microstructure, normal stresses can occur in pure shear flows. Moreover, viscoelasticity can introduce shear rate dependent viscosities resulting in shear-thinning or -thickening [31]. One possibility to model viscoelasticity is to consider materials of the Oldroyd-type, whose rheological 1D-representation consists of a parallel arrangement of a dashpot, representing a Newtonian solvent fluid and a Maxwell element (see Fig. 1). The Maxwell element itself consists of a dashpot and spring in series and introduces relaxation. The capability of predicting the aforementioned effects is summarized in Table 1 for the applied models.

In Lang et al. [32] a fully compressible density-based approach in 3D with finite-volume discretization and explicit time-stepping for the simulation of cavitating viscoelastic flows was introduced. The solver comprises compressible formulations of the UCM model, the Oldroyd-B model (denoted as OLD-B model in the following) and the simplified linear Phan-Thien Tanner (LPTT) and exponential Phan-Thien Tanner (EPTT) models and allows for the resolution of shock wave dynamics. We showed that viscoelasticity alters the bubble collapse dynamics. With the present study we provide an in-depth investigation of viscous and viscoelastic stress development during the spherical bubble collapse and the relation to the underlying kinematics. We analyze the influence of viscoelasticity on collapse dynamics and stress development by considering the influence of viscosity, elasticity and different constitutive models. The study first introduces the physical model and the governing equations. Subsequently, numerical method and boundary conditions are briefly discussed. Thereafter, problem configuration and numerical setup are described followed by the results of the conducted simulations. We discuss kinematics and show that the spherical collapse represents a purely deviatoric deformation. Viscous and viscoelastic stress development during collapse is reviewed. The collapse is additionally examined for different elasticity and viscosity. Furthermore, the collapse behavior and stress distributions are compared between a Newtonian fluid and three different viscoelastic models (UCM, OLD-B and LPTT model). It is shown that the variation of the relaxation time, the viscosity and the different models have a clear impact on the resulting stress fields and collapse dynamics. Eventually, we show the emission of shock waves during the collapse in a UCM fluid and ascertain that shock wave intensity is grid dependent for the investigated elasticity.

2. Mathematical model and governing equations

2.1. Transport and constitutive equations for compressible viscoelastic flow

We consider unsteady, 3D, compressible and cavitating flows for viscoelastic fluids in an Eulerian framework. We assume phase change to be isentropic and hence apply a barotropic equation of state. Surface tension and gravitational forces are

neglected. The governing conservation equations are the conservation of mass and momentum, written in differential form

$$\frac{\partial \rho}{\partial t} = -\nabla \cdot (\rho \mathbf{u}), \tag{1}$$

$$\frac{\partial (\rho \mathbf{u})}{\partial t} = -\nabla \cdot (\rho \mathbf{u} \otimes \mathbf{u} - \boldsymbol{\sigma}). \tag{2}$$

Therein, $\rho = \rho(\mathbf{x}, t)$, $\mathbf{u} = \mathbf{u}(\mathbf{x}, t)$ and $\boldsymbol{\sigma} = \boldsymbol{\sigma}(\mathbf{x}, t)$ represent the density field, the velocity field and the Cauchy stress tensor field in the current configuration and for the time instant t , respectively. The Cauchy stress itself is composed of the thermodynamic pressure field $p = p(\mathbf{x}, t)$ and the additional stress $\boldsymbol{\tau}(\mathbf{x}, t)$

$$\boldsymbol{\sigma} = -p\mathbf{I} + \boldsymbol{\tau}. \tag{3}$$

As introduced in Section 1 Maxwell-/Oldroyd-type constitutive equations (cf. Owens and Phillips [33]) are employed, for which the additional stress tensor is composed of the solvent (Newtonian) $\boldsymbol{\tau}_s$ and the viscoelastic contribution $\boldsymbol{\tau}_M$, referred to as Maxwell stress in the following. The resulting constitutive equations read

$$\boldsymbol{\tau} = \boldsymbol{\tau}_s + \boldsymbol{\tau}_M, \tag{4a}$$

$$\boldsymbol{\tau}_s = 2\mu_S \mathbf{d}^d, \tag{4b}$$

$$\boldsymbol{\tau}_M + \lambda \overset{\nabla}{\boldsymbol{\tau}}_M + f(\boldsymbol{\tau}_M) \boldsymbol{\tau}_M = 2\mu_M \mathbf{d}^d, \tag{4c}$$

$$\overset{\nabla}{\boldsymbol{\tau}}_M = \frac{D\boldsymbol{\tau}_M}{Dt} - \mathbf{l} \cdot \boldsymbol{\tau}_M - \boldsymbol{\tau}_M \cdot \mathbf{l}^T + (\nabla \cdot \mathbf{u}) \boldsymbol{\tau}_M, \tag{4d}$$

where μ_S, μ_M are the Newtonian and the Maxwell viscosity, respectively. $\mathbf{d}^d = \mathbf{d} - \frac{1}{3} \text{tr}(\mathbf{d})\mathbf{I}$ is the deviatoric part of the strain rate tensor $\mathbf{d} = \frac{1}{2}(\mathbf{l} + \mathbf{l}^T)$, where $\text{tr}(\mathbf{d})$ is the trace of the same. The strain rate tensor represents the symmetric part of the spatial velocity gradient $\mathbf{l} = \nabla \mathbf{u}$. The constitutive equations include the transport equations for the Maxwell stress tensor, where $\overset{\nabla}{\boldsymbol{\tau}}_M$ represents the Truesdell rate which can be identified as proper objective time derivative in a compressible context, which is explained in further detail in Appendix A. $\frac{D(\boldsymbol{\tau}_M)}{Dt}$ is the material time derivative of the Maxwell stress tensor. In both dissipation terms, for the Newtonian and the viscoelastic contribution, compressibility is considered, meaning that the isotropic part of the strain rate is explicitly excluded and only deviatoric deformations contribute to dissipation. However, the viscous stress tensor can still comprise a non-zero trace and hence have an isotropic part as demonstrated in Section 4.2. A detailed discussion and a validation of the implemented constitutive model can also be found in Lang et al. [32]. By changing the solvent viscosity μ_S and the additional term $f(\boldsymbol{\tau}_M)$ which introduces shear-rate dependent effective viscosity (see Table 1), the upper convected Maxwell model (UCM) [34], the Oldroyd-B (OLD-B) model [34] and the simplified linear Phan-Thien Tanner (LPTT) model [35] are realized. The extensibility parameter within the LPTT model is chosen to the commonly used value of $\epsilon = 0.25$.

By substituting the mass conservation Eq. (1) in the transport equation for the Maxwell stress Eq. (4c) the governing equations are reformulated in conservative form for an arbitrary control volume $\mathcal{V} \in \mathbb{R}^3$ as follows:

$$\int_{\mathcal{V}} \frac{\partial \rho}{\partial t} dV = - \int_{\mathcal{V}} \nabla \cdot (\rho \mathbf{u}) dV, \tag{5}$$

$$\int_{\mathcal{V}} \frac{\partial (\rho \mathbf{u})}{\partial t} dV = - \int_{\mathcal{V}} \nabla \cdot (\rho \mathbf{u} \otimes \mathbf{u} + p\mathbf{I} - 2\mu_S \mathbf{d}^d - \boldsymbol{\tau}_M) dV, \tag{6}$$

$$\int_{\mathcal{V}} \frac{\partial (\rho \boldsymbol{\tau}_M)}{\partial t} dV = - \int_{\mathcal{V}} \nabla \cdot (\rho \boldsymbol{\tau}_M \otimes \mathbf{u}) dV + \int_{\mathcal{V}} \mathbf{S}_{\rho \boldsymbol{\tau}_M} dV, \tag{7}$$

with the source term

$$\mathbf{S}_{\rho \boldsymbol{\tau}_M} = \rho \left[\mathbf{l} \cdot \boldsymbol{\tau}_M + \boldsymbol{\tau}_M \cdot \mathbf{l}^T - (\nabla \cdot \mathbf{u}) \boldsymbol{\tau}_M + \frac{1}{\lambda} [2\mu_M \mathbf{d}^d - f(\boldsymbol{\tau}_M) \boldsymbol{\tau}_M - \boldsymbol{\tau}_M] \right]. \tag{8}$$

Introducing the state vector $\mathbf{U} = [\rho, \rho \mathbf{u}, \rho \boldsymbol{\tau}_M]^T$, the convective fluxes \mathbf{F}^c , the diffusive fluxes \mathbf{F}^d and the source terms \mathbf{S} and applying Gauss' theorem, the governing equations are reformulated in compact notation

$$\int_{\mathcal{V}} \frac{\partial \mathbf{U}}{\partial t} dV = - \oint_{\partial \mathcal{V}} (\mathbf{F}^c + \mathbf{F}^d) dS + \int_{\mathcal{V}} \mathbf{S} dV, \tag{9}$$

with

$$\begin{aligned}
 \mathbf{F}^c &= \begin{bmatrix} F_{\rho}^c \\ \mathbf{F}_{\rho\mathbf{u}}^c \\ F_{\rho\boldsymbol{\tau}_M}^c \end{bmatrix} = \begin{bmatrix} (\rho\mathbf{u}) \cdot \mathbf{n} \\ (\rho\mathbf{u} \otimes \mathbf{u} + p\mathbf{I}) \cdot \mathbf{n} \\ (\rho\boldsymbol{\tau}_M \otimes \mathbf{u}) \cdot \mathbf{n} \end{bmatrix}, \\
 \mathbf{F}^d &= \begin{bmatrix} F_{\rho}^d \\ \mathbf{F}_{\rho\mathbf{u}}^d \\ F_{\rho\boldsymbol{\tau}_M}^d \end{bmatrix} = \begin{bmatrix} 0 \\ (-2\mu_S\mathbf{d}^d - \boldsymbol{\tau}_M) \cdot \mathbf{n} \\ \mathbf{0} \end{bmatrix}, \\
 \mathbf{S} &= \begin{bmatrix} 0 \\ \mathbf{0} \\ S_{\rho\boldsymbol{\tau}_M} \end{bmatrix} = \begin{bmatrix} 0 \\ \mathbf{0} \\ \rho \left[\mathbf{l} \cdot \boldsymbol{\tau}_M + \boldsymbol{\tau}_M \cdot \mathbf{l}^T - (\nabla \cdot \mathbf{u})\boldsymbol{\tau}_M + \frac{1}{\lambda} [2\mu_M\mathbf{d}^d - f(\boldsymbol{\tau}_M)\boldsymbol{\tau}_M - \boldsymbol{\tau}_M] \right] \end{bmatrix}, \tag{10}
 \end{aligned}$$

where \mathbf{n} represents the outward pointing unit normal vector.

The aforementioned governing equations are equally valid for single phase and multiphase flows without limitation assuming the field variables represent a volume averaged homogeneous mixture of the present components within each discrete finite-volume Ω . To calculate volume averaged discrete quantities we introduce the volume averaging operator

$$\bar{\square} := \frac{1}{V_{\Omega}} \int_{\Omega} \square \, dV. \tag{11}$$

In the context of the applied finite-volume spatial discretization we assume all quantities to be cell-centered and volume averaged over discrete control volumes Ω . Correspondingly, the phases are not treated separately, but a homogeneous mixture is considered. The applied cavitation model is based on this assumption as explained together with the equations of state in the following Section 2.2. The discretized equations for each computational cell read

$$\frac{\partial \bar{\mathbf{U}}}{\partial t} = \frac{1}{V_{\Omega}} \left\{ - \oint_{\partial\Omega} (\tilde{\mathbf{F}}^c(\bar{\mathbf{U}}) + \tilde{\mathbf{F}}^d(\bar{\mathbf{U}})) \, dS + \int_{\Omega} \tilde{\mathbf{S}}(\bar{\mathbf{U}}) \, dV \right\}. \tag{12}$$

where $\tilde{\square}$ depicts numerical approximations including flux calculations and face reconstructions as described in more detail in Section 2.3.1.

2.2. Single fluid cavitation model and equations of state

The cavitating two-phase flow with condensation and evaporation is modeled by a single-fluid homogeneous mixture model. For two-phase mixture regions, it is assumed that both phases are in thermodynamic and mechanical equilibrium. The phase change processes occur infinitely fast without time delay and is supposed to be isentropic. The approach thus considers only homogeneous fluids, either of pure liquid or homogeneous mixtures of liquid and vapor. The homogeneous fluid is described by cell-centered volume averaged quantities for each discrete volume. Fig. 2 shows the concept of the applied model. On the left-hand-side an exemplary situation of a two-phase mixture with discrete regions of vapor and

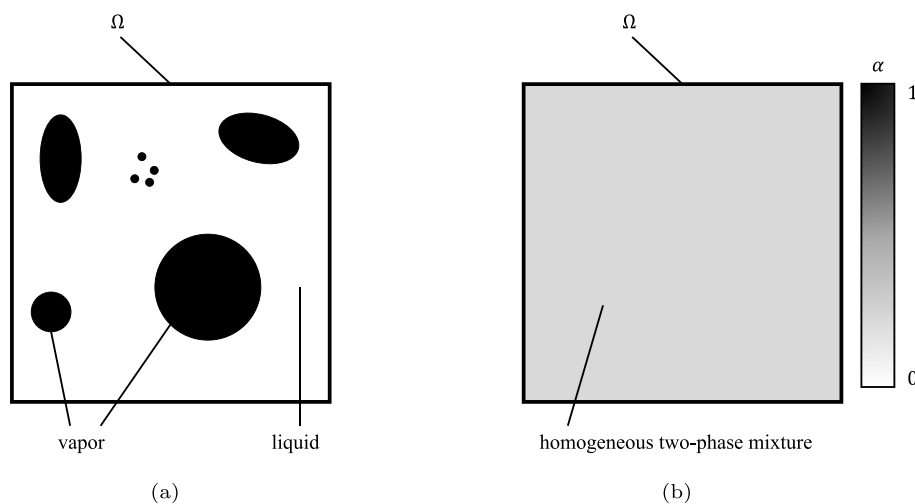


Fig. 2. Single-fluid homogeneous mixture model for a computational cell Ω . (a) Real physical situation. (b) Numerical model approximation with the corresponding vapor volume fraction α .

Table 2
Fluid properties of the barotropic model at $T_{ref} = 293.15K$.

Property	Symbol	Value
Reference temperature	T_{ref}	293.15 K
Density of saturated liquid	$\rho_{l,sat}$	998.16 kg/m ³
Density of saturated vapor	$\rho_{v,sat}$	0.01721 kg/m ³
Saturation pressure	p_{sat}	2339.3 Pa
Dynamic viscosity of saturated liquid	$\mu_{l,sat}$	1.0014×10^{-3} Pa s
Dynamic viscosity of saturated vapor	$\mu_{v,sat}$	9.7275×10^{-6} Pa s
Speed of sound of saturated liquid	$c_{l,sat}$	1482.2 m/s
Speed of sound of saturated vapor	$c_{v,sat}$	423.18 m/s
Specific heat capacity of saturated liquid	$c_{p,l,sat}$	4184.4 J/(kg K)
Specific heat capacity of saturated vapor	$c_{p,v,sat}$	1905.9 J/(kg K)
Latent heat of vaporization	l_v	2453.5×10^3 J/kg

liquid as it would occur in reality is illustrated. Assuming that the discrete cell size is larger than present vapor regions, the corresponding numerical representation resolved by our model would be a homogeneous mixture with the respective vapor volume fraction for a computational cell Ω . To appropriately simulate vapor bubbles during their collapse it is necessary to use a sufficient number of cells to resolve the bubble with sufficient accuracy.

The mixture density for two-phase mixtures calculates to

$$\bar{\rho} = \alpha \rho_{v,sat} + (1 - \alpha) \rho_{l,sat}. \tag{13}$$

Consequently, pure liquid zones and liquid-vapor mixture regions can be determined by means of the vapor volume fraction

$$\alpha = \frac{V_{v,\Omega}}{V_{\Omega}} = \begin{cases} 0, & \text{if } \bar{\rho} \geq \rho_{l,sat} \text{ (pure liquid)} \\ \frac{\rho_{l,sat} - \bar{\rho}}{\rho_{l,sat} - \rho_{v,sat}}, & \text{else (liquid-vapor mixture),} \end{cases} \tag{14}$$

defined as the occupied volume of vapor $V_{v,\Omega}$ within the computational cell. α is calculated by the help of the mixture density $\bar{\rho}$ which is obtained from the explicit time integration of the mass conservation Eq. (5). The flow is assumed to be barotropic, and we employ constant fluid properties at a constant reference temperature of $T_{ref} = 293, 15$ K as listed in Table 2. Equations of state for the liquid phase and the mixture serve as closure of the system of equations. For pure liquid regions, a modified Tait equation of state as introduced by Saurel et al. [36] is used

$$p = B \left[\left(\frac{\rho}{\rho_{l,sat}} \right)^N - 1 \right] + p_{sat}, \tag{15}$$

where $N = 7.15$ and $B = 3.3 \times 10^8$ at the stated reference temperature. The speed of sound for pure liquid is

$$c = \left(\frac{N(p + B)}{\bar{\rho}} \right)^{1/2}. \tag{16}$$

For two-phase mixtures of saturated liquid and vapor we use the isentropic speed of sound definition

$$c^2 = \left. \frac{\partial p}{\partial \rho} \right|_{s=const.} \Rightarrow p(\bar{\rho}) - p_{sat} = \int_{\rho_{l,sat}}^{\bar{\rho}} c^2 d\rho \tag{17}$$

to calculate the mixture pressure by integration. The speed of sound is substituted by the formulation of Franc and Michel [37], which considers the latent heat of vaporization:

$$\frac{1}{\bar{\rho} c^2} = \frac{\alpha}{\rho_{v,sat} c_{v,sat}^2} + \frac{1 - \alpha}{\rho_{l,sat} c_{l,sat}^2} + \frac{((1 - \alpha) \rho_{l,sat} c_{p,l,sat} - \alpha \rho_{v,sat} c_{p,v,sat}) T_{ref}}{(\rho_{v,sat} l_v)^2}. \tag{18}$$

A detailed derivation of the pressure equation is given in Lang et al. [32]. The combination of Tait equation for pure liquid and the aforementioned equation for mixture regions was validated in several studies [42–44] and proved to yield better results than the stiffened gas equation. The solvent viscosity is calculated similarly for pure liquid and mixture regions following the approach of Beattie and Whalley [38]:

$$\mu_s = (1 - \alpha) \left(1 + \frac{5}{2} \alpha \right) \mu_{l,sat} + \alpha \mu_{v,sat}. \tag{19}$$

The viscoelastic viscosity μ_M is assumed to be constant in both pure liquid and mixture regions which is reasonable since the diffusive contribution is scaled by the density accounting for mixture dependent viscous influence, i.e. the high density in liquid regions leads to strong viscous influence and low density in vapor regions corresponds to a weak influence.

2.3. Numerical approach

2.3.1. Discretization

The finite-volume discretization is performed on body-fitted, hexahedral cells with non-staggered cell-centered variables. The governing equations are formulated in Cartesian coordinates. The calculation of cell face fluxes is performed separately for convective and for diffusive fluxes or source terms, respectively. For the convective fluxes a low-Mach number consistent approximate Riemann solver with upwind-biased reconstruction procedure is used. The method combines an AUSM-type (Advection Upstream Splitting Method) based Riemann solver with a MUSCL (Monotone Upstream-Centered Schemes for Conservation Laws) reconstruction with TVD (Total Variation Diminishing) limiters for the numerical calculation of convective fluxes. The numerical flux calculation addresses the velocities and the pressure separately. For the different variables distinct limiter functions are applied. The density is reconstructed with the MinMod limiter [39], the velocities with the Koren limiter [40] and the viscoelastic stresses are reconstructed by applying the weighted essentially non-oscillatory reconstruction procedure (WENO-3) [41]. The numerical flux calculation and reconstruction procedures are described in more detail as *baseline finite-volume scheme* in Egerer et al. [42]. The diffusive flux and the source term are calculated by a second order central reconstruction. Time integration is realized by an explicit second-order accurate low-storage four step Runge-Kutta method with improved stability range. For a detailed description of the algorithm, the reader is referred to Lang et al. [32]. An appropriate timestep criterion with respect to viscoelastic flows is used. The timestep calculation is defined introducing the Courant-Friedrich-Lewy (CFL) number

$$\Delta t = \frac{\text{CFL}}{i_c + i_d}, \tag{20}$$

where $i_c = \frac{1}{\Delta t_c}$ and $i_d = \frac{1}{\Delta t_d}$ represent the inverse convective and diffusive timestep respectively. The convective and diffusive timesteps are limited by the fastest transport mechanism occurring for each computational cell. The convective timestep limitation reads

$$\begin{aligned} \Delta t_c < \frac{1}{i_c} &:= \min \left(\frac{\Delta x_i/n}{\lambda_i^{\max}} \right) \\ &= \min \left(\left[|u_i| + \sqrt{c^2 + \frac{1}{\rho} \left(\frac{4}{3} G + |\tau_{m,ii}| \right)} \right]^{-1} \frac{\Delta x_i}{n} \right), \\ & \quad i = 1, 2, 3, \quad n = 3. \end{aligned} \tag{21}$$

with cell length Δx_i in direction i and $n = 3$ for 3D flow. λ_i^{\max} describes the fastest wave in i -direction taking into account waves introduced by the viscoelastic transport equations. The corresponding wave speeds are obtained by calculating the eigenvalues of the quasi-linear form as described in Appendix B. The diffusive timestep calculation considers diffusion processes in n dimensions. It proved to be suitable to only consider the solvent viscosity for the diffusive limitations, since the viscoelastic influence on the timestep criterion is dominated by convection

$$\Delta t_d < \frac{1}{i_d} := \min \left(\frac{\rho(\Delta x_i/n)^2}{2\mu_s} \right), \quad i = 1, 2, 3, \quad n = 3. \tag{22}$$

The applied Runge-Kutta scheme has been demonstrated to provide stable results up to CFL = 1.5 [43]. We set CFL = 1.4 for all conducted simulations throughout this study. The time step criterion is calculated for every iteration and the smallest time step amongst all cells is taken globally.

2.3.2. Boundary conditions

Boundary conditions are implemented by attaching two-layers of virtual cells, called ghost cells ($|_g$), to the cells of the computational domain ($|_d$) as illustrated in Fig. 3. These ghost-cells contain data for the primitive variables in order to meet the physically correct constraints at the boundary face. In doing so, the variables within the ghost cells are not restricted to physically meaningful values but are defined so as to result in correct reconstructions at the face between the computational domain and the ghost cells. A central reconstruction at the boundary face is used (cf. Appendix C). For the problem as described in Section 3, two different boundary conditions are applied. First, we impose symmetry boundary conditions enabling us to simulate only one eighth of the bubble in order to reduce computational costs. Symmetry boundary conditions for the primitive variables in the ghost cells are

$$\begin{aligned} \nabla p|_{\Gamma_{sym}} \cdot \mathbf{n}|_{\Gamma_{sym}} &= 0 \longrightarrow p|_g = p|_d, \\ \mathbf{u}|_{\Gamma_{sym}} \cdot \mathbf{n}|_{\Gamma_{sym}} &= 0 \longrightarrow \mathbf{u}|_g = \mathbf{u}|_d - 2(\mathbf{u}|_d \cdot \mathbf{n}|_d) \mathbf{n}|_d, \\ \mathbf{t}_t|_{\Gamma_{sym}} &= 0 \longrightarrow \boldsymbol{\tau}_{s/m}|_g = 2(\mathbf{n}|_d \cdot \boldsymbol{\tau}_{s/m}|_d \cdot \mathbf{n}|_d) \mathbf{I} - \boldsymbol{\tau}_{s/m}|_d, \end{aligned} \tag{23}$$

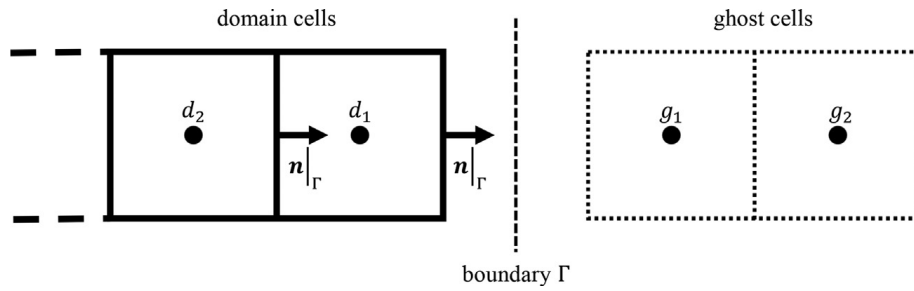


Fig. 3. Computational cells d_1, d_2 and adjacent ghost cells g_1, g_2 separated by the boundary face Γ .

where the left side of \longrightarrow depicts the physical constraint at the boundary face Γ and the right side shows the numerical implementation. $\mathbf{n}|_{\Gamma}$ describes the outward pointing unit normal vector at the boundary. For the pressure a Neumann boundary condition, specifically a zero gradient condition, is imposed. Symmetry requires normal velocities at the boundary to vanish; tangential velocities remain unchanged with respect to values within the domain. The Newtonian and viscoelastic stresses are imposed in a way, that tangential traction $t_t|_{\Gamma_{sym}} = \mathbf{n}_t|_{\Gamma_{sym}} \cdot \boldsymbol{\tau}_{s/m}|_{\Gamma_{sym}} \cdot \mathbf{n}|_{\Gamma_{sym}}$ vanishes, and only normal traction $t_n|_{\Gamma_{sym}} = \mathbf{n}|_{\Gamma_{sym}} \cdot \boldsymbol{\tau}_{s/m}|_{\Gamma_{sym}} \cdot \mathbf{n}|_{\Gamma_{sym}}$ occurs at the symmetry face. $\mathbf{n}_t|_{\Gamma}$ represents an arbitrary tangential unit vector perpendicular to the unit normal vector ($\forall \mathbf{n}_t|_{\Gamma} : \mathbf{n}_t|_{\Gamma} \cdot \mathbf{n}|_{\Gamma} = 0$). Furthermore, it is assumed that normal traction should remain unaltered by the boundary condition. The procedure is applied similarly to solvent $\boldsymbol{\tau}_s$ and viscoelastic stresses $\boldsymbol{\tau}_M$. A detailed derivation of the symmetry conditions for stresses is given in Appendix C. By using the equations of state pressure and density at the symmetry are calculated accordingly.

In the far-field of the vapor bubble the following outflow boundary conditions are used:

$$\begin{aligned}
 p|_{\Gamma_{out}} = p_{out} &\longrightarrow p|_g = p_{out}, \\
 \nabla \mathbf{u}|_{\Gamma_{out}} \cdot \mathbf{n}|_{\Gamma_{out}} = \mathbf{0} &\longrightarrow \mathbf{u}|_g = \mathbf{u}|_d, \\
 \nabla \boldsymbol{\tau}_{s/m}|_{\Gamma_{out}} \cdot \mathbf{n}|_{\Gamma_{out}} = \mathbf{0} &\longrightarrow \boldsymbol{\tau}_{s/m}|_g = \boldsymbol{\tau}_{s/m}|_d.
 \end{aligned} \tag{24}$$

The static pressure at the outlet is specified via a Dirichlet boundary condition realized by setting the pressure within the ghost cells to the specified outlet pressure. Velocities and stresses are assumed to be fully developed, thus zero gradient boundary conditions are used, realized by copying the domain cell values to the ghost cells. The density is again calculated according the pressure and the equations of state.

3. Problem description

Exploiting the spherical symmetry, the simulations are carried out for one eighth of a spherical vapor bubble with an initial radius of $R_0 = 1 \times 10^{-4}$ m as shown in Fig. 4. The computational mesh is divided in a refined cubic subdomain with

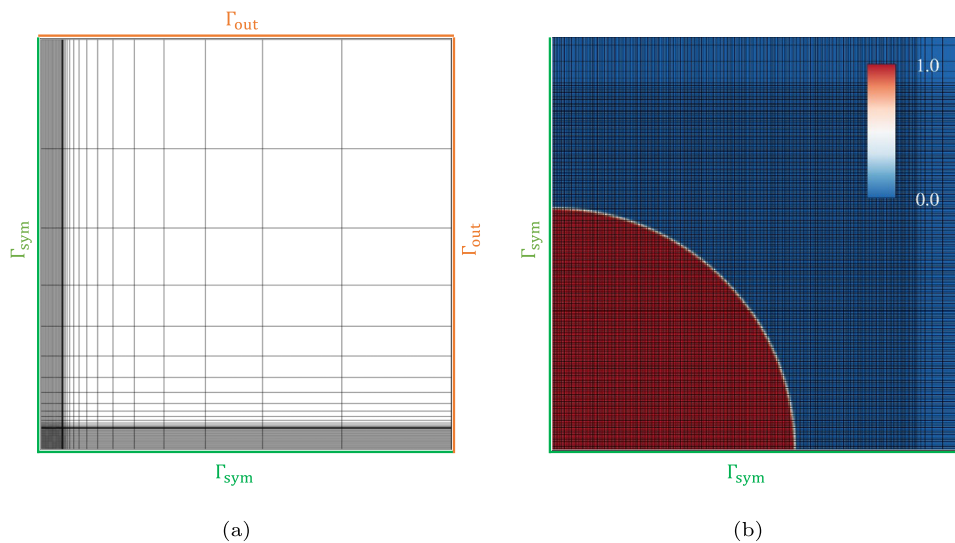


Fig. 4. Numerical setup showing a slice of the x_1/x_2 -plane and the corresponding boundary conditions: (a) Entire computational domain with refined zone and attached coarse mesh (for the refined zone in (a) only every 10th grid line is shown) (b) Closeup of the refined zone with initialized vapor volume fraction $\alpha [-]$ and the computational mesh.

Table 3
Properties of the applied computational meshes.

	Cell size refined zone $\Delta x_1 = \Delta x_2 = \Delta x_3$ [m]	Total number of cells [–]
Coarse mesh	1.0×10^{-6}	$\approx 4.91 \times 10^6$
Reference mesh	7.14×10^{-7}	$\approx 12.17 \times 10^6$
Fine mesh	5.0×10^{-7}	$\approx 32.77 \times 10^6$

an edge length of $1.5 \times R_0$ in every direction and a resolution of $140/R_0$ equidistant finite volumes per initial radius in every direction for the reference case. The applied resolution was chosen upon reviewing Trummler et al. [44], where a resolution of at least $80/R_0$ was suggested for Newtonian collapses and Schmidmayer et al. [45] where it was found, that the resolution influences the sphericity of the bubble during collapse, and simulations with a resolution up to $150/R_0$ were conducted. Other resolutions are used for a mesh study connected with shock wave emission described in Section 4.4. For all remaining simulations the reference mesh is employed. The properties of the different meshes are summarized in Table 3. For the outer part a mesh stretching is applied with an extent of $20 \times R_0$ in every direction. Symmetry boundary conditions are used for the three adjacent planes of the bubble. Outflow boundary conditions with an outlet pressure equal to the surrounding pressure $p_{exit} = p_\infty$ are applied for the far field planes to suppress reflecting waves. The pressure field is initialized with a constant saturated vapor pressure p_{sat} inside the bubble and a constant surrounding pressure $p_\infty = 10 \times 10^5$ Pa resulting in a pressure jump at the bubble interface. The densities are calculated corresponding to the initialized pressure fields and the according equations of state. The whole domain is initialized with fluid at rest $\mathbf{u}_{init} = \mathbf{0}$ and zero viscous and viscoelastic stresses $\boldsymbol{\tau}_{S,init} = \boldsymbol{\tau}_{M,init} = \mathbf{0}$.

The non-dimensional numbers characterizing the viscoelastic bubble collapse are the Reynolds and the Deborah number. The Reynolds number Re relates convective to diffusive momentum transport and is therefore appropriate to characterize the influence of viscosity. The Deborah number De describes the ratio of relaxation time λ to a characteristic flow timescale. For the viscoelastic bubble collapse Re and De are defined as follows

$$Re = \frac{R_0 \sqrt{\rho_{l,sat} \Delta p}}{\mu_0}, \quad De = \frac{\lambda}{R_0} \sqrt{\frac{\Delta p}{\rho_{l,sat}}}, \tag{25}$$

where $\Delta p = p_\infty - p_{sat}$ is the pressure difference of driving and saturation pressure of vapor inside the bubble and $\mu_0 = \mu_S + \mu_M$ is the sum of solvent and Maxwell viscosity. The non-dimensionalized radius r^* reads

$$r^* = \frac{r}{R_0}. \tag{26}$$

Furthermore, β describes the ratio of solvent to total viscosity

$$\beta = \frac{\mu_S}{\mu_0} \tag{27}$$

which is chosen to $\beta = 0.1$ for the applied fluids with solvent contribution.

4. Numerical results and discussion

First, we focus on the kinematics of the spherical bubble collapse. Second, the stress distributions during the viscoelastic bubble collapse as well as the influence of viscosity and elasticity will be discussed. Finally, we compare the collapse and underlying stresses for different viscoelastic models and review shock wave emission caused by viscoelastic bubble collapse. The results are illustrated in spherical coordinates. Since the employed numerical solver internally works with Cartesian coordinates, the quantities in spherical coordinates are obtained by a postprocessing procedure that transforms Cartesian variables to the spherical counterparts simultaneously to the numerical simulation. The position of a point is given by Cartesian (x_1, x_2, x_3) and spherical coordinates (r, ψ, ϑ) by the following transformation

$$\mathbf{r} = \begin{bmatrix} x_1 \\ x_2 \\ x_3 \end{bmatrix} = \begin{bmatrix} r \sin(\psi) \cos(\vartheta) \\ r \sin(\psi) \sin(\vartheta) \\ r \cos(\psi) \end{bmatrix} \tag{28}$$

To obtain physical components of vectors and tensors with respect to the normalized spherical base vectors

$$\mathbf{g}_r = \begin{bmatrix} \sin(\psi) \cos(\vartheta) \\ \sin(\psi) \sin(\vartheta) \\ \cos(\psi) \end{bmatrix}, \quad \mathbf{g}_\psi = \begin{bmatrix} \cos(\psi) \cos(\vartheta) \\ \cos(\psi) \sin(\vartheta) \\ -\sin(\psi) \end{bmatrix}, \quad \mathbf{g}_\vartheta = \begin{bmatrix} -\sin(\vartheta) \\ \cos(\vartheta) \\ 0 \end{bmatrix} \tag{29}$$

the following transformations for vectors of components $[\mathbf{u}]_{x_1, x_2, x_3}$, $[\mathbf{u}]_{r, \psi, \vartheta}$ and matrices of components $[\boldsymbol{\tau}]_{x_1, x_2, x_3}$, $[\boldsymbol{\tau}]_{r, \psi, \vartheta}$ in Cartesian and spherical coordinates, respectively, are applied

$$[\mathbf{u}]_{r, \psi, \vartheta} = [\mathbf{M}]^T \cdot [\mathbf{u}]_{x_1, x_2, x_3}, \quad [\boldsymbol{\tau}]_{r, \psi, \vartheta} = [\mathbf{M}]^T \cdot [\boldsymbol{\tau}]_{x_1, x_2, x_3} \cdot [\mathbf{M}]$$

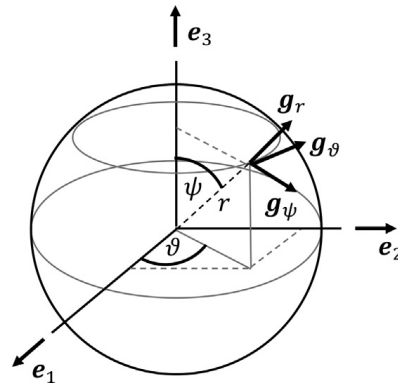


Fig. 5. Correlation of Cartesian and spherical coordinates.

$$[M] = \begin{bmatrix} \sin(\psi)\cos(\vartheta) & \cos(\psi)\cos(\vartheta) & -\sin(\vartheta) \\ \sin(\psi)\sin(\vartheta) & \cos(\psi)\sin(\vartheta) & \cos(\vartheta) \\ \cos(\psi) & -\sin(\psi) & 0 \end{bmatrix} \tag{30}$$

where $[M]$ represents the transformation matrix. The spherical coordinates are chosen as depicted in Fig. 5.

4.1. Kinematics for the spherical viscoelastic bubble collapse

In the following, we review the kinematics of the spherical bubble collapse in terms of radial velocity and deformations. The deformations are investigated considering the collapse for the UCM model and $Re = 1, De = 1$, since this case shows the relevant dynamics for the viscoelastic collapse in general. First, the bubble size and the bubble interface velocity over time are examined in Fig. 6. For comparison, the Newtonian counterpart at the same Reynolds number and the solution of the generalized Keller-Miksis equation with upper convected Maxwell constitutive model is juxtaposed. The bubble in the UCM fluid behaves entirely different compared to the bubble in the Newtonian fluid. For the viscoelastic case a damped oscillatory collapse is observed. The oscillatory behavior can be attributed to relaxation and thus to a delayed viscoelastic stress formation. An initially stronger acceleration and less viscous dissipation allows for subsequent re-expansion of the collapsing bubble as discussed in further detail in Section 4.2. Deviations from the results obtained by solving the Keller-Miksis equation can be attributed to the fact that the Keller-Miksis equation takes into account compressibility only in the far-field, whereas the near-field is treated incompressible as opposed to our simulations where compressibility is considered in the entire field. Furthermore, the Keller-Miksis equation assumes an initial pressure field with a smooth pressure distribution over the interface following the Rayleigh-Plesset equation. Our simulations, however, are initialized with a pressure jump at the interface. Fig. 7 shows the vapor volume fraction for different time instants as indicated in Fig. 6. The initial collapse followed by the re-expansion can clearly be observed.

In Fig. 8 we present the corresponding radial velocity field u_r and the strain rate fields $d_{rr}, d_{\psi\psi}$ for the aforementioned time instants. The diagonal component in $\psi\psi$ -direction is identical to the component in $\vartheta\vartheta$ -direction ($d_{\psi\psi} = d_{\vartheta\vartheta}$) just like

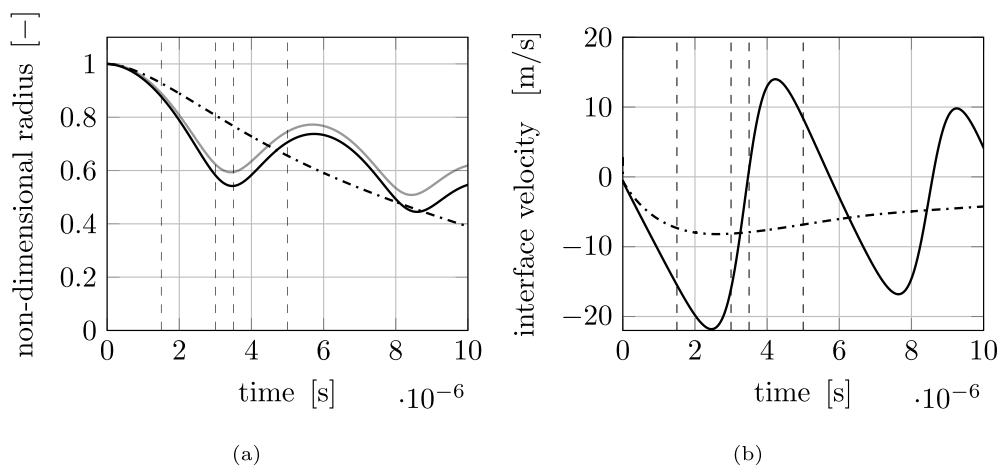


Fig. 6. Bubble collapse in a — UCM and a - - - - Newtonian fluid at $Re = 1, De = 1$. (a) Bubble radius (— shows the solution of the Keller-Miksis equation for UCM) (b) velocity of the interface over time. Dashed vertical lines represent the time instants for the following contour plots Figs. 7 and 8. (Results for bubble radius in (a) as presented in Lang et al. [32]).

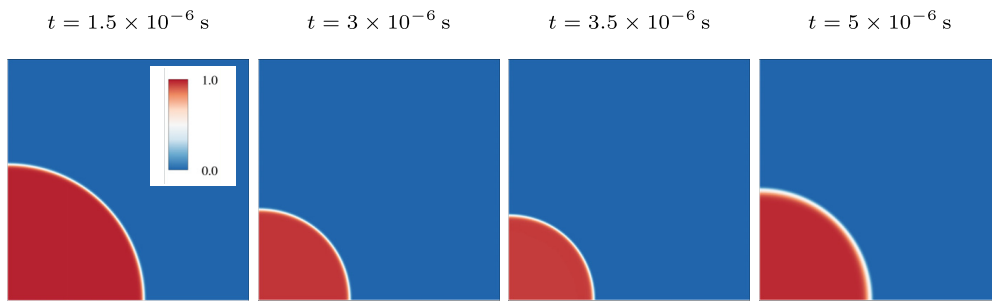


Fig. 7. Vapor volume fraction $\alpha[-]$ for different time instants as indicated in Fig. 6 for the bubble collapse in UCM fluid at $Re = 1, De = 1$.

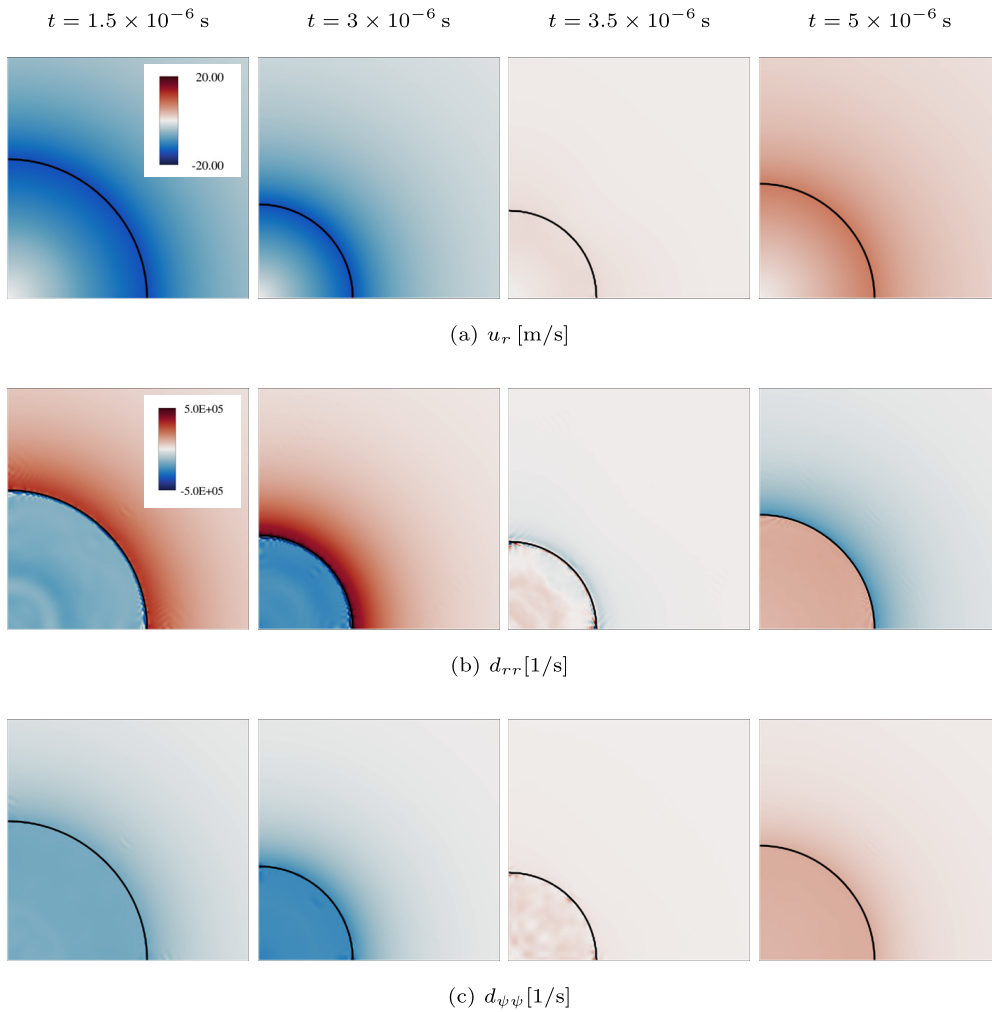


Fig. 8. Bubble collapse for the UCM model at $Re = 1, De = 1$. Contour plots through the midplane of the bubble for different time instants as tagged in Fig. 6. (a) Radial velocity field u_r , Strain rate components (b) d_{rr} and (c) $d_{\psi\psi}$. Black contour represents a vapor volume fraction of $\alpha = 0.01$.

all non-diagonal components are identical amongst themselves ($d_{r\psi} = d_{r\vartheta} = d_{\psi\vartheta}$) due to the spherical symmetry. Furthermore, all off-diagonal components are zero likewise due to spherical symmetry, wherefore those are not illustrated here. It can be observed that the largest strain rates occur close to the bubble surface and decrease with increasing distance. The radial diagonal components of the strain rate d_{rr} are much larger than the diagonal components of the strain rate in circumferential directions $d_{\psi\psi}$.

Next, the radial velocity field and deformation rates are reviewed in more detail as shown in Fig. 9. The spherical bubble collapse is known to lead to pure uniaxial and biaxial extensional flow in the surrounding liquid during the collapse and the re-expansion, respectively. The strain rate tensor $\mathbf{d} = \frac{1}{2}(\mathbf{l} + \mathbf{l}^T)$ can be decomposed into its spherical $\mathbf{d}^{sph} = \frac{1}{3}\text{tr}(\mathbf{d})$ and deviatoric $\mathbf{d}^d = \mathbf{d} - \mathbf{d}^{sph} = \mathbf{d} - \frac{1}{3}\text{tr}(\mathbf{d})\mathbf{I}$ part, accounting for shape and volumetric change, respectively. The resulting strain rate tensor comprises only deviatoric deformations due to the pure extensional deformation. We investigate the radial velocity

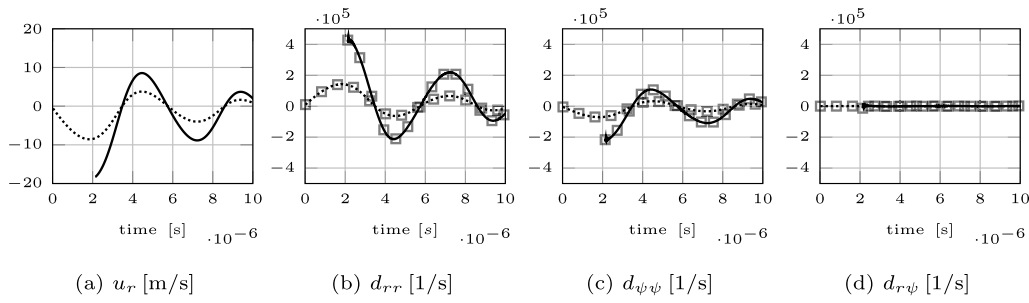


Fig. 9. Temporal evolution of (a) u_r , (b) d_{rr} , (c) $d_{\psi\psi}$, (d) $d_{r\psi}$ for the UCM model at $Re = 1$, $De = 1$ in the surrounding liquid for two positions — $r/R_0 = 0.8$, $r/R_0 = 1.2$. \square deviatoric amount of the respective strain rate component, indicating pure deviatoric strain rates.

and strain rate components over time for two positions in the surrounding liquid ($r/R_0 = \{0.8, 1.2\}$). Note that the plots of the position initially inside the bubble ($r/R_0 = 0.8$) are plotted first for times when the surrounding fluid has reached the point and are thus not plotted from the beginning. It can be observed that only the diagonal components of the deformation rate tensor \mathbf{d} have nonzero entries. Furthermore, we can ascertain that there exist no off-diagonal strain rates $d_{r\psi} = d_{r\vartheta} = d_{\psi\vartheta} = 0$. The deviatoric amounts of the respective strain rates are also depicted, which are identical to the strain rates itself, to emphasize that the motion only comprises deviatoric and no spherical deformation rates $\mathbf{d}^{sph} = \mathbf{0}$. The strain rate tensor hence is identical to its deviatoric part $\mathbf{d} = \mathbf{d}^d$. The uniaxial elongational flow during the compression of the bubble is observed by $d_{rr} = -d_{\psi\psi} - d_{\vartheta\vartheta} = -2d_{\psi\psi}$.

4.2. Viscous and viscoelastic stress distributions and the influence and elasticity

In the following, the viscous and viscoelastic stress distributions are discussed. At first, we compare the UCM-collapse to the Newtonian counterpart at $Re = 1$ and $De = 1$. Fig. 10 shows the strain rate d_{rr} and the corresponding viscoelastic stresses $\tau_{M,rr}$ and its decomposition into the deviatoric $\tau_{M,rr}^d$ and spherical part $\tau_{M,rr}^{sph}$. Furthermore, the corresponding viscous stresses for the Newtonian case $\tau_{S,rr}$ are illustrated. The plots are shown for a time instant right before rebound. For the sake of clarity, we only compare the rr -components in this figure. During the collapse, the balance of driving pressure, inertia forces, compressible damping and viscous or viscoelastic stresses, respectively, determine the collapse dynamics. It can be observed that Newtonian stresses are directly proportional to the deformation rate and the largest stresses occur much closer to the region of maximum deformation, viz. closer to the bubble surface. The Newtonian stresses induce damping such that oscillations are not observed. Looking at the spatial distribution of the viscoelastic stresses in the UCM fluid, opposed to the stresses of the Newtonian case it is observed that the viscoelastic stresses arise with a small detachment

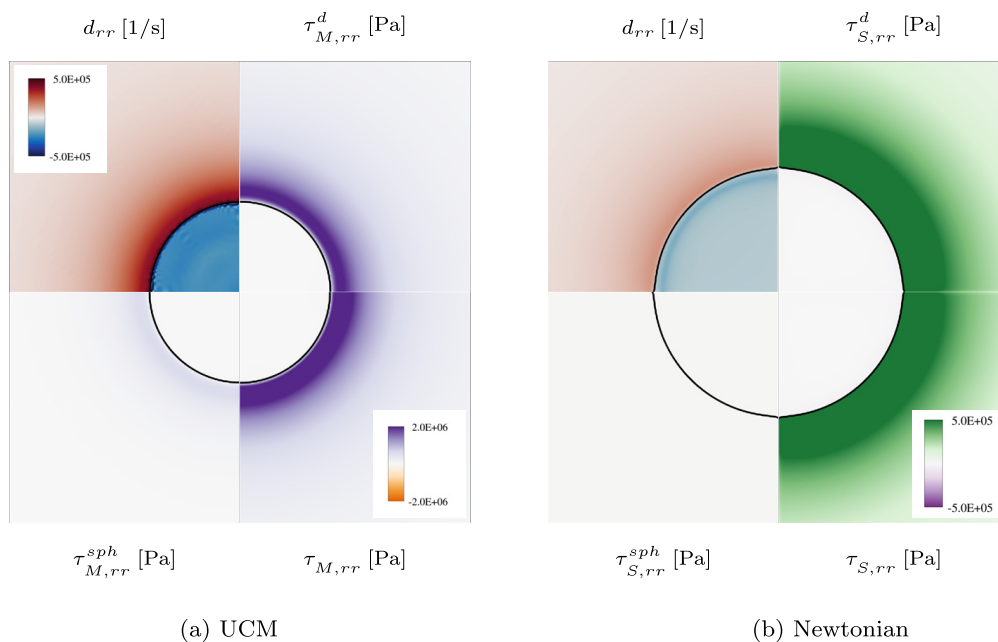
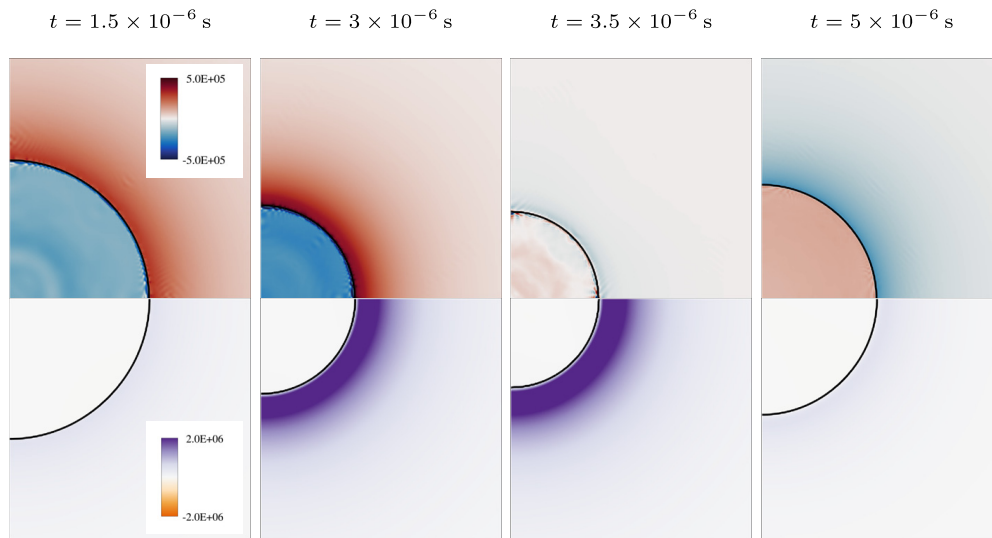


Fig. 10. Contour plots of the strain rate and stress components through the midplane of the bubble for the time instant $t = 3 \times 10^{-6}$ s (immediately before the collapse in the UCM fluid). (a): Viscoelastic collapse for the UCM model at $Re = 1$, $De = 1$. (b): Newtonian collapse at $Re = 1$. Black contour represents a vapor volume fraction of $\alpha = 0.01$.



(a) Top: d_{rr} [1/s], bottom: $\tau_{M,rr}$ [Pa]

Fig. 11. Evolution of Maxwell stresses $\tau_{M,rr}$ and the occurring deformation rates d_{rr} for different time instances during the collapse for the UCM model at $Re = 1$, $De = 1$. Time instances as indicated in Fig. 6.

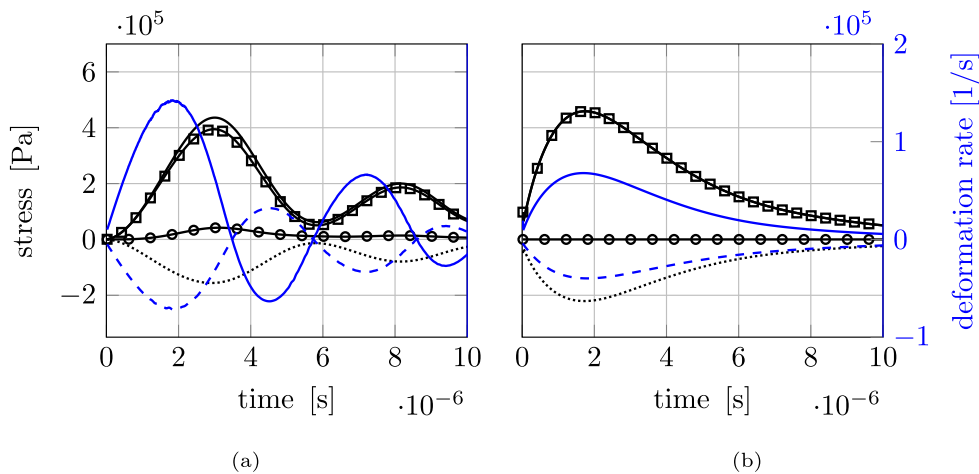


Fig. 12. Stress components over time during the collapse at the position $r/R_0 = 1.2$. (a) For the UCM fluid the viscoelastic stress components — $\tau_{M,rr}$, \dots $\tau_{M,\psi\psi}$, — $\tau_{M,rr}^d$, — $\tau_{M,rr}^{sph}$ and the related deformation rates — d_{rr} , — $d_{\psi\psi}$ at $Re = 1$, $De = 1$ are illustrated. (b) For the Newtonian model the viscous stress components — $\tau_{s,rr}$, \dots $\tau_{s,\psi\psi}$, — $\tau_{s,rr}^d$, — $\tau_{s,rr}^{sph}$ and the corresponding deformation rates — d_{rr} , — $d_{\psi\psi}$ at $Re = 1$ are depicted.

from the interface, whereas the Newtonian stresses appear closer to the interface. This can be traced back to the time-dependent and -delayed stress developed in the viscoelastic case which conversely leads to a spatial displacement. For a better understanding we combine stress and strain rate evolution in Fig. 11. The delayed appearance of viscoelastic stresses is clearly observable, especially for the time instant $t = 3.5 \times 10^{-6}$ s, where the deformation rate is very small, but the viscoelastic stresses are still fairly large. This behavior can also be seen clearly for Maxwell and solvent stresses of the OLD-B model in Section 4.3 (cf. Fig. 15). Furthermore, in the Newtonian case viscous stresses are purely deviatoric since viscous forces are only introduced by the dissipative term $2\mu_S \mathbf{d}^d$. In contrast, the viscoelastic case also shows spherical stresses during the collapse, although the dissipative term in the constitutive equation $2\mu_M \mathbf{d}^d$ also exclusively considers deviatoric deformations. Hence, the spherical stresses are introduced by the transport equation for the Maxwell stresses Eq. (4c) itself. Due to the appearance of spherical stresses it can be concluded that the trace of the stress tensor is likewise nonzero. Viscous and viscoelastic stress components over time for the viscoelastic and the Newtonian case are shown in Fig. 12. For better clarity, we only show the stresses at one position ($r/R_0 = 1.2$) in the surrounding liquid. Off-diagonal elements of the viscoelastic stresses are zero and therefore omitted. Furthermore, spherical symmetry of the underlying problem with $\tau_{M,\psi\psi} = \tau_{M,\vartheta\vartheta}$ is considered. By evaluating the diagonal components of the viscoelastic stresses a nonzero trace of the stress tensor $\text{tr}(\boldsymbol{\tau}_M) = \tau_{M,rr} + \tau_{M,\psi\psi} + \tau_{M,\vartheta\vartheta} = \tau_{M,rr} + 2\tau_{M,\psi\psi} \neq 0$ can be ascertained resulting in nonzero spherical stresses $\tau_{M,rr}^{sph} \neq 0$. There is no consent in literature whether a finite trace formulation of the stress tensor resulting in isotropic stresses should be considered. In Allen and Roy [20], the authors employ a traceless stress tensor formulation for what they call

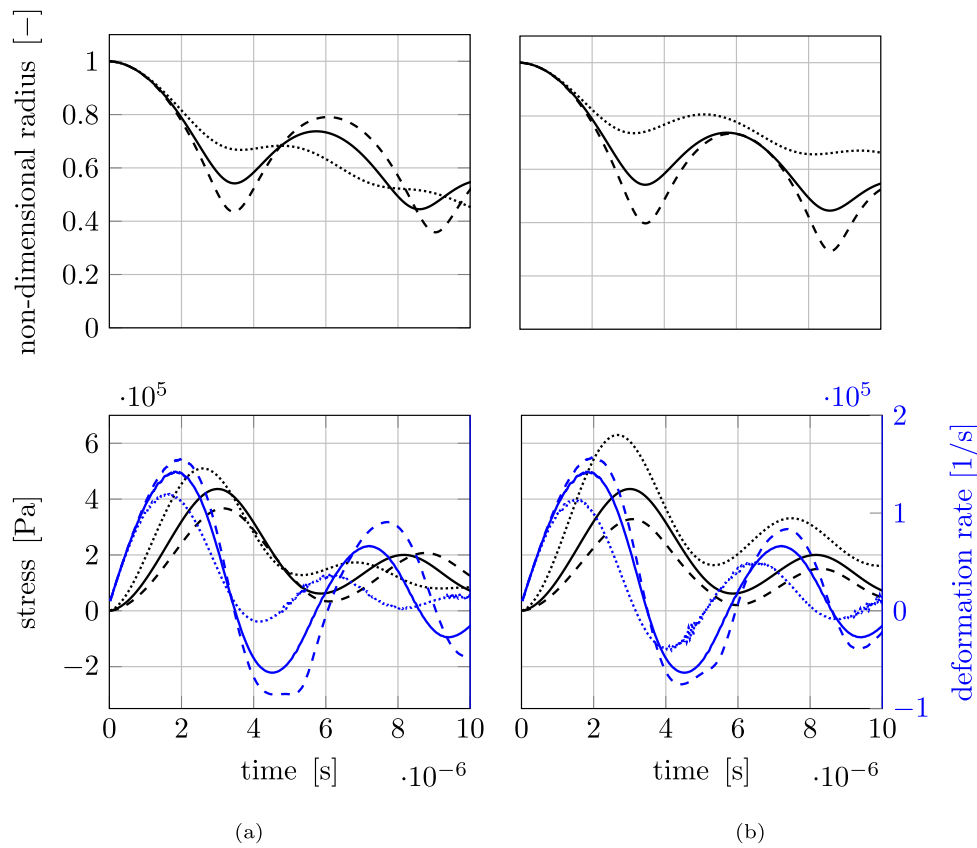


Fig. 13. The reference case $Re = 1, De = 1$ is compared to collapses for variations of elasticity and variations of viscosity. Top: Non-dimensional Radius over time. Bottom: Shear rate d_{rr} (blue) and the corresponding Stress component $\tau_{M,rr}$ (black). (a) Variation of elasticity: \cdots, \cdots, \cdots $Re = 1, De = 0.5$, $\text{---}, \text{---}, \text{---}$ $Re = 1, De = 1$, $\text{---}, \text{---}, \text{---}$ $Re = 1, De = 1.5$. (b) Variation of viscosity: \cdots, \cdots, \cdots $Re = 0.5, De = 1$, $\text{---}, \text{---}, \text{---}$ $Re = 1, De = 1$, $\text{---}, \text{---}, \text{---}$ $Re = 1.5, De = 1$.

linear-viscoelastic problems. For the nonlinear case, they apply a finite trace formulation in Allen and Roy [21]. Hua and Johnsen [27] adopt a traceless stress tensor for their 1D simulations in contrast to Warnez and Johnsen [28] where a general approach without excluding isotropic parts of the stress tensor was utilized. Brujan [12], Dollet et al. [13] explicitly mention that for nonlinear problems with large deformations a finite trace formulation is suitable. By the previously presented results we can show that isotropic stresses are a result of the constitutive (transport) equation and the underlying dynamics. Even for the relatively low Reynolds numbers and the corresponding moderate deformation rates, considerably large spherical stresses emerge.

Furthermore, the Newtonian stresses occur immediately without time delay, whereas viscoelastic stresses are spread over a finite time-interval and show a delayed development due to relaxation. The temporal and spatial distribution of viscoelastic stresses can be traced back to relaxation and convective transport of stresses. First, the viscoelastic stresses do not immediately emerge due to a present deformation rate. With reference to the 1D rheological representation of the UCM model, the series arrangement of dashpot and spring (cf. Fig. 1), the deformation is not directly acting on the dashpot. Instead, the deformation rate initially acts on the spring, and dependent on its stiffness, affects the dashpot with a respective time delay. The Newtonian stresses in contrast are directly proportional to the deformation rate. Furthermore, the constitutive equation of the applied Maxwell-/Oldroyd-type models incorporates convective transport additionally leading to a removal of viscoelastic stresses according to the velocity field. Thus, with further distance from high-velocity regions, the viscoelastic stresses are already smaller compared to the Newtonian stresses, in spite of the time-delayed stress development. Obviously, such effects strongly depend on relaxation time.

Next, we investigate the effect of elasticity and viscosity. In the rheological representation of the UCM model, an increased elasticity corresponds to a softer spring and a delayed stress development. Increased viscosity is associated with a damper with increased resistance. At top of Fig. 13 the bubble radius over time is shown for the UCM model and different values for the elasticity $De = \{0.5, 1, 1.5\}$ and different Reynolds numbers $Re = \{0.5, 1, 1.5\}$. Increasing the elasticity ($Re = 1, De = 1.5$) and thus relaxation time retards stress development and accordingly leads to a faster collapse in the initial stages. The accelerated collapse allows for larger velocity gradients or deformation rates, respectively. Interestingly, although larger deformation rates are observed for increased elasticity, the corresponding viscoelastic stresses are decreased. Increased deformation rates could be explained by the fact, that in case of increased relaxation and hence more delayed and decreased stresses the damping forces are reduced. Accordingly, increasing elasticity results in larger phase-shift between

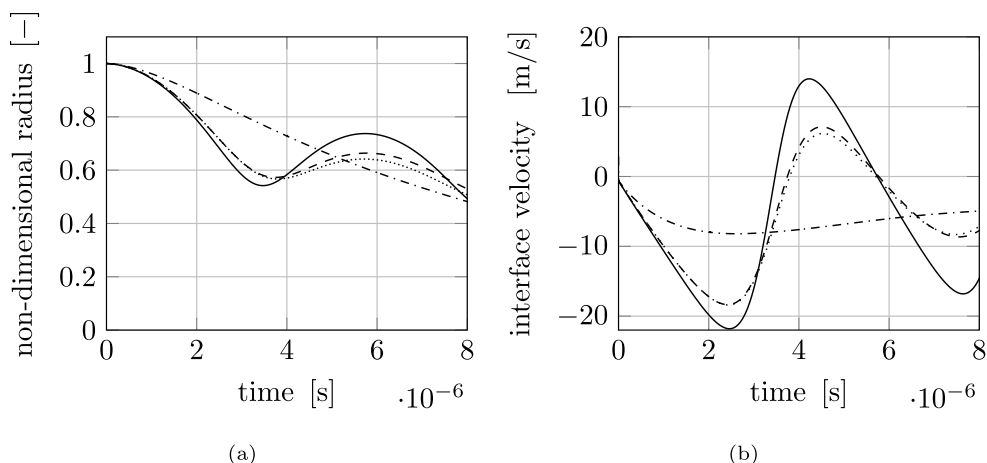


Fig. 14. Comparison of (a) non-dimensional radius and (b) interface velocity over time for the bubble collapse in different viscoelastic fluids at $Re = 1$, $De = 1$. Newtonian fluid \cdots , --- UCM model, -- -- OLD-B model and - · - · - LPTT model. (Results for the bubble radius as presented in Lang et al. [32]).

deformation rate and stress, whereas decreased elasticity ($Re = 1$, $De = 0.5$) leads to decreased phase-shift. The increased elasticity eventually leads to larger rebound radii, too. The influence of decreased viscosity and an increased inertia to viscous force ratio ($Re = 1.5$, $De = 1$) shows an acceleration of the collapse and increased rebound radii. Further increasing elasticity to very high values would result in bubble radius evolutions similar to the inviscid Rayleigh collapse [23]. This is because with further increased relaxation time, the stress development is delayed to such extent that the collapse happens faster than stress counteraction.

Decreasing the Reynolds number ($Re = 0.5$, $De = 1$) and thereby increasing the ratio of viscous to inertia forces leads to decreased deformation rates and increased Maxwell stresses. While increased Maxwell stresses for the case with decreased relaxation ($Re = 1$, $De = 0.5$) ultimately results in smaller rebound radii, increased viscoelastic stresses for decreasing the Reynolds number ($Re = 0.5$, $De = 1$) lead to the opposite effect and result in increased rebound radii. Apparently, the increased restoring forces caused by the stress outweigh the increased dissipation for this case. The comparison of the viscoelastic stresses $\tau_{M,rr}$ together with the corresponding deformation rate d_{rr} (at bottom of Fig. 13) reveals that increasing the elasticity leads to increased retardation of stress formation and changes the magnitude of stresses, whereas decreasing viscosity does not delay the formation of stresses as much but mainly decreases the magnitude of occurring stresses. By comparing the case with the smallest elasticity ($Re = 1$, $De = 0.5$) to the one with the lowest Reynolds number ($Re = 0.5$, $De = 1$) one can ascertain that the deformation rates look very similar. The magnitude of viscoelastic stresses however is much larger for the case with increased viscosity.

4.3. Collapse dynamics for different viscoelastic models

In this section the effect of distinct viscoelastic models on the stress development and distribution, and the correspondent collapse behavior shall be investigated. Firstly, the bubble size and interface velocity versus time is compared for the implemented constitutive models at $Re = 1$, $De = 1$ illustrated in Fig. 14. It can be observed that the collapse is retarded for both cases with solvent contribution (OLD-B and PTT model) compared to the collapse in the UCM fluid. The OLD-B and LPTT are represented by a parallel arrangement of Maxwell element and damper in the 1D rheological analogy. The viscous damper, representing the solvent, reacts without time delay due to an applied shear rate. The retardation of the collapse is caused by the immediate viscous stress which is developed by the Newtonian contribution. Hence, in contrast to the UCM case, where exclusively time-delayed viscoelastic stresses act against the pressure- and inertia-driven collapse, solvent stresses are additionally present without time-delay directly related to the current deformation rate. This leads to slower collapse dynamics and moreover to increased dissipation resulting in smaller rebound radii. By comparing the collapse of the OLD-B with the LPTT fluid, one can observe a faster collapse for the LPTT fluid in the later stages of the initial collapse right before rebound which is induced by the shear-thinning property of the LPTT model introducing an effective Maxwell viscosity that decreases with increasing shear rates. The higher viscoelastic stresses in LPTT can be explained by less viscous damping and result in slightly higher deformation rates in LPTT as presented in Fig. 17. Although the Maxwell viscosity is lower for LPTT fluid and consequently dissipation is decreased, and restoring forces through increased viscoelastic stresses are larger, the rebound radius is smaller than for OLD-B. Apparently, decreased dissipation and increased viscoelastic stresses are overcompensated by higher inertia due to increased acceleration before the rebound in LPTT.

The stress development for different time instants during the collapse and re-expansion is examined for OLD-B model, since it captures the distinct development of viscoelastic and solvent stresses and does not differ qualitatively from the LPTT collapse. In Fig. 15 the viscoelastic and solvent stress distributions are illustrated together with the deformation rate. For clarity, only the rr -component is presented. It is observed that solvent stresses are directly linked to the deformation rate without time delay, whereas the viscoelastic stresses show a delayed development, most evident for time $t = 3.5 \times 10^{-6}$ s,

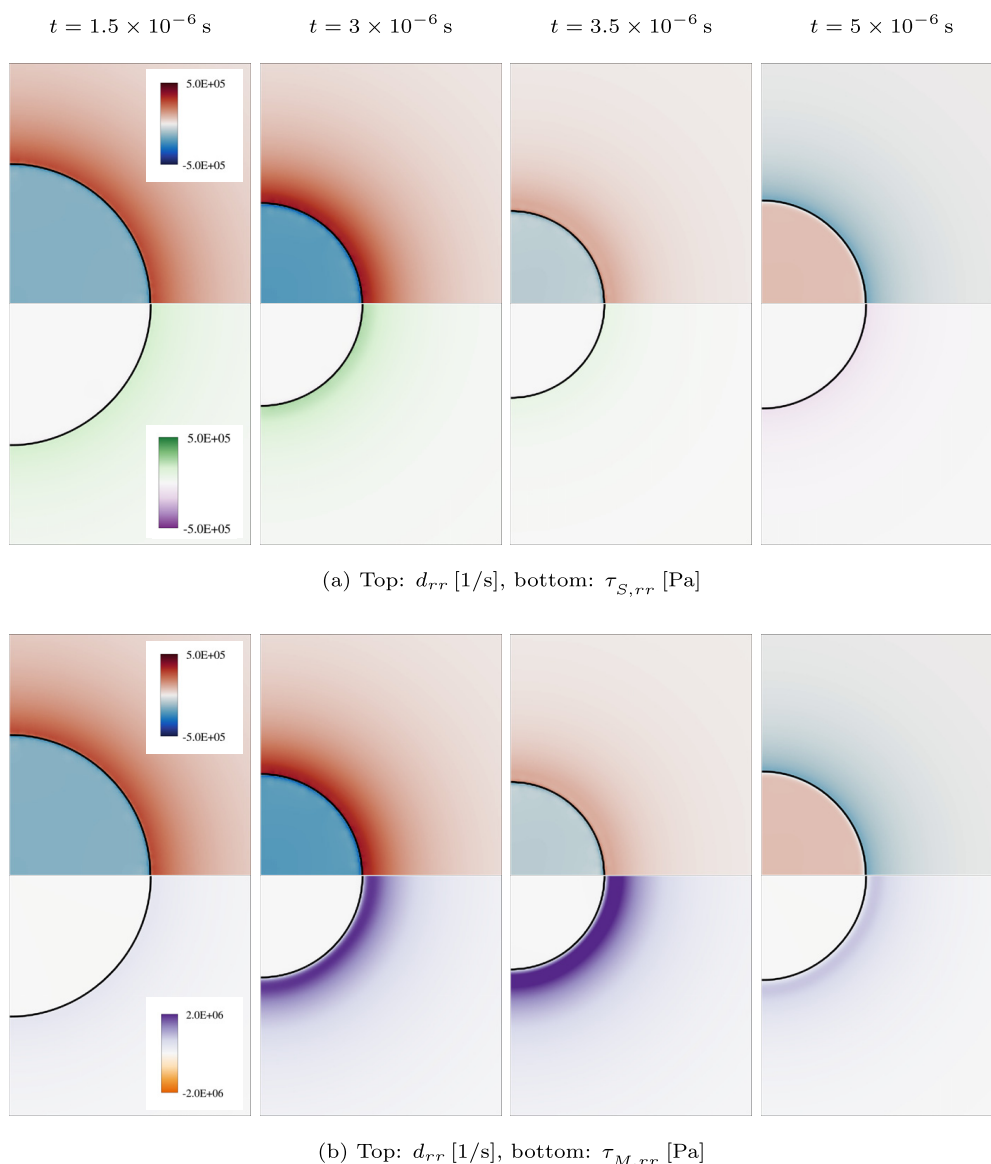


Fig. 15. Development of (a) solvent stresses $\tau_{s,rr}$ and (b) Maxwell stresses $\tau_{M,rr}$ and the occurring deformation rates d_{rr} for different time instances during the collapse for the OLD-B model at $Re = 1$, $De = 1$. Time instances as indicated in Fig. 6.

where the solvent stress is very small as opposed to the viscoelastic stresses. Moreover, one can see that the solvent stresses are directly located at the bubble surface, while viscoelastic stress occurs with a spatial displacement that is caused by the time-delayed development.

Subsequently, the stress fields for the time instant $t = 3 \times 10^{-6}$ s of the Newtonian, UCM, OLD-B and LPTT fluid are directly compared. In Fig. 16 the spatial distribution of the Maxwell stresses $\tau_{M,rr}$ and the solvent stresses $\tau_{s,rr}$ are compared. Naturally, the Newtonian collapse exhibits only solvent stresses and the UCM model only yields Maxwell stresses. Furthermore, it can be seen that the bubble collapse for the OLD-B and LPTT models has not yet progressed as far as for the UCM fluid, which can be explained by the stronger damping of instantly occurring solvent stresses. Additionally, the occurring Maxwell stresses are much smaller for those models with solvent contribution since deformation leads to both viscoelastic and solvent stresses and not exclusively to viscoelastic stresses as for the UCM model. There is no visible difference in the solvent and viscoelastic stress fields for the OLD-B and the LPTT in the contour plot. To get a more detailed insight, we examine the stress evolutions at $r/R_0 = 1.2$ for the different models in Fig. 17. We can again observe, the reduced Maxwell stresses for the models with solvent viscosity compared to the UCM model and the underlying allocation of the total stress in Maxwell and solvent stresses. When comparing OLD-B and LPTT it is observed that the Maxwell stresses are slightly smaller for OLD-B, despite the reduced effective viscosity in LPTT due to shear-thinning. The reduced viscosity apparently leads to an accelerated collapse in LPTT resulting in increased deformation rate which in turn leads to increased viscoelastic stresses. However, increased viscoelastic stresses do not suffice to outweigh the increased acceleration and related larger inertia forces resulting in a smaller rebound radius comparing LPTT to OLD-B. The solvent stresses however, exhibit virtually

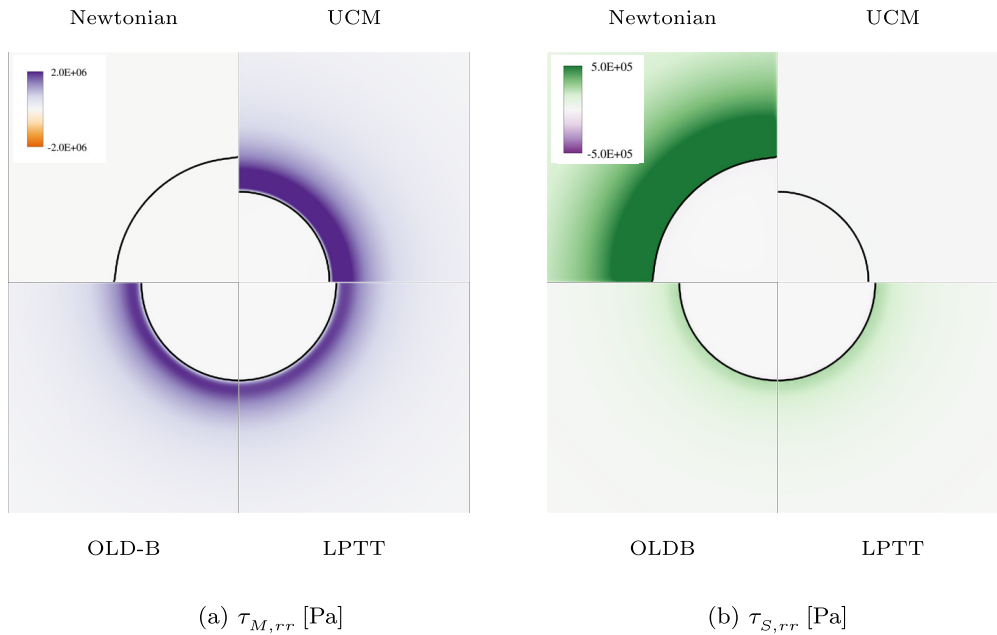


Fig. 16. Contour plots of the stress distributions for the different constitutive models during the bubble collapse through the midplane of the bubble for the time instant as indicated in Fig. 17. (a): Maxwell stress $\tau_{M,rr}$. (b) Solvent stress $\tau_{S,rr}$.

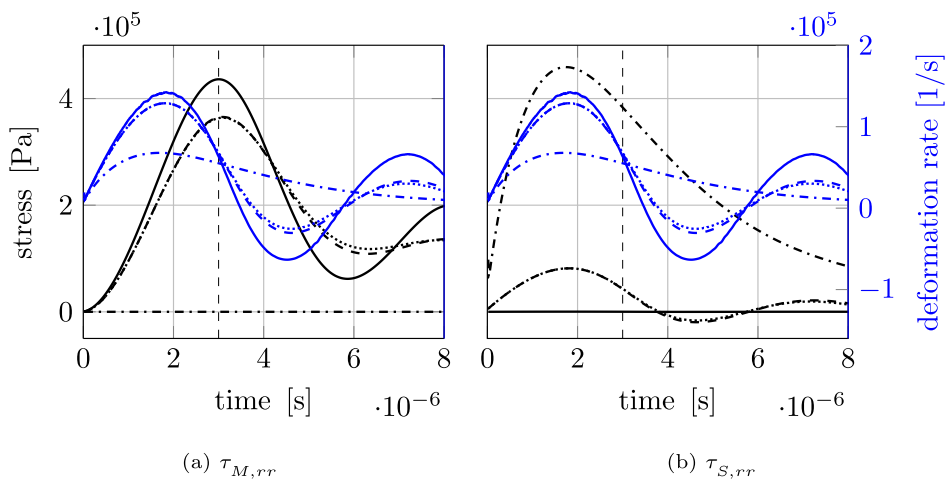


Fig. 17. Stress components and deformation rate at $r/R_0 = 1.2$ over time during the collapse for distinct viscoelastic models at $Re = 1$, $De = 1$. Deformation rate d_{rr} for the $-\cdot-\cdot-$ Newtonian model, $—$ UCM model, $-\cdot-\cdot-$ OLD-B model and the \cdots LPTT model. (a) Maxwell stress $\tau_{M,rr}$, (b) Solvent stress $\tau_{S,rr}$ for the $-\cdot-\cdot-$ Newtonian model, $—$ UCM model, $-\cdot-\cdot-$ OLD-B model and the \cdots LPTT model. Dashed vertical line represents time instant for contour plot Fig. 16.

no differences for these models. Furthermore, one can ascertain the time-delayed occurrence of Maxwell stresses to the strain rates in contrast to the immediate appearance of the Newtonian stresses.

4.4. Shock wave emission for the upper convected Maxwell (UCM) fluid

Finally, shock wave emission due to violent collapse is examined, and grid dependency is reviewed. Lang et al. [32] showed that for increased relaxation times the collapse is accelerated to such an extent that a compression wave is emitted when the bubble completely collapses right before the rebound. In this section, we want to examine whether these waves occur for a physical reason or if they are connected to the computational discretization and depend on the grid resolution. For this purpose, simulations with increased elasticity ($Re = 1$, $De = 3$) are conducted and a variation of the mesh resolution is examined. Schmidmayer et al. [45] showed that the resolution can significantly influence the sphericity of the bubble and investigated resolutions up to $150/R_0$. Apart from the reference resolution of $140/R_0$, the simulations shown in the following are performed on a coarser mesh with a resolution of $100/R_0$ and on a refined mesh with $200/R_0$. At the beginning of the collapse, a rarefaction wave is emitted due to the initial pressure discontinuity at the bubble interface.

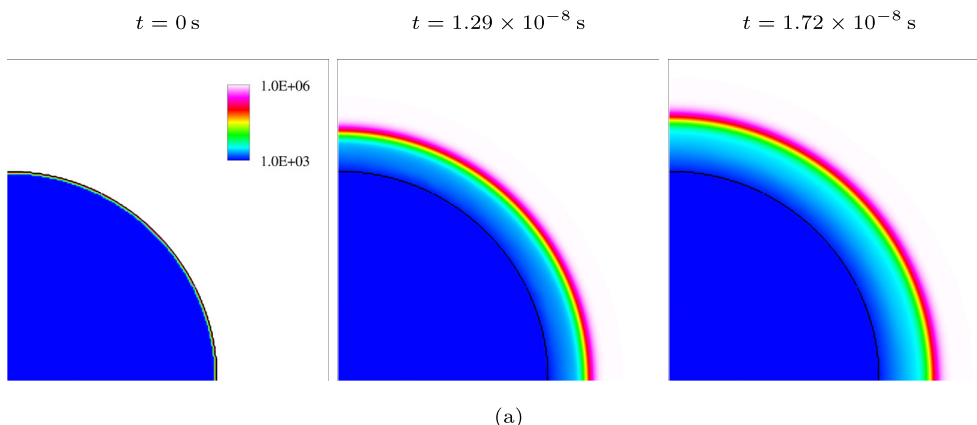


Fig. 18. Shock wave emission at the beginning of the collapse for the UCM model at $Re = 1$, $De = 3$. Contour plots for the pressure p [Pa] through the midplane of the bubble for different time instants. Black contour represents a vapor volume fraction of $\alpha = 0.01$.

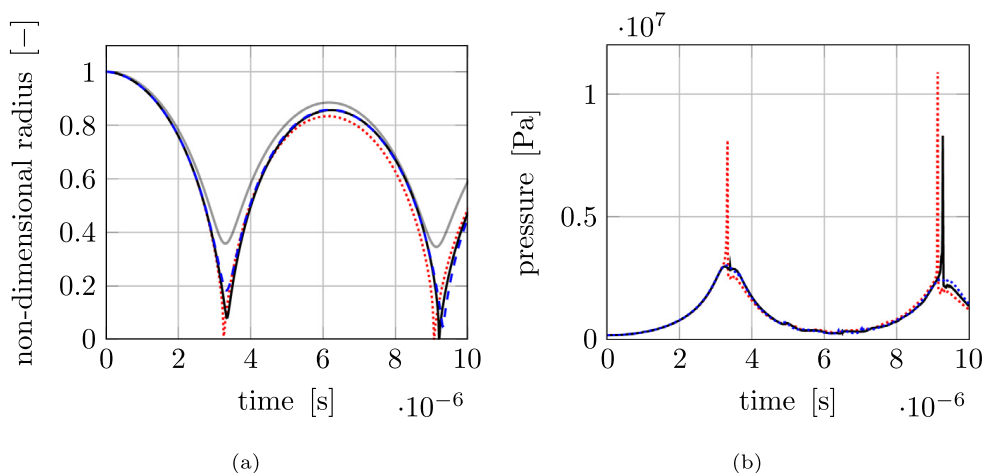


Fig. 19. (a) Radius (— shows the solution of the Keller-Miksis equation) and (b) corresponding pressures at $r/R_0 = 1.2$ over time during the collapse for the UCM model at $Re = 1$, $De = 3$ and three different grid refinements. Resolution in number of cells per initial radius: \cdots 100/ R_0 , — 140/ R_0 , - - 200/ R_0 .

Fig. 18 depicts the pressure distribution during the initial stages, showing the expansion wave emerging from the interface. This pressure wave is much weaker (depicted range $1 \times 10^3 - 1 \times 10^6$ Pa) compared to the emitted shock waves discussed hereafter.

In Fig. 19 the bubble size and the corresponding pressures over time are plotted for the different resolutions. We can ascertain that, at least for given elasticity, shock wave formation depends on grid resolution. For the reference resolution ($140/R_0$) shock wave emission is only visible after the second rebound and follows the preceding complete collapse before the second rebound. At the coarsest resolution ($100/R_0$), the bubble fully collapses before the first and second rebound and consequently shock waves are emitted before the first and the second collapse. The shock wave intensity in terms of the pressure signal is highest for the coarsest grid. For the finest grid ($200/R_0$) neither full collapses nor emitted shock waves are observed. For the investigated cases a pressure wave is only emitted following a complete collapse. We come to the conclusion that for the investigated combination of Reynolds and Deborah number the appearance of a shock wave is related to the grid resolution.

For the coarsest mesh the emitted shock waves following the first and second collapse are visualized by the pressure distributions in Fig. 20. The emission of the shock waves is clearly perceptible by a narrow region of high pressure. The high pressure region has a larger extension following the first collapse compared with the second one. For the visualized timesteps the bubble is already re-expanding. Since, with increasing mesh resolution, our simulations converge towards the result without shock emission, a physically correct shock is not expected for the investigated parameters ($Re = 1$, $De = 3$), and we assume the shock to be generated by underresolved viscoelastic stresses. However, we presume that further increasing elasticity would result in shock wave emission, since the collapse would be accelerated by more delayed stress formation.

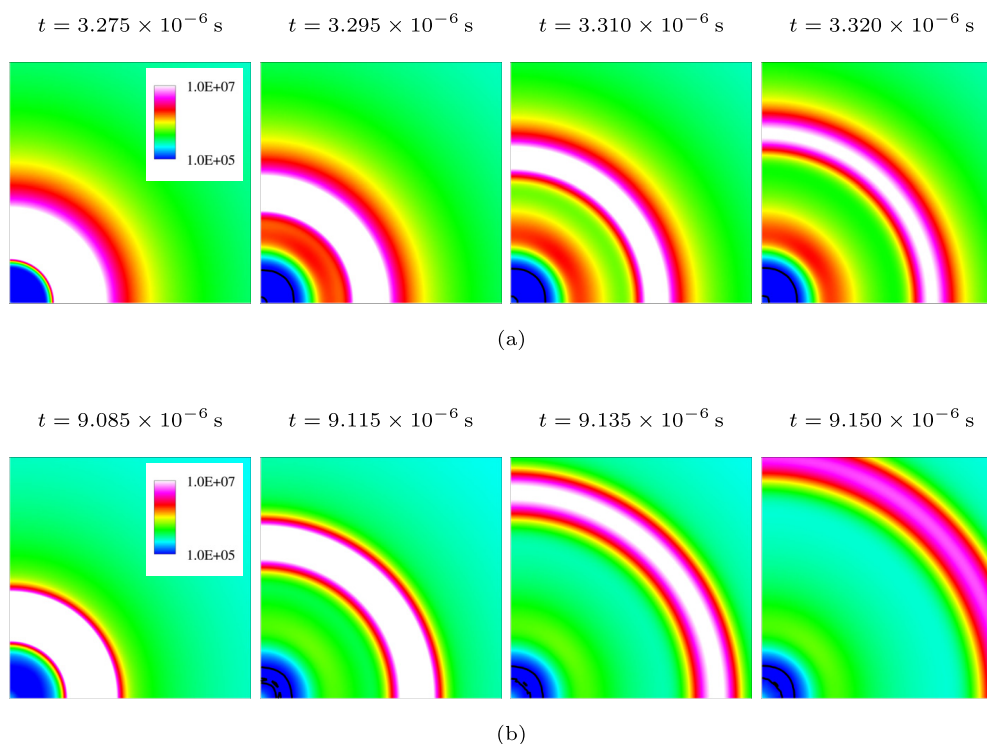


Fig. 20. Shock wave emission during the bubble collapse for the UCM model at $Re = 1$, $De = 3$. Contour plots for the pressure p [Pa] through the midplane of the bubble for different time instants for (a) the first collapse, (b) second collapse. Black contour represents a vapor volume fraction of $\alpha = 0.01$.

5. Concluding remarks

A comprehensive study of spherical vapor bubble collapses under the influence of surrounding viscoelastic fluids was conducted. For that reason 3D simulations of the two-phase flow of compressible vapor bubble collapses were conducted using a density based finite-volume approach with explicit time integration and different viscoelastic constitutive models. A detailed review of the kinematics during the collapse in viscoelastic fluid and the corresponding viscoelastic stress development was investigated for the UCM model which is representative for the other studied viscoelastic models, too. Furthermore, we have examined the impact of elasticity, viscosity and the differences between the UCM, OLD-B and LPTT model. Finally, the capability of resolving emitted shock waves during the collapse was demonstrated. The key findings can be summarized as follows:

- Viscoelasticity affects dynamics of spherical vapor bubble collapse. Compared to the corresponding collapse for a Newtonian fluid at the same Reynolds number, viscoelasticity leads to oscillations during the collapse. These oscillations can not be observed for the Newtonian fluid.
- The development of viscoelastic stresses is fundamentally different from that of solvent stresses. We illustrate that solvent stresses appear without time delay and directly proportional to the field of deformation rate. Viscoelastic stresses, in contrast, develop with a time delay proportional to the elasticity, and exhibit convective transport related to the present flow field.
- The viscoelastic constitutive model introduces isotropic stresses, although the viscoelastic dissipation term ($2\mu_M \mathbf{d}^d$) arises exclusively from the traceless deformation rate. We suggest considering the complete viscoelastic stress tensor in the momentum equations, since otherwise (by excluding the spherical part of the viscoelastic stress tensor), the spherical part introduced through the kinematics of the flow and the material response would be neglected.
- The elasticity or relaxation time, respectively, has a significant impact on the dynamics of the collapse. For the investigated parameters, increasing the elasticity accelerates the collapse in the early stages due to a delayed stress development. Furthermore, the rebound radii increase with increased elasticity since less viscous dissipation acts during the collapse.
- Different viscoelastic models have a distinct influence on the collapse dynamics. Oldroyd-type models with solvent contribution (OLD-B and LPTT model) show a retarded collapse with stronger viscous damping due to the continuously present solvent stresses that occur without time delay. Solvent contribution leads to more viscous dissipation and hence smaller rebound radii. Furthermore, the shear-thinning property of the LPTT fluid leads to an accelerated collapse and increased viscoelastic stresses. However, the increased stresses and the decreased dissipation through decreased effective viscosity are outweighed by increased inertia finally leading to a smaller rebound radius as opposed to the OLD-B model without shear-thinning behavior.

- Simulations with higher elasticities show emission of shock waves to depend on grid resolution. By carrying out simulations with three different meshes, it was demonstrated that the shock wave emission is only visible for coarser mesh resolutions. It was observed, at least for the investigated elasticity, that shock wave emission is related to a complete collapse before rebound. It was demonstrated that the employed approach is capable of resolving shock waves caused by vapor bubble collapses in viscoelastic fluids.

Data availability

Data will be made available on request.

Acknowledgments

The authors gratefully acknowledge the Leibniz Supercomputing Centre for funding this project by providing computing time and support on its Linux-Cluster. The first author is member of the Technical University of Munich (TUM) Graduate School.

Appendix A. Derivation of the Truesdell rate as objective rate of viscoelastic stresses in compressible flows

For the derivation of a consistent objective time derivative in the context of compressible flows it has to fulfill material objectivity (alias material frame invariance) [46] and the yet more restrictive requirement of work conjugacy [47]. To derive a physically consistent time rate, the concept of calculating the Lie derivative modified for compressible flow is applied [48]. First, there shall be a mapping of points from their material (reference) configuration, where \mathbf{X}_0 represents an arbitrary point in the reference configuration, to the current (spatial) configuration. The mapping for the corresponding point in current configuration \mathbf{x} and the current time t reads:

$$\mathbf{x} = \mathbf{x}(\mathbf{X}_0, t). \tag{A.1}$$

The infinitesimal material elements are then mapped by the deformation gradient \mathbf{F}

$$\mathbf{F} := \frac{\partial \mathbf{x}}{\partial \mathbf{X}_0}. \tag{A.2}$$

For an arbitrary second order tensor quantity in current configuration \mathbf{a} and its counterpart in reference configuration \mathbf{A} the pull-back operation

$$\mathbf{A} = \phi^*(\mathbf{a}) := \mathbf{F}^{-1} \mathbf{a} \mathbf{F}^{-T}, \tag{A.3}$$

and the push-forward

$$\mathbf{a} = \phi_*(\mathbf{A}) := \mathbf{F} \mathbf{A} \mathbf{F}^T, \tag{A.4}$$

can be defined. For volume specific second order tensor quantities like the Cauchy stress tensor $\boldsymbol{\sigma}$ and the second Piola-Kirchhoff stress tensor \mathbf{S} pull-back and push-forward are

$$\mathbf{S} = \phi^*(\boldsymbol{\sigma}) := J \mathbf{F}^{-1} \boldsymbol{\sigma} \mathbf{F}^{-T}, \tag{A.5}$$

$$\boldsymbol{\sigma} = \phi_*(\mathbf{S}) := J^{-1} \mathbf{F} \mathbf{S} \mathbf{F}^T, \tag{A.6}$$

referred to as Piola transformation. To derive the proper objective time derivative of the Cauchy stress tensor expressed in the current configuration it is at first pulled back to the initial configuration. The material time derivative $\frac{D(\dots)}{Dt}$ is then applied in reference configuration resulting in a similarly objective field since the reference configuration remains unchanged. Finally, the material derivative of the pulled-back tensor is pushed forward to the current configuration to receive the desired objective rate. This derivative can also be regarded as the Lie derivative of the Cauchy stress tensor with respect to the spatial velocity field $\mathcal{L}_{\mathbf{u}}[\boldsymbol{\sigma}]$ and is often abbreviated with $\overset{\nabla}{\boldsymbol{\sigma}}$. The result

$$\overset{\nabla}{\boldsymbol{\sigma}} = \mathcal{L}_{\mathbf{u}}[\boldsymbol{\sigma}] := \phi_* \left[\frac{D}{Dt} (\phi^*(\boldsymbol{\sigma})) \right] = \frac{D\boldsymbol{\sigma}}{Dt} - \mathbf{l} \cdot \boldsymbol{\sigma} - \boldsymbol{\sigma} \cdot \mathbf{l}^T + \text{tr}(\mathbf{l}) \boldsymbol{\sigma} \tag{A.7}$$

is named the Truesdell rate. Since the Truesdell rate is linear with respect to its argument and the Cauchy stress tensor comprises the sum of pressure, solvent stress tensor and Maxwell stress tensor $\boldsymbol{\sigma} = -p\mathbf{I} + 2\mu_s \mathbf{d}^d + \boldsymbol{\tau}_M$, the Truesdell rate is directly applicable to the Maxwell stress tensor itself:

$$\overset{\nabla}{\boldsymbol{\tau}}_M = \frac{D\boldsymbol{\tau}}_M}{Dt} - \mathbf{l} \cdot \boldsymbol{\tau}_M - \boldsymbol{\tau}_M \cdot \mathbf{l}^T + \text{tr}(\mathbf{l}) \boldsymbol{\tau}_M. \tag{A.8}$$

Appendix B. Quasi-linear 1D formulation for eigenvalue calculation

In order to calculate the linearized wave speeds in the corresponding differential forms of Eqs. (5) to (7) lower order terms on the right-hand sides and viscous contributions ($\mu_s = 0$) are omitted [49]. The resulting equations in x_1 -direction read

$$\begin{aligned}
 \frac{\partial}{\partial t} \rho + \frac{\partial}{\partial x_1} (\rho u_1) &= 0, \\
 \frac{\partial}{\partial t} (\rho u_1) + \frac{\partial}{\partial x_1} (\rho u_1^2 + p - \tau_{M,11}) &= 0, \\
 \frac{\partial}{\partial t} (\rho u_2) + \frac{\partial}{\partial x_1} (\rho u_2 u_1 - \tau_{M,12}) &= 0, \\
 \frac{\partial}{\partial t} (\rho u_3) + \frac{\partial}{\partial x_1} (\rho u_3 u_1 - \tau_{M,13}) &= 0, \\
 \frac{\partial}{\partial t} (\rho \tau_{M,11}) + \frac{\partial}{\partial x_1} (\rho \tau_{M,11} u_1) - \rho \left(\frac{4}{3} G + \tau_{M,11} \right) \frac{\partial u_1}{\partial x_1} &= 0, \\
 \frac{\partial}{\partial t} (\rho \tau_{M,22}) + \frac{\partial}{\partial x_1} (\rho \tau_{M,22} u_1) + \rho \left(\frac{2}{3} G + \tau_{M,22} \right) \frac{\partial u_1}{\partial x_1} - 2\rho \tau_{M,12} \frac{\partial u_2}{\partial x_1} &= 0, \\
 \frac{\partial}{\partial t} (\rho \tau_{M,33}) + \frac{\partial}{\partial x_1} (\rho \tau_{M,33} u_1) + \rho \left(\frac{2}{3} G + \tau_{M,33} \right) \frac{\partial u_1}{\partial x_1} - 2\rho \tau_{M,13} \frac{\partial u_3}{\partial x_1} &= 0, \\
 \frac{\partial}{\partial t} (\rho \tau_{M,12}) + \frac{\partial}{\partial x_1} (\rho \tau_{M,12} u_1) - \rho (G + \tau_{M,11}) \frac{\partial u_2}{\partial x_1} &= 0, \\
 \frac{\partial}{\partial t} (\rho \tau_{M,13}) + \frac{\partial}{\partial x_1} (\rho \tau_{M,13} u_1) - \rho (G + \tau_{M,11}) \frac{\partial u_3}{\partial x_1} &= 0, \\
 \frac{\partial}{\partial t} (\rho \tau_{M,23}) + \frac{\partial}{\partial x_1} (\rho \tau_{M,23} u_1) + \rho \tau_{M,23} \frac{\partial u_1}{\partial x_1} - \rho \tau_{M,13} \frac{\partial u_2}{\partial x_1} - \rho \tau_{M,12} \frac{\partial u_3}{\partial x_1} &= 0.
 \end{aligned} \tag{B.1}$$

The definition of the speed of sound for barotropic flow $c^2 := \left. \frac{\partial p}{\partial \rho} \right|_{s=const.}$ allows for rewriting the equations for primitive variables in quasi-linear form

$$\frac{\partial \mathbf{q}}{\partial t} + \mathbf{A}(\mathbf{q}) \frac{\partial \mathbf{q}}{\partial x_1} = \mathbf{0}, \tag{B.2}$$

with the vector of primitive variables \mathbf{q} and the Jacobian matrix \mathbf{A}

$$\mathbf{q} = \begin{bmatrix} \rho \\ u_1 \\ u_2 \\ u_3 \\ \tau_{M,11} \\ \tau_{M,22} \\ \tau_{M,33} \\ \tau_{M,12} \\ \tau_{M,13} \\ \tau_{M,23} \end{bmatrix}, \quad \mathbf{A}(\mathbf{q}) = \begin{bmatrix} u_1 & \rho & 0 & 0 & 0 & 0 & 0 & 0 & 0 & 0 \\ \frac{c^2}{\rho} & u_1 & 0 & 0 & -\frac{1}{\rho} & 0 & 0 & 0 & 0 & 0 \\ 0 & 0 & u_1 & 0 & 0 & 0 & 0 & -\frac{1}{\rho} & 0 & 0 \\ 0 & 0 & 0 & u_1 & 0 & 0 & 0 & 0 & -\frac{1}{\rho} & 0 \\ 0 & -\frac{4G}{3} - \tau_{M,11} & 0 & 0 & u_1 & 0 & 0 & 0 & 0 & 0 \\ 0 & \frac{2G}{3} + \tau_{M,22} & -2\tau_{M,12} & 0 & 0 & u_1 & 0 & 0 & 0 & 0 \\ 0 & \frac{2G}{3} + \tau_{M,33} & 0 & -2\tau_{M,13} & 0 & 0 & u_1 & 0 & 0 & 0 \\ 0 & 0 & -G - \tau_{M,11} & 0 & 0 & 0 & 0 & u_1 & 0 & 0 \\ 0 & 0 & 0 & -G - \tau_{M,11} & 0 & 0 & 0 & 0 & u_1 & 0 \\ 0 & \tau_{M,23} & -\tau_{M,13} & -\tau_{M,12} & 0 & 0 & 0 & 0 & 0 & u_1 \end{bmatrix}. \tag{B.3}$$

The eigenvalues of \mathbf{A} correlate with the wave speeds in the respective direction used to define the convective timestep criterion Eq. (21).

Appendix C. Derivation of the symmetry boundary condition for the stress tensor

The resultant force at a surface with the outward pointing normal vector \mathbf{n} is calculated to

$$\mathbf{t} := \boldsymbol{\tau} \cdot \mathbf{n} \tag{C.1}$$

where \mathbf{t} represents the traction vector. Vanishing tangential traction at the symmetry face corresponds with

$$\mathbf{t}_t|_{\Gamma_{sym}} := \left(\mathbf{n}_t|_{\Gamma_{sym}} \cdot \boldsymbol{\tau}|_{\Gamma_{sym}} \cdot \mathbf{n}|_{\Gamma_{sym}} \right) = 0, \quad \forall \mathbf{n}_t : \mathbf{n}_t \cdot \mathbf{n} = 0, \tag{C.2}$$

where \mathbf{n}_t represents a tangential vector perpendicular to the outward pointing normal vector \mathbf{n} . To ensure vanishing tangential traction, the conditions for the stress tensor $\boldsymbol{\tau}|_{\Gamma_{sym}}$ and the corresponding traction vector at the boundary face $\mathbf{t}|_{\Gamma_{sym}}$ are imposed with the restriction that exclusively normal traction $t_n|_{\Gamma_{sym}}$ can occur

$$\begin{aligned} \mathbf{t}|_{\Gamma_{sym}} - t_n|_{\Gamma_{sym}} \mathbf{n}|_{\Gamma_{sym}} &= \mathbf{0} \\ \mathbf{t}|_{\Gamma_{sym}} - \left(\mathbf{t}|_{\Gamma_{sym}} \cdot \mathbf{n}|_{\Gamma_{sym}} \right) \mathbf{n}|_{\Gamma_{sym}} &= \mathbf{0}, \\ \Leftrightarrow \mathbf{t}|_{\Gamma_{sym}} &= \left(\mathbf{n}|_{\Gamma_{sym}} \cdot \boldsymbol{\tau}|_{\Gamma_{sym}} \cdot \mathbf{n}|_{\Gamma_{sym}} \right) \mathbf{n}|_{\Gamma_{sym}}. \end{aligned} \quad (C.3)$$

Furthermore, the boundary condition should only suppress tangential traction. The normal traction should remain unaltered by the boundary condition

$$\begin{aligned} t_n|_{\Gamma_{sym}} &= t_n|_d \\ \left(\mathbf{n}|_{\Gamma_{sym}} \cdot \boldsymbol{\tau}|_{\Gamma_{sym}} \cdot \mathbf{n}|_{\Gamma_{sym}} \right) &= \left(\mathbf{n}|_{\Gamma_{sym}} \cdot \boldsymbol{\tau}|_d \cdot \mathbf{n}|_{\Gamma_{sym}} \right). \end{aligned} \quad (C.4)$$

By taking into account the applied central reconstruction at the face

$$\boldsymbol{\tau}|_{\Gamma} = \frac{1}{2} (\boldsymbol{\tau}|_d + \boldsymbol{\tau}|_g), \quad (C.5)$$

the stress tensor formulation in the ghost cells can be derived proceeding from the aforementioned conditions Eqs. (C.3) and (C.4). The equation for the traction vector is rewritten to

$$\mathbf{t}|_{\Gamma_{sym}} = \left(\mathbf{n}|_{\Gamma_{sym}} \cdot \boldsymbol{\tau}|_d \cdot \mathbf{n}|_{\Gamma_{sym}} \right) \mathbf{n}|_{\Gamma_{sym}} = \frac{1}{2} (\boldsymbol{\tau}|_d + \boldsymbol{\tau}|_g) \cdot \mathbf{n}|_{\Gamma_{sym}}. \quad (C.6)$$

A corresponding equation can be formulated to

$$\frac{1}{2} (\boldsymbol{\tau}|_d + \boldsymbol{\tau}|_g) - \left(\mathbf{n}|_{\Gamma_{sym}} \cdot \boldsymbol{\tau}|_d \cdot \mathbf{n}|_{\Gamma_{sym}} \right) \mathbf{I} = \mathbf{0}, \quad (C.7)$$

that allows to calculate an equation for the stress tensor in the ghost cell

$$\boldsymbol{\tau}|_g = 2 \left(\mathbf{n}|_{\Gamma_{sym}} \cdot \boldsymbol{\tau}|_d \cdot \mathbf{n}|_{\Gamma_{sym}} \right) \mathbf{I} - \boldsymbol{\tau}|_d. \quad (C.8)$$

It can be shown that the reconstructed Maxwell stresses from Eq. (C.8) at the symmetry plane fulfills the conditions Eqs. (C.2) to (C.4).

References

- [1] J.J. Choi, K. Selert, F. Vlachos, A. Wong, E.E. Konofagou, Noninvasive and localized neuronal delivery using short ultrasonic pulses and microbubbles, *Proc. Natl. Acad. Sci.* 108 (40) (2011) 16539–16544, doi:10.1073/pnas.1105116108.
- [2] I. Lentacker, I. De Cock, R. Deckers, S.C. De Smedt, C.T. Moonen, Understanding ultrasound induced sonoporation: definitions and underlying mechanisms, *Adv. Drug Deliv. Rev.* 72 (2014) 49–64, doi:10.1016/j.addr.2013.11.008.
- [3] E. Johnsen, T. Colonius, Shock-induced collapse of a gas bubble in shockwave lithotripsy, *J. Acoust. Soc. Am.* 124 (4) (2008) 2011–2020, doi:10.1121/1.2973229.
- [4] E. Vlaisavljevich, K.W. Lin, M.T. Warnez, R. Singh, L. Mancia, A.J. Putnam, E. Johnsen, C. Cain, Z. Xu, Effects of tissue stiffness, ultrasound frequency, and pressure on histotripsy-induced cavitation bubble behavior, *Phys. Med. Biol.* 60 (6) (2015) 2271–2292, doi:10.1088/0031-9155/60/6/2271.
- [5] A.K. Abu-Nab, K.G. Mohamed, A.F. Abu-Bakr, Microcavitation dynamics in viscoelastic tissue during histotripsy process, *J. Phys.: Condens. Matter* 34 (30) (2022) 304005, doi:10.1088/1361-648X/ac6e20.
- [6] M.J. Blomley, J.C. Cooke, E.C. Unger, M.J. Monaghan, D.O. Cosgrove, Science, medicine, and the future: microbubble contrast agents: a new era in ultrasound, *Br. Med. J.* 322 (7296) (2001) 1222–1225, doi:10.1136/bmj.322.7296.1222.
- [7] J.E. Kennedy, High-intensity focused ultrasound in the treatment of solid tumours, *Nat. Rev. Cancer* 5 (4) (2005) 321–327, doi:10.1038/nrc1591. <http://www.nature.com/articles/nrc1591>
- [8] R.K. Bhaskaracharya, S. Kentish, M. Ashokkumar, Selected applications of ultrasonics in food processing, *Food Eng. Rev.* 1 (1) (2009) 31–49, doi:10.1007/s12393-009-9003-7.
- [9] B. Saint-Michel, V. Garbin, Bubble dynamics for broadband microrheology of complex fluids, *Curr. Opin. Colloid Interface Sci.* 50 (2020) 101392, doi:10.1016/j.cocis.2020.101392.
- [10] J. Yang, H.C. Cramer, C. Franck, Extracting non-linear viscoelastic material properties from violently-collapsing cavitation bubbles, *Extreme Mech. Lett.* 39 (2020) 100839, doi:10.1016/j.eml.2020.100839.
- [11] S.L. Everitt, O.G. Harlen, H.J. Wilson, D.J. Read, Bubble dynamics in viscoelastic fluids with application to reacting and non-reacting polymer foams, *J. Nonnewton. Fluid Mech.* 114 (2–3) (2003) 83–107, doi:10.1016/S0377-0257(03)00108-3.
- [12] E.A. Brujan, *Cavitation in Non-Newtonian Fluids*, Springer Berlin Heidelberg, Berlin, Heidelberg, 2011, doi:10.1007/978-3-642-15343-3.
- [13] B. Dollet, P. Marmottant, V. Garbin, Bubble dynamics in soft and biological matter, *Annu. Rev. Fluid Mech.* 51 (2019) 331–355, doi:10.1146/annurev-fluid-010518-040352.
- [14] S.M. Barnett, Bubble motion and mass transfer in non-Newtonian fluids, *AIChE J.* 12 (2) (1957) 253–259.
- [15] V. Ashworth, R. Procter, Cavitation damage in dilute polymer solutions, *Nature* 258 (1975).
- [16] E.A. Brujan, Shock wave emission and cavitation bubble dynamics by femtosecond optical breakdown in polymer solutions, *Ultrason Sonochem.* 58 (March) (2019) 104694, doi:10.1016/j.ultsonch.2019.104694.
- [17] H.S. Fogler, J.D. Goddard, Collapse of spherical cavities in viscoelastic fluids, *Phys. Fluids* 13 (5) (1970) 1135–1141, doi:10.1063/1.1693042.
- [18] I. Tanasawa, W.J. Yang, Dynamic behavior of a gas bubble in viscoelastic liquids, *J. Appl. Phys.* 41 (11) (1970) 4526–4531, doi:10.1063/1.1658491.
- [19] E.A. Brujan, A first-order model for bubble dynamics in a compressible viscoelastic liquid, *J. Nonnewton Fluid Mech.* 84 (1) (1999) 83–103, doi:10.1016/S0377-0257(98)00144-X.

- [20] J.S. Allen, R.A. Roy, Dynamics of gas bubbles in viscoelastic fluids. i. linear viscoelasticity, *J. Acoust. Soc. Am.* 107 (6) (2000) 3167–3178, doi:[10.1121/1.429344](https://doi.org/10.1121/1.429344).
- [21] J.S. Allen, R.A. Roy, Dynamics of gas bubbles in viscoelastic fluids. II. nonlinear viscoelasticity, *J. Acoust. Soc. Am.* 107 (6) (2000) 3167–3178, doi:[10.1121/1.429344](https://doi.org/10.1121/1.429344).
- [22] K. Foteinopoulou, M. Laso, Numerical simulation of bubble dynamics in a phan-Thien-Tanner liquid: non-linear shape and size oscillatory response under periodic pressure, *Ultrasonics* 50 (8) (2010) 758–776, doi:[10.1016/j.ultras.2010.03.002](https://doi.org/10.1016/j.ultras.2010.03.002).
- [23] S.J. Lind, T.N. Phillips, Spherical bubble collapse in viscoelastic fluids, *J. Nonnewton. Fluid Mech.* 165 (1–2) (2010) 56–64, doi:[10.1016/j.jnnfm.2009.09.002](https://doi.org/10.1016/j.jnnfm.2009.09.002).
- [24] S.J. Lind, T.N. Phillips, Bubble collapse in compressible fluids using a spectral element marker particle method. part 2. viscoelastic fluids, *Int. J. Numer. Methods Fluids* 71 (9) (2012) 1103–1130, doi:[10.1002/flid.3701](https://doi.org/10.1002/flid.3701).
- [25] A. Aliabadi, A. Taklifi, The effect of magnetic field on dynamics of gas bubbles in visco-elastic fluids, *Appl. Math. Model.* 36 (6) (2012) 2567–2577, doi:[10.1016/j.apm.2011.09.040](https://doi.org/10.1016/j.apm.2011.09.040).
- [26] D.L. Albernaz, F.R. Cunha, Unsteady motion of a spherical bubble in a complex fluid: mathematical modelling and simulation, *Appl. Math. Model.* 37 (20–21) (2013) 8972–8984, doi:[10.1016/j.apm.2013.03.065](https://doi.org/10.1016/j.apm.2013.03.065).
- [27] J. Hua, E. Johnsen, Nonlinear oscillations following the rayleigh collapse of a gas bubble in a linear viscoelastic (tissue-like) medium, *Phys. Fluids* 25 (8) (2013), doi:[10.1063/1.4817673](https://doi.org/10.1063/1.4817673).
- [28] M.T. Warnez, E. Johnsen, Numerical modeling of bubble dynamics in viscoelastic media with relaxation, *Phys. Fluids* 27 (6) (2015) 1–28, doi:[10.1063/1.4922598](https://doi.org/10.1063/1.4922598).
- [29] Y. Laridon, D. Grenier, D. Houeix, C. Doursat, T. Lucas, D. Flick, Modelling of the growth of a single bubble in semi-hard cheese, with experimental verification and sensitivity analysis, *Appl. Math. Model.* 40 (23–24) (2016) 10771–10782, doi:[10.1016/j.apm.2016.08.018](https://doi.org/10.1016/j.apm.2016.08.018).
- [30] S. Dastjerdi, M. Malikan, B. Akgöz, Ö. Civalek, T. Wiczenbach, V.A. Eremeyev, On the deformation and frequency analyses of SARS-CoV-2 at nanoscale, *Int. J. Eng. Sci.* 170 (October 2021) (2022), doi:[10.1016/j.ijengsci.2021.103604](https://doi.org/10.1016/j.ijengsci.2021.103604).
- [31] F.A. Morrison, *Understanding Rheology*, 2001.
- [32] C. Lang, O. Boolakee, S.J. Schmidt, N.A. Adams, A compressible 3D finite volume approach for the simulation of unsteady viscoelastic cavitating flows, *Int. J. Multiphase Flow* 150 (September 2021) (2022) 103981, doi:[10.1016/j.ijmultiphaseflow.2022.103981](https://doi.org/10.1016/j.ijmultiphaseflow.2022.103981).
- [33] R.G. Owens, T.N. Phillips, *Computational rheology*, 2002, doi:[10.1142/9781860949425](https://doi.org/10.1142/9781860949425).
- [34] J.G. Oldroyd, An approach to non-newtonian fluid mechanics, *J. Nonnewton Fluid Mech.* 14 (1984) 9–46, doi:[10.1016/0377-0257\(84\)80035-x](https://doi.org/10.1016/0377-0257(84)80035-x).
- [35] N. Phan-Thien, R.I. Tanner, A new constitutive equation derived from network theory, *J. Nonnewton Fluid Mech.* 2 (4) (1977) 353–365, doi:[10.1016/0377-0257\(77\)80021-9](https://doi.org/10.1016/0377-0257(77)80021-9).
- [36] R. Saurel, J.P. Cocchi, P.B. Butler, Numerical study of cavitation in the wake of a hypervelocity underwater projectile, *J. Propul. Power* 15 (4) (1999) 513–522, doi:[10.2514/2.5473](https://doi.org/10.2514/2.5473).
- [37] J.-P. Franc, J.-M. Michel, *Fundamentals of Cavitation, Fluid Mechanics and Its Applications*, volume 76, Kluwer Academic Publishers, Dordrecht, 2005, doi:[10.1007/1-4020-2233-6](https://doi.org/10.1007/1-4020-2233-6).
- [38] D. Beattie, P. Whalley, A simple two-phase frictional pressure drop calculation method, *Int. J. Multiphase Flow* 8 (1) (1982) 83–87, doi:[10.1016/0301-9322\(82\)90009-X](https://doi.org/10.1016/0301-9322(82)90009-X).
- [39] P. Roe, Characteristic-Based schemes for the euler equations, *Annu. Rev. Fluid Mech.* 18 (1) (1986) 337–365, doi:[10.1146/annurev.fluid.18.1.337](https://doi.org/10.1146/annurev.fluid.18.1.337).
- [40] B. Koren, A robust upwind discretization method for advection, diffusion and source terms, *Numer. Method. Advect.-Diffus. Probl.* 45 (c) (1993) 117–138.
- [41] G.S. Jiang, C.W. Shu, Efficient implementation of weighted ENO schemes, *J. Comput. Phys.* 126 (1) (1996) 202–228, doi:[10.1006/jcph.1996.0130](https://doi.org/10.1006/jcph.1996.0130).
- [42] C.P. Egerer, S.J. Schmidt, S. Hickel, N.A. Adams, Efficient implicit LES method for the simulation of turbulent cavitating flows, *J. Comput. Phys.* 316 (2016) 453–469, doi:[10.1016/j.jcp.2016.04.021](https://doi.org/10.1016/j.jcp.2016.04.021).
- [43] S.J. Schmidt, *A Low Mach Number Consistent Compressible Approach for Simulation of Cavitating Flow*, Technical University of Munich, 2015 Ph.D. thesis.
- [44] T. Trummler, S.J. Schmidt, N.A. Adams, Numerical investigation of non-condensable gas effect on vapor bubble collapse, *Phys. Fluids* 33 (9) (2021), doi:[10.1063/5.0062399](https://doi.org/10.1063/5.0062399).
- [45] K. Schmidmayer, S.H. Bryngelson, T. Colonius, An assessment of multicomponent flow models and interface capturing schemes for spherical bubble dynamics, *J. Comput. Phys.* 402 (2020) 109080, doi:[10.1016/j.jcp.2019.109080](https://doi.org/10.1016/j.jcp.2019.109080).
- [46] C. Truesdell, W. Noll, *The non-Linear field theories of mechanics*, 2004.
- [47] W. Ji, A.M. Waas, Z.P. Bazant, On the importance of work-conjugacy and objective stress rates in finite deformation incremental finite element analysis, *J. Appl. Mech. Trans. ASME* 80 (4) (2013) 1–9, doi:[10.1115/1.4007828](https://doi.org/10.1115/1.4007828).
- [48] P.M. Pinsky, M. Ortiz, K.S. Pister, Numerical integration of rate constitutive equations in finite deformation analysis, *Comput. Methods Appl. Mech. Eng.* 40 (2) (1983) 137–158, doi:[10.1016/0045-7825\(83\)90087-7](https://doi.org/10.1016/0045-7825(83)90087-7).
- [49] M. Rodriguez, E. Johnsen, A high-order accurate five-equations compressible multiphase approach for viscoelastic fluids and solids with relaxation and elasticity, *J. Comput. Phys.* 379 (2019) 70–90, doi:[10.1016/j.jcp.2018.10.035](https://doi.org/10.1016/j.jcp.2018.10.035).

A.3 Viscoelastic vapor bubble collapse near solid walls and corresponding shock wave formation

(Reproduced from [74], with the permission of AIP Publishing)

Permission to Reuse Content

Reusing AIP Publishing Content

Permission from AIP Publishing is required to:

- republish content (e.g., excerpts, figures, tables) if you are not the author
- modify, adapt, or redraw materials for another publication
- systematically reproduce content
- store or distribute content electronically
- copy content for promotional purposes

Authors do **not** need permission from AIP Publishing to:

- quote from a publication (please include the material in quotation marks and provide the customary acknowledgment of the source)
- reuse any materials that are licensed under a Creative Commons CC BY license (please format your credit line: "Author names, Journal Titles, Vol.#, Article ID#, Year of Publication; licensed under a Creative Commons Attribution (CC BY) license.")
- reuse your own AIP Publishing article in your thesis or dissertation (please format your credit line: "Reproduced from [FULL CITATION], with the permission of AIP Publishing")
- reuse content that appears in an AIP Publishing journal for republication in another AIP Publishing journal (please format your credit line: "Reproduced from [FULL CITATION], with the permission of AIP Publishing")
- make multiple copies of articles—although you must contact the Copyright Clearance Center (CCC) at www.copyright.com (<https://www.copyright.com>) to do this

To request permission to reuse AIP Publishing content, use RightsLink® for the fastest response.

For RightsLink, navigate to the article you wish to license at <https://pubs.aip.org> (<https://pubs.aip.org>), and click on the Reprints and Permissions link under the TOOLS tab. (For assistance click the "Help" button in the top right corner of the RightsLink page.)

To send a permission request to rights@aip.org (<mailto:rights@aip.org>), please include the following:

- Citation information for the article containing the material you wish to reuse
- A description of the material you wish to reuse, including figure and/or table numbers
- The title, authors, name of the publisher, and expected publication date of the new work
- The format(s) the new work will appear in (e.g., print, electronic, CD-ROM)
- How the new work will be distributed and whether it will be offered for sale

Reusing Content Published by Others

To request another publisher's permission to reuse material in AIP Publishing articles, please use our Reuse of Previously Published Material form. (We require documented permission for all reused content.)

Reuse of Previously Published Material Form (pdf (https://publishing.aip.org/wp-content/uploads/AIP_Permission_Form-1.pdf))

Unless the publisher requires a specific credit line, please format yours like this:

Reproduced with permission from J. Org. Chem. 63, 99 (1998). Copyright 1998, American Chemical Society.

You do not need permission to reuse material in the public domain, but you should still include an appropriate credit line which cites the original source.

AIP PUBLISHING

1305 Walt Whitman Road,
Suite 110
Melville, NY 11747
(516) 576-2200

Resources

Researchers
Librarians
Publishing Partners
Commercial Partners



About

[About Us](#)
[Careers](#)
[Events](#)
[Leadership](#)





Support

[Contact Us](#)
[Terms Of Use](#)
[Privacy Policy](#)

© 2023 AIP Publishing LLC

RESEARCH ARTICLE | JANUARY 11 2024

Viscoelastic vapor bubble collapse near solid walls and corresponding shock wave formation

Christian Lang  ; Stefan Adami ; Nikolaus A. Adams 

 Check for updates

Physics of Fluids 36, 013110 (2024)




<https://doi.org/10.1063/5.0175807>


View
Online


Export
Citation

CrossMark

**International Journal
of Fluid Engineering**
国际流体工程

   AIP
Publishing

No Article Processing Charges (APCs)
Diamond Open Access

Viscoelastic vapor bubble collapse near solid walls and corresponding shock wave formation

Cite as: Phys. Fluids **36**, 013110 (2023); doi: [10.1063/5.0175807](https://doi.org/10.1063/5.0175807)

Submitted: 8 September 2023 · Accepted: 24 November 2023 ·

Published Online: 11 January 2024



View Online



Export Citation



CrossMark

Christian Lang,^{1,a)}  Stefan Adami,²  and Nikolaus A. Adams^{1,2} 

AFFILIATIONS

¹Technical University of Munich, TUM School of Engineering and Design, Chair of Aerodynamics and Fluid Mechanics, Boltzmannstr. 15, Garching bei München 85748, Germany

²Munich Institute of Integrated Materials, Energy and Process Engineering (MEP), Technical University of Munich, 85748 Garching bei München, Germany

^{a)}Author to whom correspondence should be addressed: c.lang@tum.de. URL: <https://www.epc.ed.tum.de/en/aer/home/>

ABSTRACT

This study investigates the influence of viscoelasticity on the collapse of aspherical vapor bubbles near a solid boundary through numerical simulations. A fully compressible three-dimensional finite volume method is employed, incorporating a single-fluid homogeneous mixture cavitation model and the simplified linear Phan-Thien Tanner viscoelastic constitutive model. The collapse dynamics, liquid jetting, shock wave formation, and associated pressure impact are analyzed, and the viscous and viscoelastic stress fields are presented. A comparison of viscoelastic to Newtonian dynamics reveals significant differences in collapse behavior and shock wave formation due to viscoelasticity. Viscoelasticity can induce jet piercing, which is not observed in the Newtonian collapse, and increases vapor re-evaporation after the first collapse. The effect of changing the initial standoff distance is examined for both viscoelastic and Newtonian fluids, where a second jet formation is present only for the viscoelastic collapse, and the second collapse's intensity is increased due to increased vapor production during rebound. Additionally, the variation of elasticity in the viscoelastic case demonstrates a correlation between the amount of vapor produced during rebound and the relaxation time for the investigated cases.

© 2023 Author(s). All article content, except where otherwise noted, is licensed under a Creative Commons Attribution (CC BY) license (<http://creativecommons.org/licenses/by/4.0/>). <https://doi.org/10.1063/5.0175807>

I. INTRODUCTION

The dynamics of aspherical bubbles near rigid walls and their potential impact on the wall, including shock wave and jet formation, are crucial in various applications involving non-Newtonian fluids. Especially in biomedical applications, where the addressed materials often show a complex microstructure, cavitating bubble collapse is of significant importance. In sonoporation, the collapse of microbubbles close to a surface of a cell, the resulting liquid jet and shock wave emission are capable of producing large forces and perforating the cell membrane.^{1,2} Drug-carrying microbubbles can be utilized together with focused ultrasound to interrupt the blood-brain barrier and deliver drugs targeted into brain tumors.³ Ultrasound and aspherical cavitating microbubbles can also be used for gene delivery by penetrating tissue.⁴ Shockwave lithotripsy also relies on aspherical bubble collapse to destroy kidney stones.⁵

Experiments proved that viscoelasticity has a significant impact on the collapse dynamics in the vicinity of a wall. Chahine and

Fruman⁶ found with their experiments that polymer additives can inhibit liquid-jet formation during the collapse of spark-generated bubbles in the vicinity of a rigid wall. Brujan *et al.*⁷ examined the collapse of ultrasound-induced bubbles close to a rigid wall experimentally with the result that polymer additives can decrease the velocity of the liquid-jet. However, most numerical studies either neglect viscous forces^{8–20} or consider Newtonian fluids.^{21–32} Only a few numerical studies have considered non-Newtonian media for the wall-influenced aspherical bubble collapse.

One of the first numerical studies by Hara and Schowalter³³ revealed that viscoelastic effects are more substantial for the aspherical than for the spherical bubble collapse by applying a modified Rayleigh–Plesset equation. For the numerical simulation of bubble dynamics close to solid walls, the boundary element method (BEM) is frequently employed. The classical BEM assumes the flow field to be irrotational and incompressible to describe the flow by a potential function. Viscous forces, hence, are only incorporated through the dynamic boundary condition at the interface, and stresses in the

remaining field are neglected. For high Reynolds number flows, where inertia is dominant and viscous forces are negligible, an irrotational flow field assumption can be appropriate. Furthermore, in the classical BEM two coinciding points or a doubly connected domain, respectively, would lead to a singularity. Thus, the simulation would fail as soon as a liquid jet pierces through the bubble, producing a toroid-shaped bubble. To overcome this limitation, methods have been developed to resolve the occurrence of fluid jets and associated toroidal bubbles. Different modifications, such as vortex-cut methods^{10,34} and vortex-ring methods,^{35,36} enable the BEM to resolve toroidal bubbles and doubly connected domains. A comprehensive comparison of the methods is provided in Han *et al.*³⁷ Lind and Phillips³⁸ use the boundary element method (BEM) to investigate the near-wall collapse of gas-filled bubbles. They consider incompressible and irrotational flow. Thus, stresses are only incorporated at the interface. The viscoelastic Maxwell model without a solvent contribution together with the material derivative as time derivative for the stress tensor is applied.^{33,38} come to the conclusion that viscoelasticity can inhibit jet formation. However, it is found in Lind and Phillips,^{23,38} that jet suppression also can be observed for highly viscous fluids with identical Newtonian viscosity. To consider viscous and viscoelastic stresses in the entire field Lind and Phillips³⁹ employ the more elaborate marker particle method together with spectral element discretization. In addition to not being restricted to irrotational flows, they account for compressibility and use a compressible Oldroyd-B model with objective rate and thus consider solvent contributions in the viscoelastic constitutive model. In both studies, the simulations are 2D, and a gas bubble is considered. Thus, evaporation and condensation are neglected. Walters and Phillips⁴⁰ introduce a singularity-free formulation of the BEM to simulate toroid-shaped bubbles and liquid jet formation. Due to the required velocity potential, incompressibility and an irrotational velocity field are assumed. Thus, stresses are likewise only introduced at the bubble interface and neglected in the remaining field. Viscoelasticity is described by the Oldroyd-B model, incorporating solvent contributions and the upper convected derivative for the viscoelastic stress tensor. The authors explain that the approach is restricted to moderate to high Reynolds number flows. Other recent numerical studies involving viscoelastic bubble dynamics investigate microbubbles in a corner geometry,⁴¹ and rising bubbles in viscoelastic fluid,⁴² respectively.

In the present study, we conduct fully compressible three-dimensional (3D) simulations for two-phase cavitating flows considering condensation and evaporation. The density-based approach⁴³ uses finite volume discretization and explicit time integration. The simplified linear Phan-Thien Tanner (LPTT) model is used to describe viscoelasticity. This viscoelasticity model is of the Maxwell-/Oldroyd-type, comprising a Newtonian (solvent) and a viscoelastic contribution. The method naturally considers viscoelastic stresses in the whole domain filled by the liquid and not only at the bubble interface. Opposed to the studies mentioned above, we consider vapor-filled bubbles in the present simulations, and jet formation and impingement on the rigid wall are resolved. Furthermore, the approach fully resolves wave dynamics throughout the collapse.

The article is structured as follows: In the subsequent Sec. II, the model and its governing equations and the numerical approach is introduced. Subsequently, Sec. III describes the setup, including

boundary conditions and the non-dimensionalized numbers characterizing the problem. Simulation results are presented in Sec. IV, starting with comparing the general dynamics in Newtonian vs viscoelastic fluids. The dynamics for variations of initial standoff distance and elasticity are presented thereafter. Finally, the key findings are summarized in Sec. V.

II. PHYSICAL MODEL AND NUMERICS

A. Governing equations

We apply an Eulerian approach for three-dimensional (3D), compressible, cavitating flows in viscoelastic fluids. Phase change is assumed to be isentropic. Consequently, we assume the flow to be barotropic, and the energy conservation is not considered. Surface tension is neglected. The resulting governing equations consist of the mass and momentum conservation equations and an additional transport equation for the viscoelastic stresses. The conservative form of the governing equations for an arbitrary control volume V with surrounding surface ∂V is given by

$$\int_V \frac{\partial}{\partial t} \mathbf{Q} dV = - \int_{\partial V} (\mathbf{F}^{conv} + \mathbf{F}^{diff}) dS + \int_V \mathbf{S} dV, \quad (1)$$

where $\mathbf{Q} = [\rho, \rho \mathbf{u}, \rho \boldsymbol{\tau}_M]^T$ represents the vector of variables consisting of the density ρ , the momentum $\rho \mathbf{u}$, and the additional viscoelastic stress contribution $\rho \boldsymbol{\tau}_M$. Here, $\boldsymbol{\tau}_M$ is the viscoelastic stress tensor, which we denote as Maxwell stress tensor referring to the series element of dashpot and spring, which is part of the 1D rheological representation⁴³ of Oldroyd-like viscoelastic constitutive models. The integral comprises convective \mathbf{F}^{conv} and diffusive \mathbf{F}^{diff} flux terms, and the source term \mathbf{S} which is introduced by the viscoelastic constitutive equations. The convective and diffusive fluxes read

$$\mathbf{F}^{conv} = \begin{bmatrix} \rho \\ \rho \mathbf{u} \\ \rho \boldsymbol{\tau}_M \end{bmatrix} \mathbf{u} \cdot \mathbf{n} + \begin{bmatrix} 0 \\ p \\ 0 \end{bmatrix} \cdot \mathbf{n}, \quad \mathbf{F}^{diff} = \begin{bmatrix} 0 \\ -2\mu_S \mathbf{d}^d \cdot \mathbf{n} - \boldsymbol{\tau}_M \cdot \mathbf{n} \\ 0 \end{bmatrix}, \quad (2)$$

where \mathbf{u} and p represent the velocity and the thermodynamic pressure. $\mathbf{d}^d = \mathbf{d} - \frac{1}{3} \text{tr}(\mathbf{d}) \mathbf{I}$ is the deviatoric part of the symmetric shear rate tensor $\mathbf{d} = \frac{1}{2} (\mathbf{I} + \mathbf{I}^T)$, where $\mathbf{I} = \nabla \mathbf{u}$ is the velocity gradient and $\text{tr}(\dots)$ represents the trace. The diffusive flux comprises Newtonian (solvent) stresses $\boldsymbol{\tau}_S = 2\mu_S \mathbf{d}^d$ and viscoelastic stresses $\boldsymbol{\tau}_M$.

We apply the simplified linear Phan-Thien Tanner (LPTT) model,⁴⁴ which is written in differential formulation as follows:

$$\boldsymbol{\tau}_M \left(1 + \epsilon \frac{\lambda}{\mu_M} \text{tr}(\boldsymbol{\tau}_M) \right) + \lambda \overset{\nabla}{\boldsymbol{\tau}}_M = 2\mu_M \mathbf{d}^d, \quad (3)$$

$$\overset{\nabla}{\boldsymbol{\tau}}_M = \frac{D\boldsymbol{\tau}_M}{Dt} - \mathbf{I} \cdot \boldsymbol{\tau}_M - \boldsymbol{\tau}_M \cdot \mathbf{I}^T + \text{tr}(\mathbf{I}) \boldsymbol{\tau}_M, \quad (4)$$

where the Truesdell rate $\overset{\nabla}{\boldsymbol{\tau}}_M$ is applied as objective rate for the viscoelastic stress tensor, which was identified in Lang *et al.*⁴³ as appropriate objective time derivative for compressible flows. μ_M represents the viscoelastic dynamic viscosity, denoted as Maxwell viscosity. λ is the relaxation time and $\frac{D\boldsymbol{\tau}_M}{Dt}$ is the material time derivative of the

viscoelastic stress tensor. The extensibility parameter ϵ in Eq. (3) is set to the commonly used value of $\epsilon = 0.25$. By using the mass conservation, the source term for the conservative formulation is obtained:

$$\mathbf{S} = \left[\begin{array}{c} 0 \\ 0 \\ \rho \left[\mathbf{I} \cdot \boldsymbol{\tau}_M + \boldsymbol{\tau}_M \cdot \mathbf{I}^T - (\nabla \cdot \mathbf{u}) \boldsymbol{\tau}_M + \frac{1}{\lambda} (2\mu_M \mathbf{d}^d - \boldsymbol{\tau}_M) \right] \end{array} \right]. \quad (5)$$

The viscoelastic implementation has been validated and grid convergence studies have been performed for single-phase channel flows in Lang *et al.*⁴³

B. Single-fluid homogeneous mixture cavitation model

Cavitating two-phase flow is modeled by a single-fluid homogeneous mixture approach,⁴⁵ assuming that a computational cell contains either pure liquid or a homogeneous water–vapor mixture. For mixtures, we assume that both phases are in mechanical and thermodynamic equilibrium with infinitely fast and isentropic phase change without time delay. The model inherently considers condensation and evaporation since the generated phase is directly reproduced according to the thermodynamic equilibrium state through the equation of state. An additional mass-transfer rate equation, such as the Schnerr–Sauer cavitation model,⁴⁶ is not required. The cavitation model was extensively used and validated for various applications such as bubble dynamics,^{31,45,47,48} fuel injectors,⁴⁹ and condensation shocks.⁵⁰ The governing Eq. (1) apply to homogeneous mixtures of multiple components without limitation. Consequently, we can assume that all quantities are represented by volume- and phase-averaged mixtures via

$$\bar{\square} := \frac{1}{V_\Omega} \int_{V_\Omega} \square \, dV \quad (6)$$

for each computational cell V_Ω , describing the homogeneous mixture. Within a discrete finite volume, the vapor volume fraction is calculated from

$$\alpha = \frac{V_{v,\Omega}}{V_\Omega} = \begin{cases} 0, & \text{if } \bar{\rho} \geq \rho_{l,sat} \text{ (pure liquid),} \\ \frac{\rho_{l,sat} - \bar{\rho}}{\rho_{l,sat} - \rho_{v,sat}}, & \text{else (liquid–vapor mixture)} \end{cases} \quad (7)$$

with the vapor volume $V_{v,\Omega}$ in a computational cell and the saturation densities of vapor $\rho_{v,sat}$ and liquid $\rho_{l,sat}$. For pure liquids, a modified Tait equation of state by Saurel *et al.*⁵¹ is applied,

$$\bar{p} = B \left[\left(\frac{\bar{\rho}}{\rho_{l,sat}} \right)^N - 1 \right] + p_{sat}, \quad (8)$$

where $N = 7.15$ and $B = 3.3 \times 10^8$ Pa at reference temperature $T_{ref} = 293.15$ K. The speed of sound in computational cells of pure liquid is calculated by

$$c = \left(\frac{N(\bar{p} + B)}{\bar{\rho}} \right)^{1/2}. \quad (9)$$

For mixtures of saturated liquid and vapor, the definition of the isentropic speed of sound

$$c^2 = \left. \frac{\partial p}{\partial \rho} \right|_{s=const.} \Rightarrow p(\rho) - p_{sat} = \int_{\rho_{l,sat}}^{\rho} c^2 \, d\bar{\rho} \quad (10)$$

allows to obtain the pressure of the mixture by integration. The speed of sound is given by

$$\frac{1}{\bar{\rho} c^2} = \frac{\alpha}{\rho_{v,sat} c_{v,sat}^2} + \frac{1 - \alpha}{\rho_{l,sat} c_{l,sat}^2} + \frac{((1 - \alpha)\rho_{l,sat} c_{p,l,sat} - \alpha\rho_{v,sat} c_{p,v,sat}) T_{ref}}{(\rho_{v,sat} l_v)^2} \quad (11)$$

containing the latent heat of vaporization l_v .⁵² A detailed derivation of the pressure calculation is given in Lang *et al.*⁴³ The solvent viscosity is calculated similarly for pure liquid and mixture regions following the approach of Beattie and Whalley,⁵³

$$\mu_s = (1 - \alpha) \left(1 + \frac{5}{2} \alpha \right) \mu_{l,sat} + \alpha \mu_{v,sat}. \quad (12)$$

The fluid properties applied in the present study are summarized in Table I.

C. Numerical approach

The finite volume discretization is applied using body-fitted, hexahedral cells with non-staggered cell-centered variables, and the governing equations are formulated in Cartesian coordinates. The cell-face fluxes are calculated separately for convective fluxes and diffusive fluxes, respectively. Convective fluxes are calculated by an upwind-biased low-Mach number consistent AUSM-type (advection upstream splitting method) approximate Riemann solver. The cell-face values for density, pressure, velocities, and viscoelastic stresses are calculated by higher-order MUSCL (monotone upstream-centered schemes for conservation laws) reconstruction on a four-point stencil with the Min-Mod⁵⁴ limiter. The convective flux calculation is described in more detail as baseline finite-volume

TABLE I. Fluid properties of the barotropic model at $T_{ref} = 293.15$ K.

Property	Symbol	Value
Reference temperature	T_{ref}	293.15 K
Density of saturated liquid	$\rho_{l,sat}$	998.16 kg/m ³
Density of saturated vapor	$\rho_{v,sat}$	0.017 21 kg/m ³
Saturation pressure	p_{sat}	2339.3 Pa
Dynamic viscosity of saturated liquid	$\mu_{l,sat}$	1.0014×10^{-3} Pas
Dynamic viscosity of saturated vapor	$\mu_{v,sat}$	9.7275×10^{-6} Pas
Speed of sound of saturated liquid	$c_{l,sat}$	1482.2 m/s
Speed of sound of saturated vapor	$c_{v,sat}$	423.18 m/s
Specific heat capacity of saturated liquid	$c_{p,l,sat}$	4184.4 J/(kg K)
Specific heat capacity of saturated vapor	$c_{p,v,sat}$	1905.9 J/(kg K)
Latent heat of vaporization	l_v	2453.5×10^3 J/kg

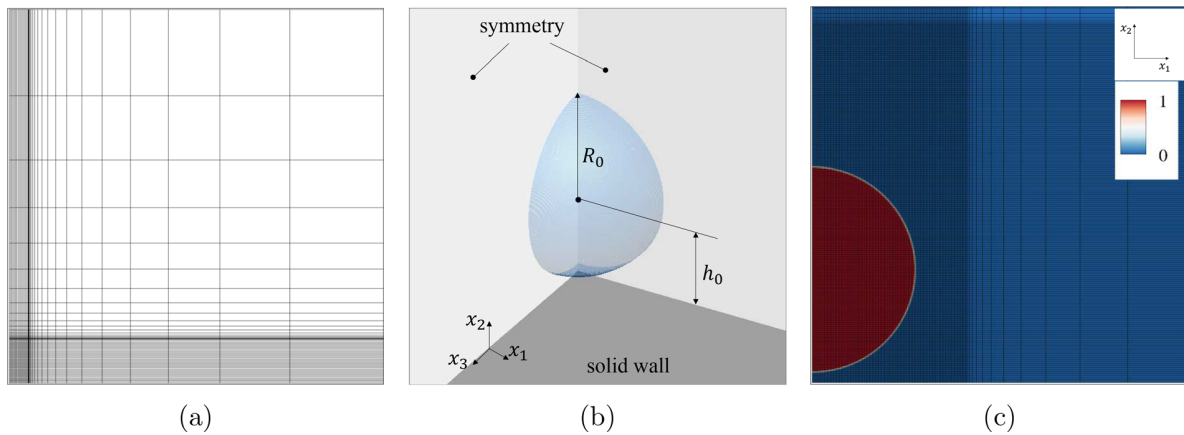


FIG. 1. Initialization of the vapor bubble and the imposed boundary conditions. (a) Entire computational domain with refined zone and attached coarse mesh [for the refined zone in (a) only every 10th grid line is shown]; (b) isosurface ($\alpha = 0.01$) visualizing initial bubble surface and adjacent boundaries; and (c) closeup of the initial vapor volume fraction α (–) and computational grid in the refined region.

scheme in Egerer *et al.*⁴⁷ The diffusive flux and the source term are calculated by a second order central reconstruction. The time discretization is realized by an explicit four-step Runge–Kutta method with a modified time step criterion considering the viscoelastic transport equation. Further information on the numerical approach, including the discretization, numerical flux term approximation, and time integration, is given in Lang *et al.*⁴³

III. NUMERICAL SETUP

The collapse of a vapor cavity with initial radius $R_0 = 1 \times 10^{-4}$ m surrounded by (viscoelastic) fluid is simulated. The pressure inside the bubble is initialized with the constant saturated vapor pressure p_{sat} and the pressure in the surrounding is initialized with a distribution,

$$p(r, t = 0) = p_\infty - \frac{R_0}{r} (p_\infty - p_{sat}), \quad r > R_0 \quad (13)$$

and driving pressure of $p_\infty = 10 \times 10^5$ Pa. The bubble and the surrounding fluid are initially at rest. The pressure field represents the solution of the Rayleigh–Plesset equation for the Besant problem,⁵⁵ and has been used to simulate similar problems³¹ to suppress artificial pressure waves due to pressure jumps at the interface. The computational mesh is depicted in Fig. 1. The initial standoff distance h_0 represents the initial distance of the bubble center from the solid wall. We exploit two symmetry planes and hence simulate only one quarter of the collapsing vapor bubble. The bubble is located inside a refined rectangular subdomain with the size of $1.5R_0 \times 3.5R_0 \times 1.5R_0$ and an equally spaced grid. The grid resolution of the refined zone is 100 cells/ R_0 . A coarsened region is attached to the refined zone to dissipate outgoing waves and minimize wave reflections toward the refined zone. The computational domain has a total size of $30R_0 \times 30R_0 \times 30R_0$. As boundary conditions, two symmetry boundary conditions in the x_1/x_2 - and x_2/x_3 -plane are applied, as well as a no-slip boundary condition in the x_1/x_3 -plane. Outlet boundary conditions apply for the remaining planes.

The viscoelastic flow can be characterized by the non-dimensional Reynolds- and Deborah number. The Reynolds number

relates the timescale for diffusive momentum transport and the Deborah number the relaxation timescale to the characteristic inertia-related timescales of the flow. The inertia-related timescale is defined from the characteristic velocity for the spherical Rayleigh collapse $u_0 := \sqrt{\Delta p / \rho_{l,sat}}$. For the viscoelastic bubble collapse, Re and De are defined as follows:

$$Re = \frac{R_0 \sqrt{\rho_{l,sat} \Delta p}}{\mu_0}, \quad De = \frac{\lambda}{R_0} \sqrt{\frac{\Delta p}{\rho_{l,sat}}}, \quad (14)$$

where $\Delta p = p_\infty - p_{sat}$ is the pressure difference of driving and saturation pressure of vapor inside the bubble and $\mu_0 = \mu_S + \mu_M$ is the sum

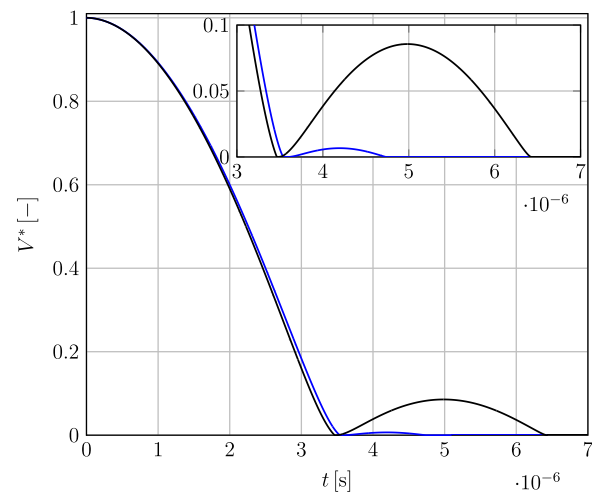


FIG. 2. Non-dimensional vapor content in the domain over time for $Re = 40$, $De = 2$, $h^* = 1.1$ with close-up of the rebound. Blue line—Newtonian fluid; black line—LPTT fluid.

of solvent and Maxwell viscosity. The non-dimensional numbers are calculated with respect to the spherical bubble collapse (Rayleigh collapse) in an infinite domain without solid wall influence. Furthermore, β describes the ratio of solvent to total viscosity,

$$\beta = \frac{\mu_s}{\mu_0}, \quad (15)$$

which is chosen to $\beta = 0.1$. The non-dimensional initial standoff distance h^* , the non-dimensional radial distance from the center in the

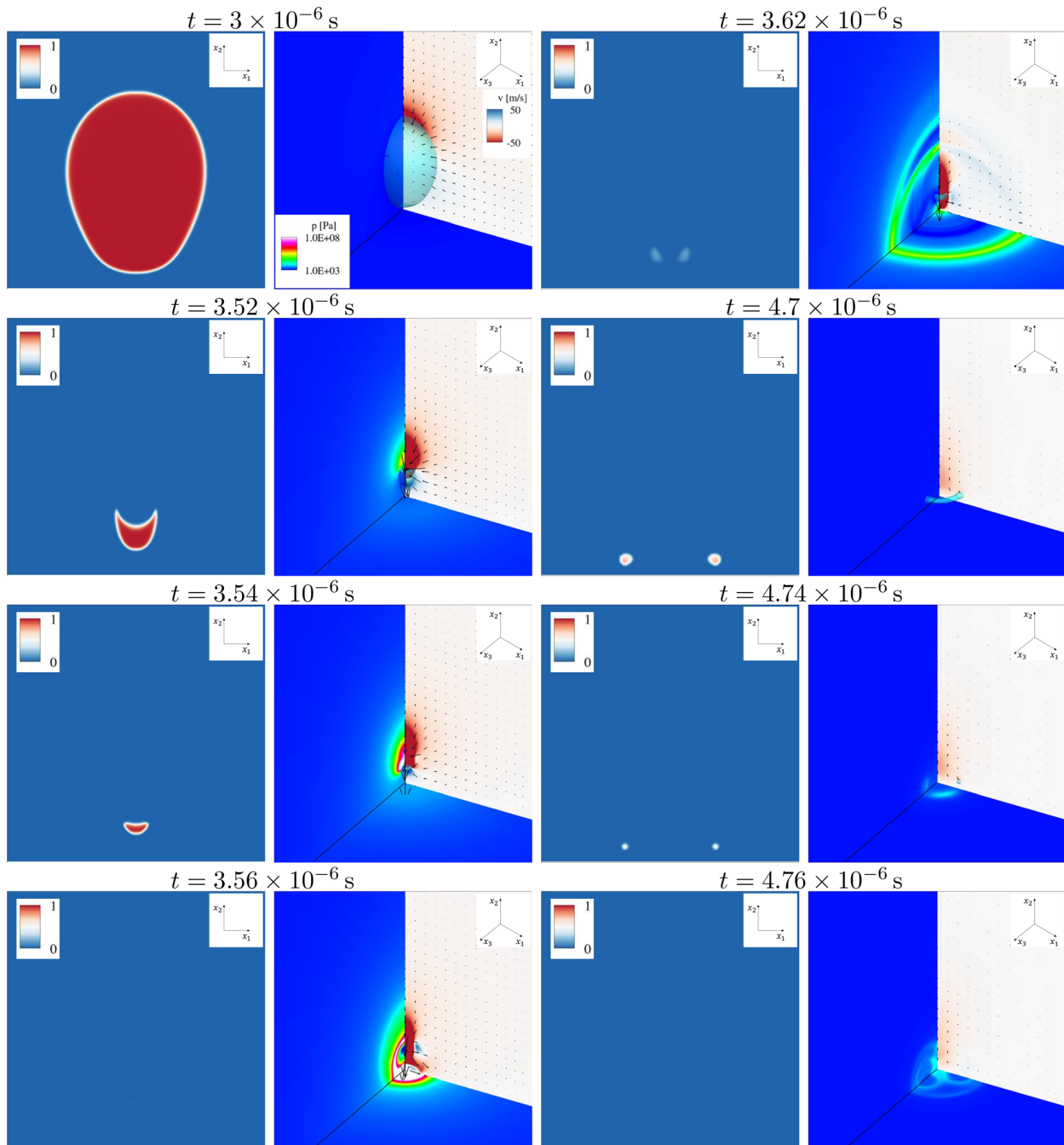


FIG. 3. Collapse in Newtonian fluid for initial standoff distance $h^* = 1.1$ and $Re = 40$. First and third column: vapor volume fraction α (—). Second and fourth columns: Wall normal velocity in x_2 -direction u_2 (m/s) through the x_1/x_2 -midplane and velocity vectors scaled by the velocity magnitude. Pressure distribution p (Pa) through the x_2/x_3 -midplane and at the wall. Isosurface shows constant vapor content of $\alpha = 0.01$.

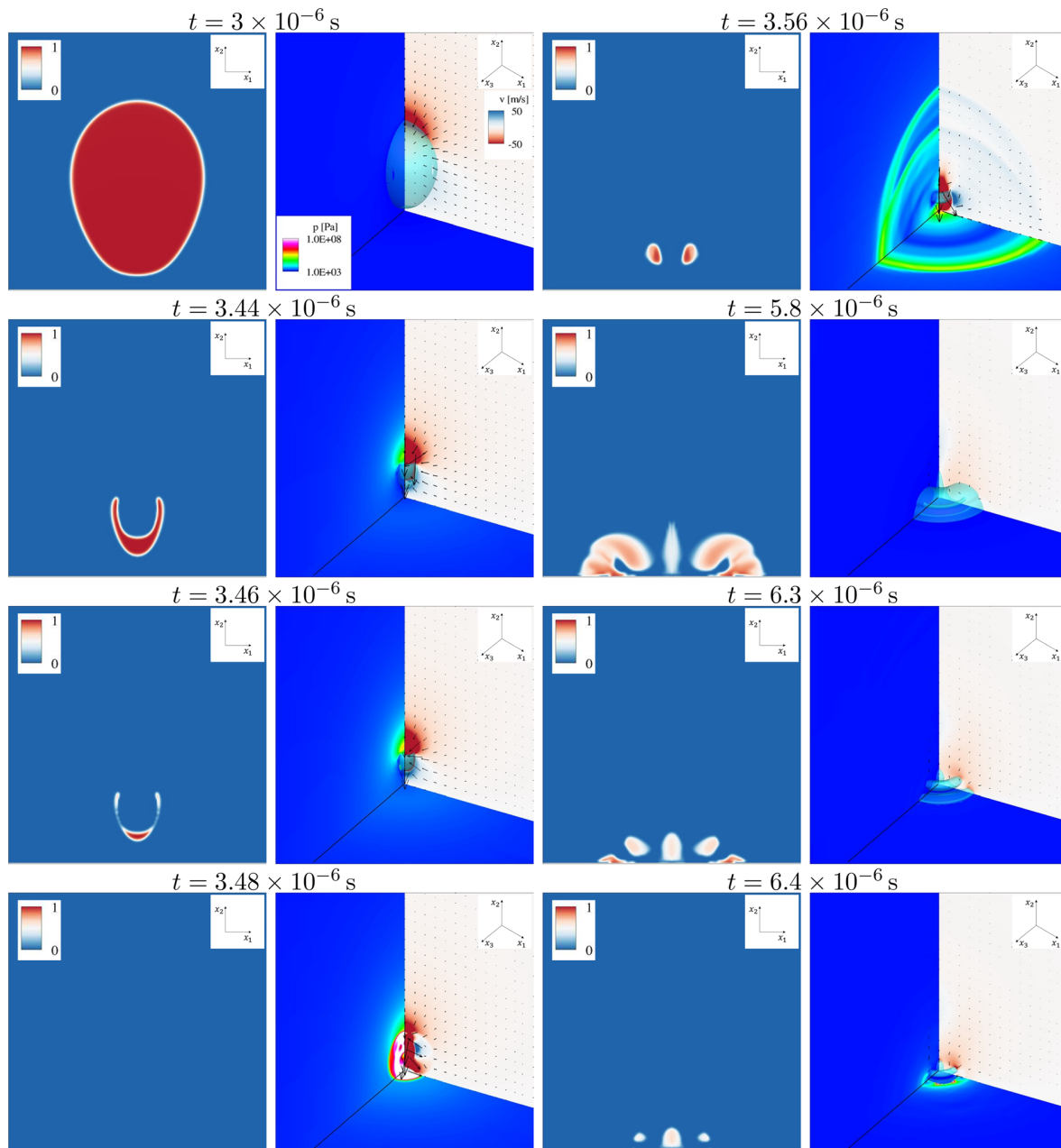


FIG. 4. Collapse in LPTT fluid for initial standoff distance $h^* = 1.1$ and $Re = 40, De = 2$. First and third column: vapor volume fraction α (–). Second and fourth columns: Velocity in x_2 -direction u_2 (m/s) through the x_1/x_2 -midplane and velocity vectors scaled by the velocity magnitude. Pressure distribution p (Pa) through the x_2/x_3 -midplane and at the wall. Isosurface shows constant vapor content of $\alpha = 0.01$.

plane of the solid wall r^* , and the non-dimensional x_2 -direction x_2^* are defined as

$$h^* := \frac{h_0}{R_0}, \quad r^* := \frac{x_1^2 + x_3^2}{R_0} \Big|_{x_3=0}, \quad x_2^* := \frac{x_2}{R_0}.$$

IV. RESULTS AND DISCUSSION

A. General dynamics of the aspherical collapse

We simulate the vapor bubble collapse with a standoff distance of $h^* = 1.1$ for highly viscous flow at $Re = 40$. This Reynolds number is chosen since rheological effects become significant for $Re < 100$

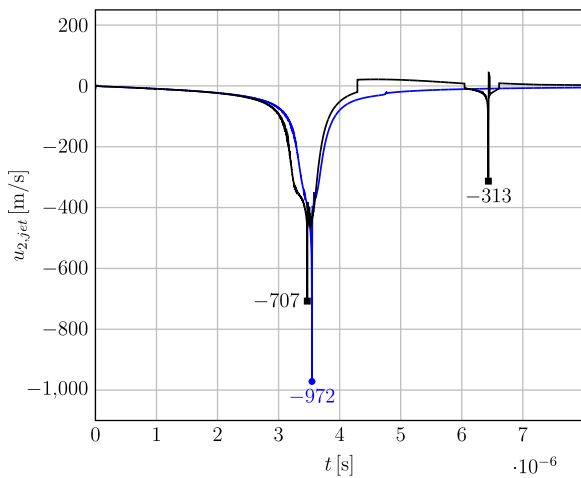


FIG. 5. Jet velocity $u_{2,jet}$ (m/s) in x_2 -direction measured at centerline over time. Blue line—Newtonian fluid; black line—LPTT fluid.

(Ref. 56), but jet formation can still be expected for such a Reynolds number.³⁸ The parameters as mentioned above represent the reference for which Newtonian and viscoelastic collapse with an elasticity of $De = 2$ are compared. Figure 2 shows the total vapor content over time for the Newtonian opposed to the LPTT case. In Figs. 3 and 4, the collapse behavior for both fluids is illustrated qualitatively. During the initial collapse, the bubble in the Newtonian fluid collapses before the water-hammer impinges onto the opposite side of the vapor bubble. Contrarily, the LPTT fluid exhibits larger bubble deformation and elongation in wall normal direction. Also, the resulting radial

water-hammer leads to an initial pressure wave already before the first collapse (cf. Fig. 6). The pressure wave emitted after the first collapse results from a superposition of the water-hammer and the collapse of the vapor cavity in the LPTT fluid as opposed to the Newtonian collapse, where only collapse is observed. Subsequently, the LPTT collapse yields larger amounts of vapor during rebound than the Newtonian fluid, where only a tiny toroidal vapor region is produced. The vapor after rebound occupies a larger coherent area in LPTT, especially during later stages of the collapse, enabling jet formation during the second collapse (cf. Fig. 5). Additionally, the vapor region in LPTT is squeezed and dragged along the solid wall after the rebound, and a splashing effect is observed. The vapor cavity in the center leads to a complex second vapor structure. In the Newtonian case, the small toroidal vapor region after rebound does not lead to jet formation during the second collapse.

In the following, the jet evolution during collapse and the pressure wave emission for the first collapse are investigated in detail. Figure 5 depicts the jet velocity during collapse for the Newtonian and the LPTT fluid. The jet velocity is identified by the maximum wall normal velocity magnitude along the centerline. Note that a finite jet velocity does not necessarily indicate that the flow from the top of the bubble actually pierces through the bubble deforming it to a toroid. We observe that during the first collapse, the jet velocity evolution for both cases agrees qualitatively, and that the maximum absolute jet velocities are larger for the Newtonian case compared to the LPTT fluid. For LPTT, a second jet forms during the second collapse, which cannot be found for the Newtonian case. The second jet results from the collapse of the vapor cavity formed after rebound.

In Fig. 6, the pressure distribution during the first collapse is examined in detail. For the collapse in a Newtonian fluid (upper row), no water penetration and corresponding piercing of the vapor cavity can be observed. The bubble sphericity increases during collapse, and

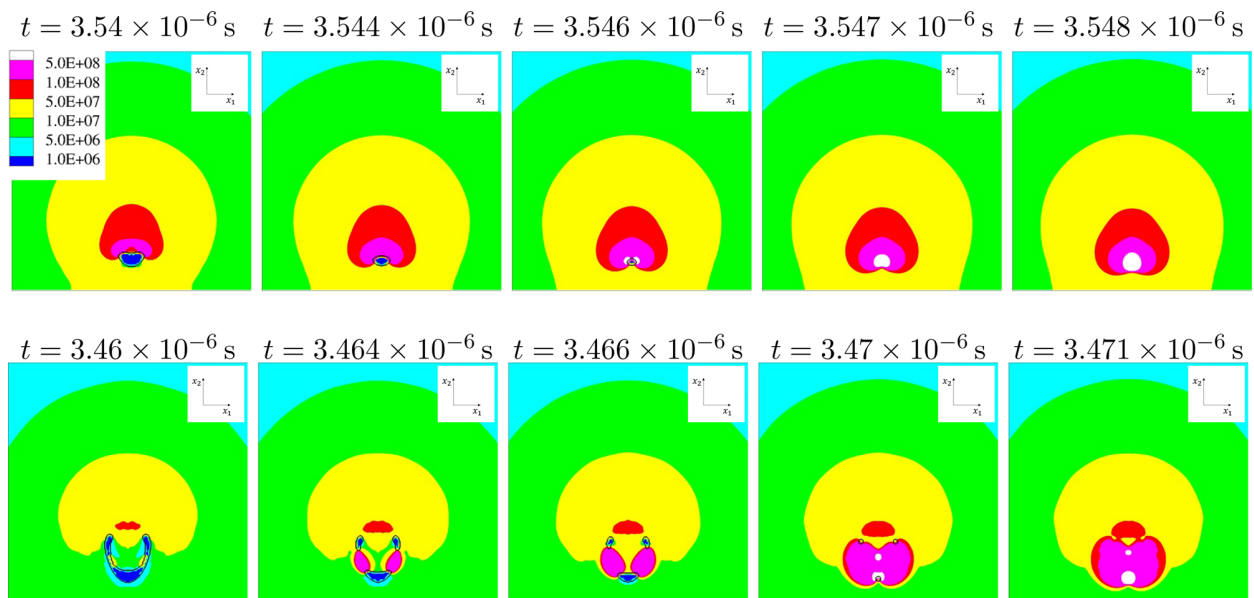


FIG. 6. Pressure distribution p (Pa) and illustration of shock formation during first collapse through the x_1/x_2 -midplane for $Re = 40$, $De = 2$, $h^* = 1.1$. Top: Newtonian fluid; bottom: LPTT fluid. Black isoline shows vapor content of $\alpha = 0.01$.

pressure increase is observed at the upper side of the bubble due to the decelerated water column. A shock wave is emitted after the full collapse. The LPTT case (lower row) shows a radial water-hammer impinging the opposite side of the vapor cavity leading to shock wave emission before condensation and separation of the remaining vapor cavities into a toroidal upper part and a droplet-like lower part. The pressure wave emission is followed by the complete collapse of the two remaining vapor cavities. Shock wave interference results in a complex pressure field.

In Fig. 7, we show pressure and vapor distribution in x_2 -direction along the centerline for both fluids. First, it can be seen that the pressure magnitudes in the vicinity of the collapsing vapor cavities are significantly larger for the Newtonian case, which can be attributed to the more focused Newtonian collapse as compared to the LPTT case (cf. Fig. 6), where two vapor cavities collapse separately. Moreover, in the LPTT fluid, a distinct pressure rise is observable right before full condensation ($t = 3.47 \times 10^{-6}$ s) caused by the pressure wave emitted from the radial water impingement. Subsequently, the pressure wave

from water impingement and the collapse of the remaining lower vapor cavity interfere. For the Newtonian fluid, however, the pressure rises not before collapse.

By comparing the Newtonian and the LPTT collapse at the identical Reynolds number, we show that jet formation, or more precisely, jet piercing through the vapor bubble, is enabled by viscoelasticity for the investigated parameters. However, Lind and Phillips^{38,39} assert that jet formation is suppressed by viscoelasticity, although they also found that jet formation is likewise suppressed for highly viscous fluids.^{23,38} Karri *et al.*⁵⁷ ascertained in their experimental study for Newtonian fluid, that high viscosity can yield bubble oscillations and jet suppression. Their viscoelastic simulations are performed for the same or even lower Reynolds numbers as in the Newtonian case. For this comparison, we cannot see clear evidence that jet suppression is purely caused by viscoelasticity. For the identical or further decreased Reynolds numbers in the viscoelastic case, jet formation is expectedly suppressed, but it is not evident whether the mitigating effect is unambiguously caused by viscoelasticity or if viscous and viscoelastic stresses similarly can

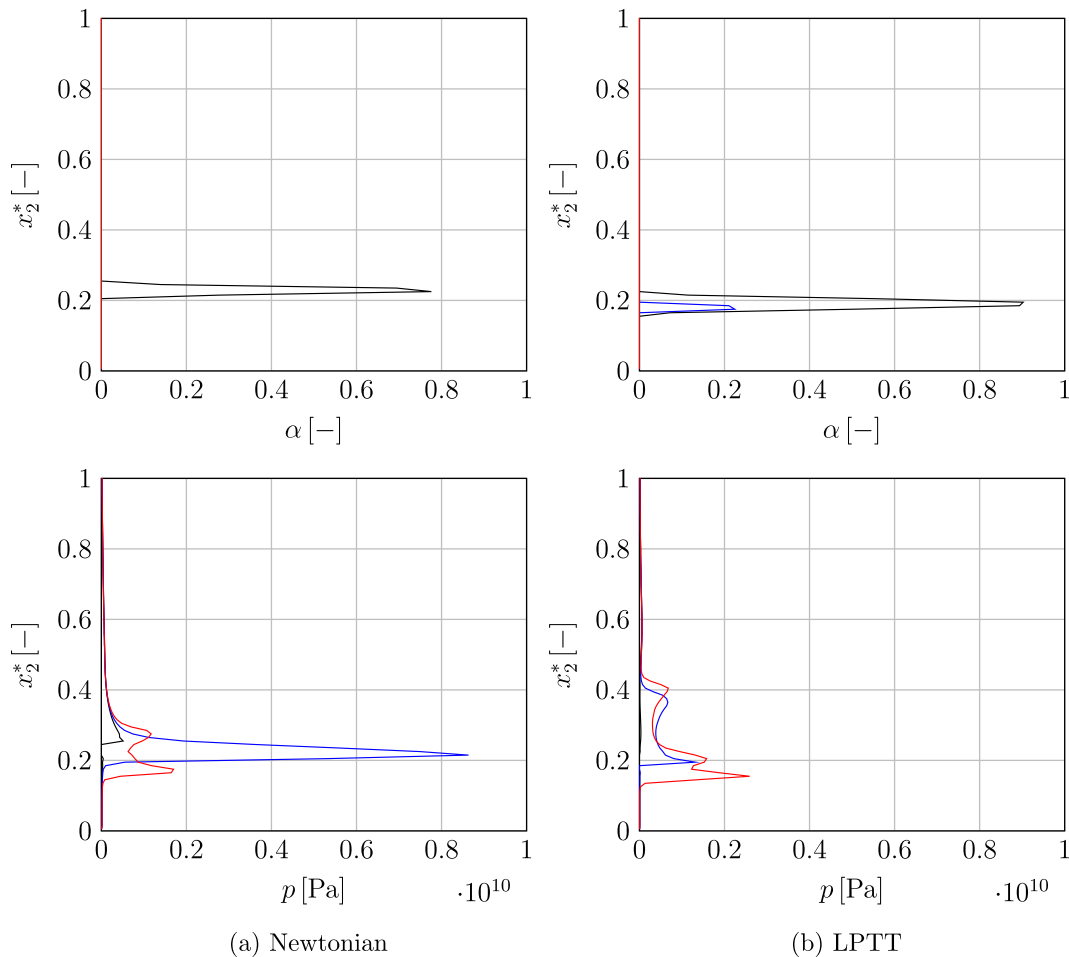


FIG. 7. Distribution of vapor volume fraction α (–) (top) and pressure p (Pa) (bottom) along the centerline in x_2 -direction for $Re = 40$, $De = 2$, $h^* = 1.1$. (a) Newtonian fluid: Black line— $t = 3.546 \times 10^{-6}$ s, blue line— $t = 3.547 \times 10^{-6}$ s, red line— $t = 3.548 \times 10^{-6}$ s. (b) LPTT fluid: Black line— $t = 3.466 \times 10^{-6}$ s, blue line— $t = 3.47 \times 10^{-6}$ s, red line— $t = 3.471 \times 10^{-6}$ s.

inhibit jet formation. Moreover, in Lind and Phillips,³⁸ a parameter study for the variation of Reynolds and Deborah number, associated with the variation of viscous and elastic influence, was conducted and determined that for given Reynolds number increasing elasticity in a viscoelastic fluid can lead to jet formation in the first place.

Figure 8 compares the pressure evolution at the position of maximum wall pressure (for $h^* = 1.1$ at the focus point $r^* = 0$) and at the maximum pressure position along the centerline for both fluids. The maximum pressures at the wall during first collapse are comparable. Opposed to the pressures at the wall, the pressure along the centerline during the first collapse is larger for the Newtonian case. Furthermore, the maximum pressure from the first collapse occurs at a larger distance from the wall for the Newtonian collapse. The overall pressure evolutions for the first collapse are qualitatively similar. A substantial pressure rise caused by the collapse (Newtonian case) or the superposition of the pressure waves from the water-hammer and collapse (LPTT case), respectively, is immediately followed by the jet impinging the rigid wall. Gonzalez-Avila *et al.*⁵⁸ observed a similar pressure

evolution at the wall for the same initial standoff distance and gas-filled bubbles. The subsequent pressure evolution shows an additional pressure peak related to the second collapse after the rebound. The second pressure peak is much stronger for the viscoelastic fluid, caused by the larger vapor cavity formed during rebound. Moreover, the second collapse for LPTT is delayed compared to the Newtonian case due to the larger vapor cavity after the rebound and the increased total stresses. Between the first and second collapse, the pressure at the wall decreases to vapor pressure in the LPTT case, since the vapor region is pushed to the center. In the Newtonian fluid, vapor is not observable at the wall before the second collapse, and hence the pressure drop between the two collapses is not as pronounced as in LPTT.

The differences in the collapse dynamics and shock wave formation are consequence of the different constitutive relations. In the following, different Newtonian and LPTT stress components are compared. Figures 9 and 10 show τ_{11} , the component which differs most distinctly when comparing the aspherical collapse of Newtonian and viscoelastic fluid.³⁹ An additional τ_{11} -stress-layer can be observed

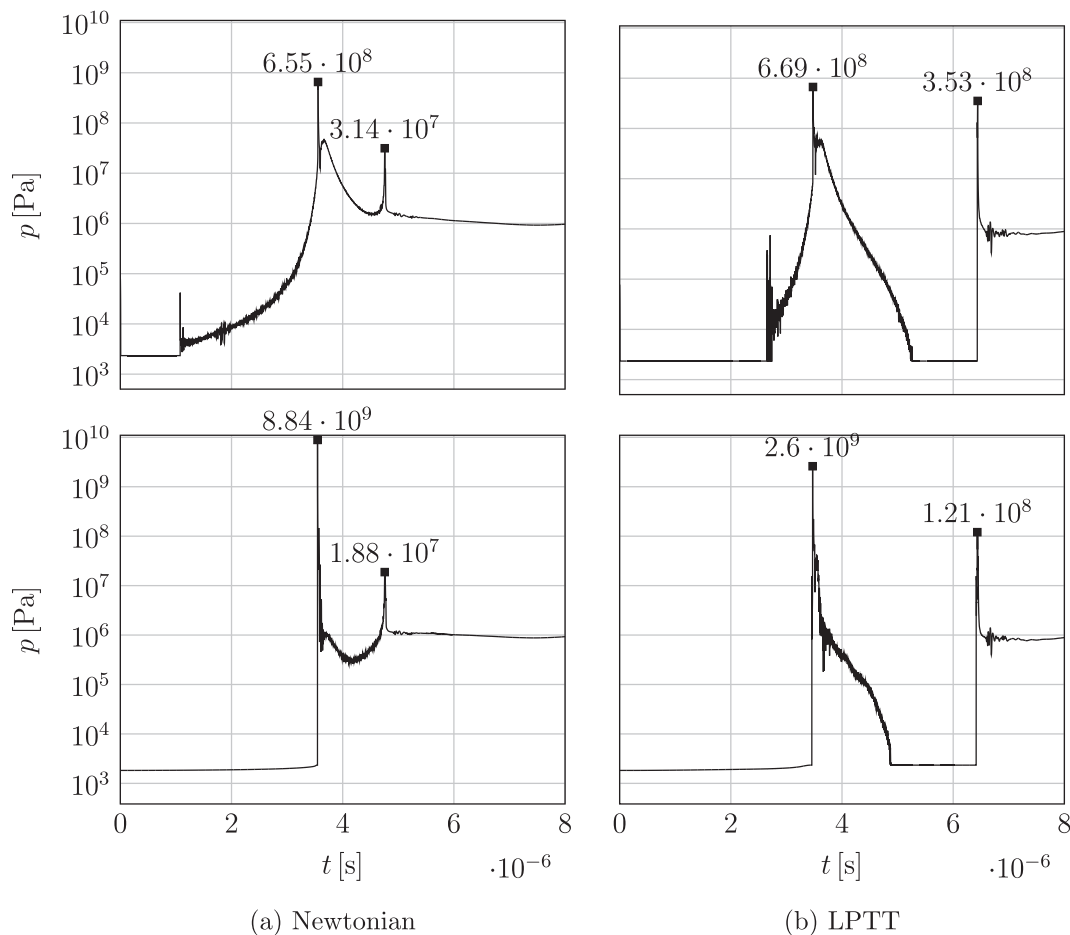


FIG. 8. Pressure p (Pa) over time for $Re = 40$, $De = 2$, $h^* = 1.1$ (logarithmic scale). Top: at the wall ($x_2^* = 0$) at the location of maximum pressure: (a) Newtonian fluid at $r^* = 0.02$ and (b) LPTT fluid at $r^* = 0$. Bottom: Along the centerline at the position of maximum occurring pressure for (a) Newtonian fluid at $x_2^* = 0.22$, and (b) LPTT fluid at $x_2^* = 0.16$.

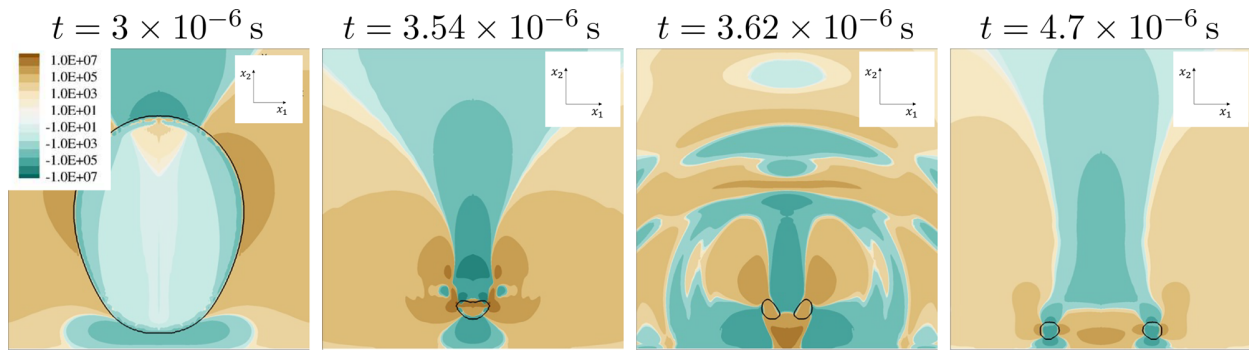


FIG. 9. Solvent stress $\tau_{S,11}$ (Pa) through x_2/x_3 -midplane for $Re = 40$, $h^* = 1.1$ in Newtonian fluid. Black isoline shows vapor content of $\alpha = 0.01$.

for the collapse in LPTT, a unique feature of viscoelastic fluids also observed by Lind and Phillips,³⁹ which is caused by normal stress effects. These positive stresses accelerate fluid along the wall away from the center and lead to splashing ($t = 5.8 \times 10^{-6}$ s) in the later instants of the collapse. By comparing solvent ($\tau_{S,11}$) and viscoelastic ($\tau_{M,11}$) stresses in general, we can observe that solvent stresses exhibit more oscillations as compared to the smoother viscoelastic stresses. This behavior can be explained by the delayed viscoelastic stress build-up, whereas solvent stresses are directly related to the occurring deformation rate. Furthermore, solvent stresses in the Newtonian case are higher than in the LPTT case since the total stress is divided into additional viscoelastic stresses, and the solvent stresses themselves.

Additionally, it is observable that in the LPTT case, large viscoelastic stresses occur at the two upper tips of the bubble and a narrow region of negative stresses at the centerline ($t = 3.46 \times 10^{-6}$ s).

For the shear stress component τ_{12} in Figs. 11 and 12, significant negative viscoelastic stresses occur in the lower part and large positive stresses in the upper part of the tips in LPTT case. Positive viscoelastic stresses cover a much larger region than the solvent stresses.

The τ_{22} component, visualized in Figs. 13 and 14, likewise shows more delayed evolution and smoother distribution of viscoelastic stresses as compared to solvent stresses. The viscoelastic stress component $\tau_{M,22}$ shows a large region of positive stresses at the centerline. This component represents the normal stress in x_2 -direction, pulling

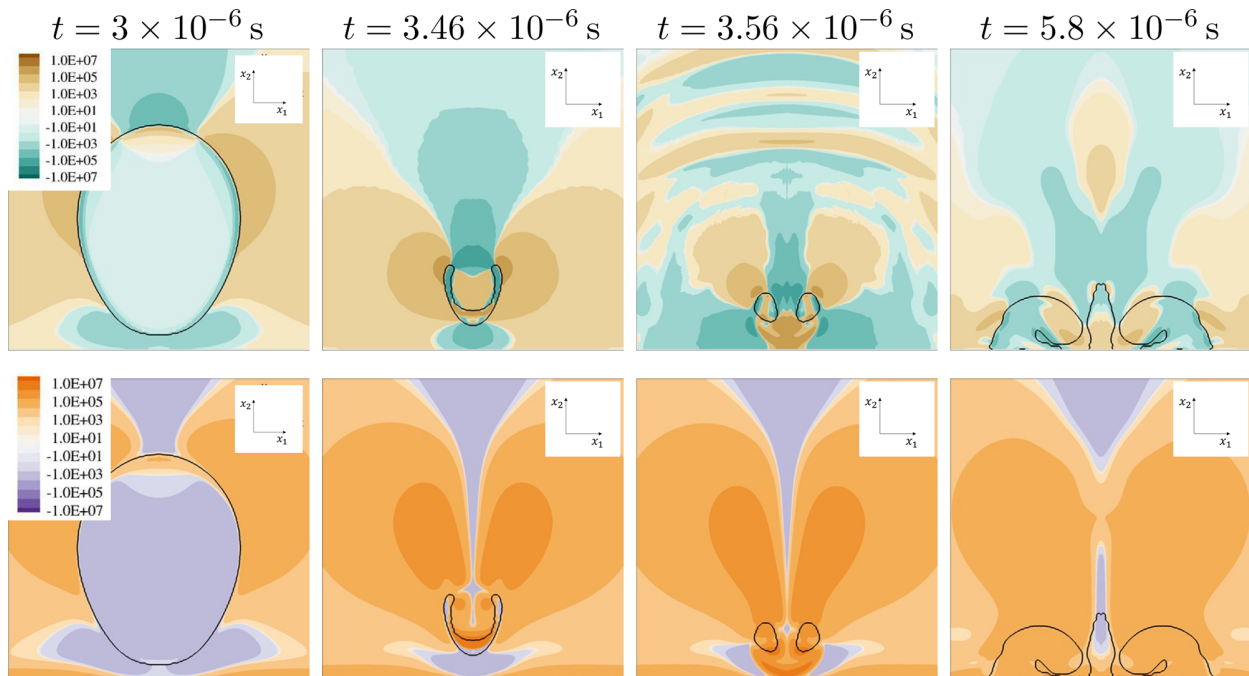


FIG. 10. Stress through x_2/x_3 -midplane for $Re = 40$, $De = 2$, $h^* = 1.1$ in LPTT fluid. Black isoline shows constant vapor content of $\alpha = 0.01$. Top: solvent stress $\tau_{S,11}$ (Pa); bottom: viscoelastic stress $\tau_{M,11}$ (Pa).

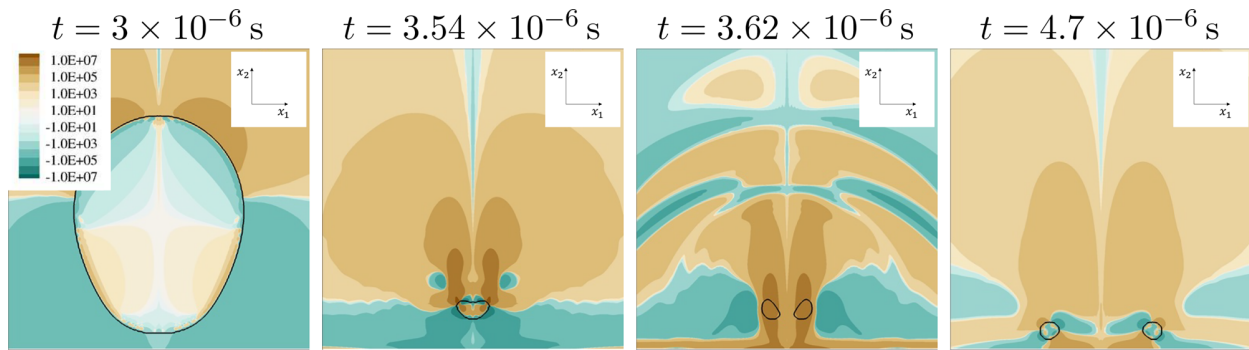


FIG. 11. Solvent stress $\tau_{S,12}$ (Pa) through x_2/x_3 -midplane for $Re = 40$, $h^* = 1.1$ in Newtonian fluid. Black isoline shows vapor content of $\alpha = 0.01$.

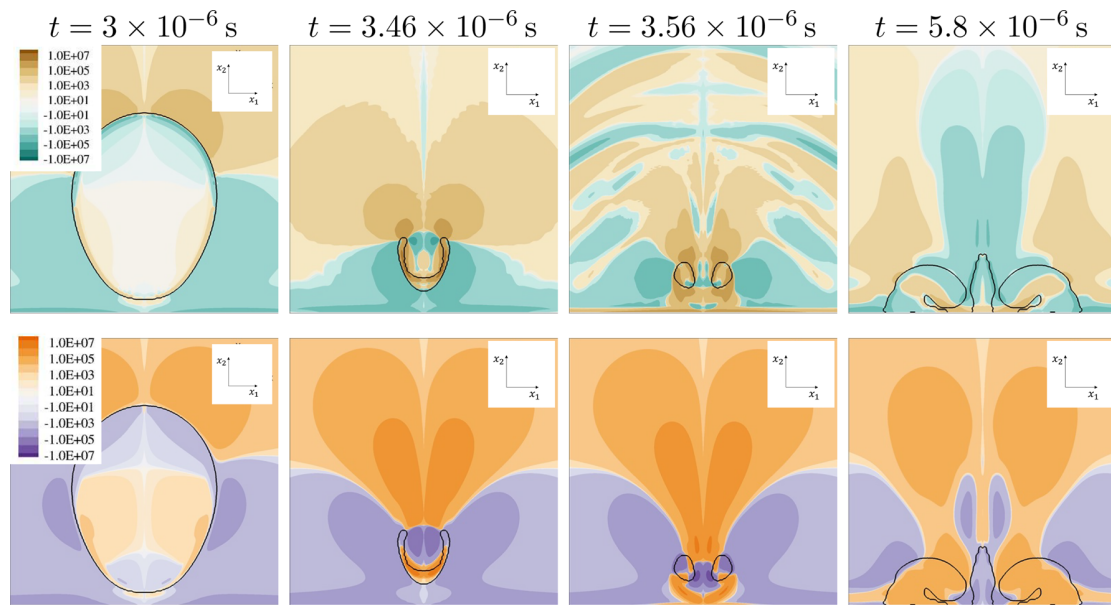


FIG. 12. Stress through x_2/x_3 -midplane for $Re = 40$, $De = 2$, $h^* = 1.1$ in LPTT fluid. Black isoline shows constant vapor content of $\alpha = 0.01$. Top: solvent stress $\tau_{S,12}$ (Pa); bottom: viscoelastic stress $\tau_{M,12}$ (Pa).

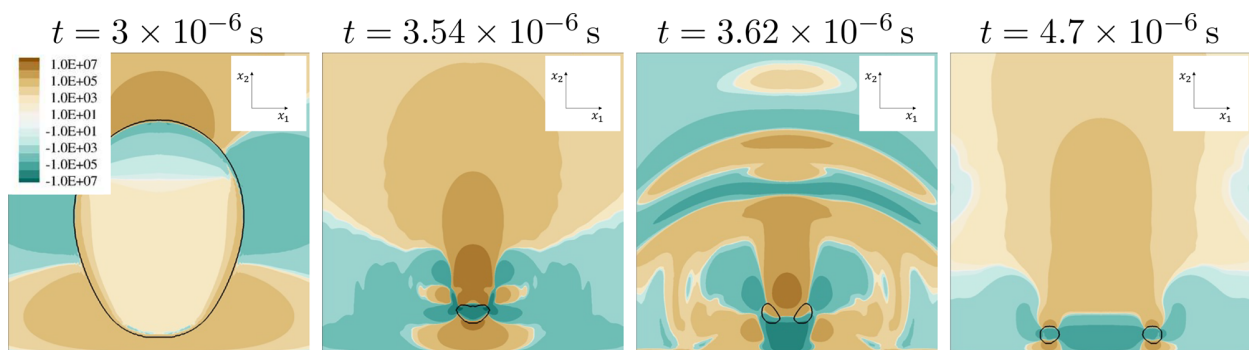


FIG. 13. Solvent stress $\tau_{S,22}$ (Pa) through x_2/x_3 -midplane for $Re = 40$, $h^* = 1.1$ in Newtonian fluid. Black isoline shows vapor content of $\alpha = 0.01$.

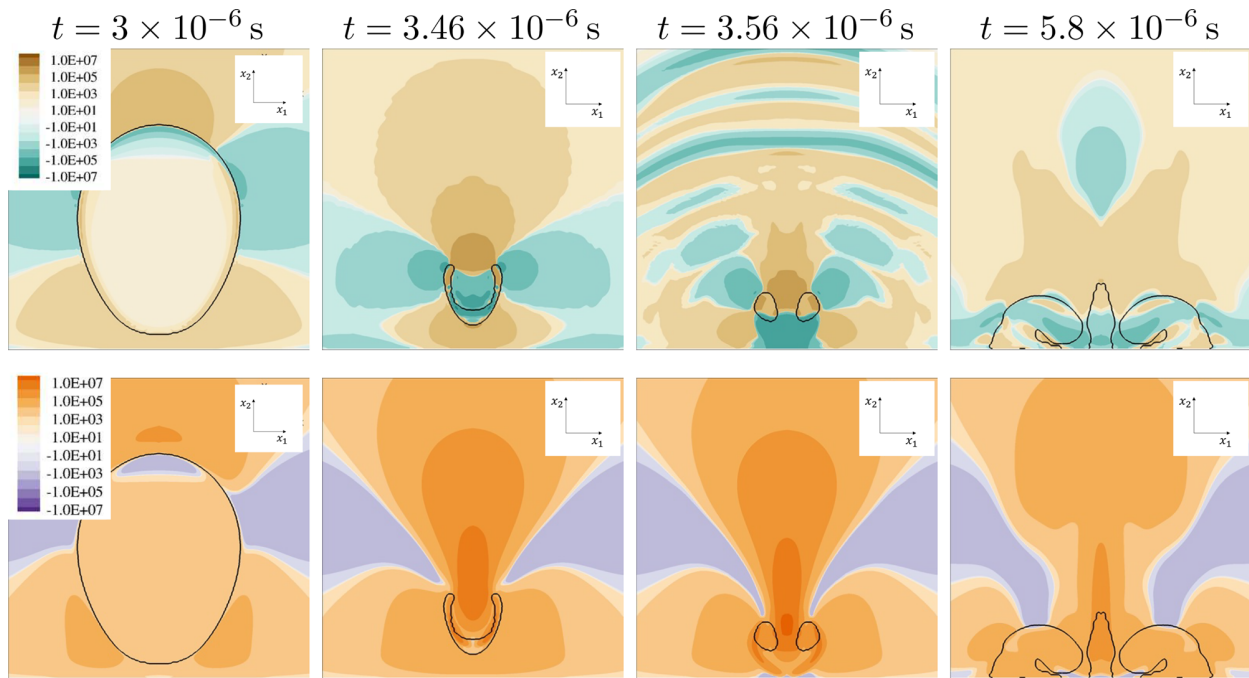


FIG. 14. Stress through x_2/x_3 -midplane for $Re = 40$, $De = 2$, $h^* = 1.1$ in LPTT fluid. Black isoline shows constant vapor content of $\alpha = 0.01$. Top: solvent stress $\tau_{s,22}$ (Pa); bottom: viscoelastic stress $\tau_{M,22}$ (Pa).

fluid in this direction, and is responsible for the re-evaporation of vapor in this region ($t = 5.8 \times 10^{-6}$ s).

B. Variation of initial standoff distance

The following simulations examine the variation of initial standoff distances ($h^* = \{0.35, 1.5\}$). Figure 15 shows the total vapor

content for the modified initial distances compared to the reference case with $h^* = 1.1$ while Re and De remain unchanged. For the Newtonian fluid, collapse time decreases for both standoff distances $h^* = 0.35$ and $h^* = 1.5$, with the shortest collapse time for $h^* = 1.5$. Furthermore, the largest vapor cavity formed during rebound is observed for $h^* = 1.1$. The general behavior for LPTT is similar. The

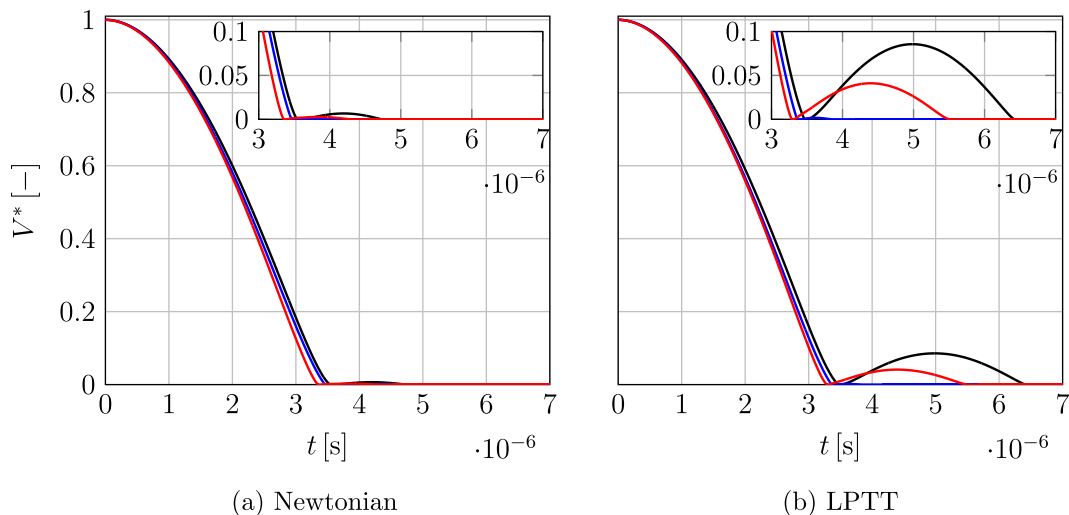


FIG. 15. Non-dimensional vapor content in the domain over time for $Re = 40$, $De = 2$ and different initial standoff distances with close-up of the rebound: (a) Newtonian fluid: blue line— $h^* = 0.35$, black line— $h^* = 1.1$, red line— $h^* = 1.5$; (b) LPTT fluid: blue line— $h^* = 0.35$, black line— $h^* = 1.1$, red line— $h^* = 1.5$.

11 January 2024 12:51:18

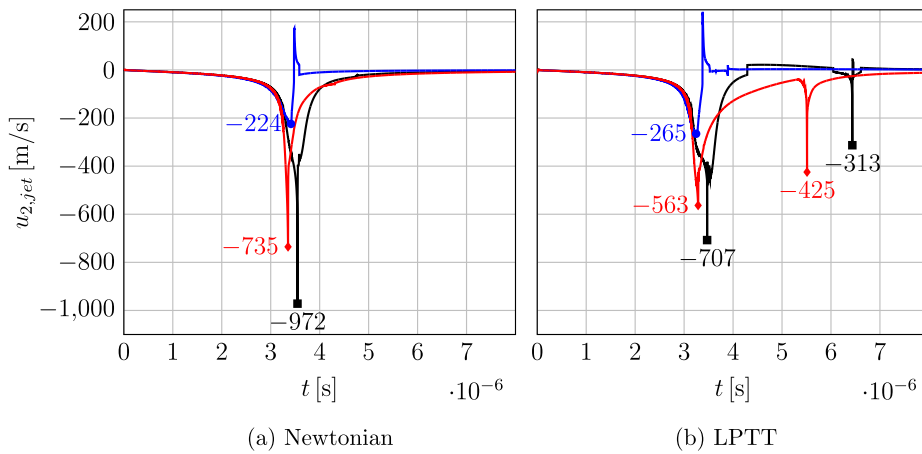


FIG. 16. Jet velocity $u_{2,jet}$ (m/s) in x_2 -direction over time measured at centerline for $Re = 40$, $De = 2$ and different initial standoff distances: (a) Newtonian fluid: blue line— $h^* = 0.35$, black line— $h^* = 1.1$, red line— $h^* = 1.5$; (b) LPTT fluid: blue line— $h^* = 0.35$, black line— $h^* = 1.1$, red line— $h^* = 1.5$.

largest cavity during rebound is formed for $h^* = 1.1$, the smallest for $h^* = 0.35$, although the formed cavities are conspicuously larger as for the Newtonian case. The shortest collapse time in LPTT is observed for $h^* = 1.5$, and the longest time can be appreciated for $h^* = 1.1$.

Jet velocities, calculated as described in Sec. IV A, are illustrated in Fig. 16. For $h^* = 0.35$, the Newtonian and the LPTT show an oscillatory behavior of the jet, with a negative and ensuing positive jet velocity. The jet velocities are smallest for an initial distance of $h^* = 0.35$ for Newtonian and viscoelastic fluid compared to the remaining standoff distances. The largest absolute jet velocities are produced for $h^* = 1.1$ for both fluids. Comparing Newtonian to viscoelastic fluid, the jet velocities for LPTT are larger than for the Newtonian fluid for $h^* = 0.35$. For $h^* = 1.1$, $h^* = 1.5$, the jet around the first collapse is faster for the Newtonian fluid. For $h^* = 1.1$ and the increased standoff distance $h^* = 1.5$, the jet velocity exhibits a second jet formation only for the LPTT fluid.

In the following, the collapse for decreased initial standoff distance $h^* = 0.35$ is examined in detail. For all subsequent variations, the evolution of the collapse is only shown for the relevant stages starting right before the first collapse. Figures 17 and 18 illustrate the collapse dynamics for selected time instants for Newtonian and LPTT fluid. We observe that the bubble is more elongated in x_2 -direction during the first collapse in the viscoelastic case (Newtonian: $t = 3.41 \times 10^{-6}$ s, LPTT: $t = 3.26 \times 10^{-6}$ s). Furthermore, while the jet penetrates the bubble and impinges the wall, more fluid is pushed below the vapor cavity in LPTT (Newtonian: $t = 3.44 \times 10^{-6}$ s, LPTT: $t = 3.3 \times 10^{-6}$ s). After the first collapse, a toroidal vapor cavity forms in the viscoelastic case, which is not observed for the Newtonian fluid. This vapor torus in LPTT yields a second collapse, less intense than the first.

Figure 19 compares the shock wave inception in the Newtonian and the viscoelastic bubble collapse for reduced standoff distance. The initial time steps look similar, despite that the vapor cavity is more elongated in wall normal direction for the viscoelastic fluid. During jet impingement on the solid wall, the liquid jet penetrates below the vapor cavity for the LPTT case. Due to the absence of liquid penetrating below the vapor cavity in the Newtonian case, a narrower and more focused jet is observed. The

subsequent high-pressure region exhibits higher pressures for the Newtonian collapse.

Figure 20 shows the pressure evolution at the position of maximum occurring pressure at the wall and along the centerline, respectively. The reference case ($h^* = 1.1$) is shown for comparison. For the Newtonian case, the maximum pressure at the wall does not occur at the center. We also show the pressure evolution at the center to compare the pressures induced by jet impingement. We observe that the maximum pressures at the wall are larger for decreased standoff distance compared to the reference case for both fluids. Pressure maxima at the wall are not caused by jet impingement but by the subsequent collapse for both fluids. The pressure curves at the wall center position reveal a pre-compression due to jet impingement, which is followed by a higher pressure peak originating from the actual collapse. Furthermore, an additional prominent pressure peak induced by the second collapse ($t \approx 3.9 \times 10^{-6}$ s) of the re-evaporation vapor can be observed for the LPTT fluid. By looking at the positions of maximum pressure along the centerline, we observe that the maximum pressures in the field are smaller than for the reference case for both fluids.

To explain the different collapse dynamics in Newtonian and viscoelastic fluid, stress evolution is examined in more detail. In the following, we only show the development of the most relevant stress components τ_{11} in Figs. 21 and 22. For the interested reader, the remaining components are included in Appendix A. We again observe a distinct viscoelastic stress layer $\tau_{M,11}$ in the LPTT fluid right above the solid wall, pulling vapor in opposite x_1 -directions and leading to the larger vapor cavity after the rebound than for the Newtonian case.

Next, the collapse dynamics for the increased initial distance $h^* = 1.5$ is investigated. Figures 23 and 24 show the evolution of the collapse in Newtonian and LPTT fluid. In the Newtonian fluid, the bubble entirely collapses before the liquid jet pierces through the bubble. After a violent collapse, a toroidal vapor cavity re-evaporates before the second collapse. In the viscoelastic fluid, the liquid jet vertically pierces through the bubble before the collapse. During rebound, a large heart-shaped vapor cavity is formed ($t = 4 \times 10^{-6}$ s). Due to the larger vapor cavity, the second collapse is more violent than in the Newtonian fluid.

Figure 25 compares the pressure wave formation during the first collapse between Newtonian and LPTT fluid. As mentioned, we can only observe jet piercing in LPTT fluid. The fundamental collapse is more focused for the Newtonian fluid since there is no separation of high-pressure regions due to piercing.

The pressure evolutions for increased standoff distance are shown in Fig. 26 and compared to the reference case. The top row of Fig. 26 shows the pressure evolution over time at the location where the maximum wall pressure occurs. For both the Newtonian and the LPTT case, the pressures are smaller than in the reference case. Yang *et al.*²⁰ also observed decreasing wall pressures for increasing standoff distances. The pressure peak during the first collapse is slightly higher for the LPTT fluid. The second collapse leads to much stronger pressure impact at the wall in LPTT as compared to the Newtonian case. We attribute this observation to the larger re-evaporated cavity during rebound in LPTT. Furthermore, a pressure rise around $t \approx 4.5 \times 10^{-6}$ s is present in LPTT, which is caused by jet impact (cf. Fig. 4) and cannot be detected in the

Newtonian case. The pressures at the position of maximum pressure along the centerline are illustrated in the lower part of Fig. 26. The peak pressures are again smaller than in the reference case for both fluids. The maximum pressure in the LPTT is associated with the second collapse of the re-evaporated vapor. Additionally, the pressure evolution for the position of the maximum pressure during the first collapse is shown. The maximum pressure during the first collapse is larger in the Newtonian case due to the more focused collapse (cf. Fig. 25). However, the second collapse in LPTT is distinctly stronger than for the Newtonian fluid due to the mentioned extensive re-evaporation area.

Subsequently, we examine the relevant stress components. τ_{11} is illustrated in Figs. 27 and 28. A large region of positive $\tau_{M,11}$ stresses formed along the solid wall can be seen for the viscoelastic stress. These stresses are responsible for the cusped concave shape ($t = 4.6 \times 10^{-6}$ s) of the bubble during the collapse, an effect also described in Lind and Phillips.^{39,59} The viscoelastic stresses along the solid wall pull fluid radially away, creating suction that

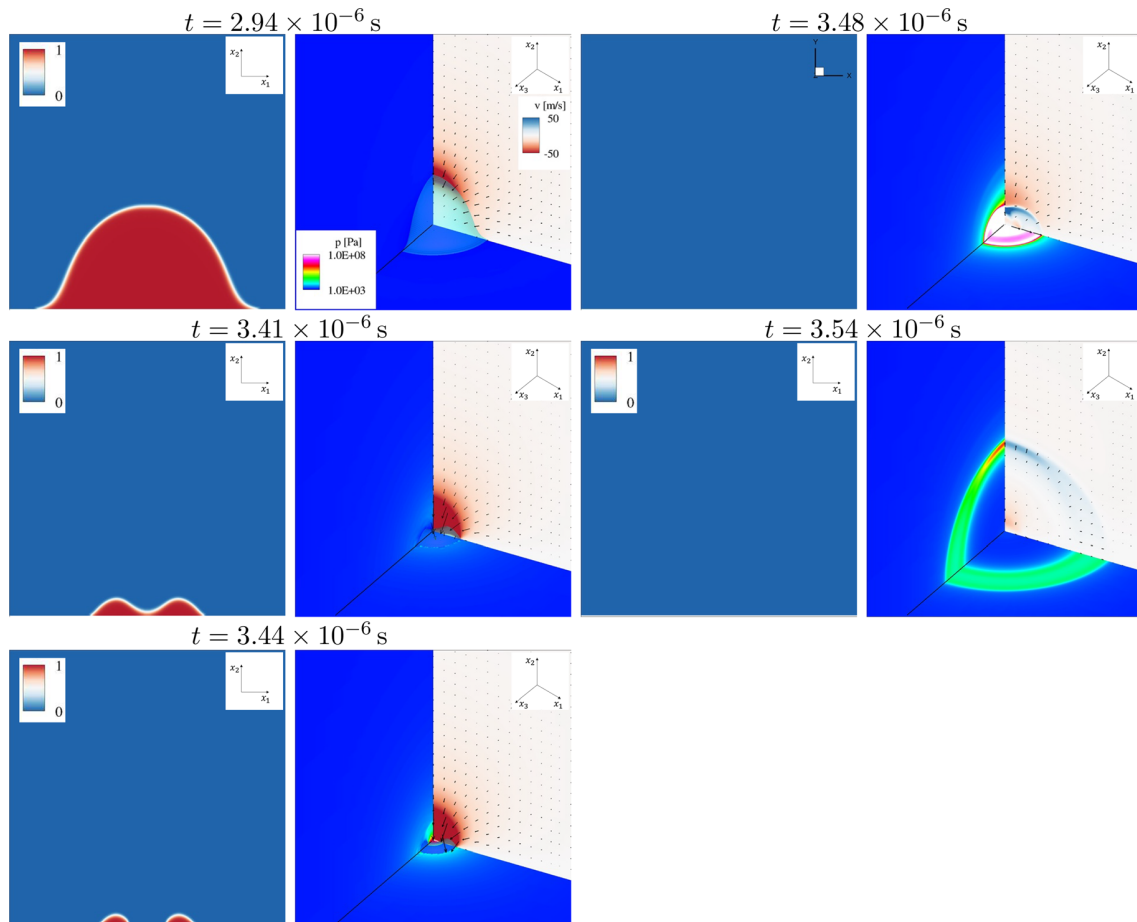


FIG. 17. Collapse in Newtonian fluid for initial standoff distance $h^* = 0.35$ and $Re = 40$. First and third column: vapor volume fraction α (—). Second and fourth columns: Velocity in x_2 -direction u_2 (m/s) through the x_1/x_2 -midplane and velocity vectors scaled by the velocity magnitude. Pressure distribution p (Pa) through the x_2/x_3 -midplane and at the wall. Isosurface shows constant vapor content of $\alpha = 0.01$.

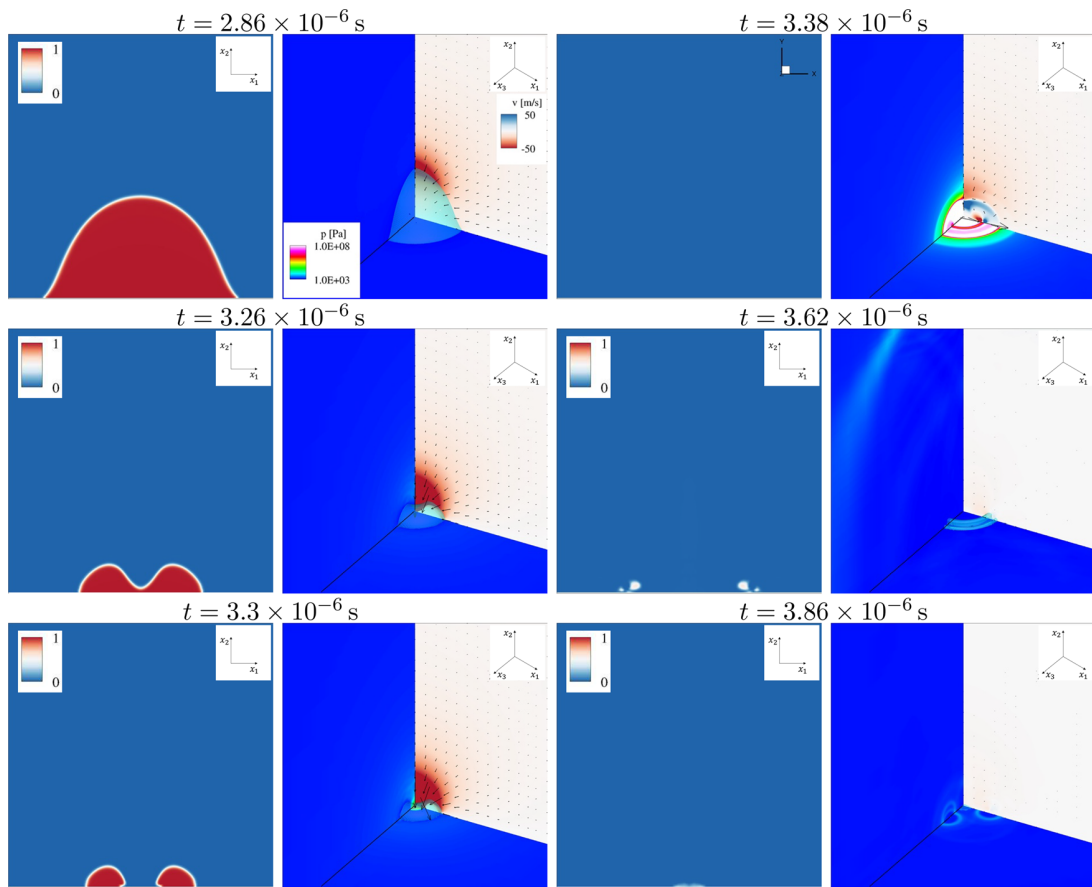


FIG. 18. Collapse in LPTT fluid for initial standoff distance $h^* = 0.35$ and $Re = 40$, $De = 2$. First and third column: vapor volume fraction α (–). Second and fourth columns: Velocity in x_2 -direction u_2 (m/s) through the x_1/x_2 -midplane and velocity vectors scaled by the velocity magnitude. Pressure distribution p (Pa) through the x_2/x_3 -midplane and at the wall. Isosurface shows constant vapor content of $\alpha = 0.01$.

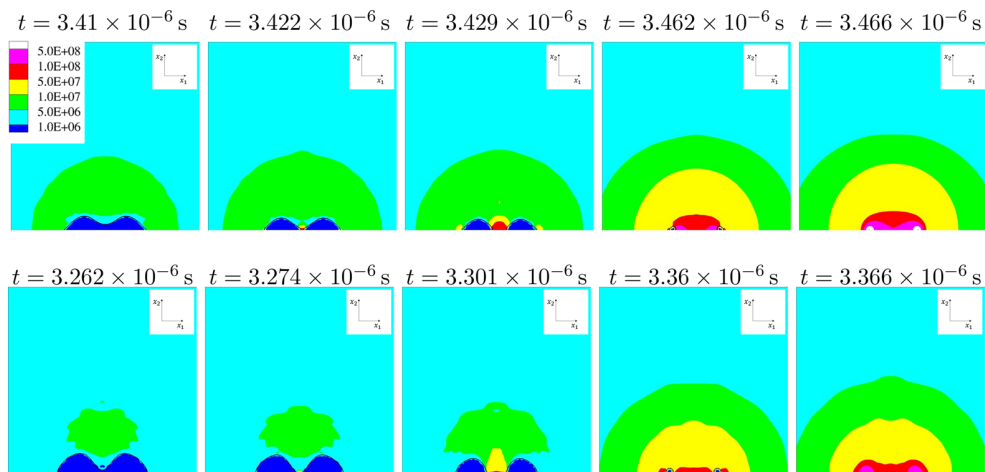


FIG. 19. Pressure distribution p (Pa) and illustration of shock formation during first collapse through the x_1/x_2 -midplane for $Re = 40$, $De = 2$, $h^* = 0.35$. Top: Newtonian fluid; bottom: LPTT fluid. Black isoline shows vapor content of $\alpha = 0.01$.

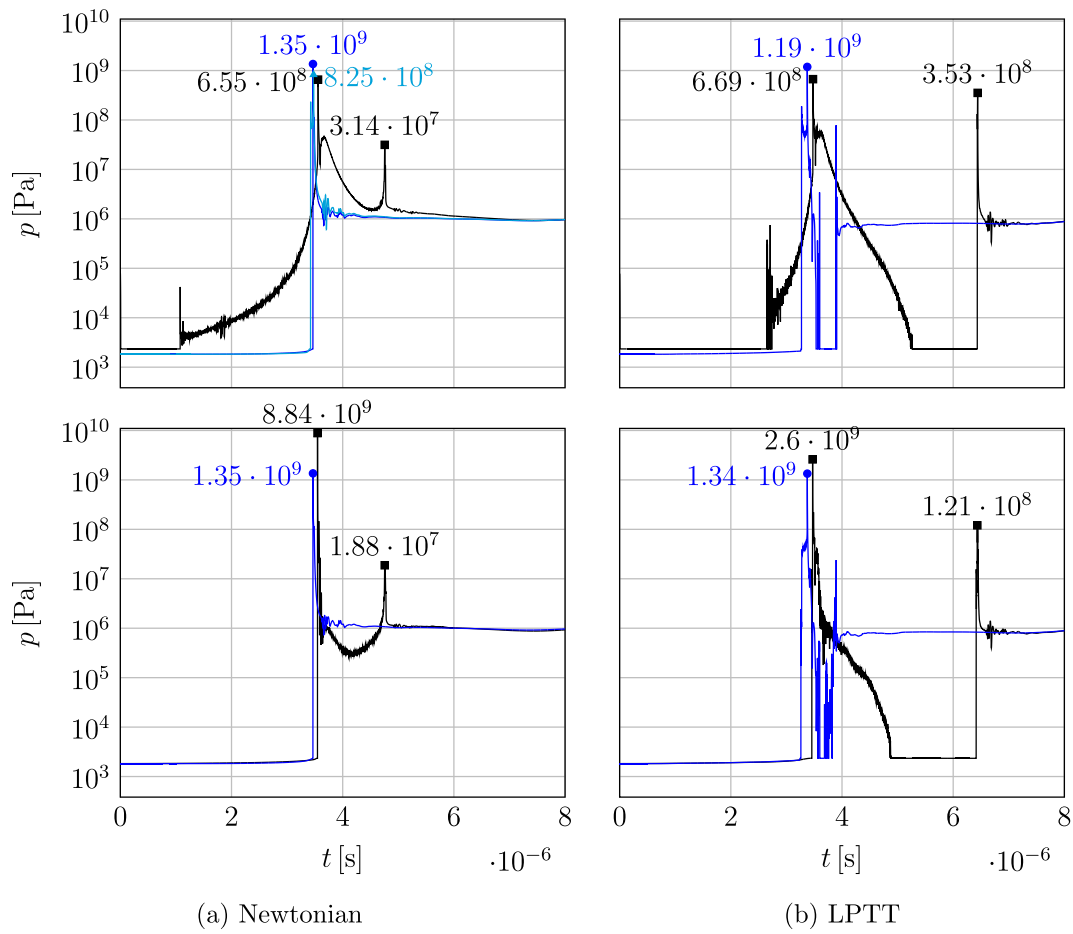


FIG. 20. Pressure p (Pa) for reduced initial standoff distance $h^* = 0.35$ vs reference case $h^* = 1.1$ at $Re = 40$, $De = 2$ (logarithmic scale). Top: at the wall ($x_2^* = 0$): (a) Newtonian fluid: blue line—at $r^* = 0.25$ (location of maximum pressure), light blue line— $r^* = 0$, black line—reference case ($h^* = 1.1$) at $r^* = 0$; (b) LPTT: blue line—at $r^* = 0$, black line—reference case ($h^* = 1.1$) at $r^* = 0$. Bottom: Along the centerline at the position of maximum pressure: (a) Newtonian fluid: blue line—at $x_2^* = 0$, black line—reference case ($h^* = 1.1$) at $x_2^* = 0.22$; (b) LPTT: blue line—LPTT fluid at $x_2^* = 0.06$, black line—reference case ($h^* = 1.1$) at $x_2^* = 0.16$.

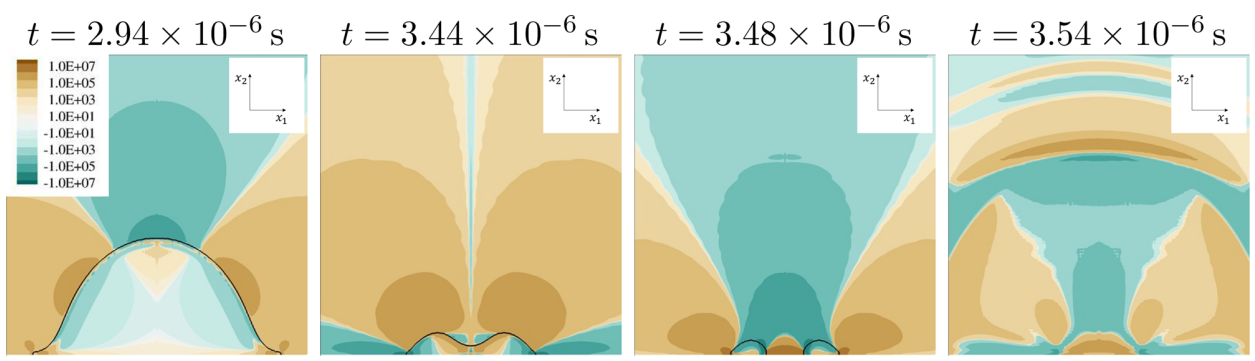


FIG. 21. Solvent stress $\tau_{S,11}$ (Pa) through x_2/x_3 -midplane for $Re = 40$, $h^* = 0.35$ in Newtonian fluid. Black isoline shows vapor content of $\alpha = 0.01$.

11 January 2024 12:51:18

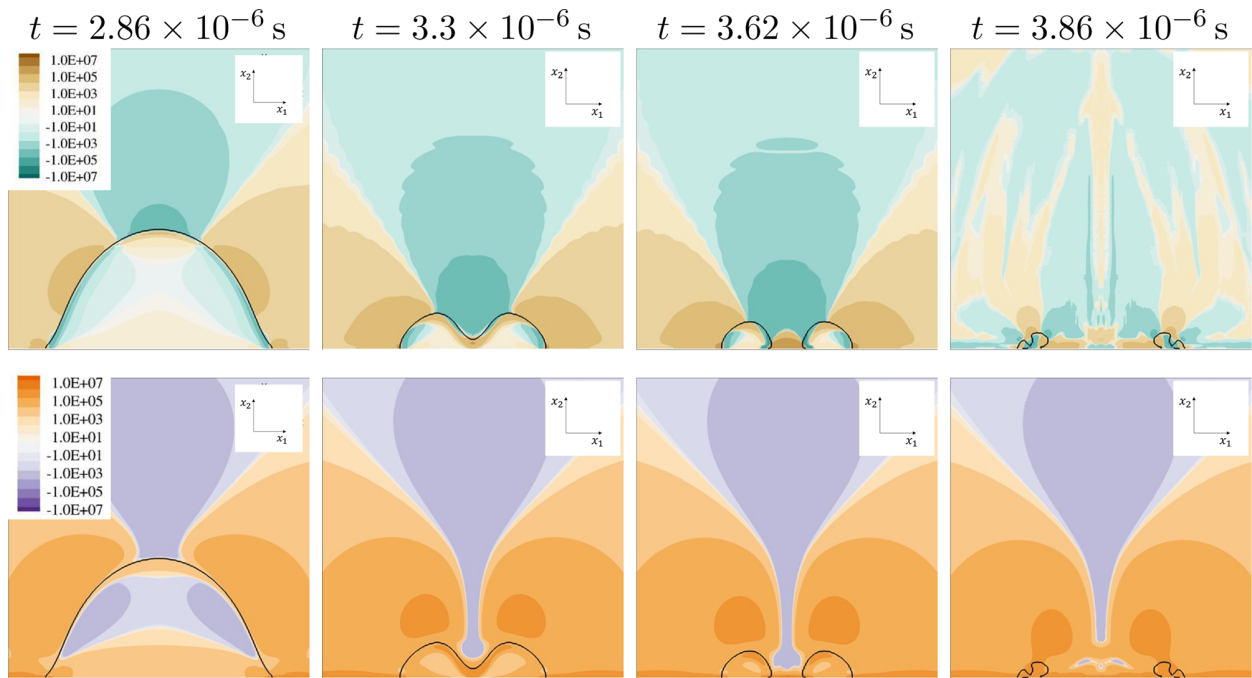


FIG. 22. Stress through x_2/x_3 -midplane for $Re = 40$, $De = 2$, $h^* = 0.35$ in LPTT fluid. Black isoline shows constant vapor content of $\alpha = 0.01$. Top: solvent stress $\tau_{S,11}$ (Pa); bottom: viscoelastic stress $\tau_{M,11}$ (Pa).

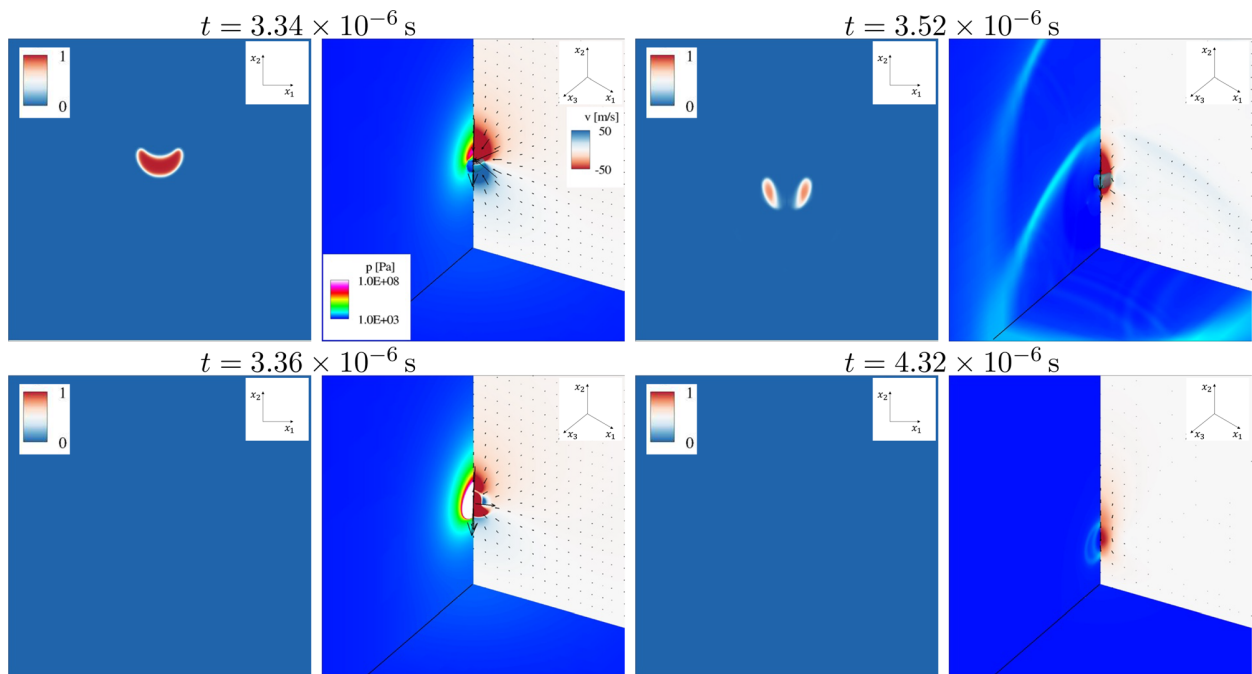


FIG. 23. Collapse in Newtonian fluid for initial standoff distance $h^* = 1.5$ and $Re = 40$. First and third column: vapor volume fraction α (-). Second and fourth columns: Velocity in x_2 -direction u_2 (m/s) through the x_1/x_2 -midplane and velocity vectors scaled by the velocity magnitude. Pressure distribution p (Pa) through the x_2/x_3 -midplane and at the wall. Isosurface shows constant vapor content of $\alpha = 0.01$.

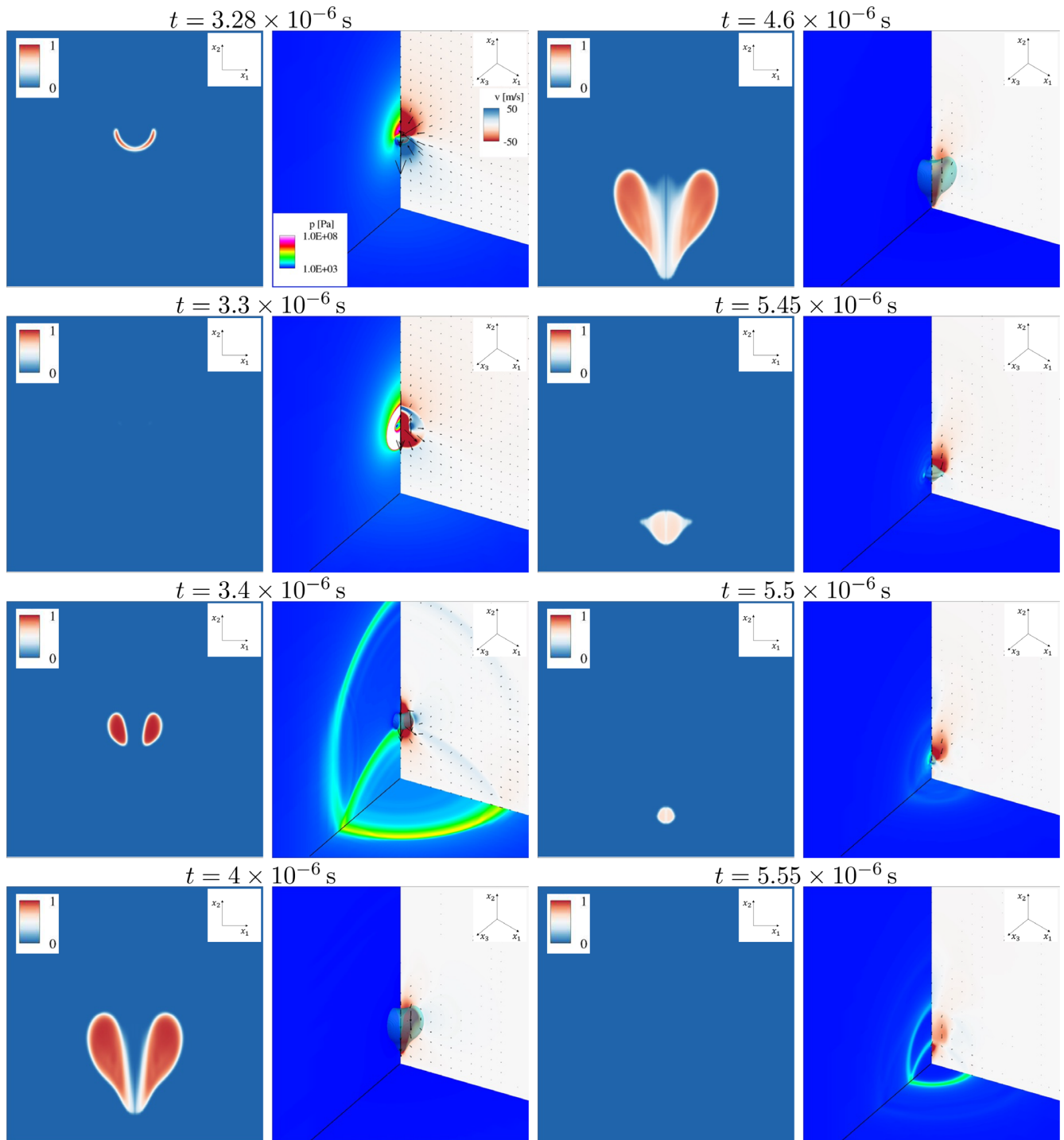


FIG. 24. Collapse in LPTT fluid for initial standoff distance $h^* = 1.5$ and $Re = 40$, $De = 2$. First and third column: vapor volume fraction α (—). Second and fourth columns: Velocity in x_2 -direction u_2 (m/s) through the x_1/x_2 -midplane and velocity vectors scaled by the velocity magnitude. Pressure distribution p (Pa) through the x_2/x_3 -midplane and at the wall. Isosurface shows constant vapor content of $\alpha = 0.01$.

11 January 2024 12:51:18

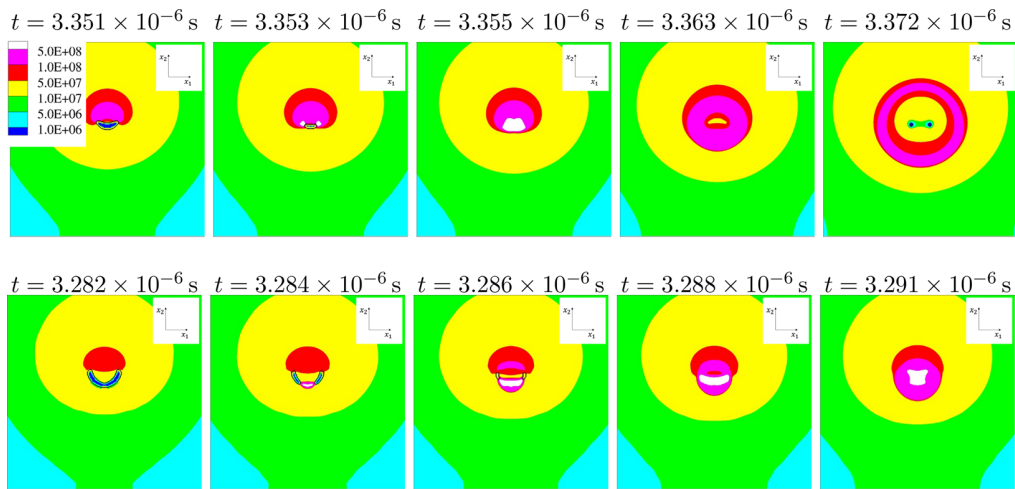


FIG. 25. Pressure distribution p (Pa) and illustration of shock formation during first collapse through the x_1/x_2 -midplane for $Re = 40$, $De = 2$, $h^* = 1.5$. Top: Newtonian fluid; bottom: LPTT fluid. Black isoline shows vapor content of $\alpha = 0.01$.

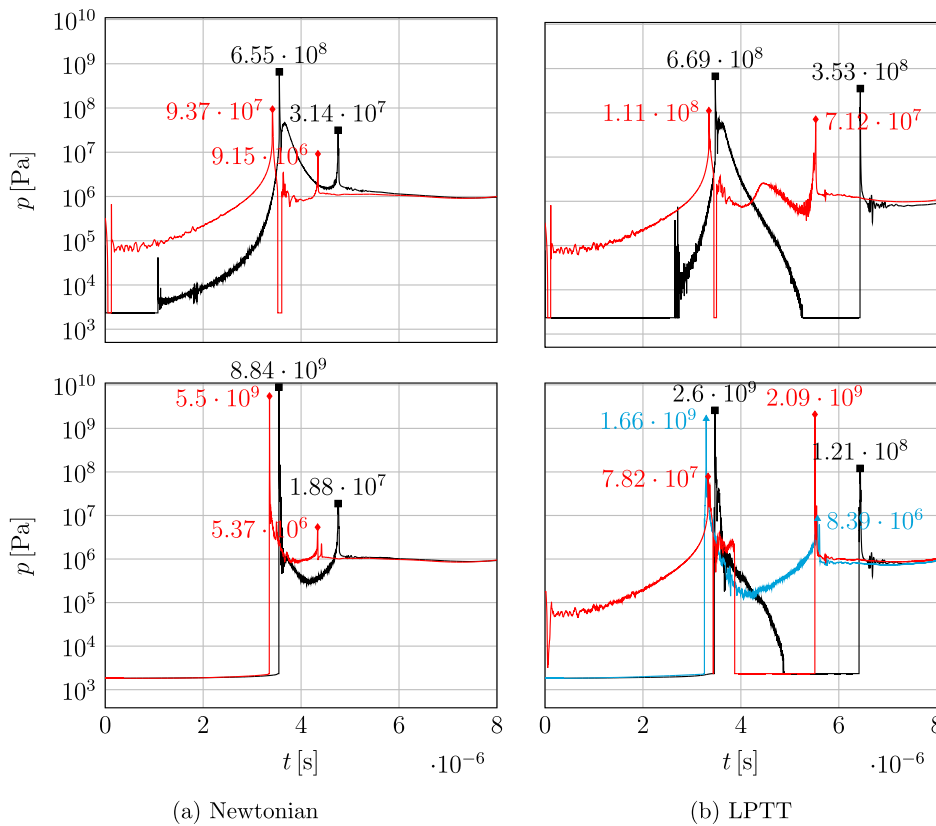


FIG. 26. Pressure p (Pa) for increased initial standoff distance $h^* = 1.5$ vs reference case $h^* = 1.1$ at $Re = 40$, $De = 2$ (logarithmic scale). Top: at the wall ($x_2^* = 0$) at the location of maximum pressure: (a) Newtonian fluid: red line—at $r^* = 0.02$, black line—reference case ($h^* = 1.1$) at $r^* = 0.02$; (b) LPTT: red line— $r^* = 0$, black line—reference case ($h^* = 1.1$) at $r^* = 0$. Bottom: Along the centerline at the position of maximum pressure: (a) Newtonian fluid: red line—at $x_2^* = 1.13$, black line—reference case ($h^* = 1.1$)—at $x_2^* = 0.22$; (b) LPTT: red line at $x_2^* = 0.29$ (location of maximum pressure), light blue line—at $x_2^* = 1.19$, black line—reference—case ($h^* = 1.1$) at $x_2^* = 0.16$.

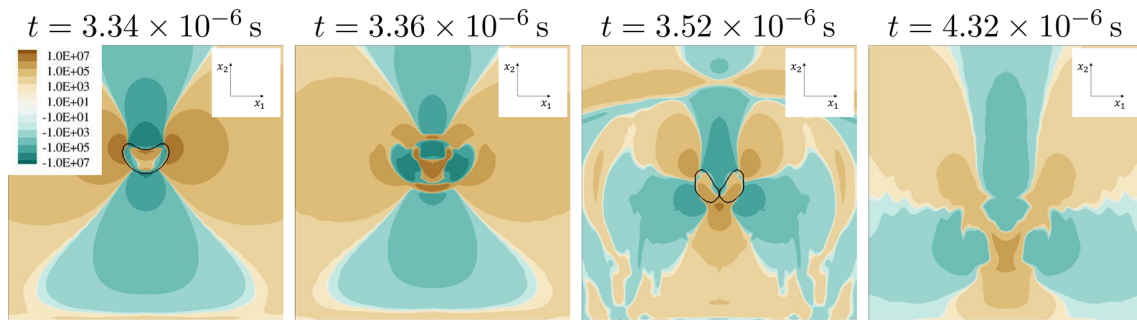


FIG. 27. Solvent stress $\tau_{S,11}$ (Pa) through the x_2/x_3 -midplane for different time instants during the collapse for $Re = 40$ and initial standoff distance $h^* = 1.5$ in Newtonian fluid. Black isoline shows constant vapor content of $\alpha = 0.01$.

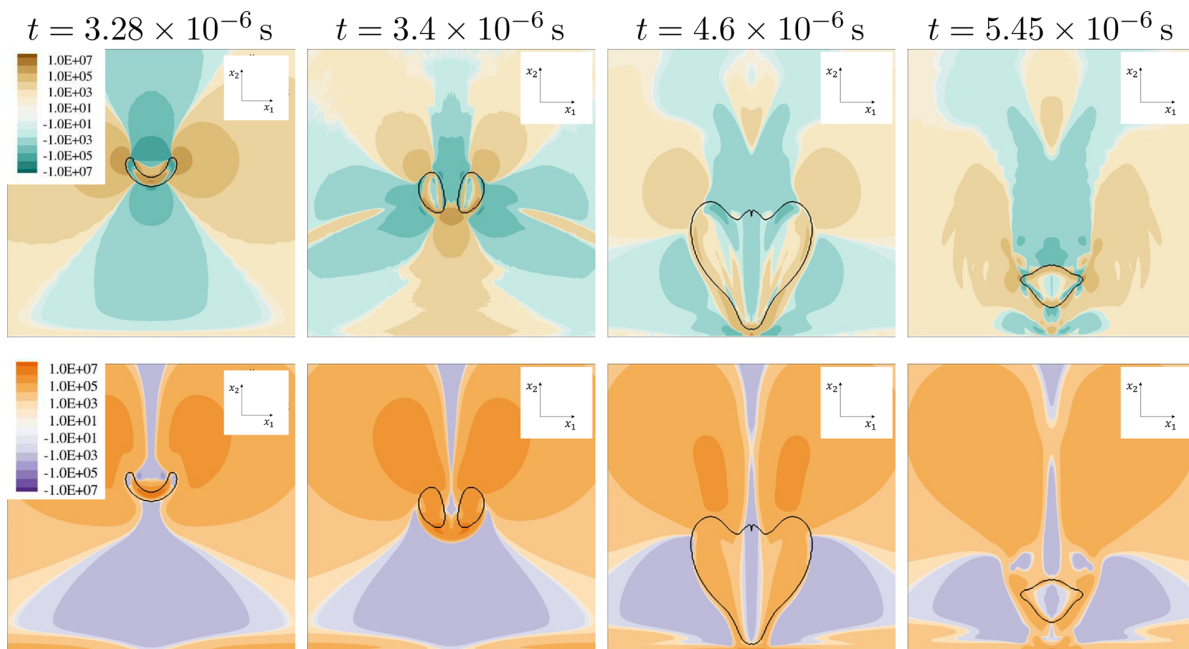


FIG. 28. Stress through x_2/x_3 -midplane for $Re = 40$, $De = 2$, $h^* = 1.5$ in LPTT fluid. Black isoline shows constant vapor content of $\alpha = 0.01$. Top: solvent stress $\tau_{S,11}$ (Pa); bottom: viscoelastic stress $\tau_{M,11}$ (Pa).

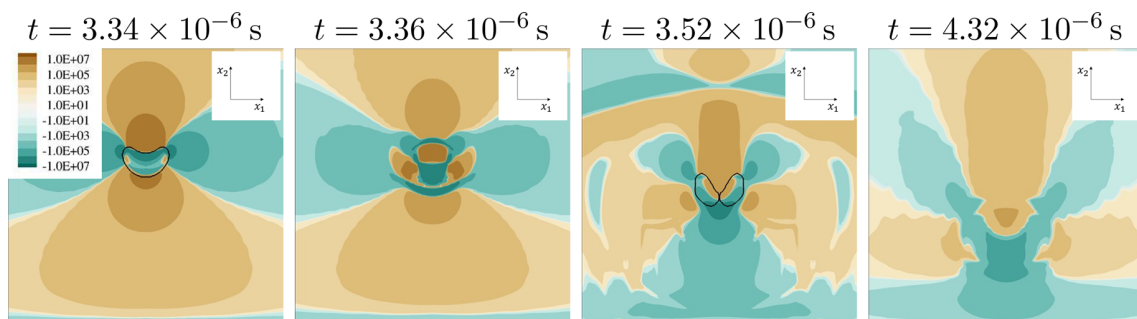


FIG. 29. Solvent stress $\tau_{S,22}$ (Pa) through the x_2/x_3 -midplane for different time instants during the collapse for $Re = 40$ and initial standoff distance $h^* = 1.5$ in Newtonian fluid. Black isoline shows constant vapor content of $\alpha = 0.01$.

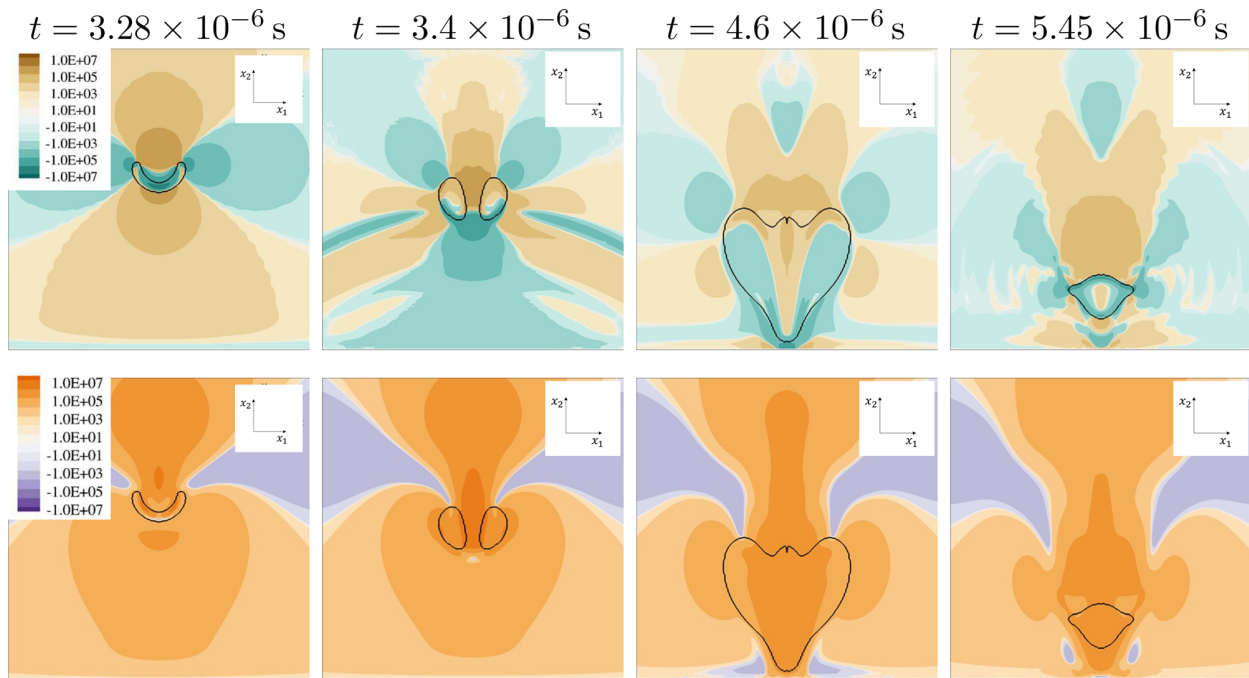


FIG. 30. Stress through x_2/x_3 -midplane for $Re = 40$, $De = 2$, $h^* = 1.5$ in LPTT fluid. Black isoline shows constant vapor content of $\alpha = 0.01$. Top: solvent stress $\tau_{s,22}$ (Pa); bottom: viscoelastic stress $\tau_{M,22}$ (Pa).

accelerates fluid from the bulk of the bubble. Furthermore, the Newtonian case exhibits larger solvent stresses than the LPTT fluid, again due to the additional viscoelastic stresses emerging in the LPTT case.

By looking at the τ_{22} stress components in Figs. 29 and 30, it can be appreciated that significant viscoelastic stresses $\tau_{M,22}$

covering two lengthy regions above the vapor cavity during rebound for the LPTT case ($t = 3.4 \times 10^{-6}$ s, $t = 4.6 \times 10^{-6}$ s). These stresses yield positive forces in x_2 -direction, resulting in the observed heart-shaped vapor cavity before the second collapse. For completeness, the remaining stress distributions are included in Appendix B.

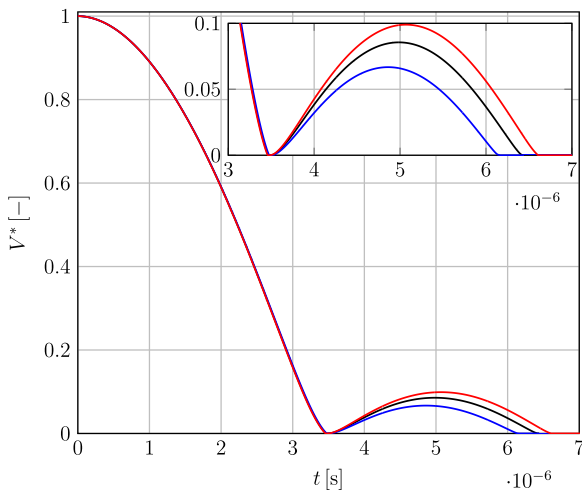


FIG. 31. Non-dimensional vapor content in the domain over time for $Re = 40$, $h^* = 1.1$ and different relaxation times in LPTT fluid; close-up of the rebound. Blue line— $De = 1$, black line— $De = 2$, red line— $De = 4$.

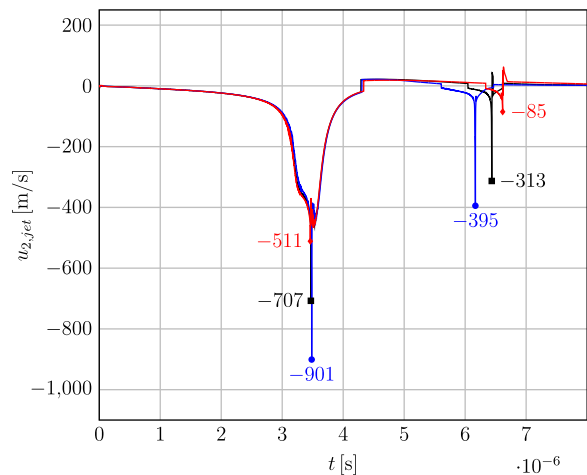


FIG. 32. Jet velocity $u_{2,jet}$ (m/s) in x_2 -direction over time measured at centerline for $Re = 40$, $h^* = 1.1$ and different relaxation times in LPTT fluid. Blue line— $De = 1$, black line— $De = 2$, red line— $De = 4$.

C. Variation of elasticity

The following section investigates the influence of elasticity, respectively, the variation of relaxation time, for the LPTT case.

The Reynolds number $Re=40$ remains unchanged. Figure 31 shows the vapor content over time for the three considered Deborah numbers $De = \{1, 2, 4\}$. For all cases, we observe a distinct rebound after the initial complete collapse. The largest vapor

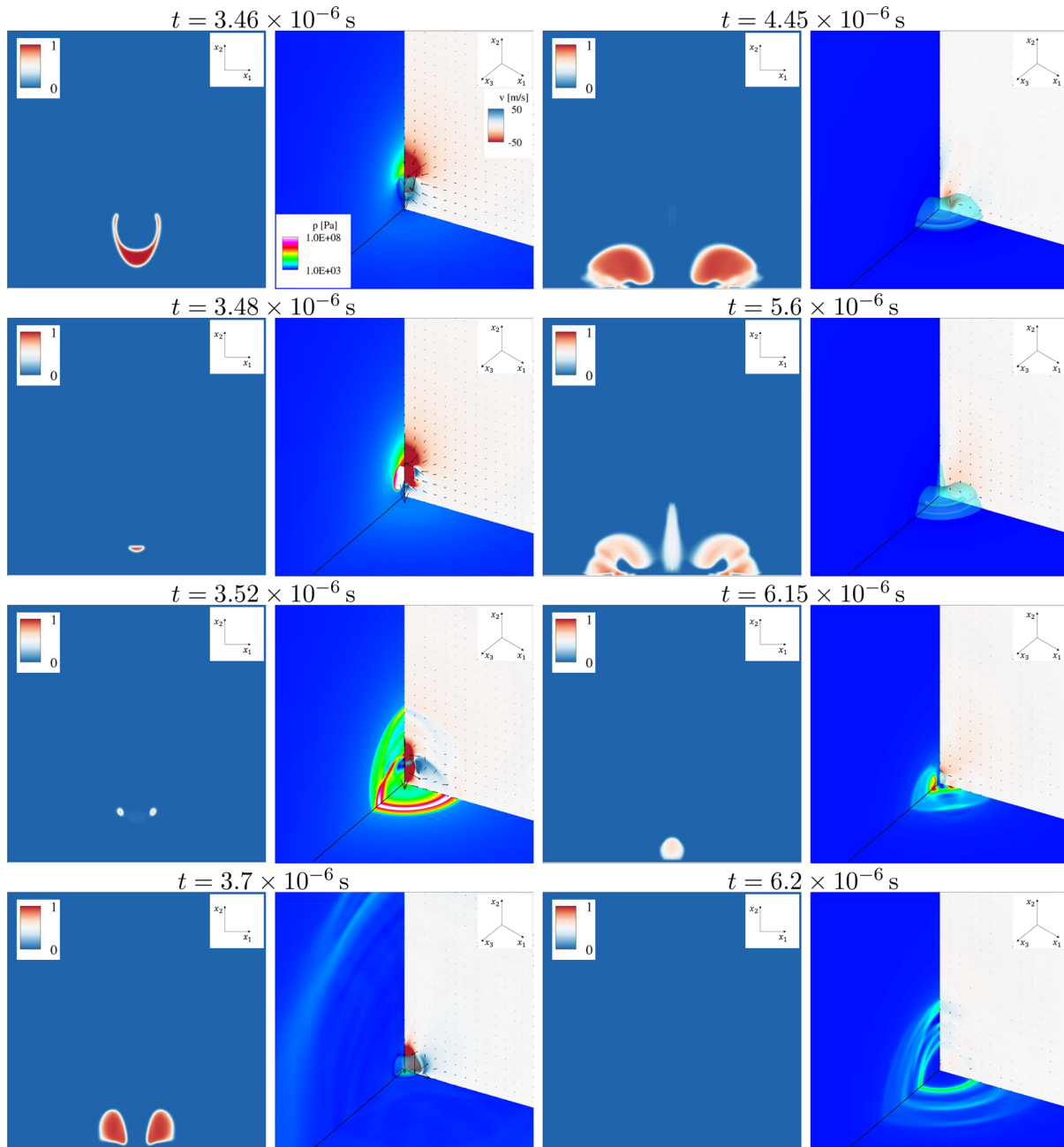


FIG. 33. Collapse in LPTT fluid for $Re = 40$, $De = 1$, $h^* = 1.1$ (increased relaxation time). First and third column: vapor volume fraction α (–). Second and fourth columns: Velocity in x_2 -direction u_2 (m/s) through the x_1/x_2 -midplane and velocity vectors scaled by the velocity magnitude. Pressure distribution p (Pa) through the x_2/x_3 -midplane and at the wall. Isosurface shows constant vapor content of $\alpha = 0.01$.

11 January 2024 12:51:18

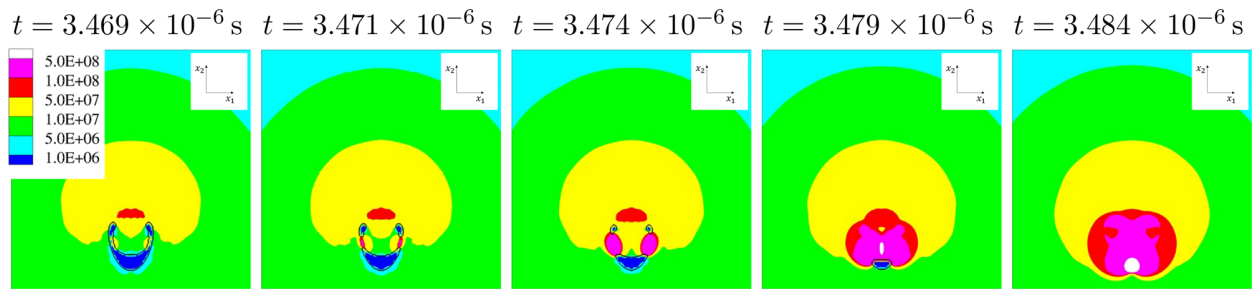


FIG. 34. Pressure distribution p (Pa) and illustration of shock formation during first collapse through the x_1/x_2 -midplane for $Re = 40$, $De = 1$, $h^* = 1.1$ in LPTT fluid. Black isoline shows vapor content of $\alpha = 0.01$.

content during re-evaporation is observed for the largest elasticity $De = 4$, whereas the smallest vapor content is produced for the smallest elasticity $De = 1$. A comparison of the jet velocities in Fig. 32 reveals that the largest jet velocity magnitudes occur for the

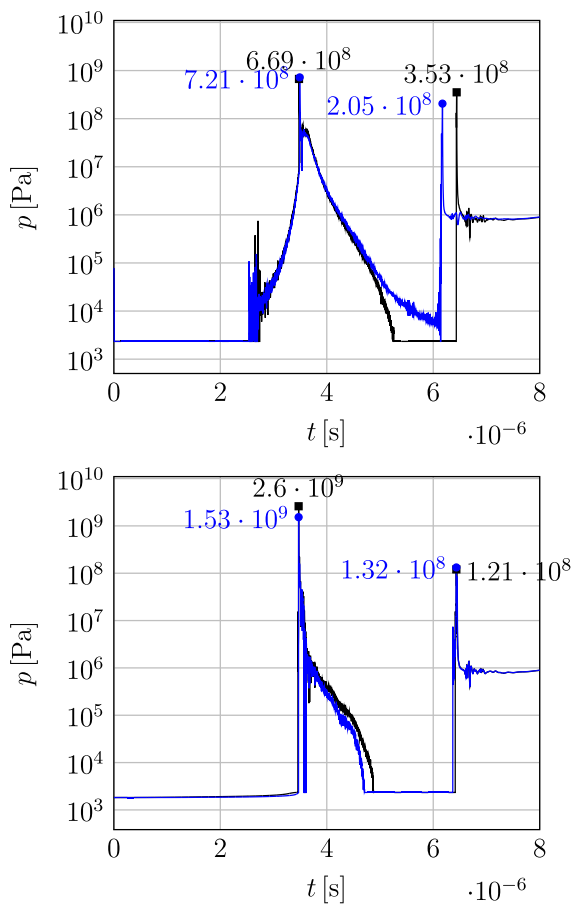


FIG. 35. Pressure p (Pa) for decreased elasticity $De = 1$ vs reference case $De = 2$ at $Re = 40$, $h^* = 1.1$ (logarithmic scale) in LPTT fluid. Top: at the wall ($x_2^* = 0$) at the location of maximum pressure: Blue line— $De = 1$ at $r^* = 0.05$ and black line—the reference case ($De = 2$) at $r^* = 0$. Bottom: Along the centerline at the position of maximum pressure blue line— $De = 1$ at $x_2^* = 0.195$ and black line—the reference case at $x_2^* = 0.155$.

smallest elasticity $De = 1$ during the first and second collapse. The jet velocities are smallest for the largest elasticity $De = 4$. In Fig. 33, the collapse behavior for decreased elasticity ($De = 1$) is depicted. It appears generally similar to the reference case, including splashing. The collapse appears to be more focused with decreasing elasticity. Figure 34 shows the formation of the emitted shock waves during the first collapse. The overall phenomenology is comparable to the reference case. Radial impingement of the water-hammer is followed by the collapse of the remaining vapor cavities, and the pressure waves of the water-hammer and collapse (complete condensation) overlap.

For the pressure evolutions at the position of maximum pressure at the wall (top of Fig. 35) and at the centerline (bottom of Fig. 35), we can observe that the maximum emitted pressure at the wall is marginally increased for $De = 1$ as compared to the reference case. The pressure at the wall due to the second collapse is larger for the reference case, which can be associated with the increased water cavity produced during rebound. For the location of the maximum pressure along the centerline, the first collapse of the reference case is more intense, while the pressure generated by the second collapse is almost similar. All stress distributions for the case with decreased and increased elasticity can be found in Appendixes C and D.

Figure 36 depicts different stages of the collapse for increased relaxation ($De = 4$). It is observed that more vapor is produced during rebound than for the other elasticity. However, the qualitative collapse evolution is similar for all cases with identical initial standoff distance $h^* = 1.1$.

The pressure distribution over time depicted in Fig. 37 shows a radial impingement of the water-hammer toward the other side of the vapor cavity, followed by the complete collapse of the bubble. The pressures over time at the locations of maximum occurring pressures in Fig. 38 reveal that the pressure at the wall is smaller for the first and second collapse compared to the reference. At the location of maximum pressure along the centerline, the pressure of the first collapse is also smaller for increased elasticity. The pressure during the second collapse is of comparable magnitude for the increased and the reference elasticity.

V. CONCLUSION

Viscoelastic vapor bubble collapse near solid walls is investigated conducting fully compressible 3D simulations using the linear Phan-Thien Tanner viscoelastic model. The following novelties apply to the investigation:

11 January 2024 12:51:18

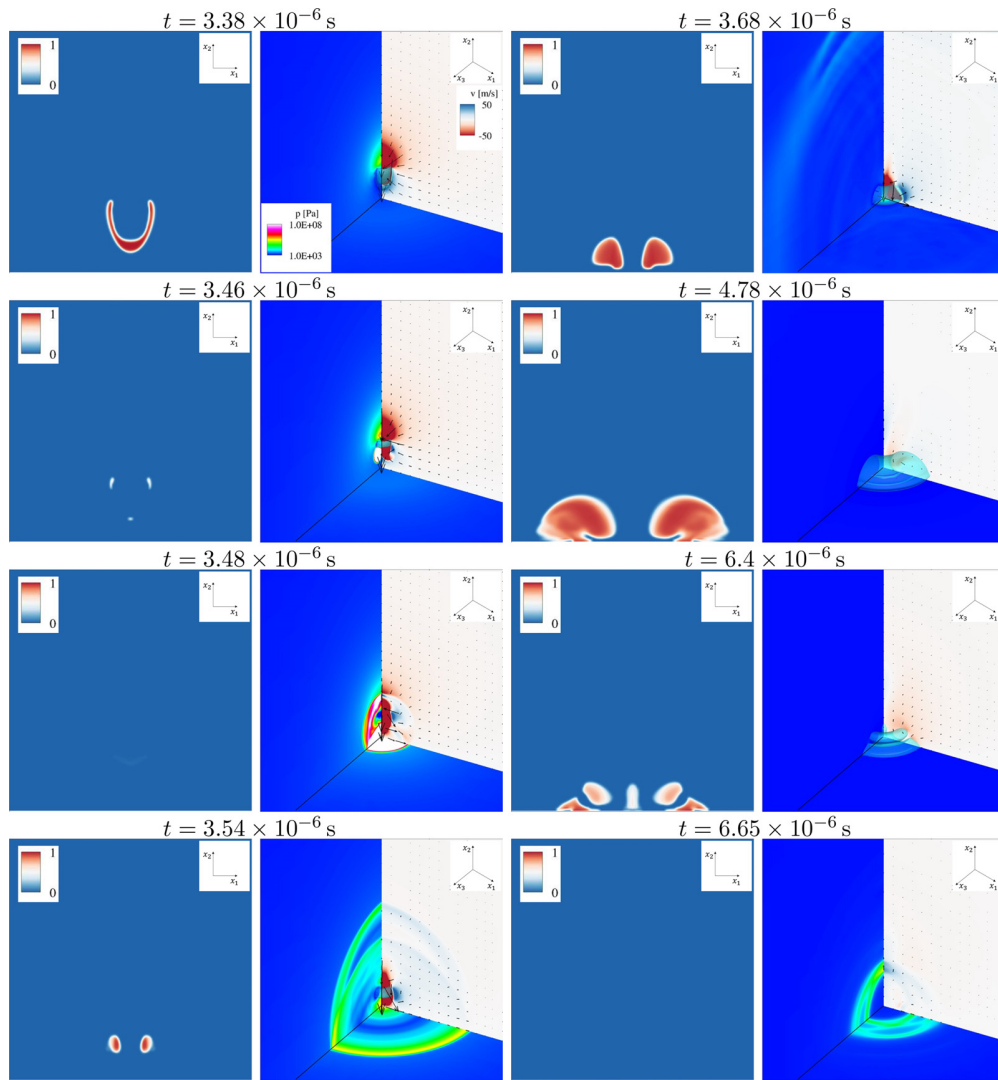


FIG. 36. Collapse in LPTT fluid for $Re = 40$, $De = 4$, $h^* = 1.1$ (increased relaxation time). First and third column: vapor volume fraction α (–). Second and fourth columns: Velocity in x_2 -direction u_2 (m/s) through the x_1/x_2 -midplane and velocity vectors scaled by the velocity magnitude. Pressure distribution p (Pa) through the x_2/x_3 -midplane and at the wall. Isosurface shows constant vapor content of $\alpha = 0.01$.

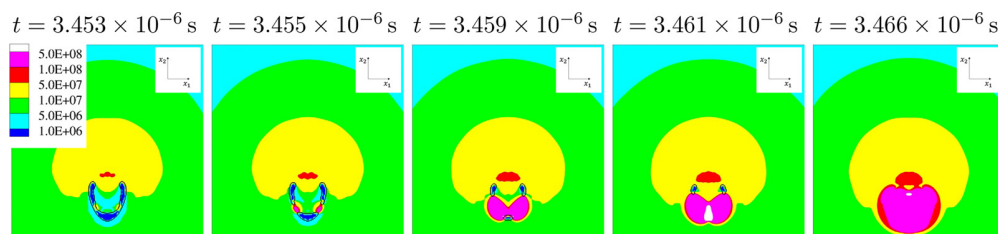


FIG. 37. Pressure distribution p (Pa) and illustration of shock formation during first collapse through the x_1/x_2 -midplane for $Re = 40$, $De = 4$, $h^* = 1.1$ in LPTT fluid. Black isoline shows vapor content of $\alpha = 0.01$.

11 January 2024 12:51:18

- Usage of viscoelastic constitutive model including solvent contribution and shear-thinning behavior (LPTT).
- Application of a fully 3D-approach.
- Fully compressible method enables resolution of shock wave formation and of emitted pressure waves.
- Simulation of a cavitating vapor bubble considering condensation and evaporation in contrast to gas-filled bubbles neglecting condensation and evaporation.^{38–40}

The near-wall collapse for different initial wall-distances by comparing the results of viscoelastic and Newtonian fluid reveals that viscoelasticity can strongly affect collapse dynamics. For wall-detached bubbles, viscoelasticity changes the shock wave formation mechanism by introducing liquid-jet-piercing, which cannot be observed for Newtonian collapse. Furthermore, viscoelasticity significantly increases

the amount of re-evaporated fluid during the rebound for the considered standoff distances. While the pressure emitted during the first collapse is larger or comparable for the Newtonian fluid, the pressure peak during the second collapse is considerably larger in the viscoelastic liquid for all cases. Furthermore, the re-evaporated fluid generates a second jet only for the viscoelastic collapse. For initially wall-attached bubbles, re-evaporation and subsequent second collapse is only observed for the viscoelastic fluid. The different collapse dynamics are caused by the additional viscoelastic stresses. Analyzing solvent and viscoelastic stress distributions shows a smoother distribution of the viscoelastic compared to the solvent stresses due to relaxation. We observe that viscoelastic stresses influence the amount of re-evaporation during rebound. The variation of elasticity shows that the vapor produced during rebound is correlated with the relaxation time. Increasing the relaxation time yields significantly more vapor, at least for the range of investigated parameters. The jet velocity is largest for the lowest elasticity.

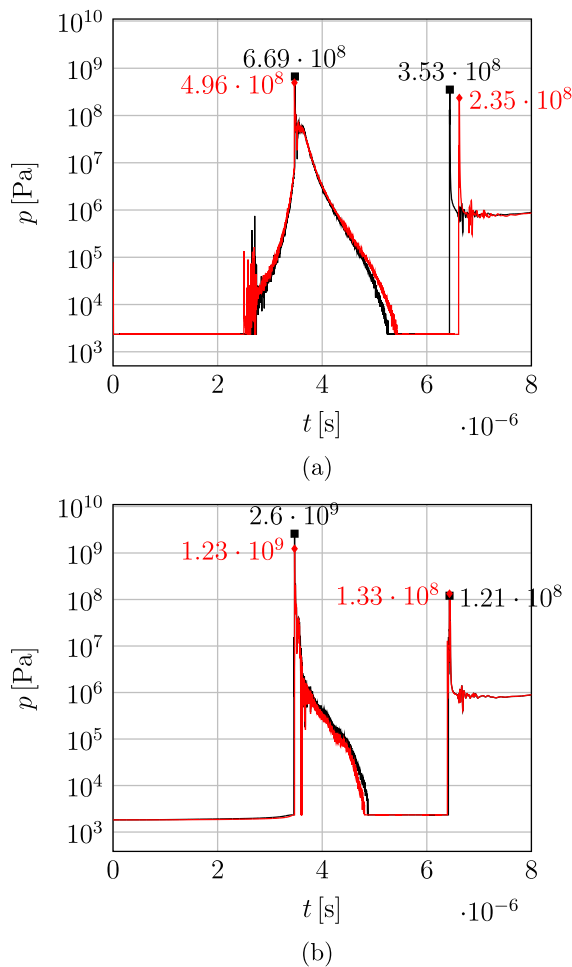


FIG. 38. Pressure p (Pa) for decreased elasticity $De = 4$ vs reference case $De = 2$ at $Re = 40$, $h^* = 1.1$ (logarithmic scale) in LPTT fluid. (a) At the wall ($x_2^* = 0$) at the location of maximum pressure: red line— $De = 4$ at $r^* = 0.035$ and black line—the reference case ($De = 2$) at $r^* = 0$. (b) Along the centerline at the position of maximum pressure: red line— $De = 4$ at $x_2^* = 0.175$ and black line—the reference case ($De = 2$) at $x_2^* = 0.155$.

ACKNOWLEDGMENTS

The authors gratefully acknowledge the Leibniz Supercomputing Centre for funding this project by providing computing time and support on its Linux-Cluster. The first author is member of the Technical University of Munich (TUM) Graduate School.

AUTHOR DECLARATIONS

Conflict of Interest

The authors have no conflicts to disclose.

Author Contributions

Christian Lang: Conceptualization (lead); Data curation (lead); Formal analysis (lead); Investigation (lead); Methodology (lead); Software (lead); Validation (lead); Visualization (lead); Writing – original draft (lead); Writing – review & editing (lead). **Stefan Adami:** Conceptualization (supporting); Formal analysis (supporting); Investigation (supporting); Supervision (equal); Visualization (supporting); Writing – original draft (supporting); Writing – review & editing (equal). **Nikolaus A. Adams:** Funding acquisition (lead); Supervision (lead); Writing – review & editing (equal).

DATA AVAILABILITY

The data that support the findings of this study are available from the corresponding author upon reasonable request.

APPENDIX A: VISCOUS AND VISCOELASTIC STRESS DISTRIBUTIONS FOR $Re = 40$, $De = 2$, $h^* = 0.35$

The following figures show the stress distributions for an initial standoff distance $h^* = 0.35$ and $Re = 40$, $De = 2$ for different time instants. Figures 39 and 41 illustrate the solvent stress distributions for the Newtonian collapse and Figs. 40 and 42 depict the solvent and viscoelastic stress distributions for the collapse in LPTT fluid.

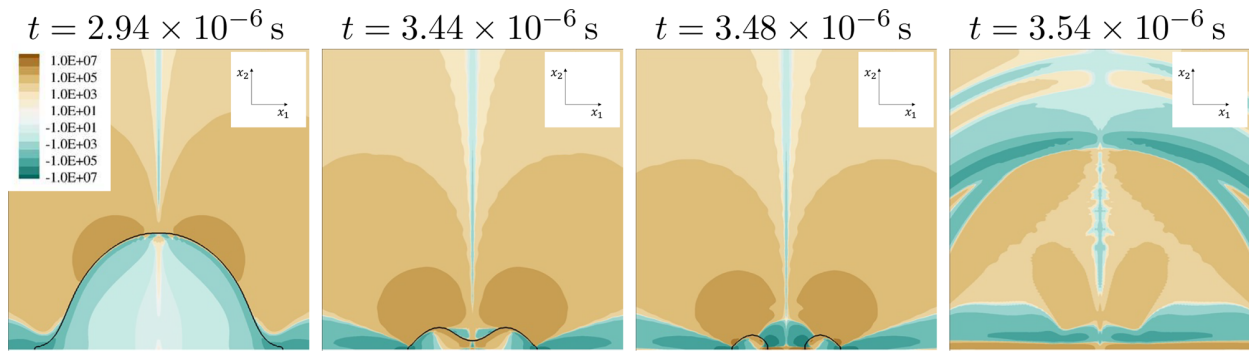


FIG. 39. Solvent stress $\tau_{S,12}$ (Pa) through x_2/x_3 -midplane for $Re = 40$, $h^* = 0.35$ in Newtonian fluid. Black isoline shows vapor content of $\alpha = 0.01$.

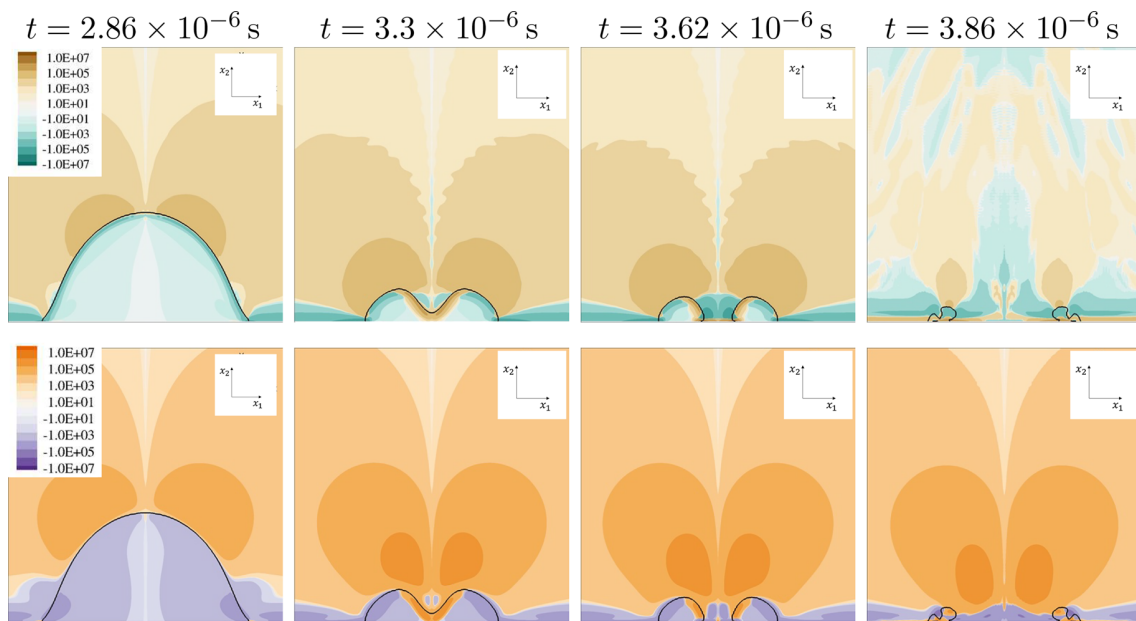


FIG. 40. Stress through x_2/x_3 -midplane for $Re = 40$, $De = 2$, $h^* = 0.35$ in LPTT fluid. Black isoline shows constant vapor content of $\alpha = 0.01$. Top: solvent stress $\tau_{S,12}$ (Pa); bottom: viscoelastic stress $\tau_{M,12}$ (Pa).

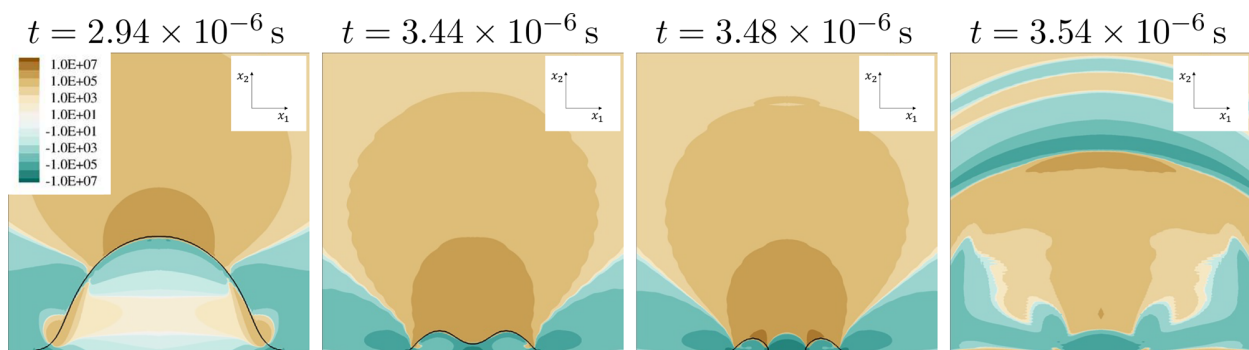


FIG. 41. Solvent stress $\tau_{S,22}$ (Pa) through x_2/x_3 -midplane for $Re = 40$, $h^* = 0.35$ in Newtonian fluid. Black isoline shows vapor content of $\alpha = 0.01$.

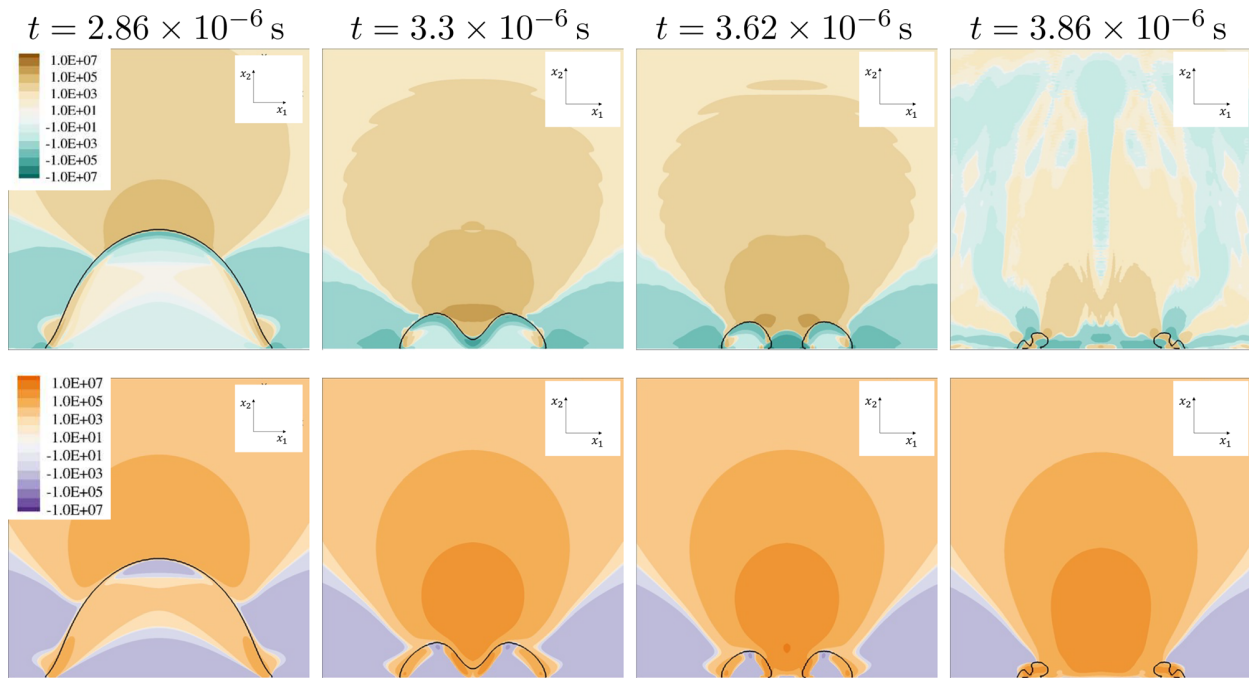


FIG. 42. Stress through x_2/x_3 -midplane for $Re = 40$, $De = 2$, $h^* = 0.35$ in LPTT fluid. Black isoline shows constant vapor content of $\alpha = 0.01$. Top: solvent stress $\tau_{s,22}$ (Pa); bottom: viscoelastic stress $\tau_{M,22}$ (Pa).

APPENDIX B: VISCOUS AND VISCOELASTIC STRESS DISTRIBUTIONS FOR $RE = 40$, $DE = 2$, $h^* = 1.5$

The following figures show the stress distributions for an initial standoff distance $h^* = 1.5$ and $Re = 40$, $De = 2$ for different time instants. Figure 43 illustrates the solvent stress distributions for the Newtonian collapse and Fig. 44 shows the solvent and viscoelastic stress distributions for the collapse in LPTT fluid.

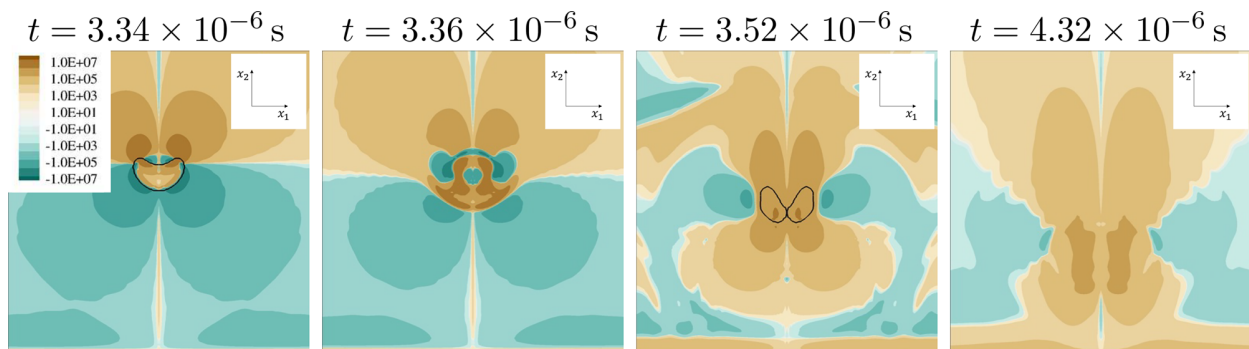


FIG. 43. Solvent stress $\tau_{s,12}$ (Pa) through the x_2/x_3 -midplane for different time instants during the collapse for $Re = 40$ and initial standoff distance $h^* = 1.5$ in Newtonian fluid. Black isoline shows constant vapor content of $\alpha = 0.01$.

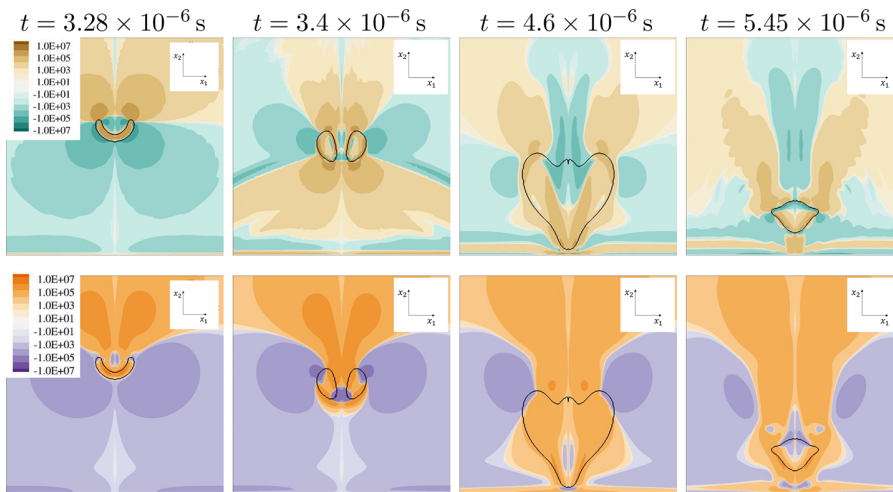


FIG. 44. Stress through x_2/x_3 -midplane for $Re = 40$, $De = 2$, $h^* = 1.5$ in LPTT fluid. Black isoline shows constant vapor content of $\alpha = 0.01$. Top: solvent stress $\tau_{s,12}$ (Pa); bottom: viscoelastic stress $\tau_{M,12}$ (Pa).

APPENDIX C: VISCOUS AND VISCOELASTIC STRESS DISTRIBUTIONS FOR $Re = 40$, $De = 1$, $h^* = 1.1$

The following figures show stress distributions for an initial standoff distance $h^* = 1.1$ and $Re = 40$, $De = 1$ for different time instants in LPTT fluid. Figures 45 to 47 illustrate the solvent and viscoelastic stress distributions during the collapse.

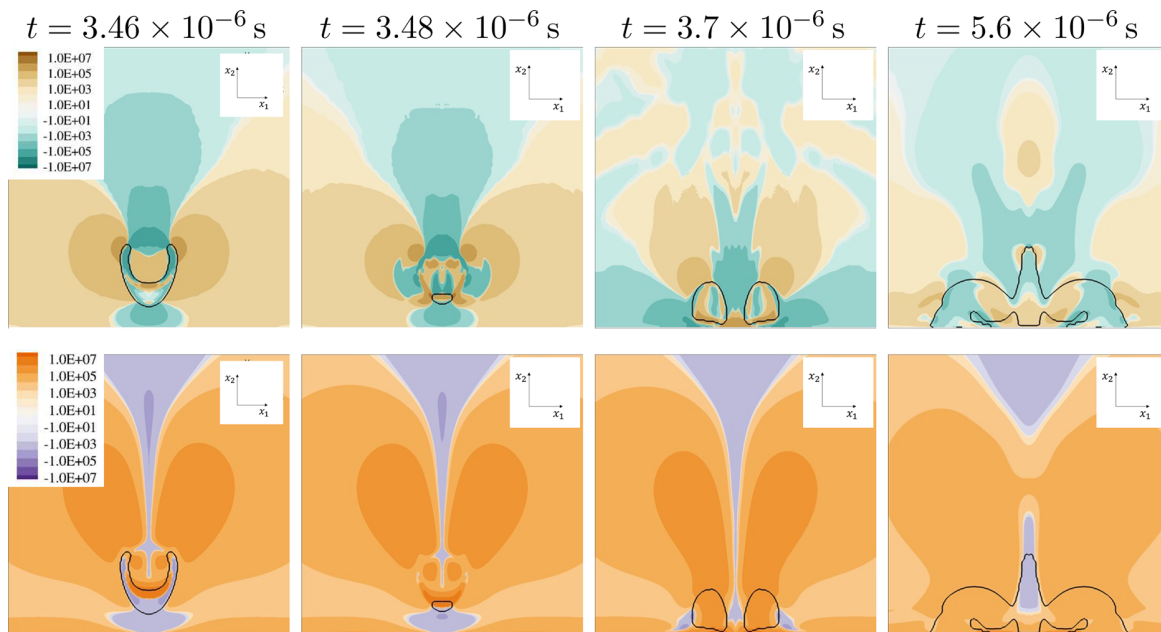


FIG. 45. Stress through x_2/x_3 -midplane for $Re = 40$, $De = 1$, $h^* = 1.1$ (decreased relaxation time) in LPTT fluid. Black isoline shows constant vapor content of $\alpha = 0.01$. Top: solvent stress $\tau_{s,11}$ (Pa); bottom: viscoelastic stress $\tau_{M,11}$ (Pa).

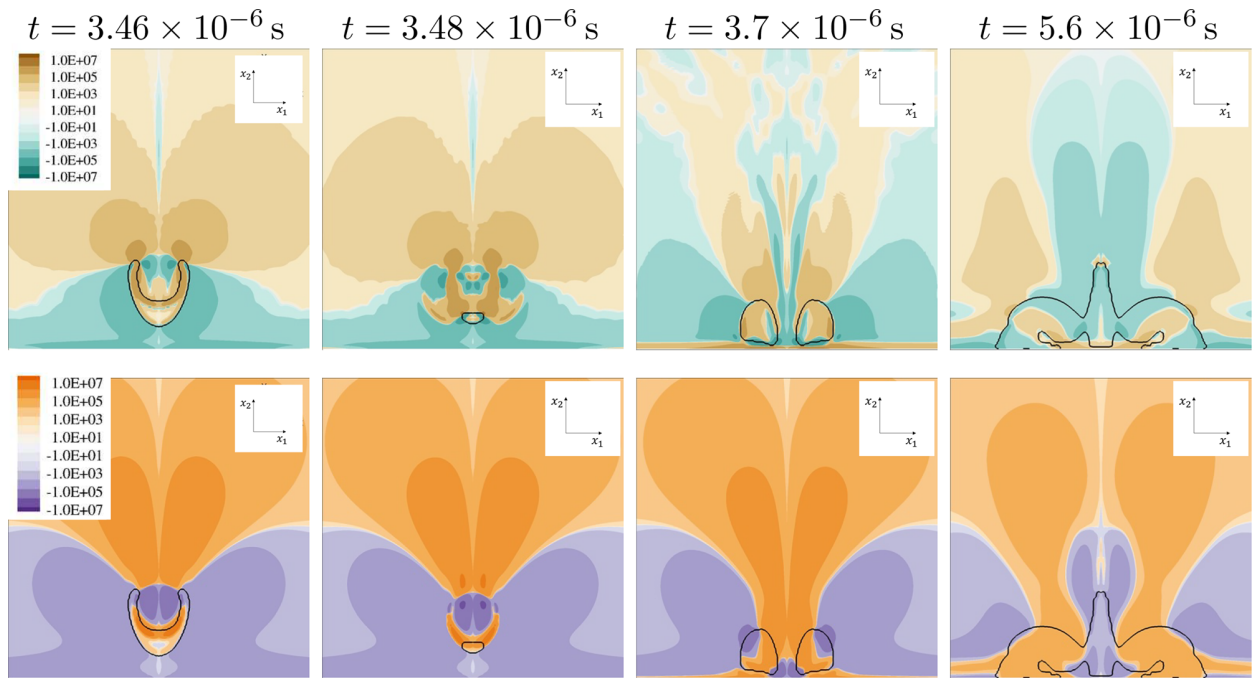


FIG. 46. Stress through x_2/x_3 -midplane for $Re = 40$, $De = 1$, $h^* = 1.1$ (decreased relaxation time) in LPTT fluid. Black isoline shows constant vapor content of $\alpha = 0.01$. Top: solvent stress $\tau_{s,12}$ (Pa); bottom: viscoelastic stress $\tau_{M,12}$ (Pa).

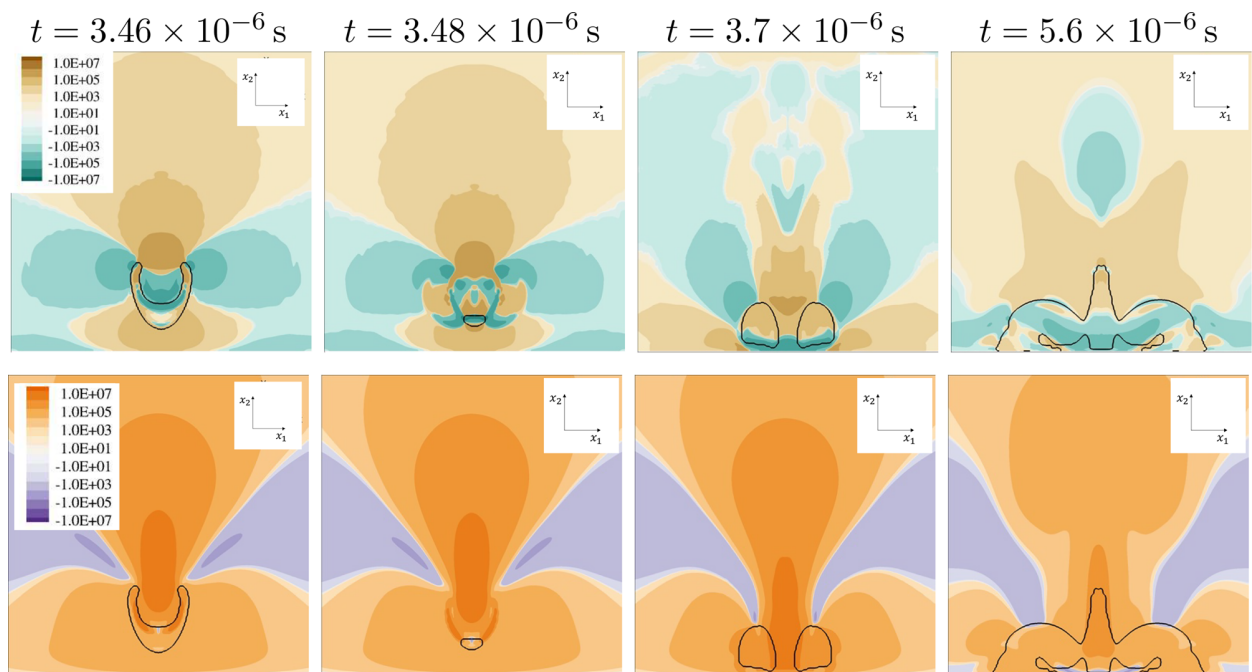


FIG. 47. Stress through x_2/x_3 -midplane for $Re = 40$, $De = 1$, $h^* = 1.1$ (decreased relaxation time) in LPTT fluid. Black isoline shows constant vapor content of $\alpha = 0.01$. Top: solvent stress $\tau_{s,22}$ (Pa); bottom: viscoelastic stress $\tau_{M,22}$ (Pa).

APPENDIX D: VISCOUS AND VISCOELASTIC STRESS DISTRIBUTIONS FOR $Re = 40$, $De = 4$, $h^* = 1.1$

The following figures show stress distributions for an initial standoff distance $h^* = 1.1$ and $Re = 40$, $De = 4$ for different time instants in LPTT fluid. Figures 48 to 50 illustrate the solvent and viscoelastic stress distributions during the collapse.

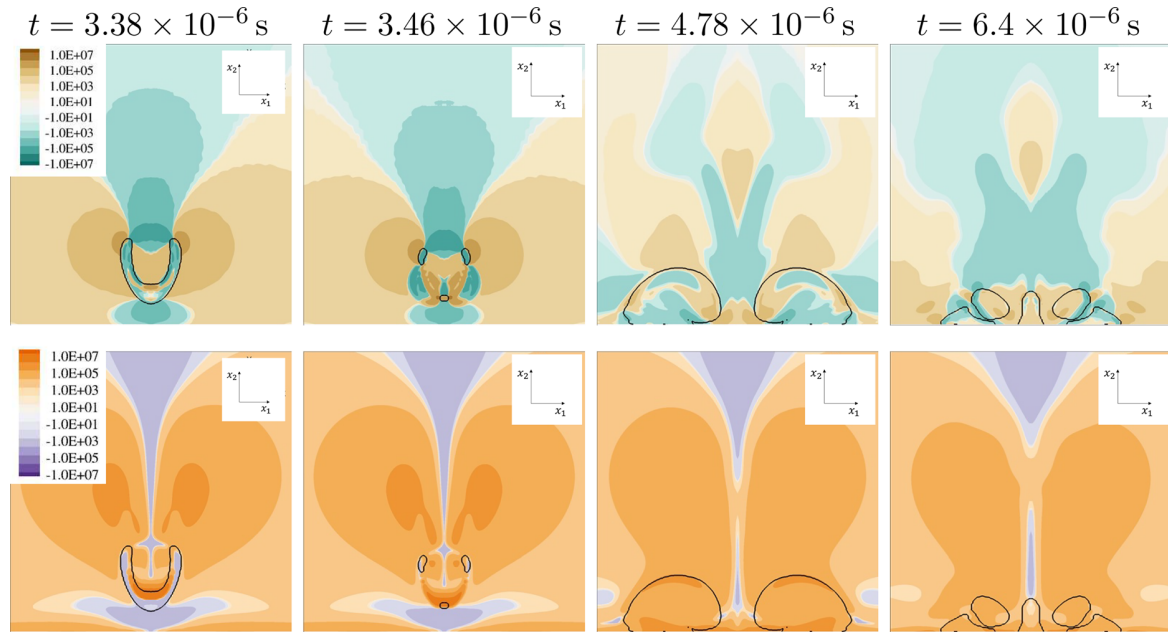


FIG. 48. Stress through x_2/x_3 -midplane for $Re = 40$, $De = 4$, $h^* = 1.1$ (increased relaxation time) in LPTT fluid. Black isoline shows constant vapor content of $\alpha = 0.01$. Top: solvent stress $\tau_{S,11}$ (Pa); bottom: viscoelastic stress $\tau_{M,11}$ (Pa).

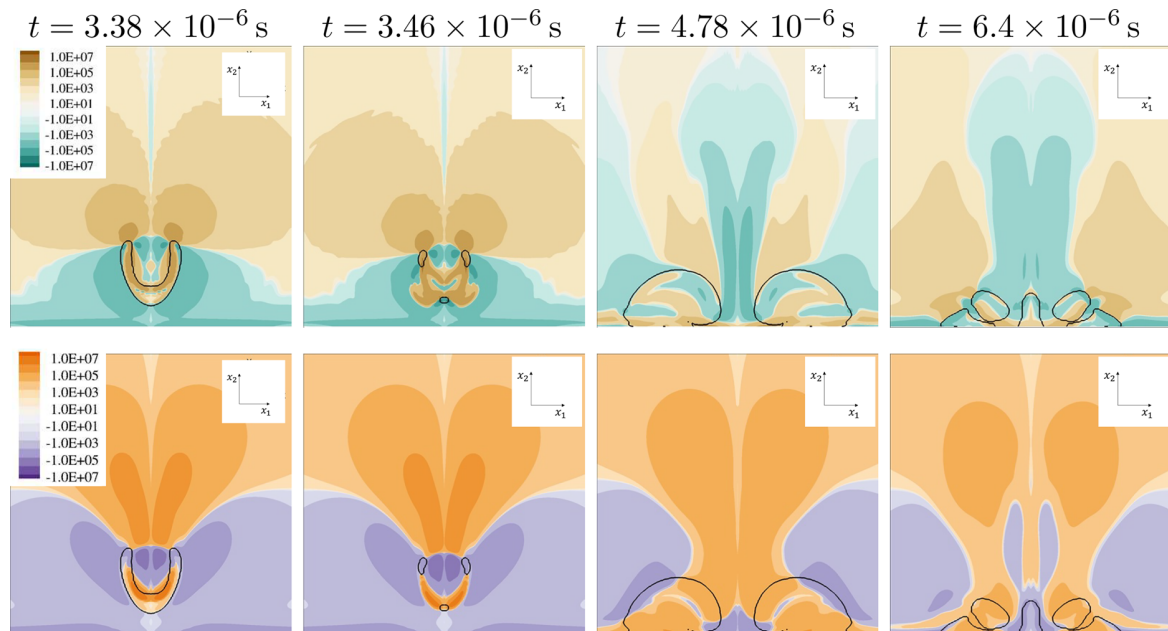


FIG. 49. Stress through x_2/x_3 -midplane for $Re = 40$, $De = 4$, $h^* = 1.1$ (increased relaxation time) in LPTT fluid. Black isoline shows constant vapor content of $\alpha = 0.01$. Top: solvent stress $\tau_{S,12}$ (Pa); bottom: viscoelastic stress $\tau_{M,12}$ (Pa).

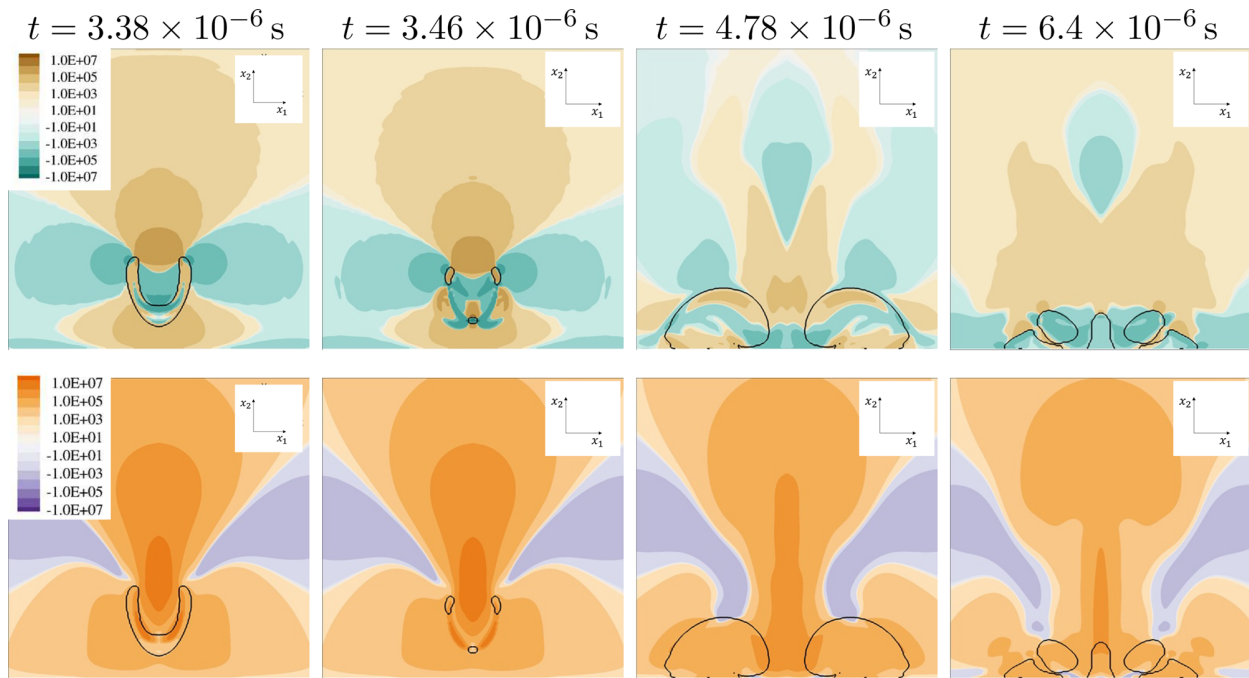


FIG. 50. Stress through x_2/x_3 -midplane for $Re = 40$, $De = 4$, $h^* = 1.1$ (increased relaxation time) in LPTT fluid. Black isoline shows constant vapor content of $\alpha = 0.01$. Top: solvent stress $\tau_{s,22}$ (Pa); bottom: viscoelastic stress $\tau_{M,22}$ (Pa).

REFERENCES

- ¹I. Lentacker, I. De Cock, R. Deckers, S. C. De Smedt, and C. T. Moonen, "Understanding ultrasound induced sonoporation: Definitions and underlying mechanisms," *Adv. Drug Delivery Rev.* **72**, 49–64 (2014).
- ²C. D. Ohl, M. Arora, R. Ikink, N. De Jong, M. Versluis, M. Delius, and D. Lohse, "Sonoporation from jetting cavitation bubbles," *Biophys. J.* **91**, 4285–4295 (2006).
- ³C. Y. Ting, C. H. Fan, H. L. Liu, C. Y. Huang, H. Y. Hsieh, T. C. Yen, K. C. Wei, and C. K. Yeh, "Concurrent blood-brain barrier opening and local drug delivery using drug-carrying microbubbles and focused ultrasound for brain glioma treatment," *Biomaterials* **33**, 704–712 (2012).
- ⁴H. J. Nesser, D. H. Karia, W. Tkalec, and N. G. Pandian, "Therapeutic ultrasound in cardiology," *Herz* **27**, 269–278 (2002).
- ⁵E. Johnsen and T. Colonius, "Shock-induced collapse of a gas bubble in shock-wave lithotripsy," *J. Acoust. Soc. Am.* **124**, 2011–2020 (2008).
- ⁶G. L. Chahine and D. H. Fruman, "Dilute polymer solution effects on bubble growth and collapse," *Phys. Fluids* **22**, 1406 (1979).
- ⁷E. A. Brujan, T. Ikeda, and Y. Matsumoto, "Dynamics of ultrasound-induced cavitation bubbles in non-Newtonian liquids and near a rigid boundary," *Phys. Fluids* **16**, 2402–2410 (2004).
- ⁸M. S. Plesset and R. B. Chapman, "Collapse of an initially spherical vapour cavity in the neighbourhood of a solid boundary," *J. Fluid Mech.* **47**, 283–290 (1971).
- ⁹J. R. Blake, B. B. Taib, and G. Doherty, "Transient cavities near boundaries. Part I. Rigid boundary," *J. Fluid Mech.* **170**, 479–497 (1986).
- ¹⁰R. P. Tong, W. P. Schiffers, S. J. Shaw, J. R. Blake, and D. C. Emmony, "The role of 'splashing' in the collapse of a laser-generated cavity near a rigid boundary," *J. Fluid Mech.* **380**, 339–361 (1999).
- ¹¹J. P. Best, "The formation of toroidal bubbles upon the collapse of transient cavities," *J. Fluid Mech.* **251**, 79–107 (1993).
- ¹²M. Sussman, "A second order coupled level set and volume-of-fluid method for computing growth and collapse of vapor bubbles," *J. Comput. Phys.* **187**, 110–136 (2003).
- ¹³M. Lee, E. Klaseboer, and B. C. Khoo, "On the boundary integral method for the rebounding bubble," *J. Fluid Mech.* **570**, 407–429 (2007).
- ¹⁴E. Johnsen and T. Colonius, "Numerical simulations of non-spherical bubble collapse," *J. Fluid Mech.* **629**, 231–262 (2009).
- ¹⁵E. Lauer, X. Y. Hu, S. Hickel, and N. A. Adams, "Numerical modelling and investigation of symmetric and asymmetric cavitation bubble dynamics," *Comput. Fluids* **69**, 1–19 (2012).
- ¹⁶C. T. Hsiao, A. Jayaprakash, A. Kapahi, J. K. Choi, and G. L. Chahine, "Modelling of material pitting from cavitation bubble collapse," *J. Fluid Mech.* **755**, 142–175 (2014).
- ¹⁷W. Lauterborn, C. Lechner, M. Koch, and R. Mettin, "Bubble models and real bubbles: Rayleigh and energy-deposit cases in a Tait-compressible liquid," *IMA J. Appl. Math.* **83**, 556–589 (2018).
- ¹⁸Y. A. Pishchalnikov, W. M. Behnke-Parks, K. Schmidmayer, K. Maeda, T. Colonius, T. W. Kenny, and D. J. Laser, "High-speed video microscopy and numerical modeling of bubble dynamics near a surface of urinary stone," *J. Acoust. Soc. Am.* **146**, 516–531 (2019).
- ¹⁹T. Trummer, S. H. Bryngelson, K. Schmidmayer, S. J. Schmidt, T. Colonius, and N. A. Adams, "Near-surface dynamics of a gas bubble collapsing above a crevice," *J. Fluid Mech.* **899**, A16 (2020).
- ²⁰X. Yang, C. Liu, D. Wan, and C. Hu, "Numerical study of the shock wave and pressure induced by single bubble collapse near planar solid wall," *Phys. Fluids* **33**, 073311 (2021).
- ²¹S. Popinet and S. Zaleski, "Bubble collapse near a solid boundary: A numerical study of the influence of viscosity," *J. Fluid Mech.* **464**, 137–163 (2002).
- ²²S. J. Kim, K. H. Lim, and C. Kim, "Deformation characteristics of spherical bubble collapse in Newtonian fluids near the wall using the finite element method with ALE formulation," *Korea Aust. Rheol. J.* **18**, 109–118 (2006).
- ²³S. J. Lind and T. N. Phillips, "Bubble collapse in compressible fluids using a spectral element marker particle method. Part I. Newtonian fluid," *Int. J. Numer. Methods Fluids* **70**, 1167 (2011).
- ²⁴N. Ochiai, Y. Iga, M. Nohmi, and T. Ikehagi, "Numerical analysis of nonspherical bubble collapse behavior and induced impulsive pressure during first and

- second collapses near the wall boundary," *J. Fluid Sci. Technol.* **6**, 860–874 (2011).
- ²⁵G. L. Chahine, A. Kapahi, J. K. Choi, and C. T. Hsiao, "Modeling of surface cleaning by cavitation bubble dynamics and collapse," *Ultrason. Sonochem.* **29**, 528–549 (2016).
- ²⁶M. Koch, C. Lechner, F. Reuter, K. Köhler, R. Mettin, and W. Lauterborn, "Numerical modeling of laser generated cavitation bubbles with the finite volume and volume of fluid method, using OpenFOAM," *Comput. Fluids* **126**, 71–90 (2016).
- ²⁷S. A. Beig, B. Aboulhasanzadeh, and E. Johnsen, "Temperatures produced by inertially collapsing bubbles near rigid surfaces," *J. Fluid Mech.* **852**, 105–125 (2018).
- ²⁸Q. Zeng, S. R. Gonzalez-Avila, R. Dijkink, P. Koukouvinis, M. Gavaises, and C. D. Ohl, "Wall shear stress from jetting cavitation bubbles," *J. Fluid Mech.* **846**, 341–355 (2018).
- ²⁹C. Lechner, W. Lauterborn, M. Koch, and R. Mettin, "Jet formation from bubbles near a solid boundary in a compressible liquid: Numerical study of distance dependence," *Phys. Rev. Fluids* **5**, 093604 (2020).
- ³⁰H. J. Sagar and O. el Moctar, "Dynamics of a cavitation bubble near a solid surface and the induced damage," *J. Fluids Struct.* **92**, 102799 (2020).
- ³¹T. Trummer, S. J. Schmidt, and N. A. Adams, "Effect of stand-off distance and spatial resolution on the pressure impact of near-wall vapor bubble collapses," *Int. J. Multiphase Flow* **141**, 103618 (2021).
- ³²A. Bussmann, F. Riahi, B. Gökce, S. Adami, S. Barcikowski, and N. A. Adams, "Investigation of cavitation bubble dynamics near a solid wall by high-resolution numerical simulation," *Phys. Fluids* **35**, 016115 (2023).
- ³³S. K. Hara and W. R. Schowalter, "Dynamics of nonspherical bubbles surrounded by viscoelastic fluid," *J. Non-Newtonian Fluid Mech.* **14**, 249–264 (1984).
- ³⁴S. Zhang, J. H. Duncan, and G. L. Chahine, "The final stage of the collapse of a cavitation bubble near a rigid wall," *J. Fluid Mech.* **257**, 147–723 (1993).
- ³⁵E. Klaseboer, K. C. Hung, C. Wang, C. W. Wang, B. C. Khoo, P. Boyce, S. Debono, and H. Charlier, "Experimental and numerical investigation of the dynamics of an underwater explosion bubble near a resilient/rigid structure," *J. Fluid Mech.* **537**, 387–413 (2005).
- ³⁶A. M. Zhang, S. Li, and J. Cui, "Study on splitting of a toroidal bubble near a rigid boundary," *Phys. Fluids* **27**, 062102 (2015).
- ³⁷L. Han, T. Zhang, D. Yang, R. Han, and S. Li, "Comparison of vortex cut and vortex ring models for toroidal bubble dynamics in underwater explosions," *Fluids* **8**, 131 (2023).
- ³⁸S. J. Lind and T. N. Phillips, "The influence of viscoelasticity on the collapse of cavitation bubbles near a rigid boundary," *Theor. Comput. Fluid Dyn.* **26**, 245–277 (2012).
- ³⁹S. J. Lind and T. N. Phillips, "Bubble collapse in compressible fluids using a spectral element marker particle method. Part 2. Viscoelastic fluids," *Int. J. Numer. Methods Fluids* **71**, 1103–1130 (2012).
- ⁴⁰M. J. Walters and T. N. Phillips, "A non-singular boundary element method for modelling bubble dynamics in viscoelastic fluids," *J. Non-Newtonian Fluid Mech.* **235**, 109–124 (2016).
- ⁴¹E. N. O'Brien, M. Mahmud, W. R. Smith, Q. X. Wang, and T. N. Phillips, "The evolution of a three-dimensional microbubble at a corner in a Maxwell fluid," *Phys. Fluids* **35**, 103120 (2023).
- ⁴²J. Ji, S. Li, P. Wan, and Z. Liu, "Numerical simulation of the behaviors of single bubble in shear-thinning viscoelastic fluids," *Phys. Fluids* **35**, 013313 (2023).
- ⁴³C. Lang, O. Boolakee, S. J. Schmidt, and N. A. Adams, "A compressible 3D finite volume approach for the simulation of unsteady viscoelastic cavitating flows," *Int. J. Multiphase Flow* **150**, 103981 (2022).
- ⁴⁴N. Phan-Thien and R. I. Tanner, "A new constitutive equation derived from network theory," *J. Non-Newtonian Fluid Mech.* **2**, 353–365 (1977).
- ⁴⁵G. H. Schnerr, I. H. Sezal, and S. J. Schmidt, "Numerical investigation of three-dimensional cloud cavitation with special emphasis on collapse induced shock dynamics," *Phys. Fluids* **20**, 040703 (2008).
- ⁴⁶J. Schnerr and G. H. Sauer, "Physical and numerical modeling of unsteady cavitation dynamics," in 4th International Conference on Multiphase Flow (ICMF), New Orleans, LA, Vol. 1 (2001).
- ⁴⁷C. P. Egerer, S. J. Schmidt, S. Hickel, and N. A. Adams, "Efficient implicit LES method for the simulation of turbulent cavitating flows," *J. Comput. Phys.* **316**, 453–469 (2016).
- ⁴⁸T. Trummer, S. J. Schmidt, and N. A. Adams, "Numerical investigation of non-condensable gas effect on vapor bubble collapse," *Phys. Fluids* **33**, 096107 (2021).
- ⁴⁹F. Örlay, S. Hickel, S. J. Schmidt, and N. A. Adams, "Large-eddy simulation of turbulent, cavitating fuel flow inside a 9-hole diesel injector including needle movement," *Int. J. Engine Res.* **18**, 195–211 (2017).
- ⁵⁰B. Budich, S. J. Schmidt, and N. A. Adams, "Numerical simulation and analysis of condensation shocks in cavitating flow," *J. Fluid Mech.* **838**, 759–813 (2018).
- ⁵¹R. Saurel, J. P. Cocchi, and P. B. Butler, "Numerical study of cavitation in the wake of a hypervelocity underwater projectile," *J. Propul. Power* **15**, 513–522 (1999).
- ⁵²J.-P. Franc and J.-M. Michel, *Fundamentals of Cavitation*, Fluid Mechanics and Its Applications Vol. 76 (Kluwer Academic Publishers, Dordrecht, 2005).
- ⁵³D. Beattie and P. Whalley, "A simple two-phase frictional pressure drop calculation method," *Int. J. Multiphase Flow* **8**, 83–87 (1982).
- ⁵⁴P. Roe, "Characteristic-based schemes for the Euler equations," *Annu. Rev. Fluid Mech.* **18**, 337–365 (1986).
- ⁵⁵C. E. Brennen, "Cavitation and bubble dynamics," [arXiv:1011.1669v3](https://arxiv.org/abs/1011.1669v3) (1995).
- ⁵⁶E. A. Brujan, "A first-order model for bubble dynamics in a compressible viscoelastic liquid," *J. Non-Newtonian Fluid Mech.* **84**, 83–103 (1999).
- ⁵⁷B. Karri, K. S. Pillai, E. Klaseboer, S. W. Ohl, and B. C. Khoo, "Collapsing bubble induced pumping in a viscous fluid," *Sens. Actuators, A* **169**, 151–163 (2011).
- ⁵⁸S. R. Gonzalez-Avila, F. Denner, and C. D. Ohl, "The acoustic pressure generated by the cavitation bubble expansion and collapse near a rigid wall," *Phys. Fluids* **33**, 032118 (2021).
- ⁵⁹S. J. Lind and T. N. Phillips, "The effect of viscoelasticity on the dynamics of gas bubbles near free surfaces," *Phys. Fluids* **25**, 022104 (2013).

Bibliography

- [1] Aboubacar, M. and Webster, M. “A cell-vertex finite volume/element method on triangles for abrupt contraction viscoelastic flows”. In: *Journal of Non-Newtonian Fluid Mechanics* 98.2-3 (2001), pp. 83–106. ISSN: 03770257. DOI: 10.1016/S0377-0257(00)00196-8.
- [2] Albernaz, D. L. and Cunha, F. R. “Unsteady motion of a spherical bubble in a complex fluid: Mathematical modelling and simulation”. In: *Applied Mathematical Modelling* 37.20-21 (2013), pp. 8972–8984. ISSN: 0307904X. DOI: 10.1016/j.apm.2013.03.065.
- [3] Aliabadi, A. and Taklifi, A. “The effect of magnetic field on dynamics of gas bubbles in visco-elastic fluids”. In: *Applied Mathematical Modelling* 36.6 (2012), pp. 2567–2577. ISSN: 0307904X. DOI: 10.1016/j.apm.2011.09.040.
- [4] Allen, J. S. and Roy, R. A. “Dynamics of gas bubbles in viscoelastic fluids. I. Linear viscoelasticity”. In: *The Journal of the Acoustical Society of America* 107.6 (2000), pp. 3167–3178. ISSN: 0001-4966. DOI: 10.1121/1.429344.
- [5] Allen, J. S. and Roy, R. A. “Dynamics of gas bubbles in viscoelastic fluids. II. Nonlinear viscoelasticity”. In: *The Journal of the Acoustical Society of America* 107.6 (2000), pp. 3167–3178. ISSN: 0001-4966. DOI: 10.1121/1.429344.
- [6] Alves, M. A., Oliveira, P. J., and Pinho, F. T. “Benchmark solutions for the flow of Oldroyd-B and PTT fluids in planar contractions”. In: *Journal of Non-Newtonian Fluid Mechanics* 110.1 (2003), pp. 45–75. ISSN: 03770257. DOI: 10.1016/S0377-0257(02)00191-X.
- [7] Ashworth, V. and Procter, R. P. M. “Cavitation damage in dilute polymer solutions”. In: *Nature* 258.5530 (1975), pp. 64–66. ISSN: 0028-0836. DOI: 10.1038/258064a0.
- [8] Baaijens, H. P. W., Peters, G. W. M., Baaijens, F. P. T., and Meijer, H. E. H. “Viscoelastic flow past a confined cylinder of a polyisobutylene solution”. In: *Journal of Rheology* 39.6 (1995), pp. 1243–1277. ISSN: 0148-6055. DOI: 10.1122/1.550635.
- [9] Al-Baldawi, A. “Modellierung und Simulation viskoelastischer Polymerschmelzen”. PhD thesis. Universität Kassel, 2012. ISBN: 978-3-89958-598-8.
- [10] Barnett, S. M., Humphrey, A. E., and Litt, M. “Bubble motion and mass transfer in non-Newtonian fluids”. In: *AIChE Journal* 12.2 (1966), pp. 253–259. ISSN: 0001-1541. DOI: 10.1002/aic.690120210.
- [11] Bazant, Z. P. “A Correlation Study of Formulations of Incremental Deformation and Stability of Continuous Bodies”. In: *Journal of Applied Mechanics* 38.4 (1971), pp. 919–928. ISSN: 0021-8936. DOI: 10.1115/1.3408976.

- [12] Bažant, Z. P. and Cedolin, L. *Stability of Structures*. World Scientific, 2010. ISBN: 978-981-4317-02-3. DOI: 10.1142/7828.
- [13] Beig, S. A., Aboulhasanzadeh, B., and Johnsen, E. “Temperatures produced by inertially collapsing bubbles near rigid surfaces”. In: *Journal of Fluid Mechanics* 852 (2018), pp. 105–125. ISSN: 0022-1120. DOI: 10.1017/jfm.2018.525.
- [14] Belblidia, F., Keshtiban, I., and Webster, M. “Stabilised computations for viscoelastic flows under compressible implementations”. In: *Journal of Non-Newtonian Fluid Mechanics* 134.1-3 (2006), pp. 56–76. ISSN: 03770257. DOI: 10.1016/j.jnnfm.2005.12.003.
- [15] Bergander, H. “Deformationsgesetze der Standardform in konvektiver Metrik”. In: *Technische Mechanik* 8 (1987), pp. 31–40.
- [16] Best, J. P. “The formation of toroidal bubbles upon the collapse of transient cavities”. In: *Journal of Fluid Mechanics* 251 (1993), pp. 79–107. ISSN: 0022-1120. DOI: 10.1017/S0022112093003349.
- [17] Bhaskaracharya, R. K., Kentish, S., and Ashokkumar, M. “Selected Applications of Ultrasonics in Food Processing”. In: *Food Engineering Reviews* 1.1 (2009), pp. 31–49. ISSN: 1866-7910. DOI: 10.1007/s12393-009-9003-7.
- [18] Blake, J. R., Taib, B. B., and Doherty, G. “Transient cavities near boundaries. Part 1. Rigid boundary”. In: *Journal of Fluid Mechanics* 170 (1986), pp. 479–497. ISSN: 0022-1120. DOI: 10.1017/S0022112086000988.
- [19] Blomley, M. J. K. “Science, medicine, and the future: Microbubble contrast agents: a new era in ultrasound”. In: *BMJ* 322.7296 (2001), pp. 1222–1225. ISSN: 09598138. DOI: 10.1136/bmj.322.7296.1222.
- [20] Böhme, G. *Strömungsmechanik nichtnewtonscher Fluide*. Wiesbaden: Vieweg+Teubner Verlag, 2000. ISBN: 978-3-519-12354-5. DOI: 10.1007/978-3-322-80140-1.
- [21] Bollada, P. C. and Phillips, T. N. “On the Mathematical Modelling of a Compressible Viscoelastic Fluid”. In: *Archive for Rational Mechanics and Analysis* 205.1 (2012), pp. 1–26. ISSN: 0003-9527. DOI: 10.1007/s00205-012-0496-5.
- [22] Brujan, E. A. “The equation of bubble dynamics in a compressible linear viscoelastic liquid”. In: *Fluid Dynamics Research* 29.5 (2001), pp. 287–294. ISSN: 0169-5983. DOI: 10.1016/S0169-5983(01)00030-2.
- [23] Brujan, E. A. *Cavitation in Non-Newtonian Fluids*. Berlin, Heidelberg: Springer Berlin Heidelberg, 2011. ISBN: 978-3-642-15342-6. DOI: 10.1007/978-3-642-15343-3.
- [24] Brujan, E. “A first-order model for bubble dynamics in a compressible viscoelastic liquid”. In: *Journal of Non-Newtonian Fluid Mechanics* 84.1 (1999), pp. 83–103. ISSN: 03770257. DOI: 10.1016/S0377-0257(98)00144-X.
- [25] Brujan, E. A. “Shock wave emission and cavitation bubble dynamics by femtosecond optical breakdown in polymer solutions”. In: *Ultrasonics Sonochemistry* 58.March (2019), p. 104694. ISSN: 18732828. DOI: 10.1016/j.ultsonch.2019.104694.

- [26] Budich, B., Schmidt, S. J., and Adams, N. A. “Numerical simulation and analysis of condensation shocks in cavitating flow”. In: *Journal of Fluid Mechanics* 838 (2018), pp. 759–813. ISSN: 0022-1120. DOI: 10.1017/jfm.2017.882.
- [27] Bußmann, A., Riahi, F., Gökce, B., Adami, S., Barcikowski, S., and Adams, N. A. “Investigation of cavitation bubble dynamics near a solid wall by high-resolution numerical simulation”. In: *Physics of Fluids* 35.1 (2023), p. 016115. ISSN: 1070-6631. DOI: 10.1063/5.0135924.
- [28] Chahine, G. L., Kapahi, A., Choi, J. K., and Hsiao, C. T. “Modeling of surface cleaning by cavitation bubble dynamics and collapse”. In: *Ultrasonics Sonochemistry* 29 (2016), pp. 528–549. ISSN: 18732828. DOI: 10.1016/j.ultsonch.2015.04.026.
- [29] Chakraborty, D. and Sader, J. E. “Constitutive models for linear compressible viscoelastic flows of simple liquids at nanometer length scales”. In: *Physics of Fluids* 27.5 (2015). ISSN: 10897666. DOI: 10.1063/1.4919620.
- [30] Choi, J. J., Selert, K., Vlachos, F., Wong, A., and Konofagou, E. E. “Noninvasive and localized neuronal delivery using short ultrasonic pulses and microbubbles”. In: *Proceedings of the National Academy of Sciences* 108.40 (2011), pp. 16539–16544. ISSN: 0027-8424. DOI: 10.1073/pnas.1105116108.
- [31] Crochet, M. and Bezy, M. “Numerical solution for the flow of viscoelastic fluids”. In: *Journal of Non-Newtonian Fluid Mechanics* 5 (1979), pp. 201–218. ISSN: 03770257. DOI: 10.1016/0377-0257(79)85014-4.
- [32] Doherty, W., Phillips, T. N., and Xie, Z. “A stabilised finite element framework for viscoelastic multiphase flows using a conservative level-set method”. In: *Journal of Computational Physics* 477 (2023), p. 111936. ISSN: 00219991. DOI: 10.1016/j.jcp.2023.111936.
- [33] Dollet, B., Marmottant, P., and Garbin, V. “Bubble Dynamics in Soft and Biological Matter”. In: *Annual Review of Fluid Mechanics* 51.1 (2019), pp. 331–355. ISSN: 0066-4189. DOI: 10.1146/annurev-fluid-010518-040352.
- [34] Dritselis, C. and Karapetsas, G. “Open-source finite volume solvers for multiphase (n-phase) flows involving either Newtonian or non-Newtonian complex fluids”. In: *Computers & Fluids* 245 (2022), p. 105590. ISSN: 00457930. DOI: 10.1016/j.compfluid.2022.105590. arXiv: 2203.09870.
- [35] Dvorkin, E. N. and Goldschmit, M. B. *Nonlinear Continua*. Computational Fluid and Solid Mechanics. Berlin, Heidelberg: Springer Berlin Heidelberg, 2005, p. 586. ISBN: 978-3-540-24985-6. DOI: 10.1007/3-540-29264-0.
- [36] Edwards, B. J. and Beris, A. N. “Remarks concerning compressible viscoelastic fluid models”. In: *Journal of Non-Newtonian Fluid Mechanics* 36 (1990), pp. 411–417. ISSN: 03770257. DOI: 10.1016/0377-0257(90)85021-P.
- [37] Egerer, C. P., Schmidt, S. J., Hickel, S., and Adams, N. A. “Efficient implicit LES method for the simulation of turbulent cavitating flows”. In: *Journal of Computational Physics* 316 (2016), pp. 453–469. ISSN: 10902716. DOI: 10.1016/j.jcp.2016.04.021.

- [38] Egerer, C. P., Hickel, S., Schmidt, S. J., and Adams, N. A. “Large-eddy simulation of turbulent cavitating flow in a micro channel”. In: *Physics of Fluids* 26.8 (2014). ISSN: 1070-6631. DOI: 10.1063/1.4891325.
- [39] Everitt, S., Harlen, O., Wilson, H., and Read, D. “Bubble dynamics in viscoelastic fluids with application to reacting and non-reacting polymer foams”. In: *Journal of Non-Newtonian Fluid Mechanics* 114.2-3 (2003), pp. 83–107. ISSN: 03770257. DOI: 10.1016/S0377-0257(03)00108-3.
- [40] Favero, J. L., Secchi, A. R., Cardozo, N. S. M., and Jasak, H. “Viscoelastic flow analysis using the software OpenFOAM and differential constitutive equations”. In: *Journal of Non-Newtonian Fluid Mechanics* 165.23-24 (2010), pp. 1625–1636. ISSN: 0377-0257. DOI: 10.1016/j.jnnfm.2010.08.010.
- [41] Fernandes, C., Vukčević, V., Uroić, T., Simoes, R., Carneiro, O., Jasak, H., and Nóbrega, J. “A coupled finite volume flow solver for the solution of incompressible viscoelastic flows”. In: *Journal of Non-Newtonian Fluid Mechanics* 265.January (2019), pp. 99–115. ISSN: 03770257. DOI: 10.1016/j.jnnfm.2019.01.006.
- [42] Ferrás, L. L., Afonso, A. M., Alves, M. A., Nóbrega, J. M., and Pinho, F. T. “Newtonian and viscoelastic fluid flows through an abrupt 1:4 expansion with slip boundary conditions”. In: *Physics of Fluids* 32.4 (2020), p. 043103. ISSN: 1070-6631. DOI: 10.1063/1.5145092.
- [43] Ferziger, J. H. and Perić, M. *Computational Methods for Fluid Dynamics*. Berlin, Heidelberg: Springer Berlin Heidelberg, 2002. ISBN: 978-3-540-42074-3. DOI: 10.1007/978-3-642-56026-2.
- [44] Figueiredo, R. A., Oishi, C. M., Afonso, A. M., Tasso, I. V., and Cuminato, J. A. “A two-phase solver for complex fluids: Studies of the Weissenberg effect”. In: *International Journal of Multiphase Flow* 84 (2016), pp. 98–115. ISSN: 03019322. DOI: 10.1016/j.ijmultiphaseflow.2016.04.014.
- [45] Fogler, H. S. and Goddard, J. D. “Collapse of Spherical Cavities in Viscoelastic Fluids”. In: *The Physics of Fluids* 13.5 (1970), pp. 1135–1141. ISSN: 0031-9171. DOI: 10.1063/1.1693042.
- [46] Foteinopoulou, K. and Laso, M. “Numerical simulation of bubble dynamics in a Phan-Thien-Tanner liquid: Non-linear shape and size oscillatory response under periodic pressure”. In: *Ultrasonics* 50.8 (2010), pp. 758–776. ISSN: 0041624X. DOI: 10.1016/j.ultras.2010.03.002.
- [47] Franc, J.-P. and Michel, J.-M. *Fundamentals of Cavitation*. Vol. 76. Fluid Mechanics and Its Applications. Dordrecht: Kluwer Academic Publishers, 2005. ISBN: 1-4020-2232-8. DOI: 10.1007/1-4020-2233-6.
- [48] Gaudron, R., Warnez, M. T., and Johnsen, E. “Bubble dynamics in a viscoelastic medium with nonlinear elasticity”. In: *Journal of Fluid Mechanics* 766.1 (2015), pp. 54–75. ISSN: 0022-1120. DOI: 10.1017/jfm.2015.7.

- [49] Giesekus, H. “A simple constitutive equation for polymer fluids based on the concept of deformation-dependent tensorial mobility”. In: *Journal of Non-Newtonian Fluid Mechanics* 11.1-2 (1982), pp. 69–109. ISSN: 03770257. DOI: 10.1016/0377-0257(82)85016-7.
- [50] Giesekus, H. “Die Elastizität von Flüssigkeiten”. In: *Rheologica Acta* 5.1 (1966), pp. 29–35. ISSN: 0035-4511. DOI: 10.1007/BF01973575.
- [51] Guy, R. D. and Fogelson, A. L. “A wave propagation algorithm for viscoelastic fluids with spatially and temporally varying properties”. In: *Computer Methods in Applied Mechanics and Engineering* 197.25-28 (2008), pp. 2250–2264. ISSN: 00457825. DOI: 10.1016/j.cma.2007.11.022.
- [52] Habla, F., Woitalka, A., Neuner, S., and Hinrichsen, O. “Development of a methodology for numerical simulation of non-isothermal viscoelastic fluid flows with application to axisymmetric 4 : 1 contraction flows”. In: *Chemical Engineering Journal* 207-208 (2012), pp. 772–784. ISSN: 1385-8947. DOI: 10.1016/j.ces.2012.07.060.
- [53] Habla, F., Waas, C., Dietsche, L., and Hinrichsen, O. “An improved conditionally volume averaged viscoelastic two-phase model for simulation of transient droplet deformations under simple shear”. In: *Chemical Engineering Science* 126 (2015), pp. 32–41. ISSN: 00092509. DOI: 10.1016/j.ces.2014.12.002.
- [54] Haupt, P. *Continuum Mechanics and Theory of Materials*. Advanced Texts in Physics. Berlin, Heidelberg: Springer Berlin Heidelberg, 2000. ISBN: 978-3-662-04111-6. DOI: 10.1007/978-3-662-04109-3.
- [55] Hirsch, C. *Numerical Computation of Internal and External Flows*. Elsevier, 2007. ISBN: 9780750665940. DOI: 10.1016/B978-0-7506-6594-0.X5037-1.
- [56] Housiadas, K. D. and Georgiou, G. C. “Perturbation solution of Poiseuille flow of a weakly compressible Oldroyd-B fluid”. In: *Journal of Non-Newtonian Fluid Mechanics* 166.1-2 (2011), pp. 73–92. ISSN: 03770257. DOI: 10.1016/j.jnnfm.2010.10.007.
- [57] Housiadas, K. D., Georgiou, G. C., and Mamoutos, I. G. “Laminar axisymmetric flow of a weakly compressible viscoelastic fluid”. In: *Rheologica Acta* 51.6 (2012), pp. 511–526. ISSN: 0035-4511. DOI: 10.1007/s00397-011-0610-x.
- [58] Hsiao, C.-T., Jayaprakash, A., Kapahi, A., Choi, J.-K., and Chahine, G. L. “Modelling of material pitting from cavitation bubble collapse”. In: *Journal of Fluid Mechanics* 755 (2014), pp. 142–175. ISSN: 0022-1120. DOI: 10.1017/jfm.2014.394.
- [59] Hua, C. and Johnsen, E. “Nonlinear oscillations following the Rayleigh collapse of a gas bubble in a linear viscoelastic (tissue-like) medium”. In: *Physics of Fluids* 25.8 (2013). ISSN: 1070-6631. DOI: 10.1063/1.4817673.
- [60] Huilgol, R. R. and Phan-Thien, N. *Fluid Mechanics of Viscoelasticity*. 1997.
- [61] Izbassarov, D., Rosti, M. E., Ardekani, M. N., Sarabian, M., Hormozi, S., Brandt, L., and Tammisola, O. “Computational modeling of multiphase viscoelastic and elasto-viscoplastic flows”. In: *International Journal for Numerical Methods in Fluids* 88.12 (2018), pp. 521–543. ISSN: 0271-2091. DOI: 10.1002/flid.4678.

- [62] Ji, W., Waas, A. M., and Bazant, Z. P. “On the Importance of Work-Conjugacy and Objective Stress Rates in Finite Deformation Incremental Finite Element Analysis”. In: *Journal of Applied Mechanics* 80.4 (2013), pp. 1–9. ISSN: 0021-8936. DOI: 10.1115/1.4007828.
- [63] Jiang, G.-S. and Shu, C.-W. “Efficient Implementation of Weighted ENO Schemes”. In: *Journal of Computational Physics* 126.1 (1996), pp. 202–228. ISSN: 00219991. DOI: 10.1006/jcph.1996.0130.
- [64] Johnsen, E. and Colonius, T. “Shock-induced collapse of a gas bubble in shockwave lithotripsy”. In: *The Journal of the Acoustical Society of America* 124.4 (2008), pp. 2011–2020. ISSN: 0001-4966. DOI: 10.1121/1.2973229.
- [65] Johnsen, E. and Colonius, T. “Numerical simulations of non-spherical bubble collapse”. In: *Journal of Fluid Mechanics* 629 (2009), pp. 231–262. ISSN: 0022-1120. DOI: 10.1017/S0022112009006351.
- [66] Johnson, M. and Segalman, D. “A model for viscoelastic fluid behavior which allows non-affine deformation”. In: *Journal of Non-Newtonian Fluid Mechanics* 2.3 (1977), pp. 255–270. ISSN: 03770257. DOI: 10.1016/0377-0257(77)80003-7.
- [67] Kennedy, J. E. “High-intensity focused ultrasound in the treatment of solid tumours”. In: *Nature Reviews Cancer* 5.4 (2005), pp. 321–327. ISSN: 1474-175X. DOI: 10.1038/nrc1591.
- [68] Keshtiban, I., Belblidia, F., and Webster, M. “Numerical simulation of compressible viscoelastic liquids”. In: *Journal of Non-Newtonian Fluid Mechanics* 122.1-3 (2004), pp. 131–146. ISSN: 03770257. DOI: 10.1016/j.jnnfm.2003.12.008.
- [69] Keshtiban, I., Belblidia, F., and Webster, M. “Computation of incompressible and weakly-compressible viscoelastic liquids flow: finite element/volume schemes”. In: *Journal of Non-Newtonian Fluid Mechanics* 126.2-3 (2005), pp. 123–143. ISSN: 03770257. DOI: 10.1016/j.jnnfm.2004.07.020.
- [70] Kim, C. “Collapse of spherical bubbles in Maxwell fluids”. In: *Journal of Non-Newtonian Fluid Mechanics* 55.1 (1994), pp. 37–58. ISSN: 03770257. DOI: 10.1016/0377-0257(94)80059-6.
- [71] Kim, S. J., Lim, K. H., and Kim, C. “Deformation characteristics of spherical bubble collapse in Newtonian fluids near the wall using the Finite Element Method with ALE formulation”. In: *Korea Australia Rheology Journal* 18.2 (2006), pp. 109–118. ISSN: 1226119X.
- [72] Koch, M., Lechner, C., Reuter, F., Köhler, K., Mettin, R., and Lauterborn, W. “Numerical modeling of laser generated cavitation bubbles with the finite volume and volume of fluid method, using OpenFOAM”. In: *Computers & Fluids* 126.November 2015 (2016), pp. 71–90. ISSN: 00457930. DOI: 10.1016/j.compfluid.2015.11.008.
- [73] Koren, B. “A robust upwind discretization method for advection, diffusion and source terms”. In: *Numerical Methods for Advection-Diffusion Problems* 45.c (1993), pp. 117–138.

- [74] Lang, C., Adami, S., and Adams, N. A. “Viscoelastic vapor bubble collapse near solid walls and corresponding shock wave formation”. In: *Physics of Fluids* 36.1 (2024). ISSN: 1070-6631. DOI: 10.1063/5.0175807.
- [75] Lang, C., Boolakee, O., Schmidt, S. J., and Adams, N. A. “A compressible 3D finite volume approach for the simulation of unsteady viscoelastic cavitating flows”. In: *International Journal of Multiphase Flow* 150.September 2021 (2022), p. 103981. ISSN: 03019322. DOI: 10.1016/j.ijmultiphaseflow.2022.103981.
- [76] Lang, C., Schmidt, S. J., and Adams, N. A. “Compressible 3D-simulations of spherical bubble collapses in viscoelastic fluids”. In: *Proceedings of the 11th International Symposium on Cavitation*. Deajon, South Korea, 2021.
- [77] Lang, C., Schmidt, S. S., and Adams, N. A. “Einfluss rein viskoser Nicht-Newtonscher Fluide auf den Einzelblasenkollaps”. In: *Drittes Kolloquium Kavitation und Kavitationserosion*. Bochum, 2018.
- [78] Lang, C., Zhang, M., Schmidt, S. J., and Adams, N. A. “On spherical vapor bubble collapse in viscoelastic fluids”. In: *Applied Mathematical Modelling* 123.1-2 (2023), pp. 484–506. ISSN: 0307904X. DOI: 10.1016/j.apm.2023.07.004.
- [79] Laridon, Y., Grenier, D., Houeix, D., Doursat, C., Lucas, T., and Flick, D. “Modelling of the growth of a single bubble in semi-hard cheese, with experimental verification and sensitivity analysis”. In: *Applied Mathematical Modelling* 40.23-24 (2016), pp. 10771–10782. ISSN: 0307904X. DOI: 10.1016/j.apm.2016.08.018.
- [80] Larson, R. G. “Rheologica acta”. In: *Rheologica Acta* 3.1 (1963), pp. 1–1. ISSN: 0035-4511. DOI: 10.1007/BF01974447.
- [81] Lauer, E., Hu, X., Hickel, S., and Adams, N. “Numerical modelling and investigation of symmetric and asymmetric cavitation bubble dynamics”. In: *Computers & Fluids* 69 (2012), pp. 1–19. ISSN: 00457930. DOI: 10.1016/j.compfluid.2012.07.020.
- [82] Lauterborn, W., Lechner, C., Koch, M., and Mettin, R. “Bubble models and real bubbles: Rayleigh and energy-deposit cases in a Tait-compressible liquid”. In: *IMA Journal of Applied Mathematics* 83.4 (2018), pp. 556–589. ISSN: 0272-4960. DOI: 10.1093/imamat/hxy015.
- [83] Lechner, C., Lauterborn, W., Koch, M., and Mettin, R. “Jet formation from bubbles near a solid boundary in a compressible liquid: Numerical study of distance dependence”. In: *Physical Review Fluids* 5.9 (2020), p. 093604. ISSN: 2469-990X. DOI: 10.1103/PhysRevFluids.5.093604. arXiv: 2005.05733.
- [84] Lee, M., Klaseboer, E., and Khoo, B. C. “On the boundary integral method for the rebounding bubble”. In: *Journal of Fluid Mechanics* 570 (2007), pp. 407–429. ISSN: 0022-1120. DOI: 10.1017/S0022112006003296.
- [85] Lentacker, I., De Cock, I., Deckers, R., De Smedt, S. C., and Moonen, C. T. “Understanding ultrasound induced sonoporation: Definitions and underlying mechanisms”. In: *Advanced Drug Delivery Reviews* 72 (2014), pp. 49–64. ISSN: 18728294. DOI: 10.1016/j.addr.2013.11.008.

- [86] LeVeque, R. *Numerical Methods for Conservation Laws*. Basel: Birkhäuser Basel, 1992. ISBN: 978-3-7643-2723-1. DOI: 10.1007/978-3-0348-8629-1.
- [87] Lind, S. J. “A Numerical study of the effect of viscoelasticity on cavitation and bubble dynamics”. PhD thesis. Cardiff University, 2010.
- [88] Lind, S. J. and Phillips, T. N. “The influence of viscoelasticity on the collapse of cavitation bubbles near a rigid boundary”. In: *Theoretical and Computational Fluid Dynamics* 26.1-4 (2012), pp. 245–277. ISSN: 0935-4964. DOI: 10.1007/s00162-011-0227-9.
- [89] Lind, S. J. and Phillips, T. N. “Bubble collapse in compressible fluids using a spectral element marker particle method. Part 2. Viscoelastic fluids”. In: *International Journal for Numerical Methods in Fluids* 71.9 (2013), pp. 1103–1130. ISSN: 0271-2091. DOI: 10.1002/fld.3701.
- [90] Lind, S. J. and Phillips, T. “Bubble collapse in compressible fluids using a spectral element marker particle method. Part 1. Newtonian fluids”. In: *International Journal for Numerical Methods in Fluids* 70.9 (2012), pp. 1167–1187. ISSN: 0271-2091. DOI: 10.1002/fld.2737.
- [91] Lind, S. and Phillips, T. “Spherical bubble collapse in viscoelastic fluids”. In: *Journal of Non-Newtonian Fluid Mechanics* 165.1-2 (2010), pp. 56–64. ISSN: 03770257. DOI: 10.1016/j.jnnfm.2009.09.002.
- [92] Lippmann, H. *Angewandte Tensorrechnung*. Berlin, Heidelberg: Springer Berlin Heidelberg, 1996. ISBN: 978-3-642-80293-5. DOI: 10.1007/978-3-642-80292-8.
- [93] Mackay, A. T. and Phillips, T. N. “On the derivation of macroscopic models for compressible viscoelastic fluids using the generalized bracket framework”. In: *Journal of Non-Newtonian Fluid Mechanics* 266. February (2019), pp. 59–71. ISSN: 03770257. DOI: 10.1016/j.jnnfm.2019.02.006.
- [94] Mackay, A. T. and Phillips, T. N. “Compressible and nonisothermal viscoelastic flow between eccentrically rotating cylinders”. In: *Theoretical and Computational Fluid Dynamics* 35.5 (2021), pp. 731–756. ISSN: 14322250. DOI: 10.1007/s00162-021-00582-y.
- [95] Mihatsch, M. S., Schmidt, S. J., and Adams, N. A. “Cavitation erosion prediction based on analysis of flow dynamics and impact load spectra”. In: *Physics of Fluids* 27.10 (2015). ISSN: 10897666. DOI: 10.1063/1.4932175.
- [96] Mompean, G. and Deville, M. “Unsteady finite volume simulation of Oldroyd-B fluid through a three-dimensional planar contraction”. In: *Journal of Non-Newtonian Fluid Mechanics* 72.2-3 (1997), pp. 253–279. ISSN: 03770257. DOI: 10.1016/S0377-0257(97)00033-5.
- [97] Naseri, H., Koukouvinis, P., Malgarinos, I., and Gavaises, M. “On viscoelastic cavitating flows: A numerical study”. In: *Physics of Fluids* 30.3 (2018). ISSN: 10897666. DOI: 10.1063/1.5011978.
- [98] Nithiarasu, P. “A fully explicit characteristic based split (CBS) scheme for viscoelastic flow calculations”. In: *International Journal for Numerical Methods in Engineering* 60.5 (2004), pp. 949–978. ISSN: 0029-5981. DOI: 10.1002/nme.993.

- [99] Ochiai, N., Iga, Y., Nohmi, M., and Ikohagi, T. “Numerical Analysis of Nonspherical Bubble Collapse Behavior and Induced Impulsive Pressure during First and Second Collapses near the Wall Boundary”. In: *Journal of Fluid Science and Technology* 6.6 (2011), pp. 860–874. ISSN: 1880-5558. DOI: 10.1299/jfst.6.860.
- [100] Ohl, C. D., Arora, M., Ikink, R., De Jong, N., Versluis, M., Delius, M., and Lohse, D. “Sonoporation from jetting cavitation bubbles”. In: *Biophysical Journal* 91.11 (2006), pp. 4285–4295. ISSN: 00063495. DOI: 10.1529/biophysj.105.075366.
- [101] Ohl, C.-D., Arora, M., Dijkink, R., Janve, V., and Lohse, D. “Surface cleaning from laser-induced cavitation bubbles”. In: *Applied Physics Letters* 89.7 (2006). ISSN: 0003-6951. DOI: 10.1063/1.2337506.
- [102] Oldroyd, J. G. “On the Formulation of Rheological Equations of State”. In: *Proceedings of the Royal Society A: Mathematical, Physical and Engineering Sciences* 200.1063 (1950), pp. 523–541. ISSN: 1364-5021. DOI: 10.1098/rspa.1950.0035.
- [103] Oldroyd, J. “An approach to non-newtonian fluid mechanics”. In: *Journal of Non-Newtonian Fluid Mechanics* 14 (1984), pp. 9–46. ISSN: 03770257. DOI: 10.1016/0377-0257(84)80035-X.
- [104] Oliveira, P., Pinho, F., and Pinto, G. “Numerical simulation of non-linear elastic flows with a general collocated finite-volume method”. In: *Journal of Non-Newtonian Fluid Mechanics* 79.1 (1998), pp. 1–43. ISSN: 03770257. DOI: 10.1016/S0377-0257(98)00082-2.
- [105] Örley, F., Trummler, T., Hickel, S., Mihatsch, M. S., Schmidt, S. J., and Adams, N. A. “Large-eddy simulation of cavitating nozzle flow and primary jet break-up”. In: *Physics of Fluids* 27.8 (2015). ISSN: 1070-6631. DOI: 10.1063/1.4928701.
- [106] Örley, F., Pasquariello, V., Hickel, S., and Adams, N. A. “Cut-element based immersed boundary method for moving geometries in compressible liquid flows with cavitation”. In: *Journal of Computational Physics* 283 (2015), pp. 1–22. ISSN: 00219991. DOI: 10.1016/j.jcp.2014.11.028.
- [107] Owens, R. G. and Phillips, T. N. *Computational Rheology*. 2002. ISBN: 9781860949425. DOI: 10.1142/9781860949425.
- [108] Perera, M. and Strauss, K. “Direct numerical solutions of the equations for viscoelastic fluid flow”. In: *Journal of Non-Newtonian Fluid Mechanics* 5.C (1979), pp. 269–283. ISSN: 03770257. DOI: 10.1016/0377-0257(79)85018-1.
- [109] Phan-Thien, N. and Tanner, R. I. “A new constitutive equation derived from network theory”. In: *Journal of Non-Newtonian Fluid Mechanics* 2.4 (1977), pp. 353–365. ISSN: 03770257. DOI: 10.1016/0377-0257(77)80021-9.
- [110] Phan-Thien, N. “A Nonlinear Network Viscoelastic Model”. In: *Journal of Rheology* 22.3 (1978), pp. 259–283. ISSN: 0148-6055. DOI: 10.1122/1.549481.
- [111] Phelan, F., Malone, M., and Winter, H. “A purely hyperbolic model for unsteady viscoelastic flow”. In: *Journal of Non-Newtonian Fluid Mechanics* 32.2 (1989), pp. 197–224. ISSN: 03770257. DOI: 10.1016/0377-0257(89)85036-0.

- [112] Pinsky, P. M., Ortiz, M., and Pister, K. S. “Numerical integration of rate constitutive equations in finite deformation analysis”. In: *Computer Methods in Applied Mechanics and Engineering* 40.2 (1983), pp. 137–158. ISSN: 00457825. DOI: 10.1016/0045-7825(83)90087-7.
- [113] Pishchalnikov, Y. A., Behnke-Parks, W. M., Schmidmayer, K., Maeda, K., Colonius, T., Kenny, T. W., and Laser, D. J. “High-speed video microscopy and numerical modeling of bubble dynamics near a surface of urinary stone”. In: *The Journal of the Acoustical Society of America* 146.1 (2019), pp. 516–531. ISSN: 0001-4966. DOI: 10.1121/1.5116693.
- [114] Plesset, M. S. and Chapman, R. B. “Collapse of an initially spherical vapour cavity in the neighbourhood of a solid boundary”. In: *Journal of Fluid Mechanics* 47.2 (1971), pp. 283–290. ISSN: 0022-1120. DOI: 10.1017/S0022112071001058.
- [115] POPINET, S. and ZALESKI, S. “Bubble collapse near a solid boundary: a numerical study of the influence of viscosity”. In: *Journal of Fluid Mechanics* 464 (2002), pp. 137–163. ISSN: 0022-1120. DOI: 10.1017/S002211200200856X.
- [116] Price, R. J. and Kaul, S. “Contrast Ultrasound Targeted Drug and Gene Delivery: An Update on a New Therapeutic Modality”. In: *Journal of Cardiovascular Pharmacology and Therapeutics* 7.3 (2002), pp. 171–180. ISSN: 1074-2484. DOI: 10.1177/107424840200700307.
- [117] Rodriguez, M. and Johnsen, E. “A high-order accurate five-equations compressible multiphase approach for viscoelastic fluids and solids with relaxation and elasticity”. In: *Journal of Computational Physics* 379 (2019), pp. 70–90. ISSN: 10902716. DOI: 10.1016/j.jcp.2018.10.035.
- [118] Rodriguez, M., Johnsen, E., and Powell, K. G. “A high-order accurate AUSM + -up approach for simulations of compressible multiphase flows with linear viscoelasticity”. In: *Shock Waves* 29.5 (2019), pp. 717–734. ISSN: 09381287. DOI: 10.1007/s00193-018-0884-3.
- [119] Roe, P. “Characteristic-Based Schemes for the Euler Equations”. In: *Annual Review of Fluid Mechanics* 18.1 (1986), pp. 337–365. ISSN: 00664189. DOI: 10.1146/annurev.fluid.18.1.337.
- [120] Rouhaud, E., Panicaud, B., and Kerner, R. “Canonical frame-indifferent transport operators with the four-dimensional formalism of differential geometry”. In: *Computational Materials Science* 77 (2013), pp. 120–130. ISSN: 09270256. DOI: 10.1016/j.commatsci.2013.04.032.
- [121] Rowlatt, C. F. and Lind, S. J. “Bubble collapse near a fluid-fluid interface using the spectral element marker particle method with applications in bioengineering”. In: *International Journal of Multiphase Flow* 90 (2017), pp. 118–143. ISSN: 03019322. DOI: 10.1016/j.ijmultiphaseflow.2016.11.010.
- [122] Sagar, H. J. and Moctar, O. el. “Dynamics of a cavitation bubble near a solid surface and the induced damage”. In: *Journal of Fluids and Structures* 92 (2020), p. 102799. ISSN: 10958622. DOI: 10.1016/j.jfluidstructs.2019.102799.

- [123] Saint-Michel, B. and Garbin, V. “Bubble dynamics for broadband microrheology of complex fluids”. In: *Current Opinion in Colloid & Interface Science* 50 (2020), p. 101392. ISSN: 13590294. DOI: 10.1016/j.cocis.2020.101392.
- [124] Sato, T. and Richardson, S. M. “Explicit numerical simulation of time-dependent viscoelastic flow problems by a finite element/finite volume method”. In: *Journal of Non-Newtonian Fluid Mechanics* 51.3 (1994), pp. 249–275. ISSN: 03770257. DOI: 10.1016/0377-0257(94)85019-4.
- [125] Saurel, R., Cocchi, J. P., and Butler, P. B. “Numerical Study of Cavitation in the Wake of a Hypervelocity Underwater Projectile”. In: *Journal of Propulsion and Power* 15.4 (1999), pp. 513–522. ISSN: 0748-4658. DOI: 10.2514/2.5473.
- [126] Schmidt, S. J. “A low Mach number consistent compressible approach for simulation of cavitating flow”. PhD thesis. Technical University of Munich, 2015.
- [127] Schnerr, G. H., Sezal, I. H., and Schmidt, S. J. “Numerical investigation of three-dimensional cloud cavitation with special emphasis on collapse induced shock dynamics”. In: *Physics of Fluids* 20.4 (2008), pp. 1–9. ISSN: 1070-6631. DOI: 10.1063/1.2911039.
- [128] Sezal, I. H. “Compressible Dynamics of Cavitating 3-D Multi-Phase Flows”. PhD thesis. Technical University of Munich, 2009.
- [129] Shen, T., Long, R., and Vernerey, F. “Computational modeling of the large deformation and flow of viscoelastic polymers”. In: *Computational Mechanics* 63.4 (2019), pp. 725–745. ISSN: 01787675. DOI: 10.1007/s00466-018-1619-0.
- [130] Surana, K. S., Ma, Y., Romkes, A., and Reddy, J. N. “The Rate Constitutive Equations and Their Validity for Progressively Increasing Deformation”. In: *Mechanics of Advanced Materials and Structures* 17.7 (2010), pp. 509–533. ISSN: 1537-6494. DOI: 10.1080/15376494.2010.509195.
- [131] Sussman, M. “A second order coupled level set and volume-of-fluid method for computing growth and collapse of vapor bubbles”. In: *Journal of Computational Physics* 187.1 (2003), pp. 110–136. ISSN: 00219991. DOI: 10.1016/S0021-9991(03)00087-1.
- [132] Tanasawa, I. and Yang, W.-J. “Dynamic Behavior of a Gas Bubble in Viscoelastic Liquids”. In: *Journal of Applied Physics* 41.11 (1970), pp. 4526–4531. ISSN: 0021-8979. DOI: 10.1063/1.1658491.
- [133] Tong, R. P., Schiffrers, W. P., Shaw, S. J., Blake, J. R., and Emmony, D. C. “The role of ‘splashing’ in the collapse of a laser-generated cavity near a rigid boundary”. In: *Journal of Fluid Mechanics* 380 (1999), pp. 339–361. ISSN: 0022-1120. DOI: 10.1017/S0022112098003589.
- [134] Toro, E. F. *Riemann Solvers and Numerical Methods for Fluid Dynamics*. Vol. 40. 6. Berlin, Heidelberg: Springer Berlin Heidelberg, 2009, p. 9823. ISBN: 978-3-540-25202-3. DOI: 10.1007/b79761.
- [135] Truesdell, C. *Corrections and Additions to "The Mechanical Foundations of Elasticity and Fluid Dynamics"*. 1953.

- [136] Truesdell, C. “The Simplest Rate Theory of Pure Elasticity”. In: *Communications on Pure and Applied Mathematics* 8.1 (1955), pp. 123–132. ISSN: 0010-3640. DOI: 10.1002/cpa.3160080109.
- [137] Truesdell, C. and Noll, W. *The Non-Linear Field Theories of Mechanics*. Ed. by Antman, S. S. Berlin, Heidelberg: Springer Berlin Heidelberg, 2004. ISBN: 978-3-642-05701-4. DOI: 10.1007/978-3-662-10388-3.
- [138] Trummler, T., Bryngelson, S. H., Schmidmayer, K., Schmidt, S. J., Colonius, T., and Adams, N. A. “Near-surface dynamics of a gas bubble collapsing above a crevice”. In: *Journal of Fluid Mechanics* 899 (2020), A16. ISSN: 0022-1120. DOI: 10.1017/jfm.2020.432. arXiv: 1912.07022.
- [139] Trummler, T., Schmidt, S. J., and Adams, N. A. “Investigation of condensation shocks and re-entrant jet dynamics in a cavitating nozzle flow by Large-Eddy Simulation”. In: *International Journal of Multiphase Flow* 125 (2020), p. 103215. ISSN: 03019322. DOI: 10.1016/j.ijmultiphaseflow.2020.103215.
- [140] Trummler, T., Schmidt, S. J., and Adams, N. A. “Effect of stand-off distance and spatial resolution on the pressure impact of near-wall vapor bubble collapses”. In: *International Journal of Multiphase Flow* 141 (2021), p. 103618. ISSN: 03019322. DOI: 10.1016/j.ijmultiphaseflow.2021.103618. arXiv: 2104.06298.
- [141] Vlaisavljevich, E., Lin, K.-W., Warnez, M. T., Singh, R., Mancina, L., Putnam, A. J., Johnsen, E., Cain, C., and Xu, Z. “Effects of tissue stiffness, ultrasound frequency, and pressure on histotripsy-induced cavitation bubble behavior”. In: *Physics in Medicine and Biology* 60.6 (2015), pp. 2271–2292. ISSN: 0031-9155. DOI: 10.1088/0031-9155/60/6/2271.
- [142] Walters, M. J. and Phillips, T. N. “A non-singular boundary element method for modelling bubble dynamics in viscoelastic fluids”. In: *Journal of Non-Newtonian Fluid Mechanics* 235 (2016), pp. 109–124. ISSN: 03770257. DOI: 10.1016/j.jnnfm.2016.07.012.
- [143] Warnez, M. T. and Johnsen, E. “Numerical modeling of bubble dynamics in viscoelastic media with relaxation”. In: *Physics of Fluids* 27.6 (2015), pp. 1–28. ISSN: 10897666. DOI: 10.1063/1.4922598.
- [144] Xue, S.-C., Phan-Thien, N., and Tanner, R. “Three dimensional numerical simulations of viscoelastic flows through planar contractions”. In: *Journal of Non-Newtonian Fluid Mechanics* 74.1-3 (1998), pp. 195–245. ISSN: 03770257. DOI: 10.1016/S0377-0257(97)00072-4.
- [145] Yang, J., Cramer, H. C., and Franck, C. “Extracting non-linear viscoelastic material properties from violently-collapsing cavitation bubbles”. In: *Extreme Mechanics Letters* 39 (2020), p. 100839. ISSN: 23524316. DOI: 10.1016/j.eml.2020.100839.
- [146] Yang, J., Tzoumaka, A., Murakami, K., Johnsen, E., Henann, D. L., and Franck, C. “Predicting complex nonspherical instability shapes of inertial cavitation bubbles in viscoelastic soft matter”. In: *Physical Review E* 104.4 (2021), p. 045108. ISSN: 2470-0045. DOI: 10.1103/PhysRevE.104.045108. arXiv: 2104.03157.

- [147] Yu, J.-D., Sakai, S., and Sethian, J. “Two-phase viscoelastic jetting”. In: *Journal of Computational Physics* 220.2 (2007), pp. 568–585. ISSN: 00219991. DOI: 10.1016/j.jcp.2006.05.020.
- [148] Yul Yoo, J. and Na, Y. “A numerical study of the planar contraction flow of a viscoelastic fluid using the SIMPLER algorithm”. In: *Journal of Non-Newtonian Fluid Mechanics* 39.1 (1991), pp. 89–106. ISSN: 03770257. DOI: 10.1016/0377-0257(91)80005-5.
- [149] Zeng, Q., Gonzalez-Avila, S. R., Dijkink, R., Koukouvinis, P., Gavaises, M., and Ohl, C.-D. “Wall shear stress from jetting cavitation bubbles”. In: *Journal of Fluid Mechanics* 846 (2018), pp. 341–355. ISSN: 0022-1120. DOI: 10.1017/jfm.2018.286.
- [150] Zilonova, E., Solovchuk, M., and Sheu, T. W. H. “Bubble dynamics in viscoelastic soft tissue in high-intensity focal ultrasound thermal therapy”. In: *Ultrasonics Sonochemistry* 40.35 (2018), pp. 900–911. ISSN: 18732828. DOI: 10.1016/j.ultsonch.2017.08.017.
- [151] Zografos, K., Afonso, A. M., Poole, R. J., and Oliveira, M. S. “A viscoelastic two-phase solver using a phase-field approach”. In: *Journal of Non-Newtonian Fluid Mechanics* 284.August (2020), p. 104364. ISSN: 03770257. DOI: 10.1016/j.jnnfm.2020.104364.
- [152] Zolfaghari, H., Izbassarov, D., and Muradoglu, M. “Simulations of viscoelastic two-phase flows in complex geometries”. In: *Computers and Fluids* 156 (2017), pp. 548–561. ISSN: 00457930. DOI: 10.1016/j.compfluid.2017.05.026.